

Multiscale quasicontinuum modelling of fibrous materials

Citation for published version (APA):

Beex, L. A. A. (2012). *Multiscale quasicontinuum modelling of fibrous materials*. [Phd Thesis 1 (Research TU/e / Graduation TU/e), Mechanical Engineering]. Technische Universiteit Eindhoven.
<https://doi.org/10.6100/IR740053>

DOI:

[10.6100/IR740053](https://doi.org/10.6100/IR740053)

Document status and date:

Published: 01/01/2012

Document Version:

Publisher's PDF, also known as Version of Record (includes final page, issue and volume numbers)

Please check the document version of this publication:

- A submitted manuscript is the version of the article upon submission and before peer-review. There can be important differences between the submitted version and the official published version of record. People interested in the research are advised to contact the author for the final version of the publication, or visit the DOI to the publisher's website.
- The final author version and the galley proof are versions of the publication after peer review.
- The final published version features the final layout of the paper including the volume, issue and page numbers.

[Link to publication](#)

General rights

Copyright and moral rights for the publications made accessible in the public portal are retained by the authors and/or other copyright owners and it is a condition of accessing publications that users recognise and abide by the legal requirements associated with these rights.

- Users may download and print one copy of any publication from the public portal for the purpose of private study or research.
- You may not further distribute the material or use it for any profit-making activity or commercial gain
- You may freely distribute the URL identifying the publication in the public portal.

If the publication is distributed under the terms of Article 25fa of the Dutch Copyright Act, indicated by the "Taverne" license above, please follow below link for the End User Agreement:

www.tue.nl/taverne

Take down policy

If you believe that this document breaches copyright please contact us at:

openaccess@tue.nl

providing details and we will investigate your claim.

Multiscale quasicontinuum modelling
of fibrous materials

Lars Beex

This research is supported by the Dutch Technology Foundation STW, which is the applied science division of NWO, and the Technology Programme of the Ministry of Economic Affairs under Project Nr. 10104.



CIP-DATA LIBRARY TECHNISCHE UNIVERSITEIT EINDHOVEN

Beex, Lars

Multiscale quasicontinuum modelling of fibrous materials

by L.A.A. Beex - Eindhoven, The Netherlands.

Eindhoven University of Technology, 2012.

Proefschrift.

A catalogue record is available from the Eindhoven University of Technology Library.

ISBN: 978-94-6191-434-7

Copyright © 2012 by Lars Beex. All rights reserved.

This thesis is prepared with $\text{\LaTeX} 2_{\epsilon}$.

Cover design: Elitsa Krumova.

Printed by Ipskamp Drukkers BV, Enschede, The Netherlands.

Multiscale quasicontinuum modelling
of fibrous materials

PROEFSCHRIFT

ter verkrijging van de graad van doctor aan de
Technische Universiteit Eindhoven, op gezag van de
rector magnificus, prof.dr.ir. C.J. van Duijn, voor een
commissie aangewezen door het College voor Promoties
in het openbaar te verdedigen op
maandag 29 oktober 2012 om 14.00 uur

door

Lars Alphonsus Antonius Beex

geboren te Tilburg

Dit proefschrift is goedgekeurd door de promotor:

prof.dr.ir. M.G.D. Geers

Copromotor:

dr.ir. R.H.J. Peerlings

Contents

Summary	vii
1 Introduction	1
1.1 Discrete network models	2
1.2 Multiscale approaches	4
1.3 Aim	5
1.4 The QC method in a nutshell	5
1.5 Outline	6
2 Experimental identification of a lattice model for woven fabrics: application to electronic textile	9
2.1 Introduction	10
2.2 In-plane experiments	12
2.3 Lattice model	16
2.4 Identification procedure	18
2.5 Simulation of an out-of-plane punch test	23
2.6 Conclusion	29
3 A discrete network model for bond failure and frictional sliding in fibrous materials	31
3.1 Introduction	32
3.2 Modelling	34
3.3 Numerical implementation	38
3.4 Results	42
3.5 Concluding remarks	49
4 A quasicontinuum methodology for multiscale analyses of discrete microstructural models	51
4.1 Introduction	52
4.2 A quasicontinuum approach for lattice models	54
4.3 Performance study	65
4.4 Conclusion	72

5	Central summation in the quasicontinuum method	75
5.1	Introduction	76
5.2	The quasicontinuum method	78
5.3	Existing summation rules	83
5.4	Relation between the interpolation and the total potential energy	85
5.5	Central summation rule	87
5.6	Algorithm for the central summation rule	91
5.7	Results	93
5.8	Conclusion	102
6	A multiscale quasicontinuum method for dissipative lattice models and discrete networks	107
6.1	Introduction	108
6.2	Structural lattice models with non-conservative interactions	110
6.3	Virtual-power-based quasicontinuum method	116
6.4	Numerical examples	122
6.5	Conclusion	128
7	A multiscale quasicontinuum framework for lattice models with bond failure and fiber sliding	129
7.1	Introduction	130
7.2	Lattice thermodynamics for bond failure and fiber sliding	132
7.3	Virtual-power-based QC method with a mixed formulation	139
7.4	Performance of the QC framework	145
7.5	Conclusion	152
8	Conclusions and outlook	155
8.1	Summary of the results	155
8.2	Application of the virtual-power-based QC method	157
8.3	Future developments	157
A	Partitioning of the linearized system	159
	Bibliography	161
	Samenvatting	173
	Acknowledgements	175
	Curriculum Vitae	177

Summary

Multiscale quasicontinuum modelling of fibrous materials

Structural lattice models and discrete networks of trusses or beams are regularly used to describe the mechanics of fibrous materials. The discrete elements naturally represent individual fibers and yarns present at the mesoscale. Consequently, relevant mesoscale phenomena, e.g. individual fiber failure and bond failure, culminating in macroscopic fracture can be captured adequately. Even macroscopic phenomena, such as large rotations of yarns and the resulting evolving anisotropy, are automatically incorporated in lattice models, whereas they are not trivially established in continuum models of fibrous materials.

Another advantage is that by relatively straightforward means, lattice models can be altered such that each family of discrete elements describes the mechanical response in one characteristic direction of a fibrous material. This ensures for a straightforward experimental identification of the elements' parameters. In this thesis such an approach is adopted for a lattice model of electronic textile. A lattice model for interfiber bond failure and subsequent fiber sliding is also formulated. The thermodynamical basis of this lattice model ensures that it can be used in a consistent manner to investigate the effects of mesoscale parameters, such as the bond strength and the fiber length, on the macroscopic response.

Large-scale (physically relevant) lattice computations are computationally expensive because lattice models are constructed at the mesoscale. Consequently, large-scale computations involve a large number of degrees of freedom (DOFs) and extensive effort to construct the governing equations. Principles of the quasicontinuum (QC) method are employed in this thesis to reduce the computational cost of large-scale lattice computations. The advantage is that the QC method allows the direct and accurate incorporation of local mesoscale phenomena in regions of interest, whereas substantial computational savings are made in regions of less interest. Another advantage is that the QC method completely relies on the lattice model and does not require the formulation of an equivalent continuum description.

The QC method uses interpolation to reduce the number of DOFs and summation rules to reduce the computational cost needed to establish the governing equations. Large

interpolation triangles are used in regions with small displacement fluctuations. In fully resolved regions the dimensions of the interpolation triangles are such that the exact lattice model is captured. Summation rules are used to sample the contribution of all nodes to the governing equations using a small number of sampling nodes. In this thesis, one summation rule is proposed that determines the governing equations exactly, even though a large reduction of the number of sampling points is obtained. This summation rule is efficient for structural lattice models with solely nearest neighbor interactions, but it is inefficient for atomistic lattice computations that include interactions over longer ranges. Therefore, a second 'central' summation rule is proposed, in which significantly fewer sampling points are selected to increase the computational efficiency, at the price of the quality of the approximation.

The QC method was originally proposed for (conservative) atomistic lattice models and is based on energy-minimization. Lattice models for fibrous materials however, are often non-conservative and energy-based QC methods can thus not straightforwardly be used. Examples are the lattice model proposed for woven fabrics and the lattice model to describe interfiber bond failure and subsequent frictional fiber sliding proposed in this thesis. A QC framework is therefore proposed that is based on the virtual-power statement of a non-conservative lattice model. Using the virtual-power statement, dissipative mechanisms can be included in the QC framework while the same summation rules suffice. Its validity is shown for a lattice model with elastoplastic trusses. The virtual-power-based QC method is also adopted to deal with the lattice model for bond failure and subsequent fiber sliding presented in this thesis. In contrast to elastoplastic interactions that are intrinsically local dissipative mechanisms, bond failure and subsequent fiber sliding entail nonlocal dissipative mechanisms. Therefore, the virtual-power-based QC method is also equipped with a mixed formulation in which not only the displacements are interpolated, but also the internal variables associated with dissipation.

Chapter one

Introduction

Fibrous materials are materials consisting of discrete fibers or yarns without a matrix. Fibrous materials are present in many technologically relevant applications, for which the mechanical reliability is a key issue. Examples are (electronic) textile, paper and collagen networks (see Fig. 1.1). For electronic textile for instance, a woven fabric with embedded conductive wires and mounted electronic components [12,29], it is essential that the conductive wires remain connected to the components during manufacture and use. Failure of these connections entails that the electronic components, such as light-emitting-diodes, lack power. This results in a useless product. The mechanical reliability of paper and paperboard products is compromised by the continuous demand for lower grammages and higher fractions of recycled fibers, for economical and environmental reasons [8]. The mechanical properties of cardiac collagen networks are of importance for the diligence of the heart and are for instance used to assess the quality of tissue-engineered heart valves [4].

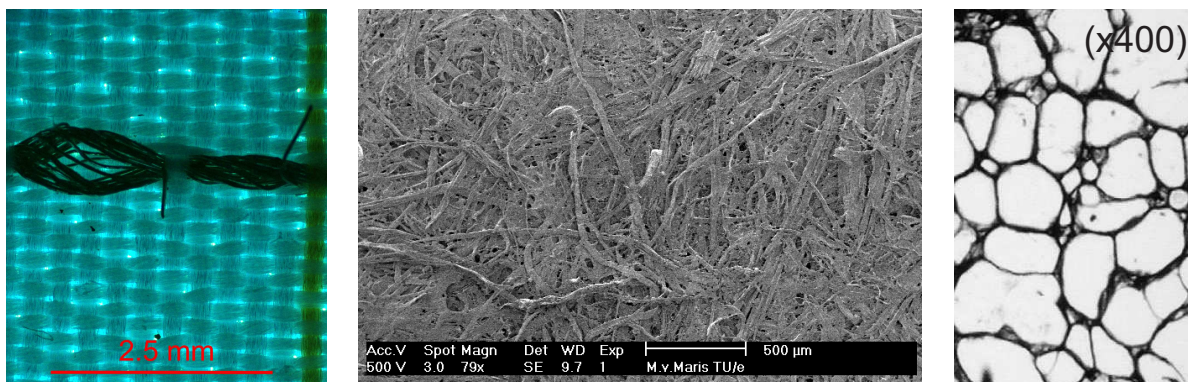


Figure 1.1: Microscopic images of three fibrous materials: (from left to right) electronic textile including a conductive wire in black, paper and cardiac collagen network [105].

The mechanical reliability of products made of fibrous materials is determined by the resistance of the fibrous material (or one of its components) to failure during loading. The failure process of fibrous materials often starts with the failure of an individual fiber [2,26,46,59,73,130,131] or an individual interfiber bond [5,44,52,55,56,59,73,100,123,129]. The failure process is thus initiated at the mesoscale ($\sim \mu m$), most likely influenced by microscale phenomena ($\sim nm$), e.g. defects in fibers, until so many individual fibers and bonds are broken that the response at the macroscale ($mm - m$) is influenced (the scale at which loads are applied in most applications). Hence, several length scales are involved in the failure process of fibrous materials, making it a multiscale process.

Numerical models that describe the mechanical behavior of fibrous materials can be used by manufacturers to assess the mechanical reliability during production and use [8,12,107]. In numerical models, different parameters can straightforwardly be varied to investigate their influence on the mechanical behavior during loading [8,10,13], whereas the influence of different parameters cannot often trivially be studied by experimental methodologies, leading to lengthy and costly product developments. Numerical models are thus important tools for an efficient product development.

1.1 Discrete network models

To virtually assess the mechanical response of fibrous materials in industrial applications, numerical models must thus be able to describe failure. Since failure in fibrous materials initiates at the mesoscale, the numerical models of fibrous materials must include information of the mesoscale behavior. The most straightforward way to accomplish this, is to define the numerical models at the mesoscale, so that the discrete constituents of the fibrous materials are individually incorporated. Since these models take the discrete constituents at the mesoscale into account, they are referred to as discrete network models, or lattice models if they are periodic.

Two examples of discrete network models are shown in Fig. 1.2. In the left image of Fig. 1.2, a discrete model is shown for (electronic) textile (see also ahead to Chapter 2). Each yarn in the textile is represented by a chain of discrete trusses in the model. The trusses, that merely have an axial stiffness, are connected to each other at lattice points (nodes), which are placed at the locations where a yarn makes contact with other yarns. The trusses in horizontal and vertical direction thus represent yarn segments, whereas the diagonal springs introduce rotational stiffness between the yarns when they rotate relative to each other. The discrete network model in the right image of Fig. 1.2 is used to describe the mechanical behavior of paper (see the center image of Fig. 1.1) at the mesoscale [20]. In this model, each paper fiber is represented by a chain of beams, which have a bending stiffness as well as an axial stiffness. As in the lattice model for textile (left in Fig. 1.2), the beams are connected to each other at nodes, that are placed at interfiber bonds.

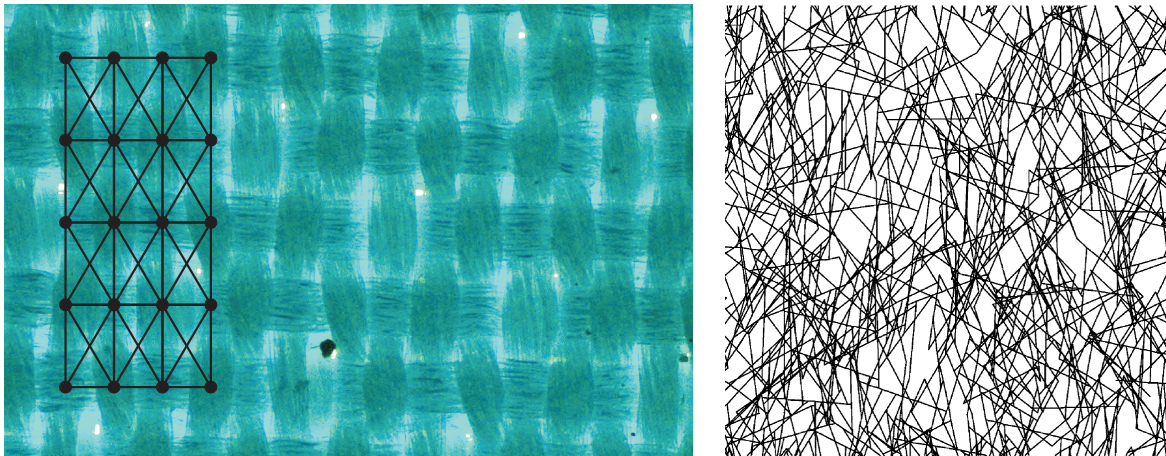


Figure 1.2: Discrete network models for electronic textile, superimposed on the electronic textile, (left) and for paper [20] (right).

Depending on the amount of behavioral detail one desires to incorporate, beams and springs can be modeled elastically, elastoplastically, rate-dependent, temperature-dependent etcetera. In several discrete network models, the individual elements (beams or trusses) fail if a critical stress is reached to describe failure at the mesoscale, see e.g. [26]. Another way to describe failure at the mesoscale, depending on the fibrous material, is to use interfiber bond models. Interfiber bonds, present in the lattice points, can be assumed perfect (see e.g. Chapter 2 and [20,107]) or to fail if their critical strength is reached (see e.g. Chapter 3 and [73,100]). Frictional fiber sliding often occurs after an interfiber bond has been broken, which can be incorporated in discrete models as well (as discussed in Chapter 3).

Discrete network models are thus able to capture (local) mechanical mesoscale phenomena that occur in fibrous materials, whereas they are not trivially incorporated in continuum models (that regard fibrous materials as a uniform material). Even global phenomena, such as large fiber and yarn rotations that are naturally incorporated in network models, are complex to take on board in continuum models [96,117,118]. Although microscale phenomena of fibrous materials, e.g. defects in fibers, cannot explicitly be incorporated in mesoscale network models, they can implicitly be dealt with. Several microscale phenomena can be lumped into the mechanical behavior of the discrete elements (beams or trusses) or that of the interfiber bonds. Defects, that locally soften fibers, can for instance be dealt with by adopting a distribution of the failure strengths of the discrete elements.

A disadvantage of discrete models is their computational cost for large-scale, physically relevant computations. The reason is that the discrete models are constructed at the mesoscale, while loads in many applications are applied at the macroscale. This leads to large computations, because of the large number of degrees of freedom (DOFs) and the substantial computational effort to construct the governing equations. In [72] for example, computation times of two weeks on a supercomputer are reported. The large

number of DOFs originates from the displacements of all lattice points and renders the governing equations costly to solve. The large computational effort to construct the governing equations originate from the fact that all discrete constituents of the model need to be visited to construct these equations.

1.2 Multiscale approaches

Multiscale techniques, that can use discrete network models at the mesoscale in combination with macroscale frameworks to prescribe loads, can be adopted to increase the efficiency of large-scale network computations. In [113], a classical homogenization scheme is used for a discrete model of a collagen network. Classical homogenization schemes are able to capture macroscale properties such as the effective stiffness, but they are unable to capture discrete events at the mesoscale, such as the failure of a single fiber. In another multiscale approach, continuum descriptions (discretized by finite elements) are coupled to network models in regions of interest. This is for instance used in [46] to model ballistic impact of a woven textile. Failure of discrete fibers and bonds can be modeled by such multiscale schemes in regions in which the discrete network model is used. Disadvantages are that the required continuum models for fibrous materials are not straightforwardly formulated and the non-trivial procedure to couple continuum regions to regions in which the network model is used.

Other multiscale approaches that seem promising for network models and lattice models of fibrous materials are methodologies developed for atomistic lattice computations. Similar to discrete models of fibrous materials after all, atomistic lattice models also include discrete interactions. Several of these methodologies combine continuum descriptions with network models, so these also have the drawbacks mentioned above [27,38,125]. An exception is the quasicontinuum (QC) method, which only relies on the discrete atomistic model [68,69,82,83,114,115]. Conveniently, a continuum description is thus not required. Several QC methods still require a coupling procedure for the internal interface between coarse domains and fully resolved domains of interest [108,109,114,115], but a number lack of such an internal interface [36,43,64]. A number of QC methodologies, amongst which those in this thesis, are thus convenient for discrete network models of fibrous materials, because they

- allow the accurate incorporation of the lattice model in regions of interest,
- completely rely on the lattice model and not on accompanying continuum descriptions that can be complex to formulate for fibrous materials and
- do not require an internal interface coupling or handshaking procedure.

1.3 Aim

The aim of this thesis is to establish a QC framework that can deal with discrete models of fibrous materials. The QC frameworks proposed so far in literature (see e.g. [36,64,82,83,108,114,115,127]), only treat conservative atomistic lattice models (that only include reversible interactions). Discrete network models and lattice models of fibrous materials however, often require dissipative mechanisms (e.g. those proposed in Chapters 2 & 3) and can thus not straightforwardly be incorporated in existing QC methodologies.

The proposed QC frameworks do not focus on the discrete model of a specific fibrous material, but are aimed to be general multiscale tools in which several discrete models of fibrous materials can straightforwardly be incorporated. A disadvantage of the fact that QC methodologies originate from atomistic computations is that they can only deal with lattice models (i.e. periodic network models such as that on the left in Fig. 1.2). On the other hand, a substantial number of fibrous materials have a periodic structure and are thus appropriate for the QC method. Furthermore, periodic lattice models are still relevant and useful models of non-periodic fibrous materials (see e.g. Chapter 3) and at least incorporate the intrinsic discreteness of non-periodic fibrous materials.

1.4 The QC method in a nutshell

The QC method uses two reductions steps to improve the computational efficiency of full lattice computations (see Fig. 1.3). First, only a small number of lattice points (reppoints) is selected to represent the displacements of all points in the lattice. The reppoints constrain the displacements of the points in between them by means of interpolation. The displacement components of the reppoints are the only remaining degrees of freedom (DOFs) of the interpolated lattice. In regions where the local deformations are small, it suffices to select few reppoints at large intervals. On the other hand, every point constitutes a reppoint in fully resolved regions, so that the exact discrete model is recovered in these regions of interest.

The second reduction step introduced in the QC method (see again Fig. 1.3) is the selection of only a small number of lattice points to approximate the governing equations, instead of visiting all lattice points to compute them exactly. The small number of lattice points used for the approximation are referred to as sampling points and the procedure that selects them as a summation rule. The sampling points are used to estimate the contribution to the governing equations of the points in their vicinity. To ensure an accurate estimate, the selection of sampling points must be carefully performed with respect to the interpolation triangulation. If this is not the case, zero-energy modes may occur [64].

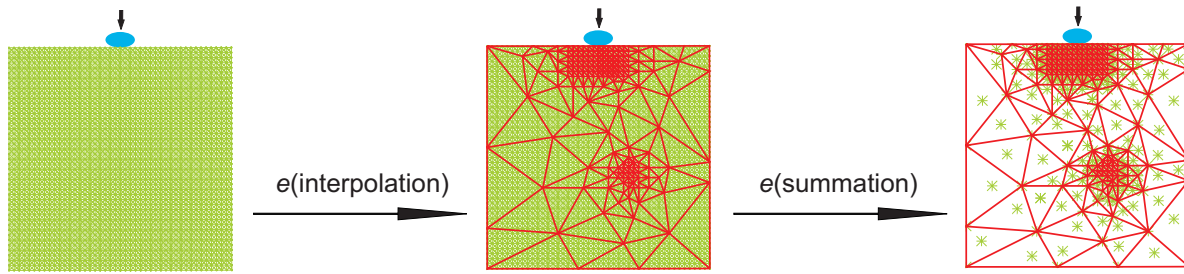


Figure 1.3: Schematic representation of the two reduction steps in the QC method. In the left image, the full lattice model is shown. In the center image, an interpolation triangulation is superimposed on the lattice model and a small number of lattice points are used to sample the governing equations in the right image. During both reduction steps an error, e , may be introduced.

1.5 Outline

The outline of this thesis is as follows. In Chapters 2 & 3, two different discrete network models are discussed. The discrete model in Chapter 2 is a lattice model for woven fabrics and is applied to electronic textile. It is constructed such that the experimental identification of the discrete elements' parameters is straightforward. The parameters of the three families of discrete elements can separately be determined by three types of tensile tests. The lattice model and its experimental parameter identification are validated based on an out-of-plane punch experiment on an electronic textile.

In Chapter 3, a discrete network model for bond failure and subsequent frictional fiber sliding is proposed. Whereas existing discrete models for bond failure and subsequent fiber sliding are somewhat ad hoc [52,73], the thermodynamical basis of the proposed model ensures that the effects of different mesoscale parameters can be investigated in a consistent manner. The capabilities of the model are demonstrated by varying mesoscale parameters such as the bond strength, fiber length and aspect ratio of a unit cell and studying the effect on the overall response.

In Chapters 4 & 5, different summation rules (i.e. selections of sampling points, see the second step in Fig. 1.3) are proposed. Several summation rules have been proposed in literature [36,43,64,83,108,109,114], but many have the disadvantage that an internal interface occurs between coarse and fully resolved domains [83,108,109,114]. This is a disadvantage, because they necessitate corrective interface procedures which come with additional assumptions and need to be updated if adaptive remeshing is used. Those methods that lack an internal interface [36,64], have a poor accuracy.

In Chapter 4 therefore, a summation rule is proposed that lacks an internal interface and determines the governing equations exactly. Nevertheless, the computational cost is substantially reduced for lattice models of fibrous materials with nearest neighbor interactions. If this summation rule is applied to atomistic lattice models, characterized by longer-range interactions, however, the achieved computational efficiency is still unsatisfactory. Therefore, a second summation rule is proposed in Chapter 5 for lattice

models with interactions at longer distances. This summation rule is referred to as the central summation rule, since the focus of this second summation rule is on the interiors of the interpolation triangles, in contrast to other summation rules that lack an internal interface [36,43,64].

So far, all QC methods are developed for (conservative) atomistic lattices and are based on energy minimization or force equilibrium (that originates from energy minimization). Lattice models of fibrous materials however often include dissipation and thus cannot be used in traditional QC methodologies. In Chapters 6 & 7 therefore, QC frameworks are proposed for (non-conservative) lattice models that include dissipation. In this way, discrepancies in the governing equations of force-based QC frameworks, that at first sight seem suitable for non-conservative lattice models, are avoided. The possibilities of the virtual-power-based QC method for a lattice model with local dissipative mechanisms are shown in Chapter 6. The lattice model considered in this chapter is a periodic network of elastoplastic trusses, similar to that proposed in Chapter 2 for woven fabrics.

In Chapter 7, the virtual-power-based QC methodology is adopted to deal with the lattice model for bond failure and subsequent fiber sliding proposed in Chapter 3. Since bond failure and subsequent fiber sliding entail non-local dissipative mechanisms (in contrast to the local dissipative mechanisms considered in Chapter 6), the virtual-power-based QC formulation in Chapter 7 is equipped with a mixed formulation. In this mixed framework, the displacement components of the lattice points are interpolated, as well as the dissipation variables. Previously proposed summation rules can still be used, because the interpolation used for the displacement components, is also used for the dissipation variables.

Finally, conclusions and the potential of the proposed QC frameworks are presented in Chapter 8. Also, recommendations for future developments of the presented virtual-power-based QC methodologies for other discrete models of fibrous materials are discussed.

Chapter two

Experimental identification of a lattice model for woven fabrics: application to electronic textile¹

Abstract

Lattice models employing trusses and beams are suitable to investigate the mechanical behavior of woven fabrics. The discrete features of the mesostructures of woven fabrics are naturally incorporated by the discrete elements of lattice models. In this chapter, a lattice model for woven materials is formulated which consists of a network of trusses in warp and weft direction, that represent the response of the yarns. Additional diagonal trusses are included that provide resistance against relative rotation of the yarns. The parameters of these families of discrete elements can separately be identified from tensile experiments in three in-plane directions which correspond to the orientations of the discrete elements. The lattice model and the identification approach are applied to electronic textile. This is a fabric in which conductive wires are incorporated to allow the embedding of electronic components such as light-emitting-diodes. The model parameters are based on tensile tests on samples of the electronic textile. A comparison between the experimental results of an out-of-plane punch test and the simulation results shows that the lattice model and its characterization procedure are accurate until extensive biaxial tensile deformation occurs.

¹ Reproduced from: L.A.A. Beex, C.W. Verberne, R.H.J. Peerlings, Experimental identification of a lattice model for woven fabrics: application to electronic textile, Submitted to Composites Part A.

2.1 Introduction

Woven materials are frequently used, for instance in clothing, bullet-proof armor and reinforced polymeric and ceramic materials. A relatively new application is electronic textile [29,35,79]. Electronic textiles are textiles which contain electronic components, such as light-emitting-diodes, sensors, switches, etcetera. The woven fabric acts as a compliant substrate for the electronic components and conductive wires are woven into it, in order to electrically connect the individual electronic components. These conductive wires and the connections of the conductive wires with the electronic components must stay intact during manufacturing and use, since failure of the wires and connections entails a malfunctioning product. Mechanical models can be used to study the mechanical interplay between the different constituents of electronic textile.

To model the mechanical behavior of woven materials, different approaches can be used. Woven materials can for instance be investigated by performing finite element simulations on a single unit cell, in which the yarns are discretized in a detailed manner so that, amongst others, yarn-to-yarn interactions are incorporated [74,75,99]. A limitation of these detailed simulations is their computational cost, which prohibits large-scale simulations.

On the other hand, continuum models are often used for large-scale simulations of woven materials [3,6,63]. They are suitable for large-scale problems, because the discrete yarns are not taken into account individually, but only in an average sense. A disadvantage of continuum models for woven materials is their inability to capture local (discrete) events, such as yarn failure and sliding of yarns. This is an important drawback for the study of electronic textile because the conductive wires are individual, small but relevant features. Other disadvantages are the relatively complex incorporation of large rotations [96] and the occurrence of numerical difficulties such as locking [118].

Lattice models that employ trusses or beams offer a more natural, intermediate description for woven materials. The discrete members of the mesostructure of these materials are represented by discrete elements such as trusses or beams in these models [14,60,107]. An example of a lattice model for a woven fabric is shown in Fig. 2.1, superimposed on an image of a textile. An individual yarn segment is modeled by a discrete element, such as a spring. At the yarn-to-yarn contacts, the discrete elements are connected to each other by nodes. The diagonal elements provide the lattice with shear stiffness. In this way the shear stiffness of the fabric, that comes into play if the yarns rotate relative to each other, can be modeled. Local events, such as slip in the member-to-member interaction [14,73] and failure of individual members, can be taken into account in a natural manner in lattice models [73], whereas they are complex to include in continuum models. Furthermore, the high computational cost of detailed sub-yarn models is avoided. An overview of several lattice models is given in [91].

Large-scale lattice computations may still be computationally costly. To overcome this, unit cells of lattice models often represent several unit cells of the woven material, i.e. one truss or beam represents several parallel yarns [107]. In some studies [17,18,45], the response of the lattice model is translated to the response of a finite element, that

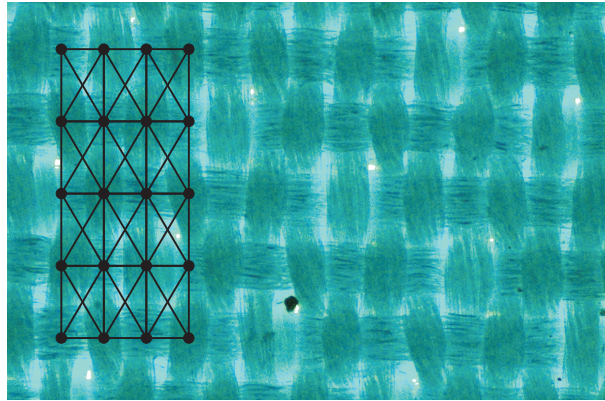


Figure 2.1: A woven fabric (blue) with 12 unit cells of a lattice model superimposed on it (black). The black lines represent springs or beams which are fixed to each other at nodes (black dots).

is also used to represent a number of unit cells. Local events such as element failure can no longer be incorporated in these approaches, but they can still easily deal with large rotations [107] and locking [45,107]. Also a number of multiscale approaches can be used to increase the efficiency of large-scale computations [9,46,88].

Identification approaches to establish the parameters of the different discrete elements in lattice models can be complex, since the discrete elements are all mechanically connected. Consequently, they influence each other during the experimental parameter identification. Identification approaches can therefore be somewhat elaborate [18,106,107]. In this chapter, a rather general two-dimensional lattice model for woven materials is proposed, that can be characterized in a straightforward manner. From three types of in-plane tensile tests, that are performed in the orientations of the three families of discrete elements, the parameters of the discrete elements are individually established. In this way, no (complex) inverse problem has to be solved to establish the material parameters.

In order to separately identify the discrete elements, the mutual influence must be negligible. To this end, the compressive responses of all elements in the lattice model proposed in this chapter vanish. The lattice model and its identification procedure are applied to a woven electronic textile including conductive wires, but it can be used for any woven material that is characterized by a compliant shear stiffness relative to the axial stiffness, e.g. metal grids to reinforce concrete [47].

The outline of this chapter is as follows. First the electronic textile is described and the in-plane experiments on the electronic textile are discussed. Also the fabric strains at which the conductive wires fail are identified. Subsequently, the lattice model is detailed and the identification procedure is discussed. In Section 2.5, the lattice model including the identification procedure is validated by a three-dimensional punch test. Overall experimental and predicted deformations are compared, as well as the experimental and numerically predicted punch-force/punch-displacement curves; failure of the conductive wires is also evaluated. Finally, conclusions are presented.

2.2 In-plane experiments

The fabric considered here is an electronic textile produced by TiTV (www.titv-greiz.de). It is a densely woven fabric with embedded conductive wires (see Fig. 2.2). The conductive wires are predominantly oriented in warp direction and on average one wire is present on 65 warp yarns. In weft direction an insignificant number of conductive wires is present. The conductive wires consist of copper filaments (see Fig. 2.2). At regular intervals they have some clearance with respect to the textile to allow the mounting of electronic components (see Fig. 2.2). The textile yarns of the fabric contain different fibers of dtex 76. The yarns in warp direction are turned 600 times per meter and those in weft direction are turned 120 times per meter. The density of the warp and weft yarns is 11000 m^{-1} and 8900 m^{-1} respectively. The warp and weft yarns are woven in a three layer pattern.

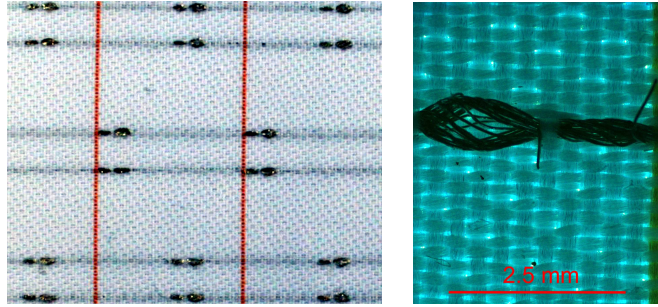


Figure 2.2: (Left) the electronic textile with the warp direction in horizontal direction and (right) a microscopic image of the electronic textile. The conductive wires are mainly oriented in warp direction. The clearance of the conductive wires is clearly visible.

2.2.1 Methodology

Tensile test samples of the electronic textile (including the conductive wires) of $100 \times 29\text{ mm}^2$ are taken in three directions; in warp and weft direction and at an angle of 45° with respect to the warp direction. The tensile test in the latter direction corresponds to the bias extension test [96,106]. The nominal thickness of the samples is measured as 0.35 mm , although this thickness is somewhat arbitrary since the samples are highly heterogeneous. The samples are fixed in between two clamps with a rough surface, together with one piece of double-sided tape to increase the fixation. The gauge length of all samples is approximately 60 mm . The used tensile tester (Instron 5566) has a load cell of 500 N . The strain rate in the experiments in warp and weft direction is $1.67 \cdot 10^{-3}\text{ s}^{-1}$ and in diagonal direction $3.33 \cdot 10^{-3}\text{ s}^{-1}$. The tensile tests are performed up to different strains.

During the experiments, images of the strained samples are recorded, to which an optical strain measurement technique is applied to determine the local strains. Undesired effects such as slip in the clamps and deformation of the load cell are therefore circumvented in the strain measurement. Furthermore, in the tensile test in diagonal direction (bias extension test), the pure shear strains that only occur in region C in Fig. 2.3, as is well described in literature [96,106,118], can be established without any influence of the constraining influence of the clamps (in regions A and B). To determine the engineering stress of the samples the measured cell force and the original nominal cross-sectional area are used.

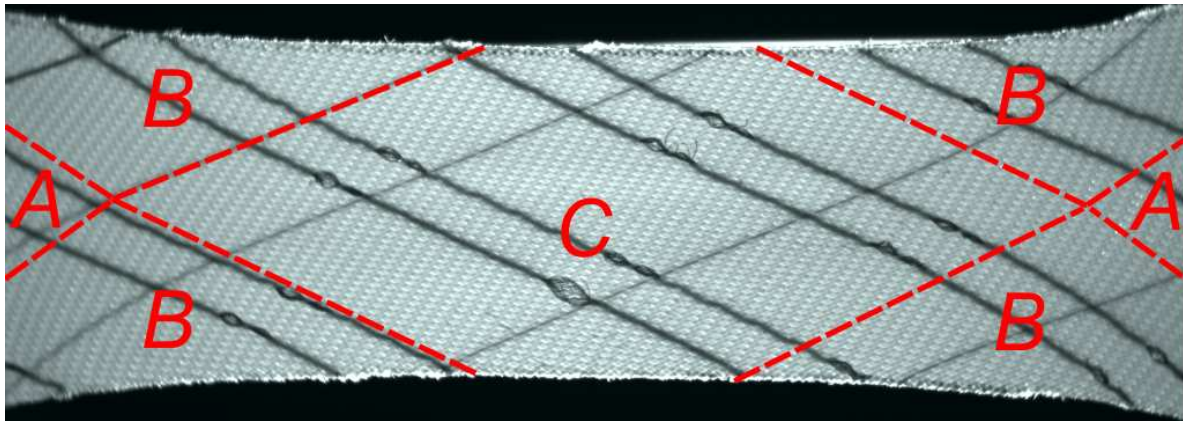


Figure 2.3: Three deformation modes (A, B and C) occur in the samples during the bias extension tests due to the influence of clamping. The conductive wires are shown in black while the red yarns (shown in grey) correspond to regular weft yarns as in Fig. 2.2.

To investigate the failure of the conductive wires within the fabric, X-ray images are made (Phoenix PCB analyzer, using 60 kV and 20 μm) after the tensile tests in warp direction. Although these images are not direct input for the experimental identification, they are used in Section 2.5 to evaluate the lattice model and the identification procedure.

2.2.2 In-plane stress-strain responses

The engineering stress-engineering strain responses of the in-plane tensile experiments are shown in Fig. 2.4. Only one response is shown in each direction; the experimental scatter of each response is relatively small [122].

The responses in warp and weft direction show similar levels of stress for the same applied strain level. However, the shapes of the curves are clearly different from each other (see Fig. 2.4). The warp response shows a nonlinear loading behavior, whereas the loading behavior of the weft direction is virtually linear. Tensile tests on single yarns and single conductive wires (both not shown here) have indicated that this different

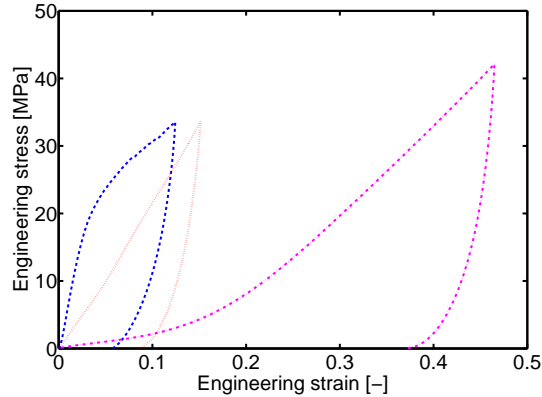


Figure 2.4: Engineering stress-engineering strain responses of the electronic textile in warp (dashed), weft (dotted) and diagonal direction (dashed-dotted).

behavior is caused by the different warp and weft yarns; they are both made from the same material, but have a different number of turns per meter. It can also be shown that the conductive wires hardly influence the macroscopic response in warp direction. All unloading responses show that a large amount of inelastic deformation has occurred during the tensile tests.

The diagonal direction exhibits an initially extremely compliant response, which stiffens at a strain of approximately 14% (see Fig. 2.4). This compliant shear behavior is typical for woven materials and also occurs for instance in woven grids to reinforce concrete [47]. The response is determined by the rotation of the warp and weft yarns relative to each other. Initially, this rotation solely experiences friction in the yarn-to-yarn. However, at higher levels of strain, and thus larger rotations, the warp and weft yarns start to make contact with each other, leading to an increasingly stiffer response. In the densely woven fabric considered here this effect occurs at moderate strains, but for less densely woven fabrics it occurs later and the nonlinear response is more pronounced [107].

2.2.3 Failure of the conductive wires

X-ray images of the electronic textile samples after the tensile experiments in warp direction are presented in Fig. 2.5. At the location where the conductive wires have some clearance, the copper filaments in each wire can be distinguished. Plastic deformation and failure of the conductive wires can only be observed at the clearances.

For the undeformed sample and the samples strained to 2% and 6% (engineering strain), no failure of the wires can be seen. Although the sample that is strained to 6% clearly shows plastic deformation in the wires, the wires are still intact and their conductivity is unaffected.

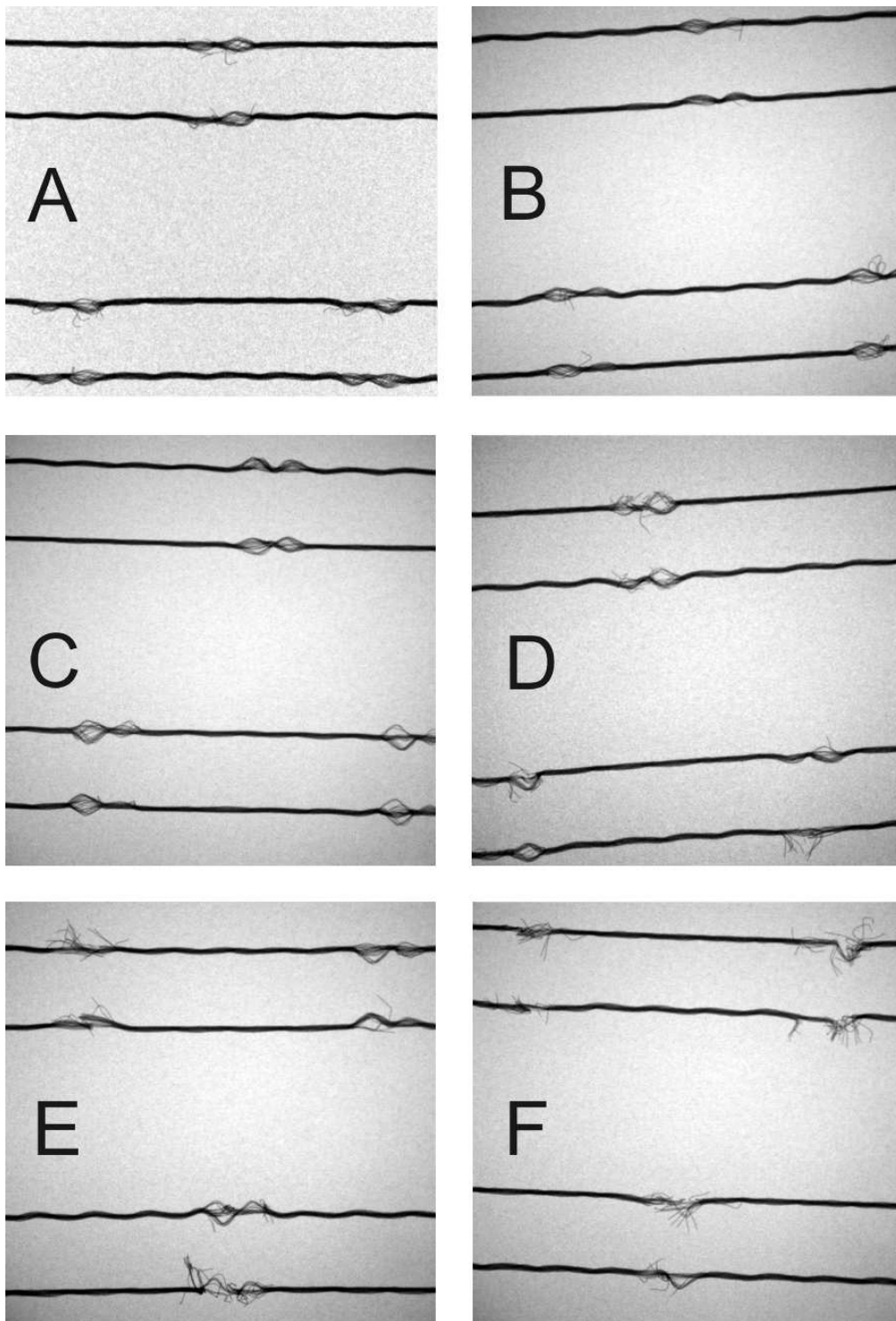


Figure 2.5: X-ray images of an undeformed sample (A) and after 2% (B), 6% (C), 7% (D), 8% (E) and 9% (F) straining in warp direction. The conductive wires can be distinguished, but not the woven fabric.

Failure of the wires starts at a strain of approximately 7%, as becomes clear from image D in Fig. 2.5. A number of copper filaments in the conductive wires are broken at the clearance of the wires. For larger strains the number of broken filaments increases and in some cases all filaments of a conductive wire are broken, so that no electrical contact is made anymore.

2.3 Lattice model

A unit cell of the proposed two-dimensional lattice model for the electronic fabric is shown in Fig. 2.6. The tow truss elements represent warp and weft yarn segments from one yarn-yarn crossing to the location of the next one. The unit cell's dimensions match the dimensions of the unit cell of the discrete mesostructure of the fabric, i.e. each yarn is represented explicitly by a (chain of) truss(es).

The diagonal trusses provide the unit cell with shear stiffness, in correspondence with the lattice model of Sharma and Sutcliffe [107], except that two diagonal elements are used instead of one. The advantage of using two diagonal elements per unit cell is that uniaxial deformation in warp and weft direction can be described at the scale of a single unit cell. In contrast to the lattice model in [61], out-of-plane phenomena such as out-of-plane contraction and undulation are not specifically modeled, but the influence of out-of-plane mechanisms on the in-plane responses are incorporated in the material descriptions of the truss elements. The out-of-plane bending stiffness is not captured however, but this is rather compliant. Furthermore, no conductive wires are individually modeled in the lattice model, since they hardly contribute to the response [122] due to their small number (one conductive wire is present on 65 warp yarns).

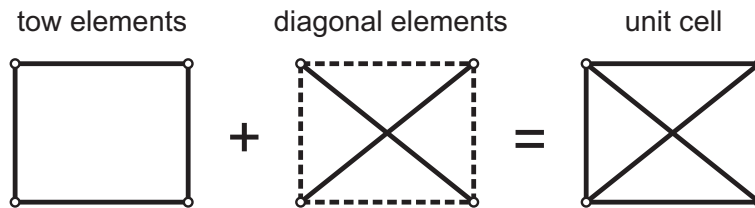


Figure 2.6: Four tow elements, representing the yarns (left), and two diagonal elements (center), providing shear stiffness, are used in a rectangular unit cell of the lattice model (right).

In the lattice model the (discrete) yarn segments, represented by the tow truss elements, carry no force when they are compressed. The reason for this is that it is assumed that they buckle as soon as they are loaded in compression. Also the diagonal truss elements are considered to carry no force in compression. As a result, the simple shear loading only charges one diagonal truss element while the other one is compressed without axial stress (see ahead to the right image in Fig. 2.8).

Since the Hencky strain is used in the numerical implementation (MSC.Marc), the axial strains of the individual trusses are expressed in terms of it:

$$\epsilon = \ln(\lambda) \quad (2.1)$$

where $\lambda = l/l_0$ is the axial stretch factor, with l and l_0 the current and initial length respectively. Since inelastic deformation occurs in the stress-strain responses of Fig. 2.4, an elastoplastic model is adopted for the trusses. The axial strain can be split in an elastic and plastic part as follows:

$$\epsilon = \epsilon_e + \epsilon_p \quad (2.2)$$

where ϵ_e is the axial elastic Hencky strain and ϵ_p the axial plastic Hencky strain.

The elastic response in each truss is governed by Hooke's law as follows:

$$\sigma = E \epsilon_e \quad (2.3)$$

where σ represents the axial true stress and E is the Young's modulus of the material. The lateral contraction due to elastic straining is neglected. The plastic deformation, on the other hand, is assumed to be incompressible. The true stress in a truss can therefore be determined from the engineering stress via the following expression:

$$\sigma = \sigma_{eng} \lambda_p \quad (2.4)$$

where σ_{eng} is the axial engineering stress and $\lambda_p = \exp(\epsilon_p)$ is the axial plastic elongation factor.

Because the typical nonlinear responses in the different directions in Fig. 2.4 show that the material behaves plastically from the very beginning of loading, the loading response of the trusses is described by plastic hardening. The elastic part of the constitutive model is used to describe the unloading response. To this end, a low initial yield stress, σ_{y0} , is used and the hardening law is progressive. This is schematically shown in Fig. 2.7.

At this point the precise hardening law is not yet formulated since the most suitable hardening law appears out of the identification procedure. For this reason, the current yield stress, σ_y , of the three types of truss elements remains a yet to be defined function of the equivalent plastic strain, $\bar{\epsilon}_p$, i.e. $\sigma_y(\bar{\epsilon}_p)$.

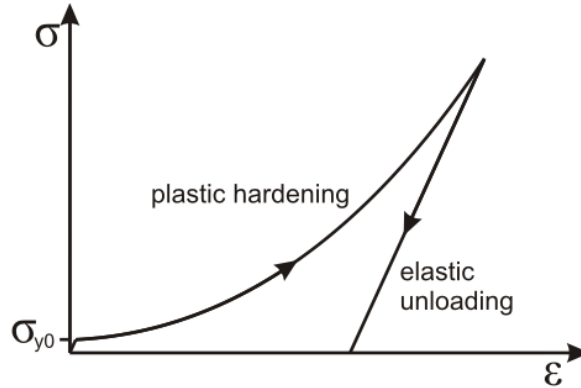


Figure 2.7: Schematic illustration of the uniaxial stress-strain response of the material description used for the trusses. The initial yield stress is indicated by σ_{y0} .

The lattice model is implemented in the software package MSC.Marc. The implementation uses an updated Lagrange approach to deal with large deformations and rotations. The current local axes and cross-sectional area of the truss elements are updated every iteration. The Mohr-Coulomb criterion is used to distinguish between tension and compression; its parameters are selected such that in compression the responses of the truss are negligible.

2.4 Identification procedure

Considering uniaxial loading in warp and weft direction of a single unit cell (see the left and center image in Fig. 2.8), it can be observed that only the discrete elements oriented in the loading direction contribute to the mechanical response. The reason for this is that the shear response (modeled by the diagonal elements) is compliant (the dashed-dotted curve in Fig. 2.4) compared to the response in warp and weft direction (the other two curves in Fig. 2.4). The diagonal elements may thus be expected to have a comparatively low stiffness. As a result only the elements oriented in the loading direction contribute to mechanical response during warp and weft loading. Note that, although the stiffness of the diagonal elements increases for strains larger than 14% (see Fig. 2.4), this strain is not exceeded, since the warp and weft strains in Fig. 2.4 remain below 14%.

On the other hand, for the bias extension test (see the right image in Fig. 2.8), only the diagonal element that is oriented in the loading direction contributes to the mechanical response. The reason for this is that the four stiffer elements, that represent yarn segments, act as a mechanism. The diagonal element oriented orthogonally to the loading direction is compressed without stress, since no resistance against compression is assumed in the lattice model.

During the three in-plane tests discussed in Section 2.2, it is thus reasonable to assume

that only the elements oriented in the respective loading directions contribute to the mechanical response. The conditions for this assumption to hold are, as mentioned above, that the intrinsic material behavior of the fabric shows a compliant shear response compared to the in-plane principal directions and that the elements under compression show no stress. The results from the three in-plane tests in Fig. 2.4 can now directly be used to determine the parameters of the three families of discrete elements associated with the three directions. Below it will be explained how the parameters of each family of elements can be established based on these tensile test results.

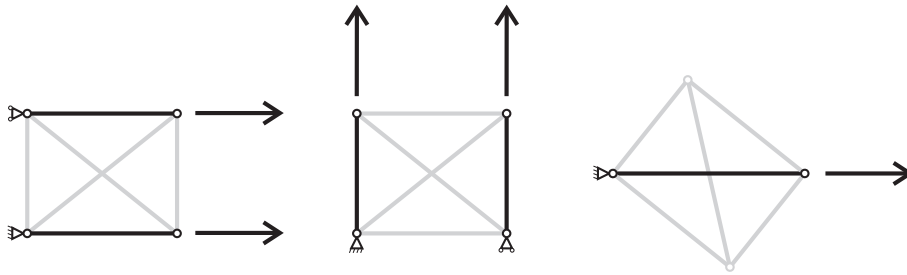


Figure 2.8: Schematic representation of three in-plane loading situations for the identification procedure in which only the truss elements oriented in the loading direction contribute to the response (black). The other truss elements (grey) are inactive or contribute negligibly. The left image represents loading in warp direction, the center image loading in weft direction and the right image diagonal loading.

Although the diagonal truss elements are oriented at an angle of 29° with respect to the warp elements and the diagonal tensile tests (bias extension tests) are performed at an angle of 45° to the warp direction, the stress-strain responses from the bias extensions tests are directly used for the identification of the parameters of the diagonal trusses. Clearly, this difference in angle is not optimal, but the predicted unit cell responses nevertheless match the experimental responses well (see ahead to Fig. 2.12).

2.4.1 From global stress to element stress

Before the material parameters of the different families of truss elements can be established, the geometric parameters are set. The nominal initial area, A_0 , of all trusses is set to 0.0155 mm^2 . This value is in the order of magnitude of the actual yarns. In principle, since only the force transmitted by the trusses matters, any diameter can be selected as long as it is dealt with in a consistent manner. The length of the elements, l_0 , is based on the microscopic images of Fig. 2.2. The geometric parameters are presented in Table 2.1.

Before the parameters of the discrete members can be fitted, first the engineering stresses obtained from the tensile tests, $\sigma_{eng,t}$ (see Fig. 2.4), must be converted to the engineering stresses of the individual discrete elements, σ_{eng} . The reason is that the engineering stresses obtained from the tensile tests, $\sigma_{eng,t}$ (see Fig. 2.4), are computed as if the

electronic textile is a continuum, whereas the engineering stresses of the discrete members are needed (see Fig. 2.9). Therefore, the ratio between the yarn area, A_0 , and the nominal cross-sectional area of the textile, A_n , must be taken into account as follows:

$$\sigma_{eng} = \frac{\sigma_{eng,t} A_n}{A_0} \quad (2.5)$$

where A_n is the nominal area associated with a single discrete element (see Fig. 2.9).

The areas are determined based on the in-plane dimensions of the unit cell (see Fig. 2.2), the dimensions of the yarns and the thickness of the electronic textile; they can be found in Table 2.1.

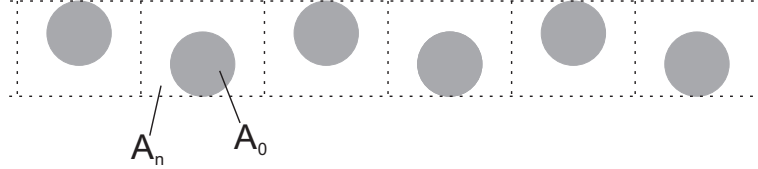


Figure 2.9: A schematic representation of a cross section of the fabric in out-of-plane direction. The (initial) area of an element is represented by A_0 and the nominal area associated with it by A_n .

2.4.2 Elastic behavior

Now that the engineering stresses of the elements can be determined, the three Young's moduli can be fitted. As mentioned before, the elastic part of the constitutive model is used to describe the three unloading responses. One has to take into account that at the moment that unloading takes place, the cross-sectional area is deformed, since during loading plastic deformation occurs in an incompressible manner. The true stress at the moment of unloading must thus be employed to fit the Young's moduli. To determine this true stress, it is assumed that all strain applied until the point of unloading is plastic strain and λ_p in Eq. (2.4) may thus be replaced by λ . The Young's moduli are fitted on the highest 40% (in terms of stress) of the unloading responses. The resulting curves and the fits of the moduli are shown in Fig. 2.10. The values of the moduli are given in Table 2.1.

2.4.3 Plastic behavior

To ensure that the plastic part of the constitutive model of the elements is used for the entire loading responses, small yield stresses are used for all three families of elements

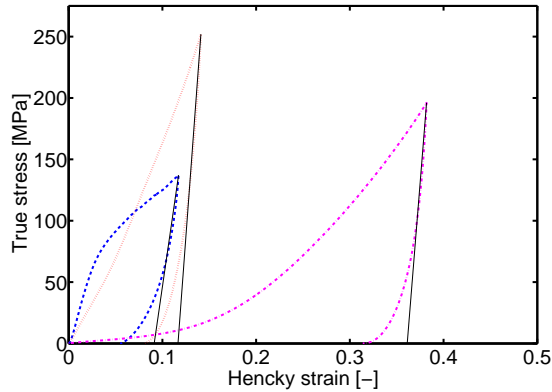


Figure 2.10: The true stress as a function of the total Hencky strain of the individual elements in warp (dashed), weft (dotted) and diagonal direction (dashed-dotted) and the corresponding fits of the Young's moduli (solid).

(see Table 2.1). A lower value than 0.2 MPa is theoretically desired, but smaller values lead to convergence problems in the final validation simulation as described in Section 2.5. Furthermore, this yield stress is sufficiently small for accurate fits (see ahead to Fig. 2.12).

To determine which hardening law can be used and to fit its parameters, the true stress-equivalent plastic strain curves are presented in a log-log diagram in Fig. 2.11. The (effective) plastic strain has been determined by subtracting, at each level of stress, the elastic strain as given by the Young's moduli determined above from the total strain. The following exponential relation seems suitable for the hardening behavior of the three responses, since the log-log diagrams are more or less linear in the regimes of influence:

$$\sigma_y = \sigma_{y0} + H(\bar{\epsilon}_p)^n \quad (2.6)$$

where $\sigma_{y0} \approx 0$ is the initial yield stress and H and n are hardening parameters. The resulting fits of the hardening behavior and the corresponding parameters are shown in Fig. 2.11 and Table 2.1 respectively.

2.4.4 Validation of the unit cell response

The responses of a unit cell of the lattice model in the three tested directions are shown together with the experimental responses in Fig. 2.12. In the lattice model, the linear Mohr-Coulomb criterion is used to make the compressive responses of the individual elements ten times more compliant than the tensile responses. The in-plane stress-strain curves in warp and weft direction, as well as the major part of the response in diagonal (45°) direction correspond well with the experimental curves. Only the final

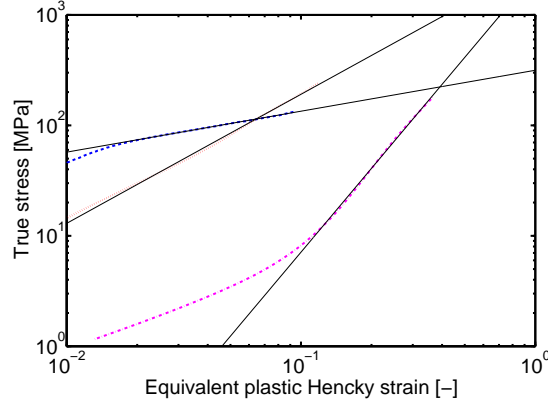


Figure 2.11: Log-log diagram of the true stress of the discrete elements as a function of the equivalent plastic Hencky strain in warp (blue, dashed), weft (red, dotted) and diagonal direction (magenta, dashed-dotted) and the fits of the hardening behavior (black, solid).

Table 2.1: Established parameters of the three families of elements.

	warp	weft	diagonal
A_0 [mm^2]	0.0155	0.0155	0.0155
l_0 [mm]	0.288	0.161	0.330
A_n [mm^2]	0.0563	0.1008	0.0492
σ_{y0} [MPa]	0.2	0.2	0.2
E [GPa]	5.276	10.32	9.500
n [-]	0.371	1.17	2.52
H [MPa]	315.4	2,816	2,372

part of the diagonal response deviates from the experimental response. A small part of this deviation, between a strain of approximately 28% and 38%, is caused by the contribution of compressive behavior of the diagonal element that is not oriented in the direction of the loading. At an engineering strain of 38% (see Fig. 2.12), all tow elements are oriented in the same direction as the loaded diagonal element and they thus no longer act as a mechanism and start to contribute to the predicted response. As a result, the response of the unit cell increases significantly. This effect is less pronounced in the experiment, in which the transition from relative rotation to a stretching dominated response is more gradual.

The material parameters of the diagonal elements are based on the bias extension test in which the loading angle is 45° with respect to the warp direction. In the unit cell of the lattice model however, the diagonal elements are oriented at angles of 29° to the warp direction. Interestingly, the response of a single diagonal element loaded in its axial

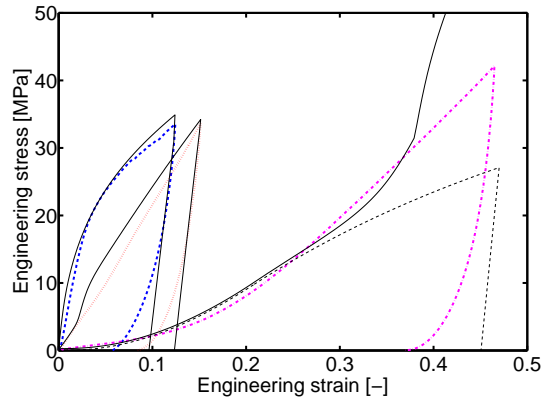


Figure 2.12: Comparison of the experimentally obtained engineering stress-engineering strain curves of Fig. 2.4 in warp (dashed), weft (dotted) and diagonal direction (dashed-dotted) and the responses of a unit cell loaded in the same directions (solid). The response of a single diagonal truss element loaded in its axial direction (dashed) is also shown for comparison.

direction (the dashed curve in Fig. 2.12) shows that there is no significant discrepancy with the response of the unit cell in diagonal (45°) direction. Only from an engineering strain of 28% onwards, the responses start to diverge due to the contribution of the remaining elements of the unit cell. The bias extension test results thus turn out to be rather insensitive to the loading direction.

2.5 Simulation of an out-of-plane punch test

To validate the lattice model, an out-of-plane punch test is simulated and predictions made for it are compared to experimental results. The test setup for this experiment is shown in Fig. 2.13. In the punch test, a sample of electronic textile with a free area of $100 \times 100 \text{ mm}^2$ is fixed between two clamps in warp direction. A sphere with a diameter of 30 mm is placed below the center of the sample and punches the sample at a velocity of 1 mm/s . This results in an average strain rate of the warp yarns at the center of the specimen of $8.3 \cdot 10^{-3} \text{ s}^{-1}$, which is of the same order of magnitude as the strain rates used in the tensile tests discussed in Section 2.2.

During the punch test, the reaction force on the punch is measured as a function of its displacement. The tensile tester is equipped with a 10 kN load cell with a stiffness of $16,400 \text{ N/mm}$ for this purpose. Since the warp yarns are fixed in the clamps at two edges and the punch is moved by a large distance ($50\text{-}60 \text{ mm}$), large global and local deformations are expected.

To simulate the punch experiment, only a quarter of the specimen is modeled using symmetry boundary conditions (see Fig. 2.13). The model consists of 9×16 unit cells in warp and weft direction respectively (170 lattice nodes). This means that one unit

cell in the punch simulation corresponds to 19.5×19.5 fabric unit cells as described in Sections 2.3 and 2.4. To ensure that a unit cell, as used in the punch simulation, has the same response as 19.5×19.5 original unit cells, the cross-sectional areas of the truss elements are 19.5 larger than those used for the identification.

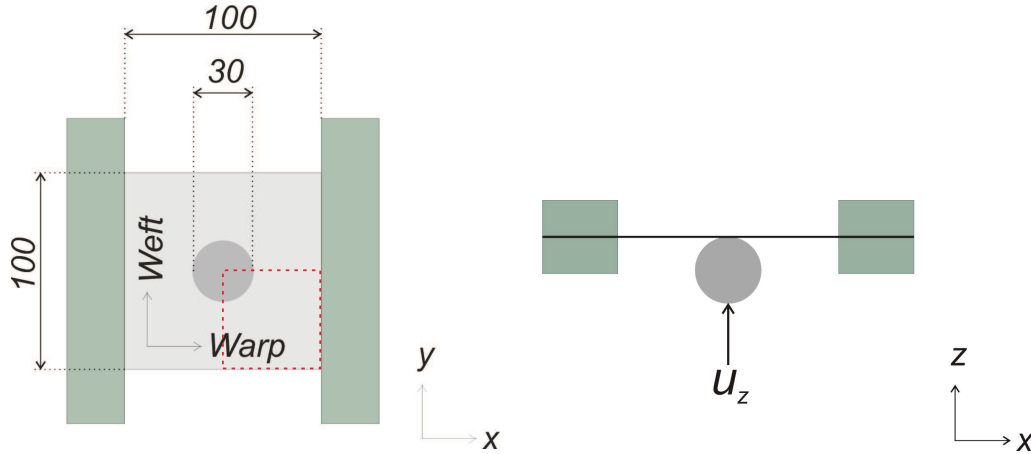


Figure 2.13: Top view (left) and side view (right) of the test setup for the punch experiment. The clamps and the spherical punch are shown in dark grey. The applied punch displacement in the experiments is denoted by u_z (right). The quarter of the electronic textile that is modeled in the simulation is indicated by the dashed square (left). The dimensions are given in mm .

The clamps in which the specimen is fixed are modeled by displacement boundary conditions on the edge of the model that is oriented orthogonally to the warp direction. The punch is considered as a frictionless rigid body in the simulation. Since the velocity of the punch is small, a quasistatic analysis can be performed. To ensure that some amount of out-of-plane stiffness is present in the model before the punch makes contact with the lattice, a bilinear initial out-of-plane displacement is given to the lattice, with an amplitude of 1 mm . In the true punch simulation the maximum displacement of 52.5 mm is reached in 51,500 increments. The convergence tolerance is formulated in terms of the relative displacements and is set to a value of 0.01. Smaller tolerances lead to the same results.

2.5.1 Force-displacement response

The force-displacement curve is presented in Fig. 2.14 together with four experimental curves. The initial response is compliant, since hardly any out-of-plane stiffness is present at the start of the test. However, the slope increases rapidly until a punch displacement of 20 mm is reached. From 20 mm onwards the slope of all experimental curves remains more or less constant until a displacement of approximately 40 mm is reached. At this punch displacement, already one of the curves has deviated from the

average trend of the remaining curves due to slip in the clamps. At a displacement of 40 *mm*, the second curve starts to deviate due to a large amount of slip in the clamps and at larger displacements this can be observed for the remaining two curves as well. In none of the experiments the electronic textile fails; slip from the clamps determines the force drop in all cases. The deformation of the samples is presented in the left parts of the four images in Fig. 2.15.

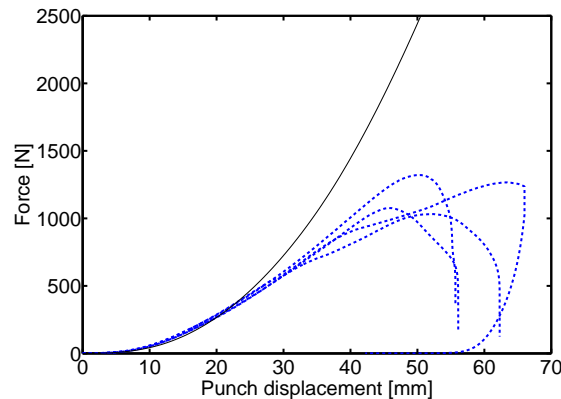


Figure 2.14: The experimental (dashed) and predicted (solid) force as a function of the punch displacement.

The numerically predicted force-displacement curve presented in Fig. 2.14 shows a good agreement with the experimental curves until a punch displacement of approximately 25 *mm*. At this displacement, the local axial strains of the warp elements on top of the punch are approximately 14%. In the warp elements between the punch and the fixed edge of the model, local axial strains of 9-10% are observed. However, towards the free edge of the model, which is parallel to the warp yarns, the local axial warp strains decay to approximately 3% over only 6 out of 16 unit cells in weft direction.

The good accuracy of the simulation until a punch displacement of 25 *mm* can also be observed in images A (at a displacement of 10 *mm*) and B (at a displacement of 20 *mm*) in Fig. 2.15, since the free edge in the simulations deforms exactly as in the experiment. For larger punch displacements (image C and D), a disagreement of these free edges can be observed.

From a displacement of approximately 25 *mm* onwards, the slope of the computed curve continues to increase, whereas that of the experimentally obtained curves remains constant and then drops. This discrepancy can be related to a number of causes, but the most important one is the poor performance of the unit cell for extensive biaxial deformation. For large biaxial deformations, the diagonal truss elements, that are only meant to describe the in-plane shear response of the textile, elongate significantly and start to contribute significantly to the mechanical response of the model.

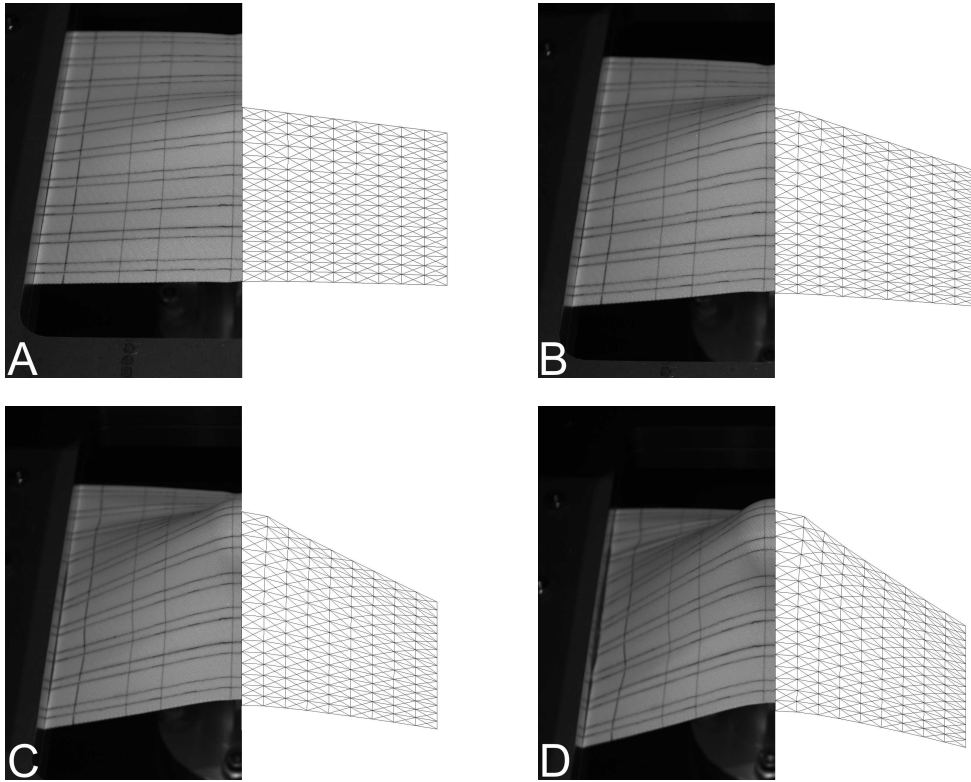


Figure 2.15: Comparisons of half of the deformed electronic textile during the punch test as obtained from the experiments (left) and the deformed model as predicted by the simulation (right). The four comparisons show the electronic textile at punch displacements of 10 *mm* (A), 20 *mm* (B), 30 *mm* (C) and 40 *mm* (D). Note that the images made during the experiment are truly three-dimensional, while the deformations computed by the simulation only give an indication of the three-dimensional shape. (This can be observed by the left fixed edge in the experimentally obtained images that is oriented at an angle with respect to the vertical axis, while the right fixed edge in the simulation results is oriented exactly along the vertical axis.)

2.5.2 Failure of the conductive wires

The strains that occur during the punch experiment cannot directly be determined from the experiments. The damage of the conductive wires however, can be investigated after the punch experiment. This gives a qualitative idea of the maximum strains that have occurred during the punch test in warp direction. To visualize the damage of the conductive wires, the same X-ray equipment is used as for the warp tensile experiments in Section 2.2.3. The damage at six locations indicated in Fig. 2.16 is shown in Fig. 2.17. One must take into account however, that the conductive wires in Fig. 2.5 have undergone uniaxial tension while the wires shown in this section have been subjected to more complex loading situations.

The engineering warp strains computed by the model at the six locations are also shown in Fig. 2.17. The warp strains are shown for a punch displacement of 52.5 mm , because at this punch displacement the experimental curves decrease on average. Slip from the clamps has taken place at this displacement, but since this is difficult to assess, it is assumed that most samples have been exposed to this punch displacement.

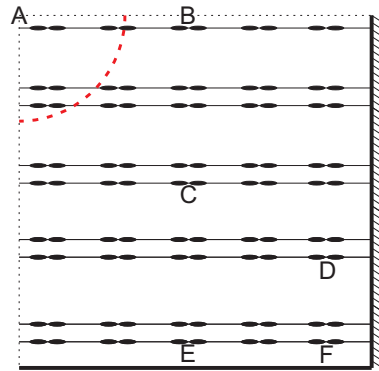


Figure 2.16: Schematic representation of the bottom right quarter of a sample in the punch test. The dashed curve represents a quarter of the punch and the horizontal lines with small ellipsoids represent the conductive wires. Six regions are indicated by A to F, at which the residual deformations of the conductive wires after the punch experiment have been visualized using X-ray imaging (see Fig. 2.17).

At locations A and B in Fig. 2.17, it is clearly visible that several conductive wires have failed. Since in Section 2.2.3 it has been established that failure of the wires starts at warp strains of 7%, significantly larger strains have occurred at these locations. This corresponds with the large engineering warp strains that are observed in the simulation results at these locations (also indicated in Fig. 2.17).

At location E, no failure can be seen, but only plastic deformation of the conductive wires. The engineering warp strain of 3% computed at this location corresponds with this observation, since it is significantly smaller than the warp strain of 7% at which failure initiates.

At locations C, D and F, a substantial amount of plastic deformation in the wires is visible (see again Fig. 2.17). The amount of damage is less than at locations A and B, but clearly a substantial number of filaments within several conductive wires have failed. This is in correspondence with the predictions, since all predicted engineering warp strains are above the threshold of 7%. The relatively large amount of damage at location F compared to locations C and D is quantitatively not completely in agreement with the predictions, since at location F a strain of 8% is predicted and the predicted strains at locations C and D are larger. However, qualitatively the model predicts failure correctly, since all predicted strains are larger than 7% at the locations where failure occurs.

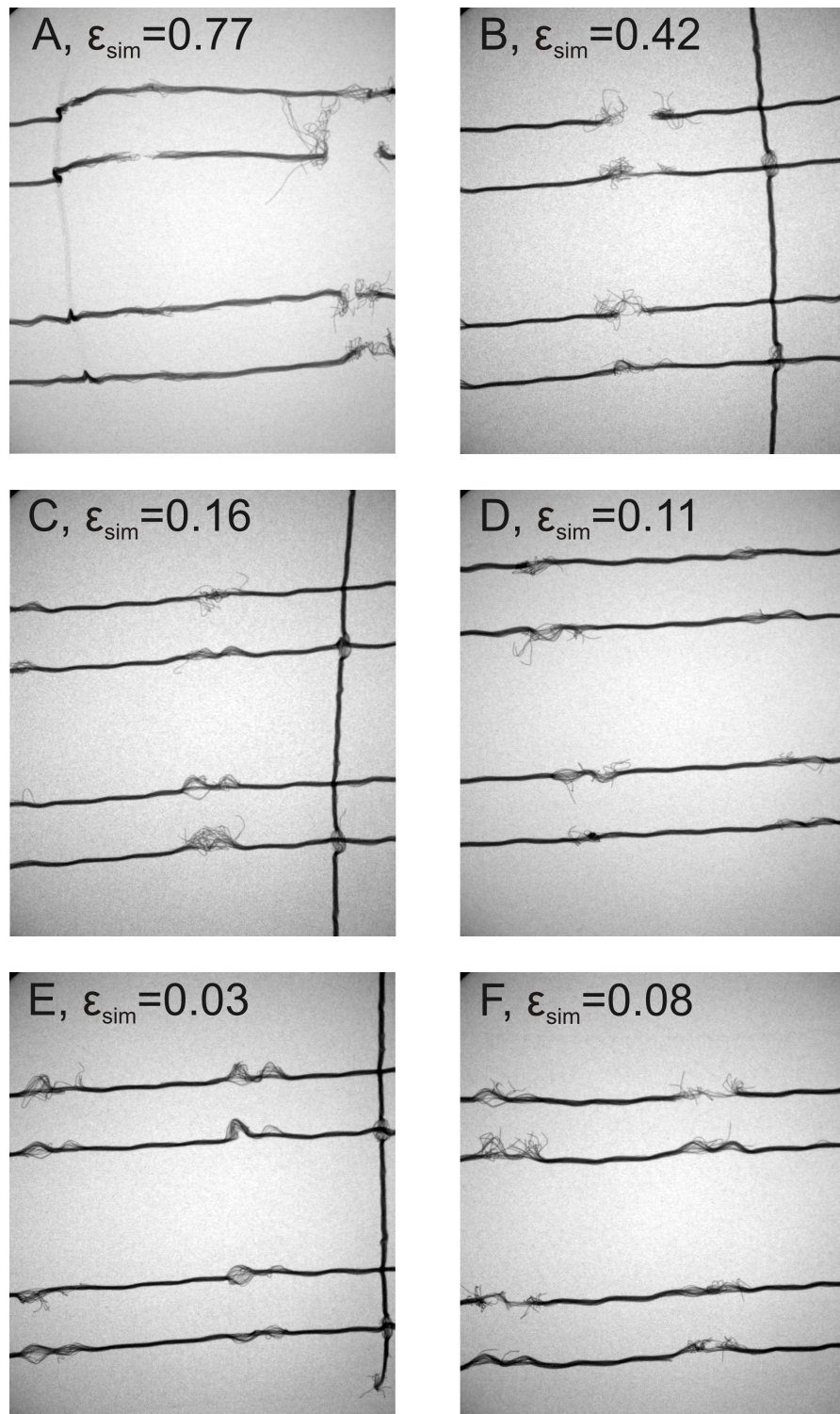


Figure 2.17: X-ray images of the electronic textile after the punch test. The damage of the conductive wires is shown for the locations A-F in Fig. 2.16. The engineering warp strains as computed in the simulation at a punch displacement of 52.5 mm, ϵ_{sim} , are also shown.

2.6 Conclusion

The aim of this chapter was to present a straightforward experimental identification procedure for an in-plane lattice model of woven fabrics. The advantage of the presented identification approach is that the tensile responses in three in-plane directions can be directly used to separately determine the parameters of the three families of discrete elements in the lattice model. This has been established by ensuring that only the family of elements that are oriented in the loading direction during one of the three tensile tests contribute to the mechanical response. Therefore, no mutual influence of the different elements occurs during each tensile test and no (complex) inverse problem needs to be solved.

To ensure that a separate identification of the families of discrete elements is allowed, two conditions must hold. First, the compressive response of the elements in the lattice model must be negligible compared to the tensile response of the elements. Second, the in-plane shear stiffness of the woven material must be compliant compared to the responses in the two principal in-plane directions. Since the latter generally holds for most woven materials, the lattice model and its identification procedure can be used more generally than for the electronic textile considered here.

The lattice model and its identification procedure are validated by an out-of-plane punch test on electronic textile, in which copper wires are incorporated to provide conductivity. In the punch test, large strains occur (local strains of 55%), so it can be considered as a stringent validation test. The results show that failure of the conductive wires is qualitatively, and to some extent quantitatively, well predicted by the lattice model; at all locations at which failure occurs in the experiments, strains larger than the failure strain of the conductive wires are predicted.

Furthermore, comparing the experimental data with the numerical results shows that the lattice model is accurate for small and moderate strains. For large biaxial deformation, the predicted response of the lattice model is stiffer than the actual response of the fabric. The cause of this is that during large biaxial deformation, the diagonal elements, used only to describe the shear response, influence the responses in the two principal directions as a result of their extensive elongation. An alternative may therefore be to use rotational springs instead of truss elements to describe the in-plane shear response.

A discrete network model for bond failure and frictional sliding in fibrous materials¹

Abstract

Discrete network models and lattice models using trusses or beams can be used to mechanically model fibrous materials, since the discrete elements represent the individual fibers or yarns at the mesoscale of these materials. Consequently, local mesoscale phenomena, such as individual fiber failure and interfiber bond failure, can be incorporated. Only a few discrete network models in which bond failure is incorporated include frictional fiber sliding that occurs after bond failure has taken place, although this occurs in the mechanical behaviour of several fibrous materials. In this chapter, a spring network model for interfiber bond failure and subsequent frictional fiber sliding is developed, which is formulated in a thermodynamical setting. The thermodynamical basis ensures that performed mechanical work is either stored in the network or dissipated due to bond failure and subsequent sliding. A numerical implementation of the framework is proposed in which the kinematic and internal variables are simultaneously solved, because the internal variables are directly coupled in the framework. Variations in network connectivity, bond strength, fiber length and anisotropy are implemented in the framework. The results show amongst others that the macroscopic yield point scales with the bond strength and that the macroscopic stiffness and the macroscopic yield point scale with the fiber length. The presented results also show that the macroscopic yield point becomes significantly less pronounced for an increase of the fiber length.

¹ Reproduced from: D.V. Wilbrink, L.A.A. Beex, R.H.J. Peerlings, A discrete network model for bond failure and frictional sliding in fibrous materials, Submitted to the International Journal of Solids and Structures.

3.1 Introduction

In the discrete modelling of materials, lattice models and network models, as for instance shown in Fig. 3.1, have received considerable attention over the past decades. They have been used for the mechanical modelling of materials at various length scales [51, 91]. The system of discrete elements and nodes allows a discrete representation of a material's microstructure and heterogeneity [71,91]. Hence, discrete networks have been applied to model various materials with a distinctively heterogenous microstructure, e.g. concrete [71,104], composites [5,19] and a variety of fibrous materials [14,52,98,100].

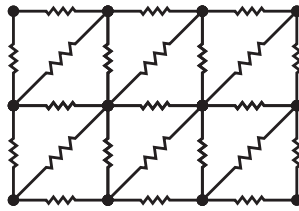


Figure 3.1: Example of a simple discrete network, a periodic (triangular) spring network, in which elements (springs) are connected at nodes.

Fibrous materials are of particular interest in this thesis. Their discrete fibers at the mesoscale can be captured individually by the discrete elements of network models. The failure process, that underlies the limiting mechanical properties, is governed by a combination of mechanical mesoscale phenomena. Examples are fiber bending, stretching and failure, as well as the loss of interfiber connectivity, sliding friction and pull-out [89,100,101]. To what extent each of these mechanisms contributes to failure, depends on the material of interest and can be complex to asses with experimental techniques. Network models however can be used to asses and investigate these mechanisms and several of these models can be found in the literature. Some illustrative examples are highlighted below, where a distinction is made between the constitutive behaviour of the elements and that of the nodes.

The simplest element behaviour assumed in the literature is elastic [52,100]. To simulate fiber failure in fibrous materials however, various network models allow the elements to fail in a brittle manner when subjected to specific loading conditions [26,52]. Since the fibers in many of these materials exhibit plastic behaviour before failure [55,89,93], preference may be given to elastoplastic element behaviour. This is for instance done in a pin-jointed model to simulate the tensile behaviour of paper [20].

The simplest way to connect the elements is by pin-jointed nodes. This however implies a perfect bonding, i.e. no bond failure, which can be a reason that several network models do not capture experimentally observed responses accurately. In [20] for instance, it is suggested that incorporating interfiber bond failure may improve the response of the network model for paper. Furthermore, some experimental studies have shown that the degradation of interfiber connectivity plays a role in the deformation process of various fibrous materials [55,67,100,101,129].

A number of bond models have been proposed in literature to account for the loss of interfiber connectivity. An example is a linear-brittle bond model [30,100]. In another network connectivity model for cellulose fiber fluff, bonds are considered as anisotropic elastic elements, which (under influence of mechanical loading) experience a stepwise stiffness and strength decay until complete failure [52]. Discrepancies with realistic behaviour appear to stem from both the absence of interfiber frictional sliding after bond failure has taken place and the energy dissipation associated with it.

Recently, models have been proposed in [67,100,101] to account for the effects of interfiber frictional sliding after bond failure has occurred. The model in [67] is used to predict interfiber bond failure in a disordered fiber network. Subsequent frictional fiber sliding is introduced by the use of a Coulomb friction model for the bonds. In the model in [100], which is used to simulate the in-plane mechanical behaviour of glass fiber nonwoven materials, the normal force has a bilinear decay as a function of the sliding distance. Compared to a linear, brittle bond model, the frictional bond model (with a fitting procedure for the normal load's bilinear decay) is proven to be in better agreement with the gradual loss of load-carrying capacity witnessed in tensile experiments. This is explained by its ability to dissipate energy in the bonds.

It thus appears that frictional fiber sliding subsequent to bond failure is a key aspect in the accurate network modelling of the mechanical behaviour of fibrous materials to complete failure. Whereas a variety of other mesomechanical features have been dealt with in the literature, discrete models that include bond failure as well as subsequent frictional fiber sliding are relatively scarce.

The objective of the present chapter is to incorporate interfiber bond failure and the subsequent frictional fiber sliding in a thermodynamically consistent spring network model. The mesoscopic network model is proposed such that the influence of a number of mesoscopic parameters can systematically be studied.

A numerical modelling framework is proposed to this end, which is based on the thermodynamical formulation of a network model. The (isothermal) thermodynamical formulation is similar to those used for continuum mechanics [41]. However, the formulations of the stored energy and the dissipation potential are specifically derived for the spring network model with bond failure and subsequent frictional fiber sliding. In the present chapter, the formulation of the stored energy only allows for small sliding displacements. A Coulomb-like friction law is used in the dissipation potential for the fiber-bond behaviour, in which the maximum friction force is constant. This entails that the force at which bond failure takes place is the same as the force necessary to accommodate subsequent sliding. However, the dissipation potential can be altered so that different bond description can be incorporated.

This chapter consists of three parts. The first part details the model by deriving the equations that govern the mechanical deformation of discrete dissipative systems. This theory is applied to spring network models that represent fibrous structures with linear elastic elements and Coulomb nodal friction to capture dry interfiber contact. The second part proposes an algorithm that is capable of numerically approximating the model. This algorithm uses Newton-Raphson iterations to solve the nonlinear equations

which govern equilibrium, and employs an active set strategy to distinguish between active sliding and static friction. The third part explores the macroscopic response of the model for a rather straightforward spring network; a periodic X-braced spring network. The resulting macroscopic response has many features of elastoplasticity. The influence of several mesoscopic parameters, such as bond strength and fiber length, is investigated using the model.

The following notation is used throughout this chapter. Matrices, including column matrices, are denoted by bold letters. Subscripts denote the components of column matrices and matrices. Quantities x_i (where $i = 1, \dots, n$) are stored in a column matrix \mathbf{x} and quantities A_{ij} (where $i = 1, \dots, n$ and $j = 1, \dots, m$) are stored in matrix \mathbf{A} of size $n \times m$. Inequalities of column matrices apply to each of their individual components, e.g. $\mathbf{x} \leq \mathbf{y}$ is equivalent to $x_i \leq y_i$ for all $i = 1, \dots, n$. An element-wise multiplication $\mathbf{x} * \mathbf{y} = \mathbf{z}$ results in $z_i = x_i y_i$ for all $i = 1, \dots, n$.

3.2 Modelling

The objective of the following development is to describe the thermodynamical setting that describes the deformation of a spring network which may dissipate energy. The first part of the thermodynamical setting is similar to those that are regularly used for (isothermal) continuum models [41] and results in a model that includes dissipation, for instance by plasticity, damage or friction. The theory is afterwards specifically developed for spring network models with nodal friction, by deriving formulations for the stored energy and the dissipation potential.

3.2.1 Governing equations for a dissipative system

Here we derive the governing equations of (isothermal) mechanical models on a thermodynamical basis, along the lines of [41]. The system is characterized by (controllable) kinematic variables (degrees of freedom), that are stored in column matrix \mathbf{u} , and (uncontrollable) internal variables, that are stored in column matrix \mathbf{s} . The kinematic variables \mathbf{u} include the displacements of the nodes in the network, but may also include additional kinematic quantities, such as rotations if a beam network is considered. The total rate of work of the system, the internal power P_{int} , is the sum of the work performed by internal forces, present in column matrix \mathbf{F}_u , that are associated with the rate of the kinematic variables \mathbf{u} , i.e.

$$P_{int} = \dot{\mathbf{u}}^T \mathbf{F}_u. \quad (3.1)$$

The forces \mathbf{F}_u may be accompanied by externally imposed forces, \mathbf{F}_{ext} , such that the external power of the system, P_{ext} , can be written as:

$$P_{ext} = \dot{\mathbf{u}}^T \mathbf{F}_{ext}. \quad (3.2)$$

The principle of virtual power dictates that in static equilibrium, we have:

$$P_{int} = P_{ext} \quad \forall \dot{\mathbf{u}}. \quad (3.3)$$

An implication of this so-called virtual-power-statement (using Eq. (3.1) & (3.2)) is that

$$\mathbf{F}_u = \mathbf{F}_{ext}. \quad (3.4)$$

This equation may be recognized as static equilibrium, i.e. each of its components expresses the force equilibrium in a particular node in a certain direction.

The energy stored in the model is a function of the sets of kinematic variables \mathbf{u} and internal variables \mathbf{s} . Consequently, the rate of internal (elastic) energy \dot{E} can be written as:

$$\dot{E} = \dot{\mathbf{u}}^T \frac{\partial E}{\partial \mathbf{u}} + \dot{\mathbf{s}}^T \frac{\partial E}{\partial \mathbf{s}}. \quad (3.5)$$

The first law of thermodynamics dictates that energy can neither be created nor destroyed. This implies that the rate of dissipation \dot{D} can be expressed as $\dot{D} = P_{int} - \dot{E}$. By substitution of Eq. (3.1) & (3.5) in this expression, the dissipation rate \dot{D} can be expressed as:

$$\dot{D} = \dot{\mathbf{u}}^T \left(\mathbf{F}_u - \frac{\partial E}{\partial \mathbf{u}} \right) - \dot{\mathbf{s}}^T \frac{\partial E}{\partial \mathbf{s}}. \quad (3.6)$$

It is now assumed that all dissipative processes are characterized by \mathbf{s} ; hence, no dissipation occurs for constant \mathbf{s} . This can be satisfied for arbitrary $\dot{\mathbf{u}}$ by defining the forces \mathbf{F}_u as:

$$\mathbf{F}_u = \frac{\partial E}{\partial \mathbf{u}}. \quad (3.7)$$

Furthermore, we define a column matrix with dissipation forces, \mathbf{F}_s , as the derivatives of the stored energy with respect to the internal variables as:

$$\mathbf{F}_s = -\frac{\partial E}{\partial \mathbf{s}}, \quad (3.8)$$

such that by substituting Eq. (3.7) & (3.8) in Eq. (3.6), the dissipation rate can be expressed as

$$\dot{D} = \dot{\mathbf{s}}^T \mathbf{F}_s. \quad (3.9)$$

The second law of thermodynamics dictates that dissipation is irreversible, such that

$$\dot{D} \geq 0. \quad (3.10)$$

The evolution of the internal variables \mathbf{s} must be such that this condition (in Eq. (3.10)) is satisfied. Given the fact that the forces \mathbf{F}_s are energetically conjugate to $\dot{\mathbf{s}}$, it is natural to define the evolution of \mathbf{s} in terms of \mathbf{F}_s , taking into account the constraint imposed by Eq. (3.8) & (3.9).

3.2.2 Application: network of elastic springs with dry nodal friction

The relations derived above are now applied to a network model of springs that includes interfiber bond failure and subsequent frictional fiber sliding using a Coulomb friction model.

If it is assumed that the network model represents a fictitious fibrous material, chains of elements in the network can be considered as fibers (or fiber bundles). Hence, each element represents a fiber segment. This is illustrated in the left image of Fig. 3.2, in which element e between nodes A and B is a segment of the fiber that is marked by the dashed gray line in the undeformed configuration and solid in the deformed configuration. Fibers are connected to other fibers in nodes. Nodes allow multiple fibers to interact in one point, as shown in the right image of Fig. 3.2. The kinematic variables \mathbf{u} are defined as the set of nodal displacements in space; they are used to formulate a set of vectors that describe the nodal displacements (e.g. \vec{u}_A and \vec{u}_B in the left image of Fig. 3.2).

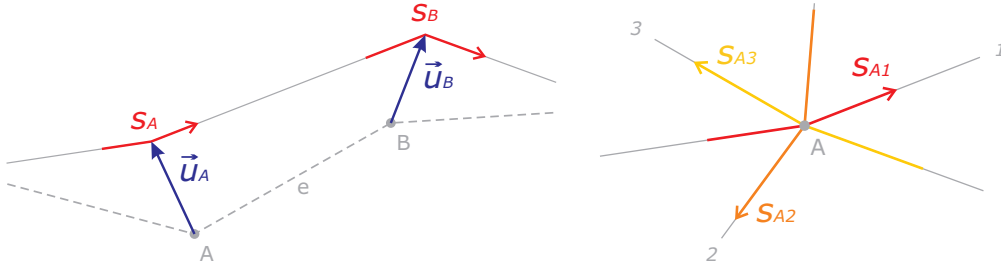


Figure 3.2: Illustration of the variables of the spring network with dry interfiber friction. (Left) element e between nodes A and B is part of a fiber (dashed in the undeformed configuration and solid in the deformed configuration). The nodes are displaced in space (characterized by \vec{u}_A and \vec{u}_B) and the fiber may slide through both nodes by distances s_A and s_B . (Right) in node A , three fibers are linked together, each has its own sliding displacement through this node.

Fibers and nodes can be viewed as separate bodies and fibers may slide with respect to the nodes. Note that fiber sliding with respect to a node changes the length of the fiber's segments adjacent to the node and thus lets the spring force increase in one of the

fiber's elements and decrease in another. For the i th fiber-node interaction, the amount of sliding is characterized by the fiber's axial sliding displacement, s_i , relative to the node. The fact that the sliding displacement is a scalar (its direction is governed by the local fiber orientation as Fig. 3.2 shows), implies that it retains its validity regardless of a possible change of direction of the fiber in a node. As a node includes the interaction of a number of fibers, multiple internal variables may be associated with each node - one for each fiber. The column matrix \mathbf{s} comprises all sliding displacements s_i of all nodes.

As Eq. (3.7) & (3.8) show, a key factor in the model is the system energy E . The system energy may have a nonlinear dependence on the variables \mathbf{u} and \mathbf{s} . For a network with n_e elastic springs where the e th element ($e = 1, \dots, n_e$) has constant stiffness, k_e , and an equivalent elongation, ω_e , the system energy can be expressed as follows:

$$E(\mathbf{u}, \mathbf{s}) = \sum_{e=1}^{n_e} E_e(\mathbf{u}, \mathbf{s}) = \sum_{e=1}^{n_e} \frac{1}{2} k_e \omega_e^2, \quad (3.11)$$

with

$$\omega_e = \|\vec{x}_B + \vec{u}_B - \vec{x}_A - \vec{u}_A\| - \|\vec{x}_B - \vec{x}_A\| + s_B - s_A. \quad (3.12)$$

Here, \vec{x}_A and \vec{x}_B are the position vectors of nodes A and B , respectively, to which the element is attached (see Fig. 3.2). This definition allows large rotations, but no large sliding displacements, since they do not influence the stiffness, k_e . As a result, the effect of fiber sliding on E with respect to a node is equivalent to the displacement of that node in fiber direction for a one dimensional chain of elements.

For the node-fiber behaviour, the choice is made to use a constant friction resistance. This entails that the static friction force and dynamic friction force are constant and equal to each other for every fiber-node interaction. This corresponds to a Coulomb friction model with a constant normal force. The sliding displacement s_i for the i th fiber-node interaction is assumed to depend on the force F_{si} (i.e. the i th component of \mathbf{F}_s) associated with this interaction. In the following discussion of an individual fiber-node interaction, the subscripts i are dropped for convenience, except for cases where this conflicts with previous definitions.

Sliding may occur if the magnitude of the driving force F_s exceeds the critical sliding force $F_{sc} > 0$, which quantifies the friction resistance. A loading function, ϕ , is defined according to:

$$\phi = |F_s| - F_{sc}, \quad (3.13)$$

using which the sliding criterion can be formulated as $\phi = 0$. The sliding velocity is described using a monotonically increasing Lagrange multiplier ξ :

$$\dot{s} = \dot{\xi} \frac{\partial \phi}{\partial F_s} = \dot{\xi} \text{sign}(F_s). \quad (3.14)$$

In case the sliding criterion $\phi = 0$ is met, a change of ξ prevents the sliding force F_s from exceeding its limit F_{sc} , i.e. to maintain $\phi \leq 0$ at all times. If the criterion is not met, the driving force F_s is insufficient to induce sliding, hence, $\dot{\xi} = 0$. These conditions are mathematically expressed by the following so-called Kuhn-Tucker (KT) conditions:

$$\phi \dot{\xi} = 0 \quad \phi \leq 0 \quad \dot{\xi} \geq 0. \quad (3.15)$$

Note that since $\text{sign}(\dot{s}) = \text{sign}(F_s)$, the irreversibility requirement for dissipation is satisfied component-wise (i.e. $\dot{D}_i = \dot{s}_i F_{si} \geq 0$) and therefore also for the entire network.

The present model shows similarities with conventional elastoplasticity models, which are also governed by equilibrium and plasticity laws and characterized by sets of kinematic and internal variables. A substantial difference with these models is that in the present model, the sliding displacement s_i in the i th fiber-node connection depends on F_{si} (through the loading function ϕ_i), which is a function of several sliding displacements, present in \mathbf{s} , through Eq. (3.8), (3.11) & (3.12). This renders the plasticity (the sliding displacements) in the present model intrinsically nonlocal, whereas in conventional elastoplasticity problems these quantities are governed locally and are merely indirectly coupled through the equilibrium equations.

3.3 Numerical implementation

3.3.1 Incremental-iterative procedure

For the numerical implementation, we consider that the network model is deformed significantly slowly so that a quasi-static analysis suffices. The loading process is divided into time increments Δt , where Δ refers to an incremental change. At time t , the entire solution is known and characterized by displacements $\mathbf{u}^{(t)}$ and sliding displacements $\mathbf{s}^{(t)}$. From time t to time $t + \Delta t$, additional external forces and/or displacements may be imposed, under which equilibrium is to be regained at time $t + \Delta t$. For time $t + \Delta t$, we wish to determine the displacement solution; i.e. all nodal displacements \mathbf{u} and sliding displacements \mathbf{s} , where the superscript, $t + \Delta t$, is dropped for ease of notation. The following discusses the solution procedure for one increment; this procedure is repeated for each new increment to obtain the solution for the entire time interval considered.

As was shown in the model derivation, equilibrium dictates that the forces that correspond to the displacement solution must obey the following conditions at time $t + \Delta t$.

First, the force equilibrium in Eq. (3.4) must be satisfied. Second, the KT-conditions in Eq. (3.15), dictated by the Coulomb friction model, must be obeyed. These are formulated for the entire system as follows:

$$\phi * \dot{\xi} = 0 \quad \phi \leq 0 \quad \dot{\xi} \geq 0. \quad (3.16)$$

Eq. (3.4) as well as Eq. (3.16) have a nonlinear dependence on the variables \mathbf{u} and \mathbf{s} , due to the formulation of the elastic energy E in Eq. (3.11) & (3.12). Consequently, an iterative solution procedure is used within every increment.

As a consequence of the intrinsically nonlocal plasticity in the present model, the elastic predictor-plastic corrector algorithms, see e.g. [111], that are commonly used to solve elastoplastic problems are not usable. The problem outlined above shows similarities with nonlinear programming problems in constrained optimization, for which a range of solution algorithms may be employed, such as an augmented Lagrangian formulation [50].

Here, the choice is made for the Newton-Raphson method in which the nonlinear governing equations are solved iteratively, since it allows for quadratic convergence. Because of the method's limited robustness, small incremental loading steps are required. This method is combined with an active set strategy to deal with the inequality constraints imposed by the Coulomb friction model.

This solution procedure is similar to the generalized reduced gradient (GRG) method, first proposed in [1], combined with an active set strategy. Both the GRG and the present method rely on linearization of the governing equations. Rather than explicitly formulating the reduced gradient, performing a line search in its direction and subsequently restoring the state variables, as in the GRG method, one linear system is formulated and solved in the present method. This allows for applying indirect solution methods rather than explicitly determining large inverse matrices, which is computationally more efficient for large systems (containing hundreds of nodes or more).

3.3.2 Linearization

The following discusses the linearization for one Newton-Raphson iteration. Boundary conditions and variations in sliding activity are treated separately below. For the moment these are left out of consideration, such that \mathbf{u} and \mathbf{s} can be changed freely. For now, it is also assumed that all sliders are active, i.e. $\phi = \mathbf{0}$, which is equivalent to $|\mathbf{F}_s| = \mathbf{F}_{sc}$ due to Eq. (3.13). The forces \mathbf{F}_u and \mathbf{F}_s both depend on \mathbf{u} and \mathbf{s} , such that the linearized iterative force changes $\delta\mathbf{F}_u$ and $\delta\mathbf{F}_s$ may be expressed as:

$$\begin{aligned} \delta\mathbf{F}_u &= \mathbf{K}_{uu}\delta\mathbf{u} + \mathbf{K}_{us}\delta\mathbf{s}, \\ \delta\mathbf{F}_s &= \mathbf{K}_{su}\delta\mathbf{u} + \mathbf{K}_{ss}\delta\mathbf{s}, \end{aligned} \quad (3.17)$$

where δ indicates an iterative change. The tangent matrices of the form \mathbf{K}_{pq} are found by differentiating E with respect to both variables denoted in the subscript, e.g.:

$$\mathbf{K}_{us} = \frac{\partial \mathbf{F}_u}{\partial \mathbf{s}} = \frac{\partial^2 E}{\partial \mathbf{s} \partial \mathbf{u}}. \quad (3.18)$$

More precisely the components of this matrix \mathbf{K}_{us} are given by:

$$(K_{us})_{ij} = \frac{\partial^2 E}{\partial s_j \partial u_i} \quad (3.19)$$

where i and j run over all components of \mathbf{u} and \mathbf{s} respectively.

Boundary conditions are applied to particular nodes. Since external forces are already incorporated in column matrix \mathbf{F}_{ext} , the boundary conditions discussed here are solely displacement constraints. Since \mathbf{s} contains internal variables that cannot be controlled, constraints only act on a part of the kinematic variables \mathbf{u} . Hence, a distinction is made between the constrained displacements, indicated with subscript c , and the other, ‘free’ displacements, with subscript f . The constrained displacements are kept constant during all but the first iteration of every increment, such that $\delta \mathbf{u}_c = \mathbf{0}$. The displacement correction $\delta \mathbf{u}$ can thus be written as:

$$\delta \mathbf{u} = \begin{pmatrix} \delta \mathbf{u}_f \\ \delta \mathbf{u}_c \end{pmatrix} = \begin{pmatrix} \delta \mathbf{u}_f \\ \mathbf{0} \end{pmatrix}. \quad (3.20)$$

In every iteration, the sliding displacements may only be altered for sliding mechanisms which are found to be active: i.e. for which the sliding criterion $\phi = 0$ is met. How this sliding activity is determined is discussed below; for now we consider it as given. Hence, a distinction between active mechanisms (subscript a) and passive mechanisms (subscript p) is made. By partitioning Eq. (3.16) according to this distinction, it can be reformulated as:

$$\begin{aligned} \phi_a &= \mathbf{0} & \dot{\xi}_a &\geq \mathbf{0} \\ \phi_p &< \mathbf{0} & \dot{\xi}_p &= \mathbf{0}. \end{aligned} \quad (3.21)$$

This set of equations shows that an equality constraint applies to each sliding mechanism, either in terms of ϕ_a or ξ_p . These constraints will be used to determine the iterative correction of the sliding displacements $\delta \mathbf{s}$. To this end, $\delta \mathbf{s}$ is also partitioned according to sliding activity. Since the passive sliders \mathbf{s}_p must remain constant, $\delta \mathbf{s}_p = \mathbf{0}$. Hence, the sliding displacement correction $\delta \mathbf{s}$ can be formulated as:

$$\delta \mathbf{s} = \begin{pmatrix} \delta \mathbf{s}_a \\ \delta \mathbf{s}_p \end{pmatrix} = \begin{pmatrix} \delta \mathbf{s}_a \\ \mathbf{0} \end{pmatrix}. \quad (3.22)$$

On the basis of these distinctions, the linearized expressions for the force changes (see Eq. (3.17)) can be partitioned. The details of this process are given in appendix A. Using the resulting expressions, a solvable system can be formulated by specifying the force changes $\delta\mathbf{F}_{u,f}$ and $\delta\mathbf{F}_{s,a}$. Eq. (3.4) dictates that the nodal force residual $\mathbf{F}_u - \mathbf{F}_{ext}$ should be reduced to zero, such that $\delta\mathbf{F}_{u,f} = \mathbf{F}_{ext,f} - \mathbf{F}_{u,f}$, where $\mathbf{F}_{u,f}$ are the values obtained in the previous iteration. Furthermore, to satisfy $\phi_a = \mathbf{0}$, the magnitudes of the driving forces for the active sliding mechanisms should be reduced to the critical level in the direction of the forces, such that $\delta\mathbf{F}_{s,a} = -(|\mathbf{F}_{s,a}| - \mathbf{F}_{sc,a}) * \text{sign}(\mathbf{F}_{s,a})$. Substitution of these expressions in the partitioned linearized system (see Eq. (A.4) in Appendix A) allows one to formulate this system as:

$$\begin{aligned} \mathbf{K}_{uu,ff}\delta\mathbf{u}_f + \mathbf{K}_{us,fa}\delta\mathbf{s}_a &= \mathbf{F}_{ext,f} - \mathbf{F}_{u,f}, \\ \mathbf{K}_{su,af}\delta\mathbf{u}_f + \mathbf{K}_{ss,aa}\delta\mathbf{s}_a &= -(|\mathbf{F}_{s,a}| - \mathbf{F}_{sc,a}) * \text{sign}(\mathbf{F}_{s,a}). \end{aligned} \quad (3.23)$$

By solving these coupled systems of equations and substituting the obtained corrections $\delta\mathbf{u}_f$ and $\delta\mathbf{s}_a$ in Eq. (3.20) & (3.22) respectively, the iterative displacement corrections $\delta\mathbf{u}$ and $\delta\mathbf{s}$ are found. Subsequently, the variables \mathbf{u} and \mathbf{s} can be updated according to:

$$\begin{aligned} \mathbf{u} &:= \mathbf{u} + \delta\mathbf{u} \\ \mathbf{s} &:= \mathbf{s} + \delta\mathbf{s}, \end{aligned} \quad (3.24)$$

and the forces \mathbf{F}_u and \mathbf{F}_s may be computed. This process is repeated until convergence is reached.

3.3.3 Active set strategy

Fluctuations in \mathbf{F}_s may necessitate an update of the active set (i.e. the set of sliding mechanisms that are active) in every iteration. This update consists of checks for activation and deactivation, which are discussed below. Since these checks are done for each sliding mechanism individually, we focus on an individual sliding mechanism and drop its index i for ease of notation.

An essential part of the active set update is the possibility of sliding mechanism activation. A characteristic of every passive sliding mechanism is that it satisfies $\phi < 0$ as dictated by Eq. (3.21). A sliding mechanism is activated if it no longer satisfies this condition. As a consequence, its sliding displacement may be changed to prevent the magnitude of the sliding force from violating the threshold in the following iterations.

As a validation of every active sliding mechanism, it is evaluated if, according to Eq. (3.14), $\text{sign}(F_s) = \text{sign}(\Delta s)$, where $\Delta s = s - s^{(t)}$ is the incremental correction of s so far. Once an active sliding mechanism is found to violate this requirement, it is removed from the active set and thus becomes passive. Since its iterative sliding displacement value s is unreliable in this case, its value is reset to that at time t : $s := s^{(t)}$. The iteration process is then continued with $s = s^{(t)}$ for the following iteration.

In the first iteration of each increment, the last known sliding activity of the previous time increment is used as an initial estimate. In this manner, the incremental solution is found in a single iteration if no change in sliding activity occurs. This is efficient if small time steps are used. Furthermore, multiple sliding mechanisms may in principle be (de)activated simultaneously in one iteration. It is therefore important that the incremental loading steps are sufficiently small to prevent multiple sliding mechanisms from being activated and afterwards deactivated simultaneously.

3.4 Results

This section illustrates the capabilities of the proposed framework for a straightforward discrete network; an X-braced lattice. It serves to provide better insight into how the mechanical aspects modelled on the microscale, especially fiber sliding, affect the macroscopic mechanical response. The influence of various parameters is investigated for this purpose.

3.4.1 Problem description

A two-dimensional lattice of 16×16 nodes is subjected to a tensile deformation (see Fig. 3.3). The lattice is characterized by a square X-braced unit cell. The undeformed length of the vertical and horizontal springs is l_0 , such that the unit cell has dimensions $l_0 \times l_0$. The entire network has a size $L_0 \times L_0$, with $L_0 = 15l_0$. For smaller lattices boundary effects are expected to strongly dominate the mechanics, whereas much larger networks require excessive computational expenses.

Inspired by most real fibrous materials, e.g. as treated in [100], the fibers in the network are given a finite length (see Fig. 3.3). Moreover, this introduces disorder in the lattice, which reduces the influence of boundary effects. In the following, fibers consist of straight chains of a constant number of elements e_f . In the reference case, $e_f = 4$, as in Fig. 3.3. To implement the uniform fiber length in the lattice, one element is first removed from every straight chain of elements at a randomly chosen position. This simulates a first ‘cut’, since the two free fiber ends formed by a cut cannot transfer load. Along the remainder of the chain of elements, every $(e_f + 1)$ th element away from the first cut is also removed to divide the element chain into finite fibers of e_f elements (or less near the boundaries). Instead of actually removing an element, its stiffness is set to a small nonzero value (10^{-5} times its original stiffness) to promote computational stability.

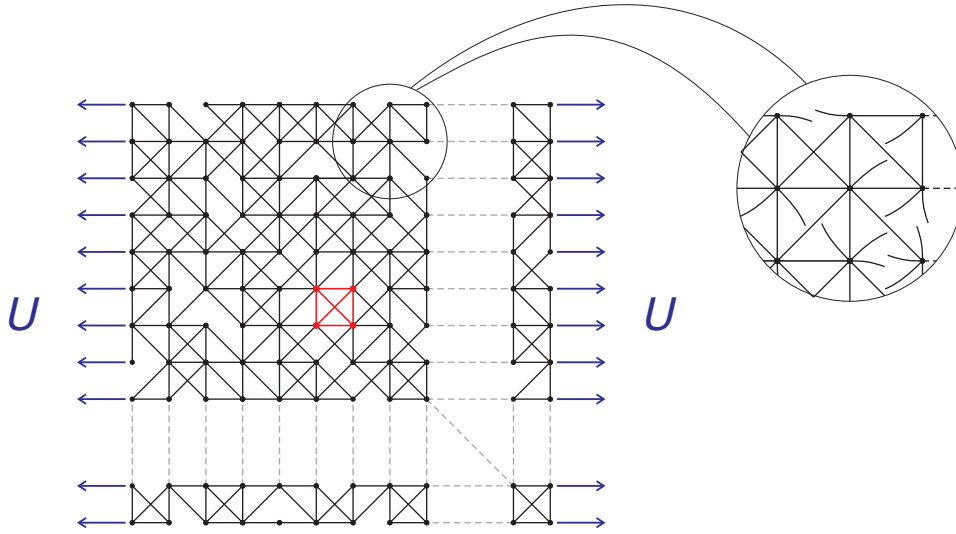


Figure 3.3: Illustration of the lattice characterized by a square X-braced unit cell, cut to finite fibers of length $e_f = 4$ elements. A horizontal displacement U in outward directions is imposed to the nodes on the vertical edges. The fibers are assumed to have free ends, as illustrated on the right.

The tensile tests are performed quasi-statically, by imposing a monotonically increasing displacement, U , to the nodes on the vertical edges of the network. The vertical displacement of these nodes is restricted. As a result, the nodes in the lattice are displaced (described by \mathbf{u}) and fibers may slide through the nodes (described by \mathbf{s}). Four principal fiber orientations are distinguished in the lattice (i.e. one horizontal, one vertical and two diagonal), such that four sliding mechanisms are present in each node. No sliding is allowed in the nodes on the vertical edges, such that the displacement U imposed on these nodes is effectively transferred to the rest of the lattice.

The increments of imposed displacement ΔU are small compared to l_0 . To obtain the results presented below, $\Delta U = l_0/1600$ is used in each simulation. Smaller increments do not significantly affect the results, whereas larger increments may lead to inaccurate results or may even cause the solution algorithm fail to converge.

For the sake of simplicity, all springs have the same stiffness k (thus, also the diagonal springs). A distribution of bond strengths (or critical sliding forces) is used (i.e. the values in \mathbf{F}_{sc} are not the same) to avoid singularities. The bond strengths are randomly selected from a uniform distribution around the mean bond strength \bar{F}_{sc} with an interval $((1 - \eta)\bar{F}_{sc}, (1 + \eta)\bar{F}_{sc})$. Here, η characterizes the scatter of the bond strengths ($0 < \eta < 1$)

In the tensile testing of fibrous materials, fiber pullout plays a role in the failure process [55]. The numerical networks studied here are assumed to be loaded up to a point where pullout has not occurred yet, by assuming that free fiber ends are sufficiently long to maintain the initial interfiber connection (see Fig. 3.3). Fibers are also assumed to have long free ends outside the upper and lower edges of the network, such that vertical or diagonal sliding may occur through the nodes at these edges.

Each result shown below is based on seven simulations, unless indicated otherwise. The simulations have varying lattice connectivity, i.e. for every simulation a new geometry is generated by initiating the cutting of the fibers at random positions. This introduces scatter, which is visualized by a colored band that envelopes the results of all (seven) simulations. The solid line inside this band represents the mean result of these simulations.

3.4.2 Reference case

Let us first consider a reference set of mesoscopic parameter values, which are given as $\bar{F}_{sc} = kl_0/200$, $\eta = 0.1$ and $e_f = 4$. Fig. 3.4 shows the evolution of the sum of the horizontal reaction forces, F , as a function of the imposed displacement U for these parameters. The two quantities are normalized to the stiffness and length of a single horizontal element. The elastic responses of the same networks are also shown for comparison.

The diagram shows that for relatively small displacements, the response is purely elastic and thus is solely governed by fiber stretching. The linear elasticity of the modelled fibers renders the force-displacement relation linear for small displacements U . As the imposed displacement increases, the response gradually starts to deviate from the elastic response and is eventually dominated by inelastic fiber sliding. This result qualitatively compares well with experimentally found force-displacement curves of a variety of fibrous materials [8,20,89,100,101].

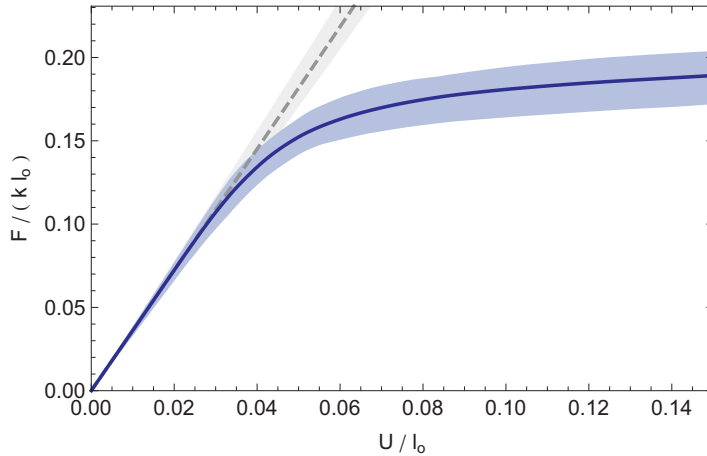


Figure 3.4: The normalized horizontal reaction force ($F/(kl_0)$) as a function of the normalized imposed displacement (U/l_0) for the reference situation (solid, blue) and the purely elastic case (dashed, gray).

The band with scatter relative to the mean values of F observed in Fig. 3.4 appears to be approximately constant. From this it can be concluded that this scatter is primarily induced by geometric variations rather than variations in F_{sc} .

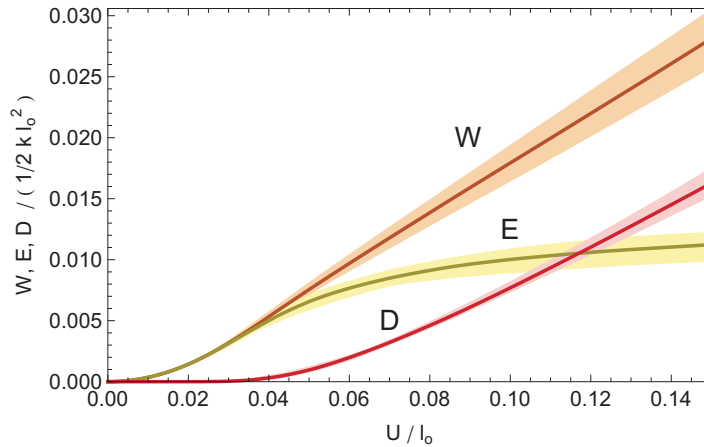


Figure 3.5: The normalized total work performed by the system W , the normalized elastic energy stored in the lattice E and the normalized accumulated amount of total dissipation D , all normalized by $\frac{1}{2}kl_0^2$, as functions of the normalized imposed displacement (U/l_0).

The transition from elastic to plastic deformation witnessed in Fig. 3.4 is further illustrated by Fig. 3.5. This figure shows the total work performed on the system, W , (which is the supplied energy by the imposed displacement U), the elastic energy stored in the lattice, E , and the accumulated amount of dissipation, D , (which is the energy dissipated by all sliding displacements) as functions of the imposed displacement, U . Fig. 3.5 shows that the initial response is governed by the buildup of elastic energy in the discrete elements. From the yield point onwards ($U \approx 0.025l_0$), energy is increasingly dissipated by friction in the fiber-node connections, which is responsible for the plasticity witnessed in Fig. 3.4. At the end of the deformation process (at $U \approx 0.14l_0$), the stored energy tends to stagnate and almost all supplied energy is dissipated by friction. The fact that the stored energy still slightly increases indicates that element straining plays a role in the slight hardening witnessed in this regime in Fig. 3.4. Note that Fig. 3.5 shows that the first and second laws of thermodynamics are obeyed, since $W = E + D$ (which is consistent with $P_{ext} = \dot{E} + \dot{D}$) and $\dot{D} \geq 0$.

The distribution of sliding activity over the nodes for one of the seven simulations (arbitrarily chosen) is illustrated in the left image of Fig. 3.6. It shows that for the plasticity-dominated response at $U = 0.125l_0$, dissipation has localized into a number of nodes, whereas no dissipation has occurred in the majority of nodes. The dissipation appears to be more or less localized in a band that runs between the upper and lower edges of the specimen. The deformation of the network, which is also shown, is consistent with this localization band. Similar localization bands can also be observed in the results presented in [67,100].

An examination of the nodal dissipation of the other six simulations (not shown here) reveals that no consistent pattern can be identified in the dissipation localization, except that the localization bands are generally oriented perpendicular to the loading direction. This inconsistency is induced by both the geometric variations and the variations in

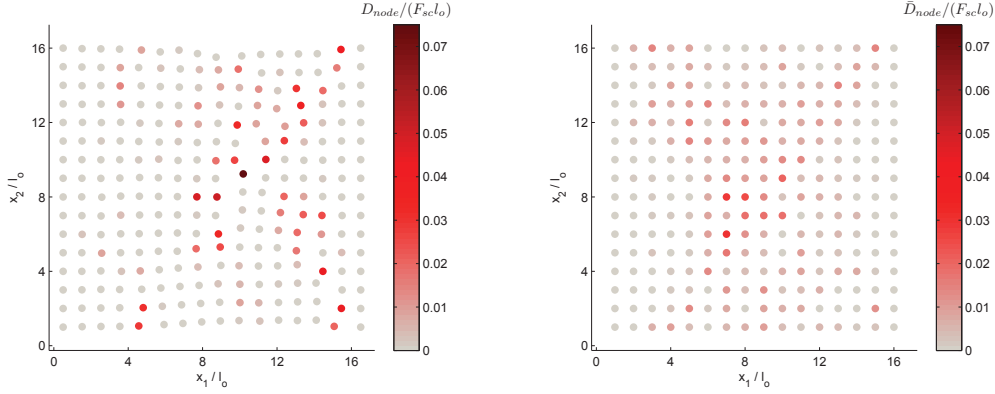


Figure 3.6: Node-wise amount of energy dissipated by sliding at $U = 0.125l_0$; (left) for one of the seven simulations, shown on the deformed geometry (displacements are scaled by a factor 4 in each direction for clarity) and (right) for the average of seven simulations, shown on the undeformed geometry.

the values of \mathbf{F}_{sc} . The averaged distribution of dissipation over the nodes for the seven simulations in the right image of Fig. 3.6 shows that no distinct pattern can be identified. Two boundary layers in which hardly any sliding occurs are observed along the vertical edges of the network.

Fig. 3.7 shows the mean force-displacement curve of the reference case for cyclic loading (one cycle). It is clear that the unloading is initially elastic and takes place along approximately the initial loading stiffness. This is similar to the behaviour of continuum-based elastoplasticity models and in agreement with the unloading behaviour of fibrous materials such as paper [119]. Under a continued decrease of the imposed displacement, an elastoplastic response is found in compression. Plastic yielding (i.e. fiber sliding) however occurs at a (compressive) stress which is substantially lower than the initial yield strength, indicating a strong Bauschinger effect (kinematic hardening). This is due to the elastic energy stored in the system, which helps to overcome the friction resistance upon reverse loading. Note that a similar effect occurs upon renewed tensile loading.

3.4.3 Parameter study

To study the influence of the mean bond strength \bar{F}_{sc} , the simulations are repeated using half the reference value of \bar{F}_{sc} and twice the reference value, while η is kept constant. Fig. 3.8 shows a comparison of the force-displacement curves for the three situations. Each set of simulations is stopped when the slope is 7% of the original stiffness. It is clear that the yield point is increased with increasing \bar{F}_{sc} . The strength (i.e. the reaction force for which the response is purely governed by sliding) appears to be proportional to \bar{F}_{sc} . This is expected, since \bar{F}_{sc} quantitatively controls the sliding forces for which the response is sliding-dominated. The range in U over which the elastic-plastic transition

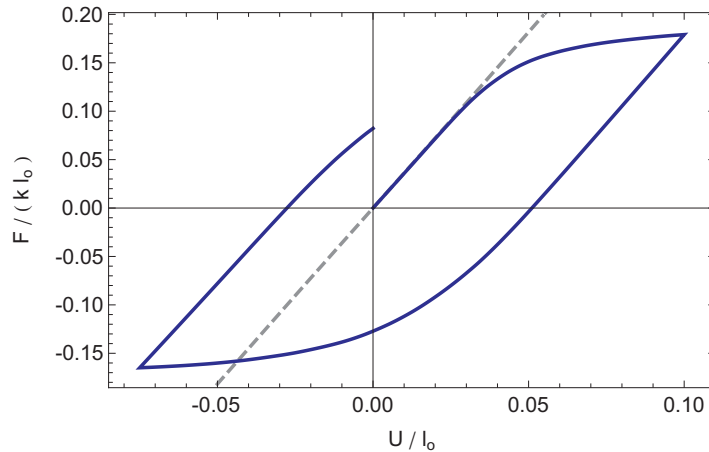


Figure 3.7: The normalized mean horizontal reaction force ($F/(kl_0)$) as a function of the normalized imposed displacement (U/l_0) which is increased from $U = 0$ to $U = 0.1l_0$, then decreased to $U = -0.075l_0$ and increased again to $U = 0$ for the reference situation (solid, blue). The purely elastic response is shown by the dashed grey curve.

takes place in Fig. 3.8 approximately increases with the ultimate strength, since the scatter (characterized by η) is relative to \bar{F}_{sc} . This implies that the absolute width of the distribution that determines \mathbf{F}_{sc} scales with \bar{F}_{sc} .

The influence of the fiber length e_f (measured in element lengths) is illustrated in Fig. 3.9. This diagram shows that the elastic network stiffness increases with the fiber length. The network strength also increases with the fiber length. It approximately doubles upon doubling the fiber length. It can also be observed that for an increasing fiber length, the transition from elastic-dominated to plastic-dominated deformation is more gradual. The elevated stiffness, elevated strength and less distinctive yield point are all explained by the higher level of connectivity in the network for larger fiber lengths. The level of scatter relative to the mean of the tensile curve decreases with an increase of the fiber length, since a higher level of connectivity reduces the effects of geometric variations on the macroscopic response.

Fibrous materials are often characterized by preferred fiber orientations leading to anisotropic material responses. Anisotropy can be captured in the considered lattice model straightforwardly by changing the unit cell's aspect ratio. In Fig. 3.10 the influence of the aspect ratio is shown for the response in horizontal direction. The dimensions of the unit cell are now defined as $l_{0,x} \times l_{0,y}$. Since the unit cell in the reference situation is square ($l_{0,x} = l_{0,y} = l_0$), its aspect ratio equals one. For the other situations $l_{0,x}$ is either increased or decreased by a factor 1.5 while $l_{0,y}$ and all other parameters have the same values as in the reference situation. Note that the horizontal and vertical axes in Fig. 3.10 have been normalized by $l_{0,x}$ and $l_{0,y}$ respectively. The figure shows that a higher aspect ratio corresponds to an increased relative (normalized) stiffness of the lattice in the horizontal direction (i.e. that of the long cell edge). This is explained by

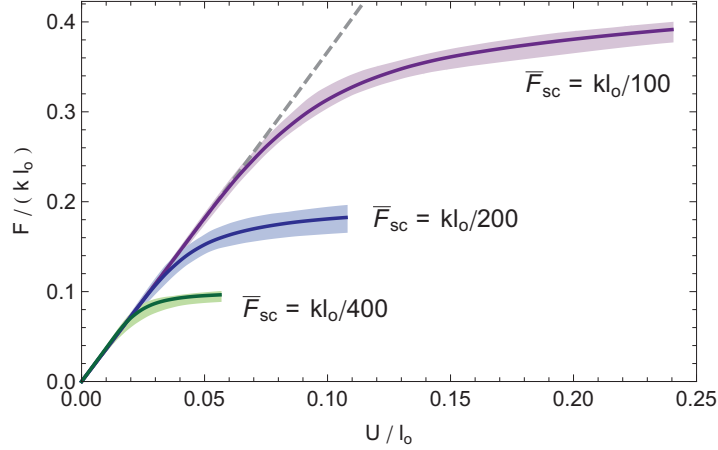


Figure 3.8: The normalized reaction force ($F/(kl_0)$) as a function of the normalized imposed displacement (U/l_0) for three values of the normalized mean bond strength ($\bar{F}_{sc}/(kl_0)$). The curve of the reference case is indicated by $\bar{F}_{sc} = kl_0/200$ and the dashed curve shows the purely elastic response.

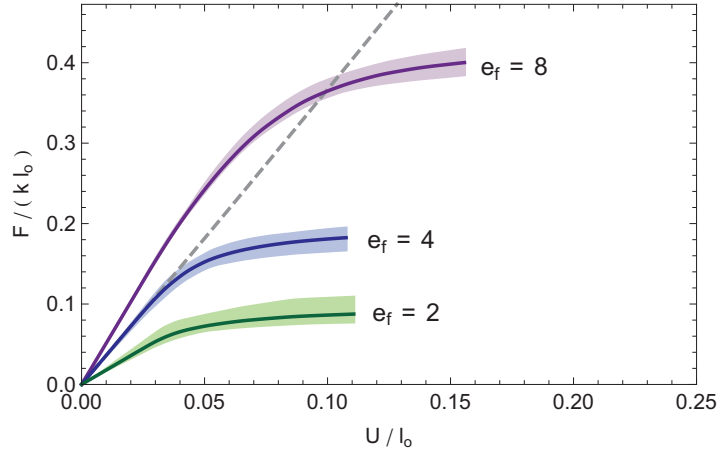


Figure 3.9: The normalized horizontal reaction force ($F/(kl_0)$) as a function of the normalized imposed displacement (U/l_0) for three finite fiber lengths (e_f). The curve of the reference case is indicated by $e_f = 4$ and the purely elastic response of the reference case is shown by the dashed curve.

the smaller angle between the diagonal elements and the loading direction. For higher aspect ratios, the increased stiffness and identical yield forces result in a less gradual transition from elastic to plastic lattice deformation. The vertical response (not shown here) exhibits the opposite trend, and the degree of anisotropy thus increases with the aspect ratio.

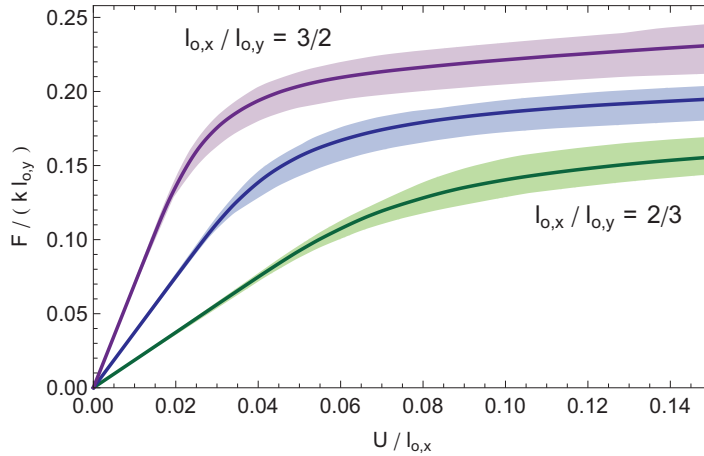


Figure 3.10: The normalized horizontal reaction force ($F/(kl_{0,y})$) as a function of the normalized imposed displacement $U/l_{0,x}$ for three unit cell aspect ratios ($l_{0,x}/l_{0,y}$). The curve of the reference case is presented without an aspect ratio ($l_{0,x}/l_{0,y} = 1$).

3.5 Concluding remarks

Interfiber bond failure and subsequent frictional fiber sliding are important aspects of the deformation process of several fibrous materials [55,67,100,101,129]. In this chapter, interfiber bond failure in mesoscopic spring network models, followed by frictional fiber sliding, is incorporated in an isothermal thermodynamical setting. The model is applied to an X-braced lattice with finite fibers. Each finite fiber is modelled by a chain of elastic springs and the behaviour of the interfiber bonds is described by dry friction. However, the model can be adapted so that different network connectivities, element behaviours and bond descriptions (e.g. a viscoplastic description) can be studied. A framework to numerically approximate the nonlinear model for simulating lattice deformation is proposed as well. It is used to systematically investigate the influence of different mesoscopic parameters on the macroscopic response.

The results for the X-braced lattice with finite fibers illustrate that, with simple descriptions for fiber stretching and interfiber friction, the model exhibits an elastoplastic macroscopic response that mimics the macroscopic mechanical behaviour of several fibrous materials. Energy is dissipated due to localized fiber sliding, that is typically concentrated in a path across the network. The network model exhibits kinematic hardening under cyclic loading. It is furthermore shown that an increase of the fiber length leads to a stiffer macroscopic response, a higher macroscopic strength and a less pronounced macroscopic yield point. Finally, anisotropy is implemented by changing the aspect ratio of the unit cell. The results show an elevated stiffness and a less smooth transition from elastic to plastic deformation for an increasing aspect ratio.

The present model may serve as a basis for the construction of discrete network models that connect several key aspects of the deformation witnessed in fibrous materials. For instance, elastoplastic fibers (present in paper [20,93]) may enter the model through the

thermodynamical setting. To capture the degradation of interfiber bond response under the influence of sliding (e.g. modelled in [100]) alternative relations for sliding can be incorporated. The brittle failure of fibers and bonds (e.g. modelled in [19,71,73] and [52,73,100], respectively) may be modelled by dictating thresholds for the corresponding forces. The ability of such network models to quantitatively reproduce experimental results using estimates of the model parameters remains a subject for further research.

Chapter four

A quasicontinuum methodology for multiscale analyses of discrete microstructural models¹

Abstract

Many studies in different research fields use lattice models to investigate the mechanical behavior of materials. Full lattice calculations are often performed to determine the influence of localized microscale phenomena on large-scale responses but they are usually computationally expensive. In this chapter the quasicontinuum (QC) method [Tadmor EB, Ortiz M, Philips R, Quasicontinuum analysis of defects in solids. *Phil. Mag. A* 1996; 73:1529-1563] is extended towards lattice models that employ discrete elements such as trusses and beams. The QC method is a multiscale approach that uses a triangulation to interpolate the lattice model in regions with small fluctuations in the deformation field, while in regions of high interest the exact lattice model is obtained by refining the triangulation to the internal spacing of the lattice. Interpolation ensures that the number of unknowns is reduced while summation ensures that only a selective part of the underlying lattice model must be visited to construct the governing equations. Since the QC method has so far only been applied to atomic lattice models, the existing summation procedures have been revisited for structural lattice models containing discrete elements. This has led to a new QC method that makes use of the characteristic structure of the considered truss network. The proposed QC method is, to the best of the authors' knowledge, the only QC method that does not need any correction at the interface between the interpolated and the fully resolved region and

¹ Reproduced from: L.A.A. Beex, R.H.J. Peerlings, M.G.D. Geers, 2011, A quasicontinuum methodology for multiscale analyses of discrete microstructural models, *International Journal for Numerical Methods in Engineering*, Vol. 87, 701-718.

at the same time gives exact results unlike the cluster QC methods. In its present formulation, the proposed QC method can only be used for lattice models containing nearest neighbor interactions, but with some minor adaptations it can also be used for lattices with next-nearest neighbor interactions such as atomic lattices.

4.1 Introduction

A vast amount of structural lattice models (using springs, trusses or beams) have been successfully developed for discrete microstructures of fibrous and heterogeneous materials. These conceptually simple models are able to accurately describe complex mechanisms in these materials, caused by the discrete character of their microstructures. A major advantage of lattice models is the fact that they intrinsically incorporate the discreteness of microscale phenomena, while continuum models often have to be complex or extensive to (partially) include them. Especially localized phenomena as for instance fiber failure and bond failure can be adequately captured with lattice models.

The variety of lattice models for fibrous materials and structures ranges from cardboard packages and woven structures for aerospace industry to collagen networks and other fibrous biological materials. Recent examples are the lattice models of Heyden [52]; Arnoux et al. [5]; Bronkhorst [20]; Clyne et al. [24]; Potluri and Manan [98]; Lomov et al. [75]; Ben Boubaker et al. [14]; Stylianopoulos and Barocas [113]; Zohdi [131] and Hatami-Marbini and Picu [48]. For heterogeneous materials which do not consist of a discrete network at the microscale, a discrete representation containing trusses and beams is less natural, but it can still be physically relevant. This has been shown for instance by Lilliu and Van Mier [72] and Cusatis et al. [28] for concrete, by Ostoja-Starzewski and Wang [92] for epoxy plates, by Rinaldi et al. [102] for polycrystalline microstructures and by Kim and Buttlar [62] for asphalt concrete. An overview of different structural lattice models is presented by Ostoja-Starzewski [91].

Although lattice models have the advantage that they naturally resolve microscale phenomena in discrete microstructures, their use can be computationally expensive. Lilliu and Van Mier [72] for instance, report that a supercomputer needed more than two weeks to analyze a 449,179 beam model. A solution to avoid huge calculation times is a multiscale approach in which the discrete representation of trusses and beams at the microscale is used to characterize the mechanical constitutive behavior at the macroscale. Examples of such studies are those of Heyden [52] for cellulose fiber fluff, of Boisse et al. [17] for textile and Mohr [86] for an ideal truss lattice. In the study of Stylianopoulos and Barocas [113], a collagen network is represented by trusses and coupled to the macroscale model via a computational homogenization scheme. These homogenization-based approaches however are not very appropriate to study localized phenomena such as failure.

An alternative multiscale methodology that takes discrete lattice defects into account is to combine continuum models with lattice models. The lattice model is used in small regions of interest around the defects, while continuum models - discretized using the

finite element (FE) method - are used for the remaining domain. This combined approach is widely used for atomic crystals (for instance by Xiao and Belytschko [125] and Fish et al. [38]) but it can only be used if the effective behavior of the lattice is adequately captured in a continuum model. Capturing the continuum equivalent behavior of the lattice however becomes more difficult as the amount of detail required in the lattice description increases. This occurs for example if plasticity is included [86], if the complexity of the lattice increases [27], or if beams are used instead of trusses, since such models also involve rotational degrees of freedom [91]. Even general phenomena such as an evolving microstructure due to fiber-reorientation can lead to complex continuum models [96], while such phenomena are intrinsically included in the underlying lattice models. Another substantial difficulty of a combined continuum-lattice model approach is the coupling between both domains, which is far from trivial [125,38].

An approach proposed for crystals which combines the best of both, is the quasicontinuum (QC) method [114,115]. In this method a number of representative atoms is defined and the positions of the remaining atoms is interpolated between them. For this purpose, the crystal is triangulated, where large interpolation triangles are used in uniformly deforming regions and the triangle size is reduced to the atomic spacing near features and events of interest. The equations which govern the remaining equilibrium equations, i.e. those associated with the representative atoms, are constructed by approximating the contributions of large numbers of atoms to the energy of the system via a so-called summation rule. The method exclusively relies on the lattice model and does not require the definition of an accompanying continuum model. The triangular interpolation regions are thus not traditional finite elements (for the discretization of a continuum) but they only serve to interpolate the lattice discrete model. Furthermore, no continuum-atomistic coupling procedure is required, since only the lattice model is used. Different QC methods have been developed that all have their specific scope, advantages and disadvantages [114,115,108,64,36]. Overviews are given by Miller and Tadmor [83] and Curtin and Miller [27].

Although the QC method was originally proposed by Tadmor et al. [114] for atomic crystals and applications such as nanoindentation [115] and intergranular fracture [82], it offers appealing possibilities for structural lattice models incorporating trusses and beams. As a first step towards complex structural lattice models, this chapter focuses on the development of the QC method for truss networks. The considered truss network can be regarded as a lattice model of a straightforward discrete microstructure. The existing QC methods based on atomic lattices are therefore revisited with a new emphasis towards this truss network, which leads to a new QC method for these type of lattice models that also solves certain disadvantages of the classical QC methods.

The newly proposed QC method has the advantage that, similar to the cluster QC methods [64,36], no internal interface is introduced. As a result, the fully resolved regions around lattice defects can remain small, thus limiting the global number of unknowns. The proposed QC method is therefore computationally efficient. However, unlike the existing approaches, no estimate of the total potential energy is made but the exact total potential energy is recovered. Although the method has been developed

for a lattice model containing simple trusses, it can be used for general lattices with nearest neighbor interactions and, with some simple modifications, also for lattices with next-nearest neighbor interactions such as atomic lattices.

This chapter aims to establish the basis for a QC method for lattice models of fibrous and heterogeneous materials. In particular, we consider a two-dimensional, regular linear elastic truss network, which acts as the discrete representation of a fictitious microstructure. Three different loading situations are considered to investigate the accuracy of the QC method in combination with this lattice model. Uniform deformation is analyzed as a reference case, followed by bending as an example of a slowly fluctuating deformation. Finally, a truly multiscale example of a defect in an otherwise uniformly deforming lattice is modeled to investigate computational cost versus accuracy.

The outline of the chapter is as follows. In Section 4.2, the new QC method based on the considered structural lattice model is introduced. In Section 4.3, results obtained for three examples are compared to direct simulations of the full lattice model and a semi-QC method without summation. Finally, conclusions are presented in Section 4.4.

4.2 A quasicontinuum approach for lattice models

4.2.1 Lattice model

Structural lattice models are widely used to describe material behavior of fibrous and heterogeneous materials. Depending on characteristic properties of the discrete microstructures, trusses or beams (or both) are commonly used to model the discrete interactions. Rotational springs or trusses can also be used to include a rotational stiffness between discrete elements. Different discrete failure mechanisms may be included as well, e.g. fiber breakage in fibrous materials or interfiber bond failure between discrete particles in heterogeneous materials. Bond failure of fibrous materials may be modeled by sliding of the discrete elements.

Within the wide scope of structural lattice models, this chapter aims to establish a QC methodology for a relatively simple lattice model in order to show the potential of the method for fibrous and heterogeneous materials. The considered reference lattice model is a two-dimensional X-braced linear elastic truss network as shown in Fig. 4.1. This simple lattice model can be regarded as the discrete representation of a fictitious material. In it, each of the nodes, which are organized in a square pattern, is connected by trusses to its immediate neighbors in the horizontal, vertical and diagonal sense. No truss nodes are present at the crossings of (only) the diagonal trusses.

To determine the equilibrium state of the (loaded) network, we minimize its total potential energy. Half of the potential energy of the truss between nodes i and j , E_{ij} , is assigned to node i and the other half to node j . The obtained nodal energy E_i can be expressed as follows:

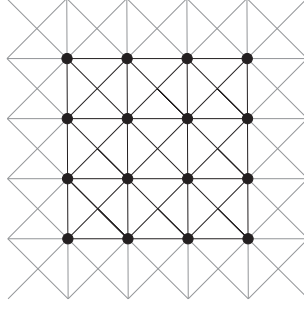


Figure 4.1: Schematic representation of 9 unit cells (dark) of the considered two-dimensional, regular linear elastic truss network. The dots are nodes of the truss network.

$$E_i = \frac{1}{2} \sum_{j \in B_i} E_{ij} = \frac{1}{4} \sum_{j \in B_i} k_{ij} (\Delta L_{ij})^2 \quad (4.1)$$

where the index j refers to the neighboring truss nodes of node i , which form a subset B_i of the index set $N = \{1, \dots, n\}$ of the truss nodes of the lattice ($B_i \subseteq N$). The potential energy E_{ij} of a single truss element is expressed in terms of its stiffness k_{ij} and the truss elongation ΔL_{ij} . The fully non-linear elongation ΔL_{ij} , which allows large rotations, is used here and therefore the total potential energy is non-convex.

Now that the nodal energies of all truss nodes of the lattice have been established according to Eq. (4.1), the internal potential energy E_{int} of the entire lattice can be obtained by summing all nodal potential energies of the entire lattice:

$$E_{int}(\mathbf{u}) = \sum_{i=1}^n E_i. \quad (4.2)$$

E_{int} is a function of the displacement vectors of all n truss nodes of the lattice. The components of all displacement vectors are collected in a column matrix \mathbf{u} with length nd , where d equals the number of spatial dimensions of the lattice.

The total potential energy E_{tot} can now be expressed as a function of the internal potential energy E_{int} and the external forces \mathbf{f}_{ext} :

$$E_{tot}(\mathbf{u}) = E_{int}(\mathbf{u}) - \mathbf{f}_{ext}^T \mathbf{u}. \quad (4.3)$$

The total potential energy can subsequently be minimized with respect to all degrees of freedom (DOFs), which are the displacement components present in column \mathbf{u} :

$$\min_{\mathbf{u}} E_{tot}(\mathbf{u}). \quad (4.4)$$

The minimum of E_{tot} can be determined using the classical variational principle, leading to:

$$\delta E_{tot}(\mathbf{u}) = \delta \mathbf{u}^T \mathbf{f}(\mathbf{u}) = 0 \quad \forall \delta \mathbf{u} \quad (4.5)$$

where $\mathbf{f}(\mathbf{u})$ represents the column with the conservative forces $\partial E_{tot}/\partial \mathbf{u}$ and has length nd . It can be assembled from contributions \mathbf{f}_i by each node i according to

$$\mathbf{f}(\mathbf{u}) = \sum_{i=1}^n \mathbf{f}_i(\mathbf{u}) \quad (4.6)$$

where

$$(f_i)_p = \frac{\partial E_i}{\partial u_p}. \quad (4.7)$$

A standard Newton-Raphson procedure can be used to solve Eq. (4.5):

$$\delta \mathbf{u}^T \left(\mathbf{f}(\mathbf{u}^*) + \mathbf{K}(\mathbf{u}^*) d\mathbf{u} \right) = 0 \quad \forall \delta \mathbf{u} \quad (4.8)$$

where \mathbf{u}^* are the displacement components of the previous iteration and $d\mathbf{u}$ a correction to these displacements computed in the present iteration. The overall stiffness matrix is represented by $\mathbf{K}(\mathbf{u})$. Its elements are given by:

$$K_{pq} = \frac{\partial^2 E_{tot}}{\partial u_p \partial u_q} = \sum_{i=1}^n \frac{\partial^2 E_i}{\partial u_p \partial u_q} \quad (4.9)$$

where p and q run over all nd displacement components in the column \mathbf{u} . It has size $nd \times nd$ and is symmetric. It is again convenient to think of \mathbf{K} consisting of contributions K_i by each node, i.e.

$$\mathbf{K} = \sum_{i=1}^n \mathbf{K}_i \quad (4.10)$$

where

$$(K_i)_{pq} = \frac{\partial^2 E_i}{\partial u_p \partial u_q} \quad (4.11)$$

After taking the essential boundary conditions and partitioning the overall stiffness matrix, the remaining part of the stiffness matrix necessary to solve the system must be positive definite to obtain a locally stable configuration of the lattice.

A full lattice calculation is computationally inefficient for two reasons. First, it includes a large number of DOFs, which produces a large stiffness matrix - here with size $nd \times nd$. Solving the linear system in Eq. (4.8) becomes computationally expensive, even if Cholesky decomposition or an iterative solution method is applied. The second computational concern results from the fact that in order to construct the overall stiffness matrix, all n truss nodes must be visited individually (see Eq. (4.9)).

4.2.2 Interpolation

The QC method (proposed by Tadmor et al. [114]) was developed to overcome both of the above problems. First, interpolation is used to reduce the number of DOFs of the model. For this purpose the lattice is triangulated as shown in Fig. 4.2. The interpolation relates the displacement vectors of truss nodes within each triangle to the displacement vectors of the three corner nodes of the triangle. Since in QC methods the nodes of the triangles are placed on truss nodes and these truss nodes therefore represent the displacements of the truss nodes surrounding them, they are referred to as representative nodes or repnodes, in accordance with the term *repatoms* used in existing QC methods for atomic crystals. The interpolation constrains truss nodes within interpolation triangles and the displacements of the repnodes are the remaining DOFs. So far only linear interpolation has been used in the QC methods, for which nodes or atoms behave in an affine manner within the triangles.

In the QC method, the triangulation is done in such a way that the exact lattice model is recovered in regions where small details need to be fully resolved, while in other regions the lattice model is interpolated by coarsening the triangulation (see Fig. 4.2). Regions require modelling with full accuracy if locally high strain gradients occur due to missing truss nodes, failure of trusses, stiffer trusses or locally imposed deformation. To ensure that the exact lattice model is captured in these fully resolved regions, all truss nodes in fully resolved regions are repnodes (see Fig. 4.2).

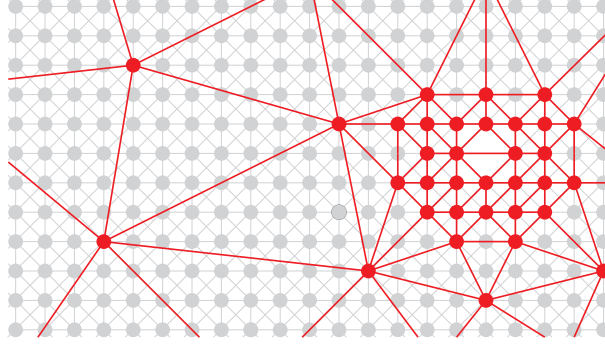


Figure 4.2: Schematic representation of a part of the two-dimensional X-braced truss lattice and a superimposed triangulation. The size of the triangles is reduced around the lattice defect so the exact lattice model is captured.

The set R containing the r repnodes is a subset of N ($R \subseteq N$). Since $r \ll n$, the solution space is drastically reduced by the interpolation and therefore the solution will generally obtain a higher energy. The displacement components of all n truss nodes can be expressed as a function of the displacement components of the r repnodes, stored in column \mathbf{u}_r as follows:

$$\mathbf{u} = \Psi \mathbf{u}_r \quad (4.12)$$

where Ψ is the condensation matrix of size $nd \times rd$, containing the values of the interpolation functions evaluated in the nodal positions. Since now the total potential energy only depends on the displacements of the repnodes, the minimization of the total potential energy must be performed with respect to this reduced set of DOFs, i.e. the minimization problem (4.4) is replaced by

$$\min_{\mathbf{u}_r} E_{tot}(\Psi \mathbf{u}_r). \quad (4.13)$$

This results in the following linearization instead of (4.8):

$$\delta \mathbf{u}_r^T \left(\Psi^T \mathbf{f}(\mathbf{u}^*) + \Psi^T \mathbf{K}(\mathbf{u}^*) \Psi d\mathbf{u}_r \right) = 0 \quad \forall \delta \mathbf{u}_r. \quad (4.14)$$

In Eq. (4.14) $\Psi^T \mathbf{f}$ can be identified as the condensed force column \mathbf{f}^c and $\Psi^T \mathbf{K} \Psi$ the condensed stiffness matrix \mathbf{K}^c . The condensed force column and stiffness matrix are of

size $r d \times 1$ and $r d \times r d$ respectively and therefore considerably reduce the computational solution effort.

The interpolation used here for lattices has some similarities with finite element (FE) methodologies for continua, in which FEs are used to discretize a continuum. For this reason characteristic features of conventional FE methods such as adaptivity can conveniently be adopted in QC methods. However, a substantial difference is that whereas in continua we are dealing with continuous displacement fields and the interpolation thus applies to every point in the domain, here the displacements of a discrete set of points govern the system and the interpolation thus also applies to a finite number of discrete points. Correspondingly, the energy of the system consists of a sum of pointwise contributions, whereas in the FE method integrals need to be evaluated.

Although the solution space is reduced at this stage, the assembly of the condensed force column and the condensed stiffness matrix remains a computationally expensive procedure, since all n truss nodes must be visited for it:

$$\mathbf{f}^c(\mathbf{u}_r) = \sum_{i=1}^n \mathbf{\Psi}^T \mathbf{f}_i, \quad (4.15)$$

$$\mathbf{K}^c(\mathbf{u}_r) = \sum_{i=1}^n \mathbf{\Psi}^T \mathbf{K}_i \mathbf{\Psi}. \quad (4.16)$$

Note that the nodal energy E_i , and thus the force column \mathbf{f}_i and the stiffness matrix \mathbf{K}_i in Eq. (4.15) & (4.16), only depend on the displacements of truss node i and its neighbors, which results in a large amount of zeros in the force column and stiffness matrix. Consequently, only a part of the condensation matrix $\mathbf{\Psi}$ is used for the matrix multiplications in Eq. (4.15) & (4.16), allowing one to exploit the sparsity of the matrices in the numerical implementation of the method.

4.2.3 Summation

Although the number of DOFs and thus the size of stiffness matrix and right hand side is substantially reduced by the interpolation, still all n truss nodes of the lattice must be visited to assemble the force column and the stiffness matrix (see Eq. (4.15) & (4.16)). To overcome this expensive assembly the QC method uses only a small number of s truss nodes to approximate the total internal potential energy, and thus the force column and the stiffness matrix, instead of determining them via Eq. (4.15) & (4.16). This operation has some similarity with the use of integration points to numerically integrate the stiffness matrix in the FE method. Here, however, we are dealing with a sum of discrete contributions, which are associated with discrete points in space.

Consequently, the rules used to construct approximations for this sum are referred to as summation rules.

The truss nodes selected to sample the nodal energies of their surrounding truss nodes, are referred to here as sampling nodes. They are gathered in index set $S \subseteq N$. Sampling nodes may coincide with the repnodes, as for instance in the node-based QC framework of Knap and Ortiz [64] in which the two sets are identical ($S = R$).

The number of surrounding nodes that are represented by one sampling node must be carefully determined and constitutes the weight factor of the corresponding nodal energy. The assembly procedures of Eq. (4.15) & (4.16) can now be rewritten as follows to obtain the condensed force column and stiffness matrix:

$$\mathbf{f}^{c,s}(\mathbf{u}_r) = \sum_{i \in S} w_i \Psi^T \mathbf{f}_i, \quad (4.17)$$

$$\mathbf{K}^{c,s}(\mathbf{u}_r) = \sum_{i \in S} w_i \Psi^T \mathbf{K}_i \Psi \quad (4.18)$$

where the nodal energy of sampling node i is used to approximate the nodal energies of w_i nodes. The sizes of \mathbf{f}_i , \mathbf{K}_i and Ψ remain $nd \times 1$, $nd \times nd$ and $nd \times rd$ respectively. To ensure that the computational burden is reduced, the number of sampling nodes must be substantially smaller than the total number of nodes, i.e. $s \ll n$.

The question arises which sampling nodes must be selected to establish an accurate estimate of the total potential energy (and thus the condensed force column and stiffness matrix). It is important that the selection of sampling nodes is in accordance with the triangulation. If the selection is poorly done an incorrect solution or even zero-energy modes may occur, as is shown in [64]. Different QC methods can be distinguished based on different selection procedures (summation rules): the local-nonlocal QC method, the node-based QC variant and its generalization, the cluster QC method.

The local-nonlocal QC method is characterized by a different energy evaluation of the sampling atoms for the interpolated domain and the fully resolved domain. In the QC methods of Tadmor et al. [114], Miller et al. [82] and Shenoy et al. [108] and Shimokawa et al. [109] all repatoms are selected as sampling atoms but the computation of the sampling atoms in the fully resolved region is nonlocal while it is local in the interpolated domain. In the fully resolved domain all atoms are repatoms and all repatoms are sampling atoms to ensure the accuracy of the exact lattice model. This part of the domain is called nonlocal because (atomic) interactions at finite distances are fully preserved.

In the interpolated region, the repatoms are selected as sampling atoms as well. However, the site-energies of these sampling atoms are determined as if the atoms were embedded in an infinitely large, perfect crystal. This is referred to as local QC, since

the computation of sampling atoms is local, and is equivalent with homogenization towards a continuum according to the Cauchy-Born rule. The corresponding weight factor w_i equals the number of atoms in the considered triangle and can be determined in various ways [108].

A major disadvantage of this summation rule is that an internal interface occurs between the fully resolved (nonlocal) regions and the interpolated (local) regions. This is caused by the fact that in the local QC method separation of scales cannot be guaranteed close to the fully resolved regions. As a consequence, non-physical forces (ghost forces) occur at the interface. The interface must therefore be located relatively far away from the phenomena (e.g. defects) in which one is interested. This leads to large fully resolved regions, i.e. a large number of repatoms and sampling atoms, and thus to a relatively large computational burden. Corrective procedures have been formulated to deal with the internal interface [108,109], but they are not without disadvantages. Corrective forces at the interface are for instance modeled as dead loads and they are therefore assumed not to change [108].

The QC method of Knap and Ortiz [64] has the major advantage above the local-nonlocal QC method that an internal interface between the interpolated and fully resolved region does not occur. For this reason small fully resolved regions are in principle sufficient and thus the number of repatoms can remain small. The reason that no interface occurs is that the method uses the same sampling point (atom) computation for both domains and it does not use local computation of sampling atoms but merely non-local computation. If the repatoms are selected as sampling atoms, i.e. the node-based approach, this is dual to a Newton-Cotes integration scheme for continuum-based FE methods.

An important disadvantage of the node-based approach is that it may lead to zero-energy modes [64]. As a remedy for zero-energy modes, the use of clusters of sampling atoms around the repatoms has been suggested [64,36]. To retrieve the exact lattice model in fully refined domains, these clusters need to be truncated if they overlap.

A disadvantage of the cluster approach is the fact that the total potential energy is poorly estimated for any given cluster radius, as shown by Luskin and Ortner [76]. Moreover, the large number of sampling atoms and elaborate bookkeeping costs, partially caused by checks to determine if the clusters overlap, make the cluster QC method more inefficient than the local-nonlocal QC approach [83,27].

Even though the cluster QC method gives an inaccurate estimate of the total potential energy, it demonstrates that, in order to avoid an internal interface, one single selection procedure for the interpolated and the fully resolved domain is needed whereby the site-energy of all sampling atoms is computed nonlocally (i.e. the Cauchy-Born rule is not applied).

4.2.4 Novel summation rule

In order to formulate a summation rule (i.e. a rule governing selection and weight factor of sampling points) that satisfies the above conditions and nevertheless provides an accurate estimate, we first return to the interpolated system without summation (see Fig. 4.3). This means that all truss nodes are visited, i.e. $S = N$, resulting in the exact potential energy of the interpolated system according to Eq. (4.16). We will refer to this (expensive) method of constructing the reduced equations as the semi-QC method below.

Since linear interpolation is used for the displacement vectors of the truss nodes within a triangle and since the nodal energies of the truss nodes only depend on their own displacements and the displacements of their nearest neighbors, the nodal energies of all truss nodes within a triangle are equal to each other if their nearest neighbors are located in the same triangle. An example of this is shown in Fig. 4.3, in which the neighboring truss nodes of truss node i are located in the same triangle as truss node i . Since the neighboring truss nodes of truss node $i + 1$ are also located in the same triangle (see Fig. 4.3), the trusses associated with these nodes are deformed identically and their nodal energies are equal to each other. Note that, in terms of Eq (4.6) and (4.10) this also implies that $\mathbf{f}_i = \mathbf{f}_{i+1}$ and $\mathbf{K}_i = \mathbf{K}_{i+1}$. On the other hand, the nodal energy of truss node j does not have to be equal to that of truss nodes i and $i + 1$ since one of the neighbors of truss node j is located in another triangle than j and therefore the nodal energy of truss node j also depends on the deformation of the neighboring triangle.

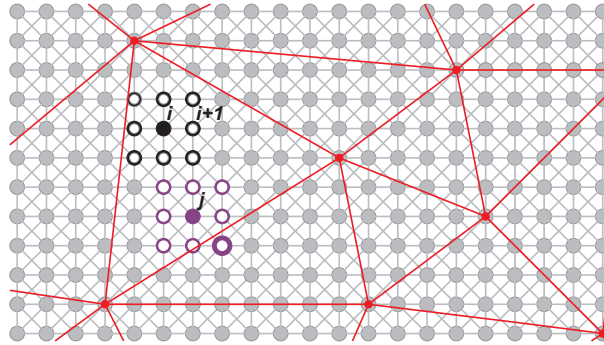


Figure 4.3: Schematic representation of a part of a two-dimensional regular truss network with a superimposed triangulation. The neighboring truss nodes of truss nodes i and j are visible as open circles. The bold neighboring truss node of truss node j indicates that it is located in a different triangle than truss node j .

In interpolated regions with large triangles, the majority of nodes have their neighbors in the same triangle. The energies of these nodes, which are all equal, may be poorly represented by the renodes or clusters around them, as proposed in the cluster QC method [64,36]. For this reason, the cluster QC method gives an inaccurate estimate

of the potential energy. Even if the cluster radius is large enough so that every node is used in the summation ($S = N$) and the improved method of Eidel and Stukowski [36] is used, the cluster summation rule determines the weight factors (w_i in Eq. (4.17) & (4.18)) in such a way that the exact internal potential energy is not found (see also the study of Luskin and Ortner [76]).

Instead of sampling the energy at (or near) the renodes, the above observations suggest a focus on the central regions of each triangle, where the nodal energy is constant, and therefore also the contributions \mathbf{f}_i and \mathbf{K}_i to the linearized equilibrium equations. According to the aforementioned analysis of the semi-QC approach, in which only interpolation is performed ($S = N$), the total potential energy is not affected if only truss nodes with all their neighbors in the same triangle are summed. Therefore the new QC method uses only one of these nodes for sampling, i.e. only one of them is included in S and its corresponding weight factor w_i is set equal to the number of truss nodes within the triangle that have no neighbors in other triangles.

In practice we use the first node encountered which has all of its neighbors in the triangle. It is emphasized that this is an arbitrary choice and any other choice among the internal nodes would also give an exact result. An exact summation is obtained if all other truss nodes, that have one or more neighbors in another triangle, are taken into account individually. They can also be regarded as sampling nodes (i.e. they also belong to S), with a weight factor equal to one ($w_i = 1$) since they 'estimate' only their own energy. We refer to these nodes as discretely modeled nodes. Because in this summation rule only truss nodes are eliminated that have the same energy as the corresponding sampling node, whereas all the nodes that have a potentially unique energy are individually taken into account, no summation error is introduced. The computed potential energy therefore equals the exact potential energy of the interpolated system and the condensed, summed force column and stiffness matrix in Eq. (4.17) & (4.18) equal the condensed force column and stiffness matrix in Eq. (4.15) & (4.16).

The proposed summation rule naturally avoids the introduction of an internal interface, since all (internal and discretely modeled) sampling nodes are computed nonlocally. This ensures that the discretely modeled sampling nodes interact with their actual neighbors in the adjacent triangles. For these nodes, it is important to emphasize that not only trusses crossing triangle edges are modeled but all trusses must be taken into account to correctly establish their nodal energy according to Eq. (4.1).

As a result of the summation rule, bands of discretely modeled sampling nodes are obtained along edges of the interpolation triangles, while truss nodes inside the triangles are eliminated all but one, as can be seen in Fig. 4.4. In small triangles, most notably in fully resolved regions, all truss nodes may have one or more neighboring truss nodes in other triangles and they are therefore all discretely modeled (see Fig. 4.4). A smooth transition is achieved in this way towards fully resolved regions (where the exact lattice model is necessary) whereby the summation rule automatically uses fewer sampling nodes if fewer truss nodes become available in triangles with decreasing dimensions - cf. the shrinking of clusters in the cluster QC approach.

The bands of discretely sampled truss nodes along edges as shown in Fig. 4.4 imply that still a relatively large number of truss nodes must be visited compared to e.g. the local QC method. For lattices with next-nearest neighbor interactions, such as atomic lattices or three dimensional lattices, these bands become wider and the computational efficiency may be too low. In follow-up work, we propose solutions to this concern, by no longer requiring that the estimate potential energy is exact, but accepting some error. However, for two-dimensional structural lattice models with only nearest neighbor interactions such as the example considered in this chapter, the computational cost of the exact method remains acceptable as will be shown in Section 4.3.

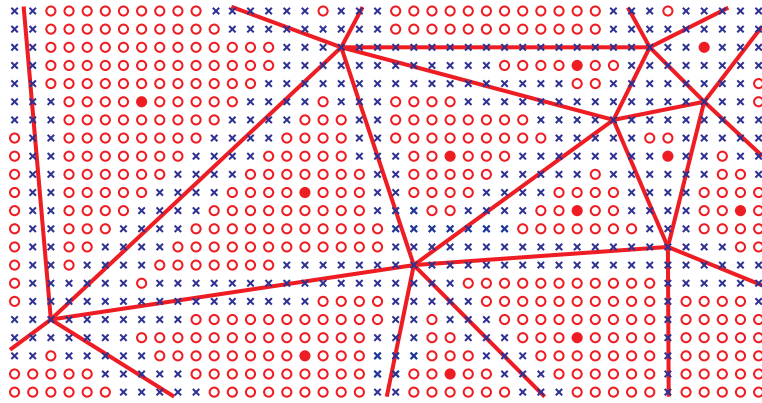


Figure 4.4: Sketch of the novel summation rule applied to a truss network. For clarity only the truss nodes are shown. Open circles represent truss nodes whose contributions are replaced by those of the internal sampling nodes (solid). Crosses represent discretely modeled nodes (for which $w_i = 1$).

4.2.5 Algorithm

The proposed summation rule does not result in an internal interface, which leads to a simple and efficient algorithm. The algorithm for the new QC method is presented in Table 4.1. The new summation, and thus the algorithm, is triangle-based and separately deals with each triangle. Therefore, the algorithm is relatively straightforward to implement and it can be parallelized with some minor adaptations to increase its efficiency.

The essential step of the summation rule is the second step in Table 4.1, in which the location of the neighbors of every truss node of the lattice is used to determine whether it is selected as a sampling node and thus belongs to S . First the truss nodes of a particular triangle are selected in an efficient manner, for which the interpolation functions are evaluated at the lattice positions. It is advantageous to use the evaluated interpolation functions for this decision because they are also necessary in the fourth step of the algorithm. At this point all truss nodes of the considered triangle are known and by a simple count if a truss node has eight neighbors in this triangle it can be

decided if the truss node must be selected as discretely modeled node and therefore must be assigned to set S with $w_i = 1$. Otherwise, the truss node is summed and one of the internal truss nodes is selected as sampling node with a corresponding weight factor that equals the number of summed truss nodes. After all truss nodes of the lattice model have been processed, the set S of sampling nodes is established.

To correctly determine the nodal energy of all sampling nodes in a nonlocal manner, all neighboring nodes of all sampling nodes must be available for the nonlocal computation of the sampling nodes' site-energies. Therefore, in the third step of the algorithm the neighbors that are not in S are recovered.

In the fourth step the evaluated interpolation functions are assembled to one matrix Ψ that is used to condense the summed force column and stiffness matrix (see Eq. (4.17) & (4.18)) in the Newton-Raphson procedure of the fifth step.

Table 4.1: Algorithm of the proposed QC method.

1. Incorporate boundary conditions in \mathbf{u}_r and \mathbf{f}_{ext}
2. Determine sampling nodes per triangle based on the location of neighbors
▷ for every triangle t
- produce truss nodes in a rectangle circumscribing triangle t
- evaluate interpolation functions at the locations of all truss nodes
- use interpolation function evaluations to decide which truss nodes belong to triangle t
▷ for every truss node i in triangle t
- determine number of neighbors of truss node i in triangle t
▷ if number of neighbors in triangle $t < 8 \rightarrow$ select truss node i as discretely modeled sampling node ($w_i = 1$)
▷ else \rightarrow sum truss node by adding 1 to the weight factor of triangle t
▷ if no internal sampling node in triangle t is selected yet \rightarrow select truss node i as internal sampling node
3. Recover missing neighbors of all sampling nodes with corresponding evaluated interpolation functions
4. Assemble condensation matrix Ψ with evaluated interpolation functions of sampling nodes and neighbors
5. Use Newton-Raphson procedure
▷ for each increment until residual meets tolerance
- Assemble condensed, summed force column $\mathbf{f}^{c,s}$ and stiffness matrix $\mathbf{K}^{c,s}$
- Partition $\mathbf{f}^{c,s}$ and $\mathbf{K}^{c,s}$, solve system and update solution according to Eq. (4.14)

4.3 Performance study

In this section, the proposed QC method is applied to three different loading situations in order to assess its performance. First uniform tension is considered, by way of a patch test. This test demonstrates the accuracy of the calculated weight factors of the

sampling truss nodes (see Fig. 4.5a). Bending is the second considered deformation mode because it imposes gradual nonuniform deformation which triggers trusses that cross triangle edges to behave differently than trusses within triangles (Fig. 4.5b). A case including a lattice defect is used to assess the accuracy of the proposed QC method for microscale lattice defects in a large-scale model (Fig. 4.5c). Finally, the impact of the scale/size of the problem domain on the efficiency is examined by successively increasing the model size while keeping the defect constant.

A lattice model consisting of 70 by 50 unit cells (Fig. 4.1) in horizontal and vertical direction respectively is used as a reference model. The stiffnesses of the horizontal and vertical trusses are equal and the stiffness of the diagonal trusses equals a factor $1/\sqrt{2}$ times that of the horizontal and vertical trusses. The trusses along the four outer boundaries are given half the usual stiffness to ensure that a state of uniform deformation is recovered for uniform tension. The results are compared to the direct lattice simulation and to the semi-QC method, which gives the best achievable result for a given triangulation.

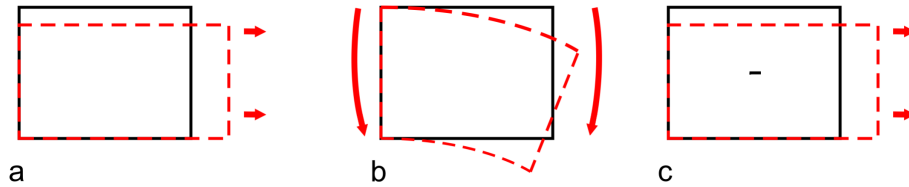


Figure 4.5: The three numerical test cases: a. uniform tension, b. bending, c. uniform tension with a missing truss in horizontal direction.

4.3.1 Uniform tension

Uniform deformation is simulated for six triangulations as presented in Fig. 4.6 by applying 0.5% strain in horizontal direction to the right edge of the model. The model is free to contract in vertical direction. In the direct simulation (not shown) a perfectly uniform deformation is obtained and the site-energies of all nodes in the interior of the model are therefore equal. The linear interpolation used in the QC method should be perfectly capable of capturing uniform deformation and should therefore not introduce any error. In Fig. 4.6, it can be clearly seen that for large triangles the new summation rule leads to a relatively large reduction of the number of sampling nodes compared to small triangles, since in small triangles relatively many truss nodes have one or more neighbors in an adjacent triangle and are therefore selected as (discretely modeled) sampling nodes.

The total internal energies for uniform deformation are presented in the left graph of Fig. 4.7. The results for the proposed QC method equal the results of the direct simulation and the semi-QC result for all triangulations. This indicates that all weight factors are correctly determined in the new QC method, consistently with the selected

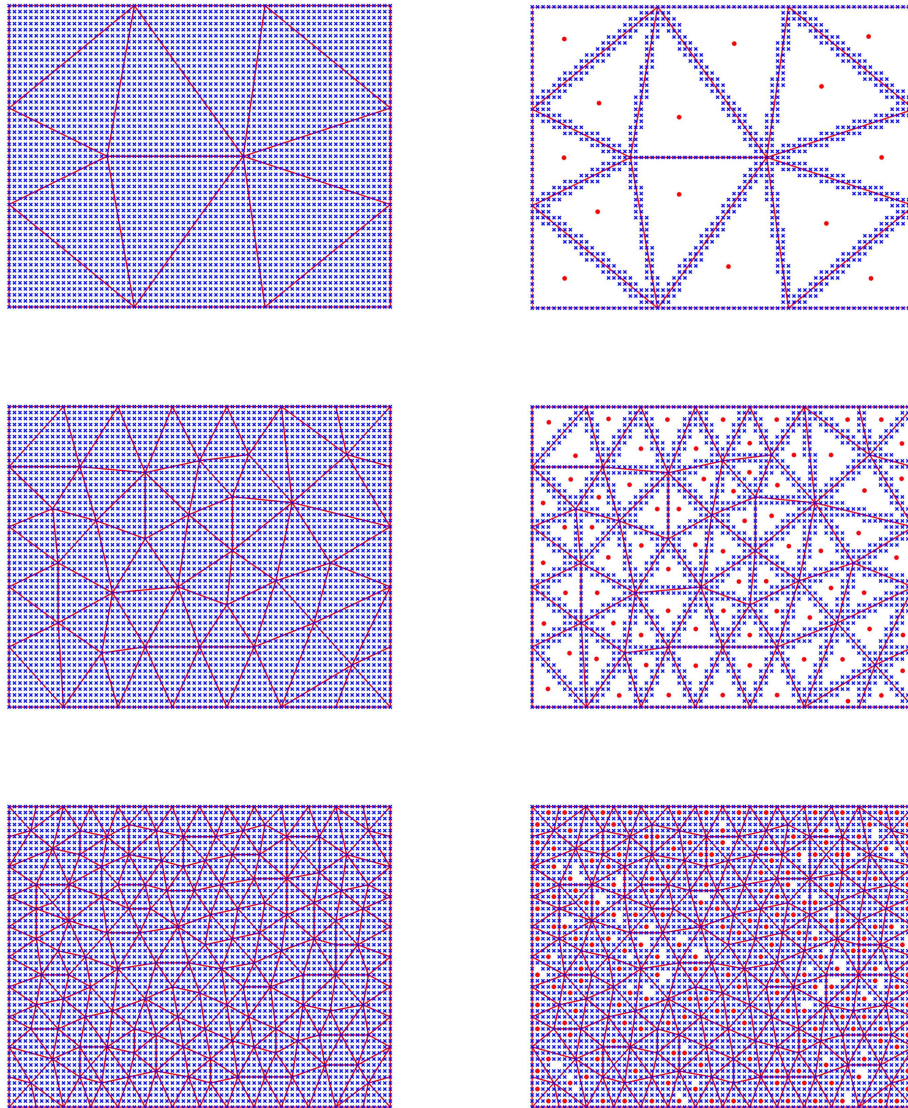


Figure 4.6: A coarse, intermediate and fine triangulation are shown from top to bottom, with average triangle sizes of 250, 49 and 12 unit cells respectively. On the left the semi-QC variant with solely interpolation is depicted (no summation) while on the right the new summation rule is applied. The full circles indicate internal sampling nodes that represent all other truss nodes in a triangle which have their neighbors in the same triangle. The blue crosses represent discretely modeled nodes.

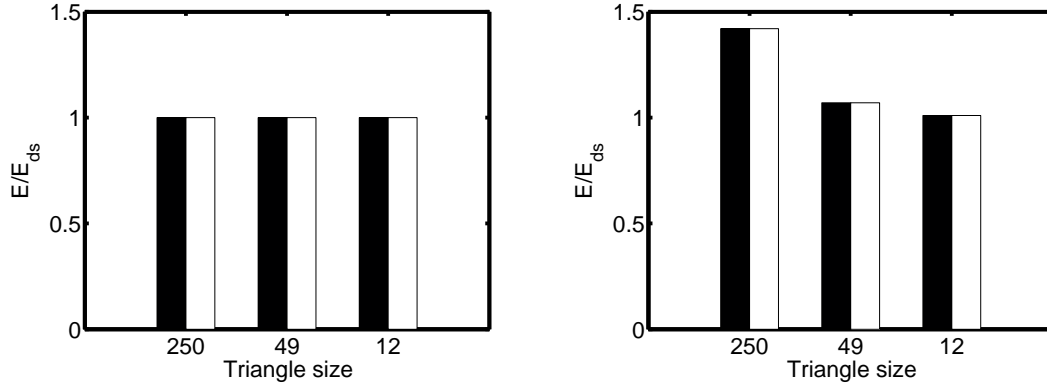


Figure 4.7: (Left) Computed energy in case of uniform deformation normalized by the energy of the direct simulation for different average triangle sizes in terms of unit cells. (Right) Bending energy normalized by the energy of the direct simulation for different average triangle sizes. Black bars: semi-QC method; white bars: the novel QC method.

sampling nodes. Although it may seem trivial that the exact result is obtained in this patch test, not all existing QC methods pass this test.

4.3.2 Bending

The same lattice and triangulations are used for bending, where the applied strain in horizontal direction increases linearly from -0.5% at the bottom to 0.5% at the top of the truss network. Comparing the total internal energies of the proposed QC method and the exact lattice model in the right graph in Fig. 4.7, it is clear that the coarse triangulation is not fine enough to predict the bending energy of the direct lattice simulation, which is expected for a linear interpolation - cf. the poor performance of linear finite elements in bending. For the finer triangulations the total internal energies of the proposed QC method tend towards the full lattice result, i.e. towards $E/E_{ds} = 1$, but the exact internal energy is not reached. However, the energy computed by the proposed QC method does equal that of the semi-QC method, indicating that the summation remains optimal in the proposed QC method. The correct summation implies that not only intra-triangular interactions, i.e. the weight factors and corresponding sampling nodes, are exact but also inter-triangular interactions are adequately resolved.

4.3.3 Single lattice defect

To investigate the multiscale character of the QC method, an example with a horizontal lattice defect is studied. The same 70 by 50 unit cell lattice model is used, subjected to a uniform deformation at the boundary as in the patch test of Section 4.3.1. However, a horizontal lattice defect has been introduced by removing the right horizontal truss of the center truss node, as shown in Fig. 4.5.

Six different triangulations as shown in Fig. 4.8 are used to investigate the influence of the defect and the capability of the QC method to resolved it. Triangulations *a* to *e* in Fig. 4.8 have fully resolved regions of 2×2 , 4×4 , 6×6 , 8×8 and 10×10 lattice distances respectively. The triangle size in the interpolated region doubles with every ring of triangles away from the fully resolved region. Triangulation *f* has a fully resolved region of 4×4 lattice distances, like triangulation *b*, but the triangle size in the interpolated region doubles only after every second triangle.

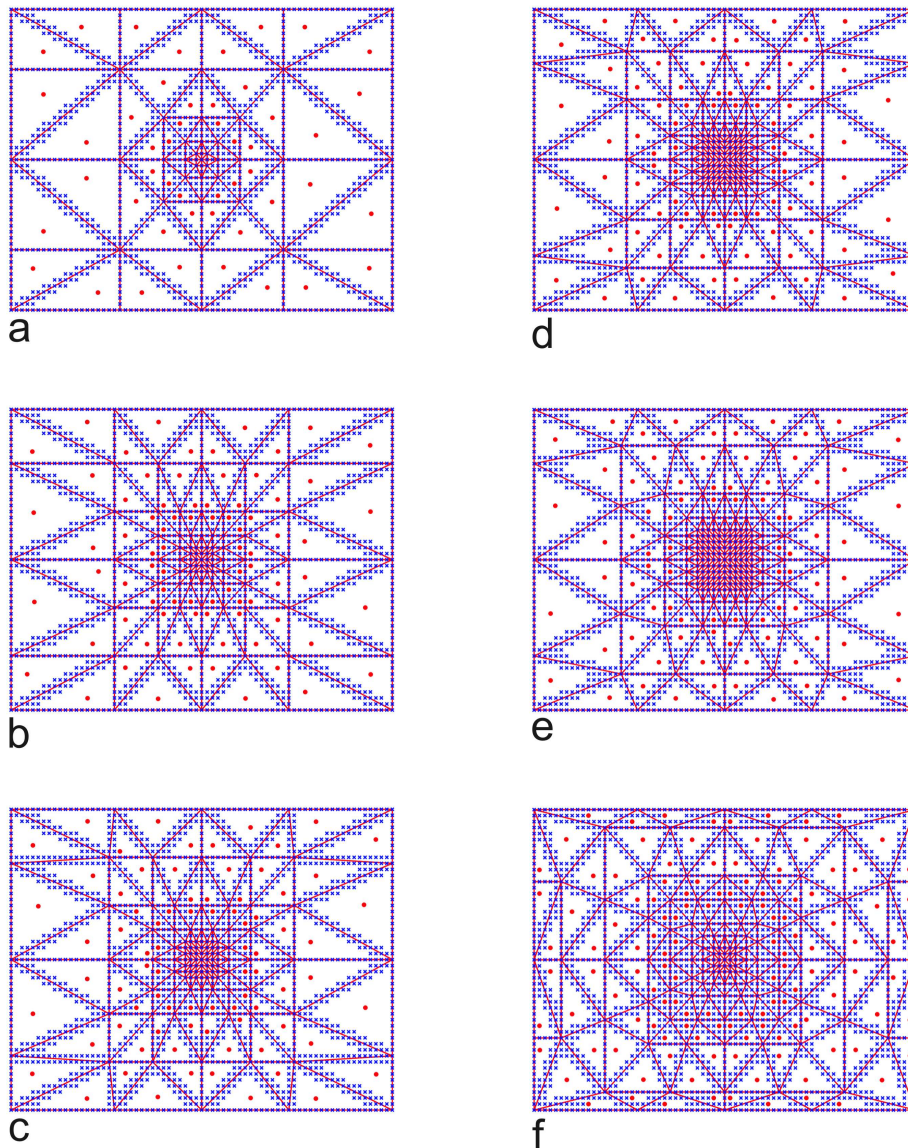


Figure 4.8: Six different triangulations to investigate the influence of the lattice defect. Full circles represent internal sampling nodes that represent all other truss nodes within one triangle that have all neighbors inside that triangle and crosses symbolize discretely modeled nodes.

In the left graph of Fig. 4.9 the number of renodes and sampling nodes relative to the 3621 truss nodes of the complete lattice are shown for each triangulation. The relative number of renodes is smaller than 5% for all triangulations but the relative number of sampling nodes reaches almost 70% for triangulation f . The reason for the large number of sampling nodes is that a small model is considered here; for large models the relative number of sampling nodes is substantially smaller (see Section 4.3.4). The difference in number of renodes and sampling nodes between triangulation a and b is relatively large compared to the differences between triangulations b and c , c and d and d and e . This is due to the degree of refinement of the triangles in the interpolated region, which is clearly less complex for triangulation a compared to triangulations b to e . The number of sampling nodes for triangulations b to e increases similarly as the number of renodes. This is caused by the fact that only the fully resolved region is enlarged while the refinement of the interpolated region remains almost the same (i.e. every extra renode is also a sampling node). Comparing triangulation b to triangulation f , it is clear that the number of sampling nodes is substantially larger for triangulation f while the increase of the number of renodes is small. The reason for this is the fact that the fully resolved regions are similar but the interpolated region of triangulation f is more refined. Therefore more additional sampling nodes are created than renodes.

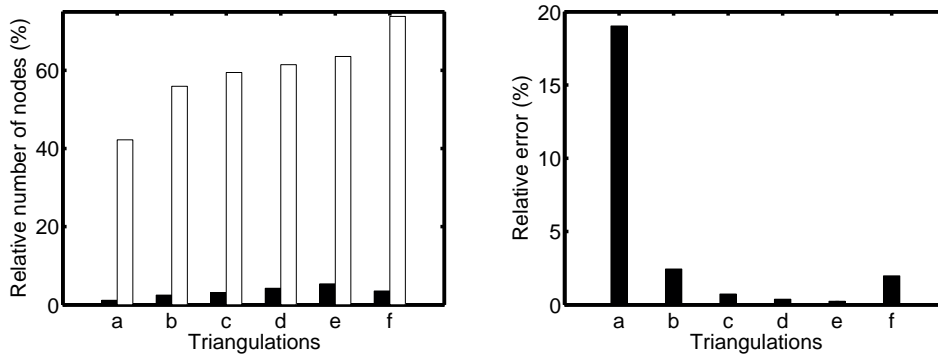


Figure 4.9: (Left) Black bars: the relative number of renodes for the six triangulations; white bars: the relative number of sampling nodes. (Right) The maximum error of the relative displacements of the two truss nodes where the lattice defect is introduced.

Instead of focussing on the total internal energies - which hardly differ due to the presence of only one lattice defect - it is more interesting to establish if the proposed QC method predicts the displacements in the region around the lattice defect correctly. The horizontal components of the displacement vectors of the truss nodes clearly show the fluctuation field caused by the defect, particularly if the displacements of the perfect lattice are first subtracted according to:

$$u_x^{rel}(\vec{x}_i) = u_x(\vec{x}_i) - E_{xx} x_i \quad (4.19)$$

where the relative horizontal component of the displacement vector is denoted by u_x^{rel} and E_{xx} is the applied overall strain in x -direction.

For triangulation c the relative horizontal displacements around the lattice defect as computed with the proposed QC method are presented in Fig. 4.10. The defect causes two peaks at the two ends of the missing truss. Only the displacements in regions to the left and right of the lattice defect are influenced significantly while in the regions above and below the defect the relative displacement needs only a couple of lattice spacings to decay to zero.

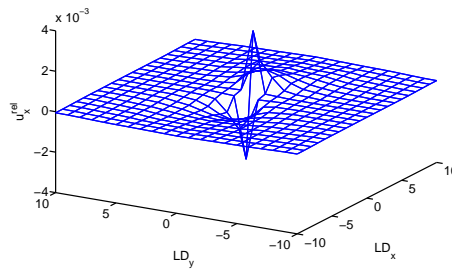


Figure 4.10: The relative horizontal displacements of the truss nodes, u_x^{rel} , for triangulation c around the horizontal lattice defect as a function of the lattice distance in horizontal direction and vertical direction, denoted by LD_x and LD_y respectively.

The results of the proposed QC method are only compared to those of the direct lattice simulation since it is now clear that also for true multiscale models the results of the proposed QC method equal those of the semi-QC approach (not shown here). The maximum error of the fluctuation field of Fig. 4.10 of the two truss nodes where the peaks occur is considered for this comparison. It is normalized by the maximum relative displacement in the direct simulation. Note that the defined error is a sensitive error measure since the normalization involves the displacements relative to the uniformly deforming lattice.

The maximum errors for the six triangulations are shown in the right graph of Fig. 4.9. The error of triangulation a is large since the missing truss is located at the edge of the interpolated region due to the fully resolved region of only 2×2 lattice spacings. If the distance between the lattice defect and the interpolated region is increased, the error is substantially reduced. For triangulation b , which has a fully resolved region of 4×4 lattice spacings, the relative error is reduced by a factor of ten. If the fully resolved region is further increased, the relative error decreases as well but by a smaller factor. For triangulation c , which has a fully resolved region of 6×6 lattice spacings, the error is less than 1%, indicating that the proposed QC method gives an accurate result for a rather small fully resolved region.

Comparing triangulation b and triangulation f , it is visible in the right graph of Fig. 4.9 that a more refined interpolated region - as in triangulation f - only leads to a marginal reduction in the error. Since the number of repnodes and the number of sampling nodes increases substantially, it is more efficient to increase the size of the fully resolved region in order to reduce the error. Note, however, that this analysis is performed for uniform deformation while other loading situations might require a refined interpolated region instead of a larger fully resolved domain.

4.3.4 Influence of model size

The computational burden of the six models in Fig. 4.8 is substantially reduced by the QC method compared to the direct lattice calculation. Especially the number of DOFs (displacement components of the repnodes) is reduced, while the obtained solution is almost identical to the direct lattice calculation. To ensure that the summation is exact, the number of selected sampling nodes remains rather high in the problem studied above (see the left diagram in Fig. 4.9). However, for larger (physically relevant) models the number of sampling nodes is also reduced since in larger problems the interpolated regions comprise a relatively large part of the domain. This is illustrated in Fig. 4.11, in which the size of the model has been increased while keeping the lattice spacing and defect size constant. This implies that the scale separation between the lattice and model is increased. The four triangulations shown have fully resolved regions of 6×6 lattice spacings and different sizes of interpolated regions around them. As can be seen in the graph in Fig. 4.11 the number of repnodes and sampling nodes relative to the total number of truss nodes decreases for an increasing problem size and the efficiency of the QC method thus improves for larger scale-separations between the fully resolved regions of interest and the complete model.

4.4 Conclusion

The quasicontinuum (QC) method has so far only been used to reduce the computational cost of atomistic simulations [114,115,108,64,36,83,82,109]. In this chapter it is demonstrated that QC approaches also have a potential for structural lattice models containing discrete elements such as trusses and beams. The high accuracy of the QC method proposed for structural lattice models has been illustrated in this chapter by comparing the QC results to those of direct lattice calculations for a regular truss network. Furthermore, the large reduction of the number of degrees of freedom, achieved by interpolation, and the fact that only a selective part of the truss nodes of the lattice model, so-called sampling nodes, has to be visited to construct the total internal potential energy, ensure that the QC method is markedly more efficient than direct simulations.

The main reasons that a QC type method is attractive for structural lattice models based on fibrous and heterogeneous materials are twofold. First, only a simple lattice

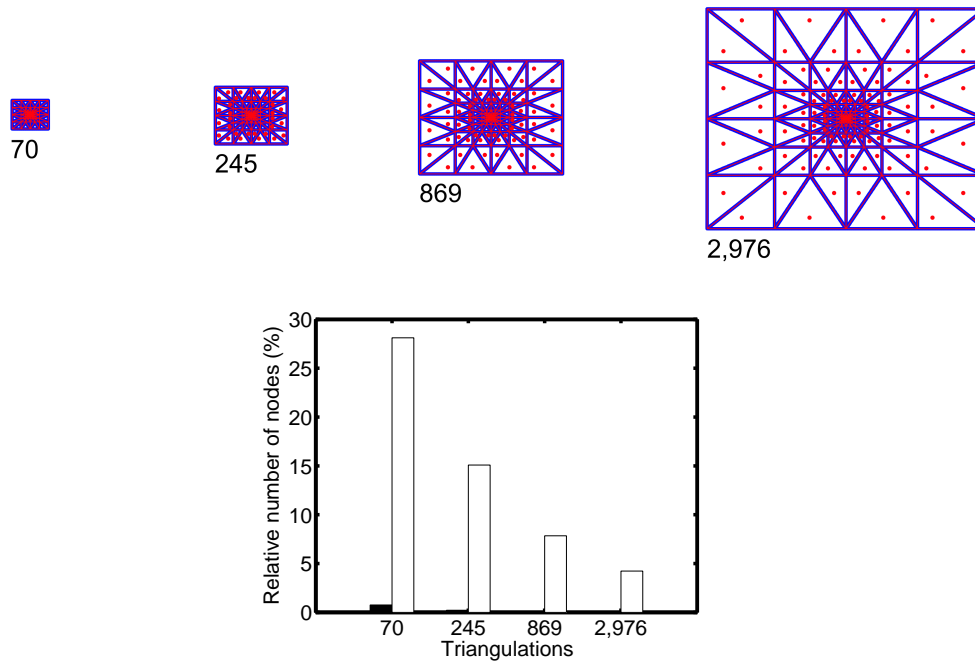


Figure 4.11: (Top) Four triangulations with fully resolved regions of 6×6 lattice spacings and average triangle sizes of 70, 245, 869 and 2,976 unit cells. Every consecutive triangulation has an extra ring of triangles in the interpolated domain. (Bottom) Black bars: the relative number of renodes for the four triangulations; white bars: the relative number of sampling nodes.

model is needed in a QC approach. The method operates directly on this discrete model and no equivalent continuum model is required. This is an advantage because phenomena such as large rotations, re-orientation, anisotropy, bond fracture, sliding of nodes and fracture of the discrete elements are difficult to capture in continuum models.

Second, if a fully resolved domain must be incorporated to investigate local events, no special coupling between the interpolated (continuum) domain and the fully resolved (discrete) domain is necessary. This is an advantage since such a coupling often invokes additional assumptions. Most QC methods use a coupling procedure to avoid interface problems between both domains but in this chapter a QC variant is proposed that does not require such a coupling.

The QC method proposed here for structural lattices is the only QC method that determines the potential energy exactly while avoiding an internal interface between the interpolated and fully resolved domain. It is based on a clear understanding of how the total potential energy depends on the interpolation and how this should be reflected in the summation. This means that no summation error is introduced and the only occurring error is due to the interpolation.

The QC method has been evaluated for a relatively simple truss network which has a single lattice defect. For a relatively small fully resolved region (and thus a high com-

putational efficiency) errors of less than 1% compared with the direct simulation have been observed. The same accuracy can be expected in case the damage progresses by subsequent removal of trusses. However, in this case the interpolation must be modified adaptively to ensure that the failure of trusses always takes place well within the fully resolved domain and the selection of sampling nodes must be updated accordingly. The damage progression is then completely dependent on the lattice model and independent on the triangulation since the triangle size in the fully resolved region is fixed to the lattice spacing and no failure of trusses occurs in the interpolated domain. The fact that the triangle size used in the interpolation has a natural minimum (corresponding to the fully resolved case) ensures that no pathological localization and mesh dependency occur upon refinement of the interpolation. In the limit of a fully resolved lattice model, the width of the process zone is set by the (physical) discrete lattice spacing.

Although the examples treated here are two-dimensional, the extension of the QC methodology to three-dimensional lattice models is straightforward. However, a concern may be that the computational efficiency of the summation rule used here is reduced. The reason for this is that tetrahedra contain relatively more nodes that have one or more neighbors in another tetrahedron, which are all taken into account discretely, than triangles. This is even more of a concern if lattice models with next-to-nearest neighbor interactions are considered, such as atomistic models. Modifications of the summation rule which deal with this issue will be discussed in a forthcoming publication.

Further research will also focus on applying the QC method to beam lattices, which contain next to translational degrees of freedom also rotational degrees of freedom. This combination of displacements and rotations may require a more advanced interpolation, akin to shell formulations in the finite element method, which preserves consistency of the two sets of degrees of freedom. Interestingly, such an approach would lead to an enriched quasicontinuum on a natural discrete basis, and would allow us to make contact with Cosserat-type of continuum formulations [21].

Central summation in the quasicontinuum method¹

Abstract

The quasicontinuum (QC) method [Tadmor, E.B., Phillips, R., Ortiz, M., 1996, Mixed atomistics and continuum models of deformation in solids, *Langmuir*, Vol. 12, 4529-4534] is a multiscale methodology to reduce the computational cost of atomistic lattice simulations. The method ensures an accurate incorporation of small-scale atomistic effects in large-scale models. It essentially consists of an interpolation of displacements of large numbers of atoms between representative atoms (repatoms) and an estimation of the potential energy of the atomistic lattice by a so-called summation rule. In this chapter, a novel energy-based summation rule is presented for the QC method that allows for a seamless coupling between coarse domains and fully resolved domains. In the presented summation rule only the repatoms are used, in combination with one extra sampling atom in the center of each interpolation triangle. The presented summation rule is therefore straightforward and computationally efficient. The performance of the proposed summation rule is evaluated for a number of two-dimensional and three-dimensional multiscale atomistic test cases in which a vacancy is considered. The results correspond well with those of direct simulations.

¹ Reproduced from: L.A.A. Beex, R.H.J. Peerlings, M.G.D. Geers, Central summation in the quasicontinuum method, Submitted to the *Journal of the Mechanics and Physics of Solids*.

5.1 Introduction

The quasicontinuum (QC) method [114,115] is a multiscale approach that reduces the computational cost of atomistic lattice computations. The QC method directly takes atomistic effects into account in large-scale models. In different studies the methodology has been used to investigate vacancies [40,109], dislocations [49,114], cracks [82], grain boundaries [82,109], nanovoids [77] and carbon nanotubes [95]. A substantial part of the QC studies has focused on nanonindentation [36,84,64,65,69,97,108,115,116]. Furthermore, extensions of the method have been developed to deal with phase transformations [33], density functional theory [40,49], finite temperatures [68,78] and long-range interatomic interactions [127]. Although the QC method was so far mainly used for atomistic lattice models, it may also be extended to structural lattice models employing trusses or beams, as shown by Beex et al. [9].

The QC method uses two approximations to reduce the computational cost of full atomistic computations. First, only a small number of atoms (repatoms) is selected to represent the displacements of all atoms in the lattice. The repatoms constrain the displacements of the atoms in between them by means of interpolation. The displacement components of the repatoms are the only remaining degrees of freedom (DOFs) of the interpolated atomistic lattice. In regions where the local deformations are small, it suffices to select repatoms far away from each other. In fully resolved regions however, every atom constitutes a repatom so that the exact atomistic model is recovered in these regions of interest.

The second approximation introduced in the QC method is the selection of only a small number of atoms (to which we will refer as sampling atoms) to estimate the total potential energy of the lattice, by a so-called summation rule, instead of visiting all atoms of the crystal to compute it exactly. The sampling atoms are used to sample the site-energies of the atoms in their vicinity. To ensure an accurate estimation of the total potential energy, it is important that the selection of sampling atoms is carefully performed with respect to the interpolation triangulation. If this is not the case, zero-energy modes may for instance occur [64].

Based on the type of summation rule, two general classes of QC methodologies can be distinguished. In the local-nonlocal QC method [82,108,114,115] the site-energies of the sampling atoms in the interpolated domain are locally computed using the Cauchy-Born rule and the site-energies of the sampling atoms in fully resolved domains are computed in a nonlocal manner. This leads to an internal interface between both domains at which an error is introduced due to so-called ghost-forces. To ensure that the ghost-forces at the interface have no significant influence at the solution in the center of the region of interest, the fully resolved region must be relatively large. As a result, the interface is located relatively far away from the center of the region of interest. This increases the computational cost. Corrective procedures have been developed [108,109], but they come with additional assumptions and therefore only allow a slight decrease of the fully resolved regions.

The second class of summation rules is based on the cluster summation rule [36,64] and treats the coarse domain and the fully resolved region similarly. For this reason no internal interface occurs and both domains can thus be seamlessly coupled to each other. Luskin and Ortner [76] however, have shown that even for large clusters this summation rule gives a poor estimate of the potential energy. Reviews of different QC methods and related multiscale methods are presented in [83,85] and [27].

In addition to the above two established classes, new summation rules have recently been proposed. In [43] and [127], the selection of sampling atoms is based on numerical quadrature as used in the finite element (FE) method. The atoms located at (or nearby) the Gauss points are selected as sampling atoms. The obtained results are more accurate than those obtained with the cluster QC variant for a one-dimensional chain of atoms. This summation rule has so far only been applied one dimension. The one-dimensional quadrature-type summation rule has recently been compared to the nodal variant of the cluster summation rule [57].

In the previous chapter, an exact summation rule is proposed for structural lattice models in which only nearest neighbor interactions exist. It is based on the proper understanding of how the potential energy is related to the triangulation. As a result, the computed total potential energy is not an estimate, but exact for the given interpolation. Consequently, the remaining error is only due to the interpolation itself. However, if this summation rule is applied to atomistic crystals, the number of sampling atoms becomes prohibitively large, so that the method becomes computationally inefficient.

The aim of this chapter is to develop a new summation rule, inspired by the one in the previous chapter, for two-dimensional and three-dimensional atomistic crystals. It ensures a seamless coupling between coarse domains and fully resolved domains as a result of the nonlocal site-energy computation of the sampling atoms in coarse domains, as well as in fully resolved domains. The absence of an internal interface increases the computational efficiency, because no updating of interface corrections is necessary if fully resolved regions are adapted or moved through the coarse domain. This leads to a simple and unified multiscale QC approach, like the cluster QC method. However, since it is based on the exact recovery of the potential energy, in contrast to the cluster summation rule, a better estimate of the potential energy is obtained.

The computational cost of the energy-based summation rule is low, because it selects the repatoms as sampling atoms, plus one sampling atom in the center of each triangle (or tetrahedron) of the interpolation. The repatoms only sample themselves (i.e. have a weight factor of one), so that in the fully resolved region the exact atomistic model is recovered. One sampling atom near the center of each interpolation triangle (or tetrahedron for three-dimensional crystals) is used to sample the remaining atoms. Since the focus of the summation rule is on the center of the triangles and tetrahedra, we refer to the new summation rule as the central summation rule.

The outline of this chapter is as follows. In Section 5.2, the QC method is briefly reviewed and in Section 5.3 the existing summation rules are explained in somewhat more detail. In Section 5.4, the exact relation between the total potential energy and the interpolation triangulation is discussed. In Section 5.5, the central summation rule

is derived. The algorithm for the central summation rule in which the sampling atoms are selected is considered in Section 5.6. The results of the central summation rule are discussed in Section 5.7 for a two-dimensional atomistic lattice and a three-dimensional atomistic lattice. Furthermore, a comparison is made with the results of the cluster QC method [64], as improved by Eidel and Stukowski [36], for the two-dimensional atomistic lattice. In all numerical tests, the solution near a vacancy at the center of the fully resolved domain is investigated and compared. Finally, conclusions are presented in Section 5.8.

5.2 The quasicontinuum method

The descriptions of the direct atomistic lattice computations and quasicontinuum lattice computations in this section are formulated in terms of potential energy and minimization thereof. The central summation rule formulated below is energy-based, as for instance those in [36,9]. For force-based formulations, the study of Knap and Ortiz [64] may form a starting point.

Atomistic computations are often based on the minimization of the lattice's potential energy. The total potential energy is the sum of the internal and external potential energy, where the internal potential energy is assumed to be the sum of the site-energies of all atoms of the lattice:

$$E_{tot}(\mathbf{u}) = \sum_{i=1}^n E_i(\mathbf{u}) - \mathbf{f}_{ext}^T \mathbf{u}, \quad (5.1)$$

in which the total potential energy is denoted by E_{tot} and the site-energy of atom i by E_i . The n atoms of the lattice are stored in index set $N = \{1, \dots, n\}$. The external potential energy, E_{ext} , is a function of the components of the externally applied forces, stored in column matrix, \mathbf{f}_{ext} , and the displacement components of all atoms which are stored in column matrix \mathbf{u} . Columns \mathbf{f}_{ext} and \mathbf{u} are both of length $n d$, where d represents the number of spatial dimensions. The site-energy, E_i , is formulated as the sum of the interatomic potential energies E_{ij} between atom i and its neighbors within its cut-off radius, which are stored in subset B_i ($B_i \subseteq N$):

$$E_i(\mathbf{u}) = \frac{1}{2} \sum_{j \in B_i} E_{ij}(\mathbf{u}). \quad (5.2)$$

Half of the interatomic potential energy, E_{ij} , between atom i and neighboring atom j is thus assigned to atom i and the other half to atom j . For the interatomic potential energy, E_{ij} , the Lennard-Jones potential [70] is used in this chapter, as for instance in [64]

and [65]. In other studies, many-body potentials, such as the embedded atom method (EAM), are used [85,109]. As a result of using the EAM, an additional contribution must be added to the site-energy, E_i , that corrects for the electron density.

Now the total potential energy has been established, it can be minimized with respect to the DOFs of the system. The DOFs are in this case the displacement components of all atoms, stored in column matrix \mathbf{u} :

$$\min_{\mathbf{u}} E_{tot}(\mathbf{u}). \quad (5.3)$$

The minimum of E_{tot} can be determined using classical variational principles. This leads to the following expression:

$$\delta E_{tot}(\mathbf{u}) = \delta \mathbf{u}^T \mathbf{f}(\mathbf{u}) = 0 \quad \forall \delta \mathbf{u}, \quad (5.4)$$

where $\mathbf{f}(\mathbf{u})$ is a column matrix containing conservative forces and is of length nd . Arbitrary variations of \mathbf{u} are represented here by $\delta \mathbf{u}$. With respect to the formulation of Eq. (5.1), it is convenient to assemble the force column matrix with the conservative forces, $\mathbf{f}(\mathbf{u})$, from contributions \mathbf{f}_i of each atom, according to:

$$\mathbf{f}(\mathbf{u}) = -\mathbf{f}_{ext} + \sum_{i=1}^n \mathbf{f}_i(\mathbf{u}), \quad (5.5)$$

where

$$(f_i)_p = \frac{\partial E_i}{\partial u_p}, \quad (5.6)$$

where p runs over all nd displacement components in \mathbf{u} . A standard Newton-Raphson process (using a Taylor expansion) can now be used to solve Eq. (5.4):

$$\delta \mathbf{u}^T \left(\mathbf{f}(\mathbf{u}^*) + \mathbf{K}(\mathbf{u}^*) d\mathbf{u} \right) = 0 \quad \forall \delta \mathbf{u} \quad (5.7)$$

where \mathbf{u}^* are the displacement components of the previous iteration and $d\mathbf{u}$ forms the correction on these displacement components computed in the present iteration. The

overall stiffness matrix in Eq. (5.7) is represented by $\mathbf{K}(\mathbf{u})$. The elements of the stiffness matrix can be established as follows:

$$K_{pq} = \frac{\partial^2 E_{tot}}{\partial u_p \partial u_q} = \sum_{i=1}^n \frac{\partial^2 E_i}{\partial u_p \partial u_q}, \quad (5.8)$$

where p and q run over all nd displacement components. The stiffness matrix is thus of size $nd \times nd$ and is symmetric. Similarly to the force column, the stiffness matrix \mathbf{K} can also be straightforwardly assembled by contributions \mathbf{K}_i of each atom:

$$\mathbf{K}(\mathbf{u}) = \sum_{i=1}^n \mathbf{K}_i(\mathbf{u}) \quad (5.9)$$

where

$$(K_i)_{pq} = \frac{\partial^2 E_i}{\partial u_p \partial u_q}. \quad (5.10)$$

In order to solve Eq. (5.7), Neumann and Dirichlet boundary conditions must be incorporated and the system must be partitioned. A locally stable configuration of the atomistic lattice is obtained, if the part of the overall stiffness matrix that remains after partitioning is positive definite.

5.2.1 Interpolation

The first approximation used by the QC method aims to reduce the large number of DOFs in \mathbf{u} by interpolation. Interpolation is imposed by selecting a small number of r repatoms, which are used to represent the displacements of all atoms of the lattice. The index set R , containing the repatoms, is therefore a subset of N ($R \subseteq N$). The domain is subsequently triangulated such that the repatoms form the corners of the triangles (or tetrahedra in 3D). The displacements of the remaining atoms in each triangle are interpolated (and thus constrained) between those of the repatoms. Linear interpolation functions are generally used to express the displacement components of all atoms, \mathbf{u} , as a function of the displacement components of the repatoms, \mathbf{u}_r :

$$\mathbf{u} = \Psi \mathbf{u}_r. \quad (5.11)$$

In this equation, Ψ represents the condensation matrix, with size $n \times d \times r \times d$, in which the interpolation functions evaluated at the locations of all n atoms are gathered.

The total potential energy of the interpolated atomistic crystal only depends on the DOFs of the repatoms, instead of the DOFs of all atoms. In regions where displacement fluctuations are small, relatively large distances between the repatoms are allowed. In regions with large displacement fluctuations however, the repatoms must be located close to each other, where the minimal distance equals one lattice spacing to create a fully resolved region. By correctly selecting the repatoms for a specific problem, i.e. by creating a proper triangulation, the total potential energy of the condensed (triangulated) lattice, E_{tot}^r , is assumed to be similar to the total potential energy of the full lattice, E_{tot} :

$$E_{tot}(\mathbf{u}) \approx E_{tot}^r(\Psi \mathbf{u}_r) = \sum_{i=1}^n E_i(\Psi \mathbf{u}_r) - \mathbf{f}_{ext}^T \Psi \mathbf{u}_r. \quad (5.12)$$

Since the DOFs of the condensed lattice are now the displacement components of the repatoms, \mathbf{u}_r , the minimization of E_{tot}^r must also be performed in terms of this reduced set of DOFs:

$$\min_{\mathbf{u}_r} E_{tot}^r(\Psi \mathbf{u}_r). \quad (5.13)$$

Instead of Eq. (5.7), this results in the following linearization:

$$\delta \mathbf{u}_r^T \left(\Psi^T \mathbf{f}(\Psi \mathbf{u}_r) + \Psi^T \mathbf{K}(\Psi \mathbf{u}_r) \Psi d\mathbf{u}_r \right) = 0 \quad \forall \delta \mathbf{u}_r, \quad (5.14)$$

in which $\Psi^T \mathbf{f}$ symbolizes the condensed force column, \mathbf{f}^r , and $\Psi^T \mathbf{K} \Psi$ the condensed stiffness matrix, \mathbf{K}^r . They are of size $r \times d \times 1$ and $r \times d \times r \times d$ respectively and can be constructed according to the following expressions:

$$\mathbf{f}^r(\mathbf{u}_r) = -\Psi^T \mathbf{f}_{ext} + \sum_{i=1}^n \Psi^T \mathbf{f}_i(\Psi \mathbf{u}_r), \quad (5.15)$$

$$\mathbf{K}^r(\mathbf{u}_r) = \sum_{i=1}^n \Psi^T \mathbf{K}_i(\Psi \mathbf{u}_r) \Psi, \quad (5.16)$$

where \mathbf{f}_i and \mathbf{K}_i represent the force column and stiffness matrix contributions associated with atom i . Since the condensed stiffness matrix is substantially smaller than the original stiffness matrix ($r \ll n$), the condensed equation in Eq. (5.14) is computationally more efficient to solve than the uncondensed equation (Eq. (5.7)).

5.2.2 Summation

Although the number of scalar equations in Eq. (5.14) has been reduced compared to Eq. (5.7), the assembly of the condensed force column and stiffness matrix still remains computationally expensive, since all n atoms must be visited according to Eq. (5.15) & (5.16). To overcome this, the QC method proposes to select only a small number of s atoms to approximate the total potential energy, instead of visiting all n atoms to exactly determine the total potential energy. These so-called sampling atoms (stored in index set S) are used to sample the site-energies of their surrounding atoms and are selected from N , i.e. $S \subseteq N$.

The total potential energy of the sampled, condensed lattice, E_{tot}^{rs} , is assumed to be equal to the total energy of the condensed lattice, E_{tot}^r . This is the case, if the correct sampling atoms are selected. For instance for the summation rule proposed in [9], the total potential energy of the sampled, condensed lattice is exact to the total potential of the condensed lattice. The following expression is now obtained for E_{tot}^{rs} :

$$E_{tot}^r(\Psi \mathbf{u}_r) \approx E_{tot}^{rs}(\Psi \mathbf{u}_r) = \sum_{i \in S} w_i E_i(\Psi \mathbf{u}_r) - \sum_{i \in S} w_i \mathbf{f}_{ext,i}^T \Psi \mathbf{u}_r, \quad (5.17)$$

in which the site-energy of sampling atom i , E_i , represents the site-energies of the atoms in the vicinity of atom i , including sampling atom i itself. The number of atoms it represents is accounted for in the weight factor w_i . Column matrix $\mathbf{f}_{ext,i}$ only contains the external forces acting on sampling atom i . Although $\mathbf{f}_{ext,i}$ is of size $nd \times 1$, it thus only has non-zero entries on the locations that are related to atom i .

Since the DOFs of the lattice are still the displacement components of the repatoms, the minimization of the total potential energy must still be performed with respect to \mathbf{u}_r . The assembly of the condensed force column, \mathbf{f}^r , and of the condensed stiffness matrix, \mathbf{K}^r , becomes computationally more efficient to construct because of the summation. They are expressed as follows:

$$\mathbf{f}^{r,s}(\mathbf{u}_r) = - \sum_{i \in S} w_i \Psi^T \mathbf{f}_{ext,i} + \sum_{i \in S} w_i \Psi^T \mathbf{f}_i(\Psi \mathbf{u}_r), \quad (5.18)$$

$$\mathbf{K}^{r,s}(\mathbf{u}_r) = \sum_{i \in S} w_i \Psi^T \mathbf{K}_i(\Psi \mathbf{u}_r) \Psi, \quad (5.19)$$

in which $\mathbf{f}^{r,s}$ and $\mathbf{K}^{r,s}$ represent the sampled, condensed force column and the sampled, condensed stiffness matrix respectively.

To ensure that the computational cost is actually reduced, the number of sampling atoms must be substantially smaller than the total number of atoms ($s \ll n$). The question arises now which atoms must be selected as sampling atoms, i.e. which atoms need to belong to subset S , to ensure that the estimate of the total potential energy is accurate for a given interpolation.

5.3 Existing summation rules

Two general approaches for the selection of sampling atoms are proposed in QC literature in which also the computation of the site-energies and weight factors is different. We refer to a specific selection procedure, combined with its own computation of site-energies and weight factors, as a summation rule, although in the literature it is also known as summation [83].

5.3.1 The local-nonlocal summation rule

The first general class of summation rules is the local-nonlocal rule [108,109,114,115]. It computes the site-energy of sampling atoms in the fully resolved domain nonlocally, so that all neighboring atoms influence the site-energy of a sampling atom and the exact atomistic model is recovered. This ensures a high accuracy in the fully resolved regions. In the coarse domain however, the site-energy of one sampling atom per triangle is locally computed using the Cauchy-Born rule, ensuring a high efficiency. This means that the site-energy is computed as if the sampling atom were located in an infinite crystal, which is deformed uniformly. This is only accurate, if the deformation slowly fluctuates at the scale of a triangle. Therefore, the site-energy only depends on the repatoms associated with the triangles surrounding that particular sampling atom. An illustration of this summation rule is shown on the left in Fig. 5.1. The local-nonlocal summation rule leads to the use of a small number of sampling atoms. In the fully resolved regions, only the repatoms are selected as sampling atoms and one sampling atom is in principle selected per triangle in the coarse domain (of which the energy is related to the repatoms of the considered triangle [108]).

However, the coupling of the coarse (local) region to the fully resolved (nonlocal) region leads to a relatively large computational burden due to two difficulties. First, the fully resolved regions must be relatively large because at the interface of the fully resolved regions a transition towards local sampling atoms occurs, for which the strain gradients must be small. An example is shown for the local sampling atom indicated in black on the left in Fig. 5.1. Considering the corresponding cut-off radius, three nonlocal and four local sampling atoms are present within the cut-off region. The latter have no influence the site-energy of this sampling atom. To ensure that this locally computed site-energy is still rather accurate, the fully resolved regions must be relatively large.

Furthermore, at the interface between the two domains non-physical forces occur, so-called ghost-forces. These forces are caused by the fact that the site-energy computations of several nonlocal sampling atoms at the boundary of the fully resolved region are dependent on the local sampling atoms next to the fully resolved domain, while the site-energy computations of the latter are independent of the displacements of several nonlocal sampling atoms (see Fig. 5.1).

Corrective procedures have been introduced to deal with this internal interface [108,109], but since they come with additional assumptions, the relatively large fully resolved regions can only be slightly reduced. Moreover, these corrective procedures must be implemented in the algorithm and they must be updated during computations if the size and locations of the fully resolved regions change.

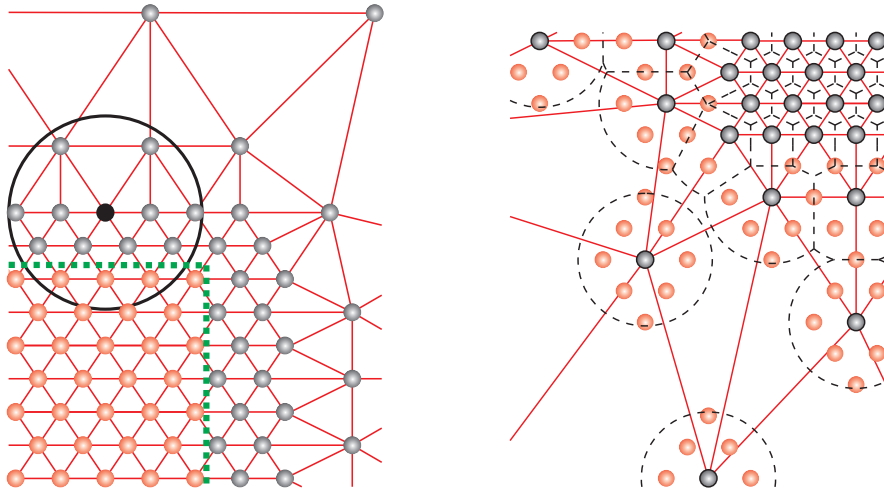


Figure 5.1: Schematic representation of a two-dimensional atomistic lattice with a triangulation in combination with (left) the local-nonlocal summation rule and (right) the cluster summation rule. (Left) The dark atoms are part of the coarse domain and the red (light) atoms are atoms as well as sampling atoms in the fully resolved domain. The cut-off radius around the bold atom is shown. The dashed line represents the location of the internal interface between the fully resolved region and the coarse region. (Right) the dark atoms are atoms (R) while both dark atoms as well as the other indicated atoms are sampling atoms (S). The dashed circles mark the clusters of sampling atoms (and are not related to the cut-off radius).

5.3.2 The cluster summation rule

The second class of summation rules is the cluster variant, which was introduced by Knap and Ortiz [64] in terms of forces and reformulated by Eidel and Stukowski [36] in terms of energy. This summation rule computes the site-energy of all sampling atoms

nonlocally; in the fully resolved domains as well as in the coarse domains. Therefore, no internal interface occurs and a seamless transition is obtained towards fully resolved regions.

According to this summation rule, clusters of sampling atoms are selected centered at the reatoms (see the right illustration in Fig. 5.1). The reatoms therefore also form sampling atoms ($R \subseteq S \subseteq N$). If the clusters tend to overlap, they are truncated so that sampling atoms are only used once. The truncation of the clusters and the nonlocal computation of the sampling atoms' energies ensures that a smooth transition is achieved towards fully resolved regions in which the full atomistic lattice is recovered (right in Fig. 5.1). A higher accuracy is achieved, at the expense of computational efficiency, if a larger cluster radius is used. Note that if the cluster radius is set to zero, the reatoms are the only sampling atoms ($S = R$) and the node-based summation rule of Knap and Ortiz [64], for which zero-energy modes may occur, is retrieved.

Disadvantages of the cluster summation rule are a relatively low accuracy and large look-up tables. The poor accuracy is caused by the use of one summation weight per cluster (w_i in Eq. (5.18) & (5.19)), as shown in [76], but also by the mere selection of clusters, as shown below.

Large look-up tables result from the nonlocal site-energy computation of all sampling atoms and increase the bookkeeping costs. On the other hand, the fact that no corrective interface procedures have to be used is considered to be an advantage. The reason is that, if adaptivity is included to allow for changing and moving fully resolved regions, no corrective procedures have to be updated.

5.4 Relation between the interpolation and the total potential energy

In order to obtain an improved summation rule that estimates the total potential energy well without introducing an internal interface, we consider more carefully how the total potential energy of the interpolated system depends on the interpolation. For this purpose, consider a semi-QC method in which interpolation is applied to an atomistic model, but no summation rule is used, i.e. $R \subseteq N$ and $S = N$. In this semi-QC method, all n atoms of the lattice must be visited to determine the total potential energy and the energy is computed exactly, albeit for the interpolated lattice. An illustration of the semi-QC method is shown in Fig. 5.2 for a two-dimensional closely packed atomistic lattice (i.e. the distances between every atom and its six nearest neighboring atoms equal one lattice spacing).

Now, consider atom p in Fig. 5.2. The site-energy of atom p depends on its own displacement and the displacements of its 18 neighboring atoms (encircled in Fig. 5.2) within its cut-off radius according to Eq. (5.2). Since all neighboring atoms of atom p are located within or exactly on the edge of the triangle in which atom p is located and the displacements are interpolated linearly within this triangle, the site-energy of atom p ultimately depends on the displacements of the three reatoms of the triangle only.

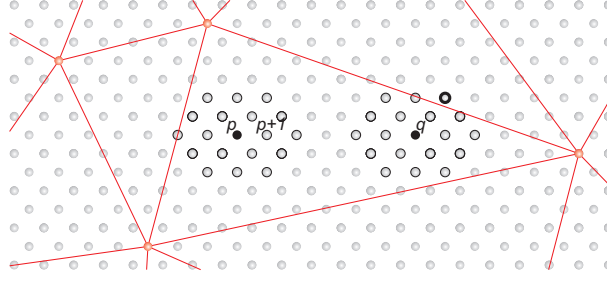


Figure 5.2: Schematic representation of the semi-QC method: a two-dimensional atomistic lattice with a superimposed triangulation between the repatoms (shown in red). The neighboring atoms of the dark atoms p and q are encircled. The neighboring atom of atom q indicated with the bold circle, is located in another triangle than atom q .

A second important aspect is that because linear interpolation functions are used, the relative displacements of all identical bonds within a particular triangle are equal. This entails that the site-energies of atom p and atom $p + 1$ in Fig. 5.2 are identical, because all their neighboring atoms are located inside the same triangle. As a consequence, the contribution made by atom $p + 1$ to the energy of the system is identical to that of atom p . This also implies that in Eq. (5.15) & (5.16) we have $\Psi^T \mathbf{f}_p = \Psi^T \mathbf{f}_{p+1}$ and $\Psi^T \mathbf{K}_p \Psi = \Psi^T \mathbf{K}_{p+1} \Psi$.

The neighboring atoms of atom q in Fig. 5.2 however, are not all located within the same triangle. Thus, the site-energy of atom q depends not only on the repatoms of the triangle in which atom q is located, but also on the repatoms of a neighboring triangle. This means that the site-energy of atom q can be different from those of atoms p and $p + 1$ and thus also $\Psi^T \mathbf{f}_p \neq \Psi^T \mathbf{f}_q$ and $\Psi^T \mathbf{K}_p \Psi \neq \Psi^T \mathbf{K}_q \Psi$.

The potential energy of the triangle in which atoms p , $p + 1$ and q are located remains thus identical if, instead of computing the site-energies of all atoms, the site-energy of atom p is computed and multiplied by the number of atoms that have their neighbors in the triangle (w_i in Eq. (5.18) & (5.19)). In principle, the sampling atom may be chosen arbitrarily among those that have their neighbors within the triangle. We refer to such a sampling atom as a central sampling atom. The site-energies of the atoms that have one or more neighboring atoms in a different triangle, such as atom q , must still be computed individually if the potential energy is to be exact. Such sampling atoms, which only sample their own site-energy (i.e. $w_i = 1$), are referred to as discrete sampling atoms.

For small triangles in which all atoms have one or more neighbors in different triangles, all atoms are discrete sampling atoms (see Fig. 5.3). Furthermore, in the triangles in fully resolved regions this type of summation leads to the use of only the repatoms as discrete sampling atoms, so that the atomistic model is automatically recovered (see Fig. 5.3). In large triangles, many atoms may be represented by the central sampling atom and the corresponding weight factor, w_i , may thus be large. Along the edges (or faces) of the triangles (or tetrahedra), a band of discrete sampling atoms however

remains.

The focus of the exact "summation" is thus on the inner part of the triangles. The reatoms, or the atoms around the reatoms, which have many neighbor interactions crossing triangle edges, are thus not appropriate to sample the site-energies of the inner atoms, which have all their neighbor interactions within the same triangle. In the cluster summation rule however, exactly these atoms with many interactions across triangle edges are used for sampling. This means that not only the specific computation of the weight factors in the cluster summation rule leads to inaccurate results, as shown in [76], but the mere selection of clusters of sampling atoms around the reatoms themselves is questionable.

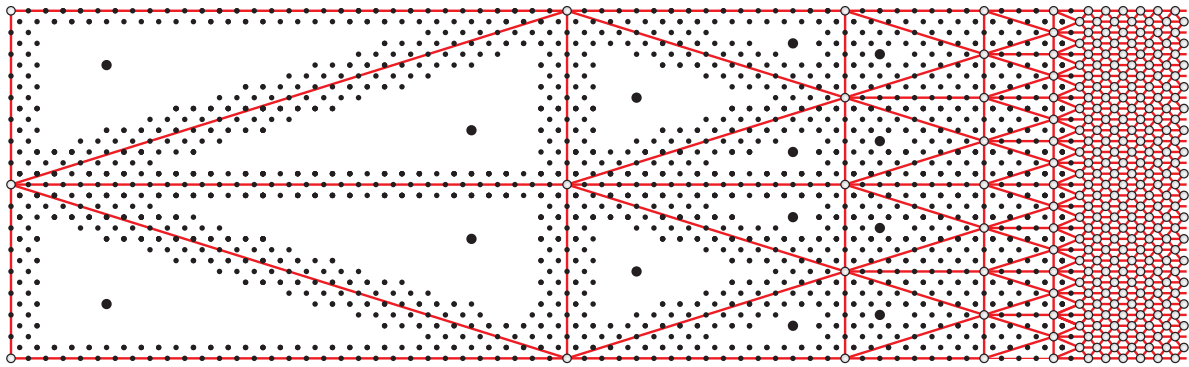


Figure 5.3: A summation rule that recovers the exact potential energy applied to a two-dimensional closely packed atomistic lattice including a fully resolved region on the right. The open circles represent the reatoms as well as discrete sampling atoms, the large dark circles represent central sampling atoms and the small dark circles indicate discrete sampling atoms.

As can be seen in Fig. 5.3, the exact summation leads to the use of a large number of sampling atoms due to the bands of discrete sampling atoms at the edges of the triangles. For lattice models that only contain nearest neighbor interactions, such as two-dimensional structural lattice models, such a summation rule is computationally viable, as shown in [9], because these bands are thin. For atomistic models in which not only nearest neighbor interactions are present, this type of summation would result in rather large (and hence expensive) bands of discrete sampling atoms. Furthermore, if three-dimensional crystals are considered, zones of thickness $2r_{cut}$ are needed along all faces of the interpolation tetrahedra, leading to an even larger number of discrete sampling atoms.

5.5 Central summation rule

The summation rule explained above is exact. For atomistic crystals it is however too inefficient because it leads to many sampling atoms, i.e. $s \approx n$. The central summation

rule proposed in this section aims to be more efficient so that $s \ll n$. Therefore, only one internal sampling atom is in principle selected in each triangle. Although it introduces some degree of approximation, the central summation rule is based on the understanding of how the total potential energy relates to the interpolation and its accuracy is therefore still high compared to a number of existing summation rules.

5.5.1 Selection of sampling atoms

We take as a starting point the exact summation as discussed above. Rather than keeping track of all interatomic interactions that cross triangle edges by defining discrete sampling atoms along these edges, these atoms are now also represented by the respective central sampling atoms (see Fig. 5.4). In this way the number of sampling atoms is largely reduced, but the total potential energy is approximated, instead of determined exactly. The introduced approximation is acceptable if the difference in deformation between neighboring triangles is small. Where large differences occur, a larger error is made, or the triangulation should be refined.

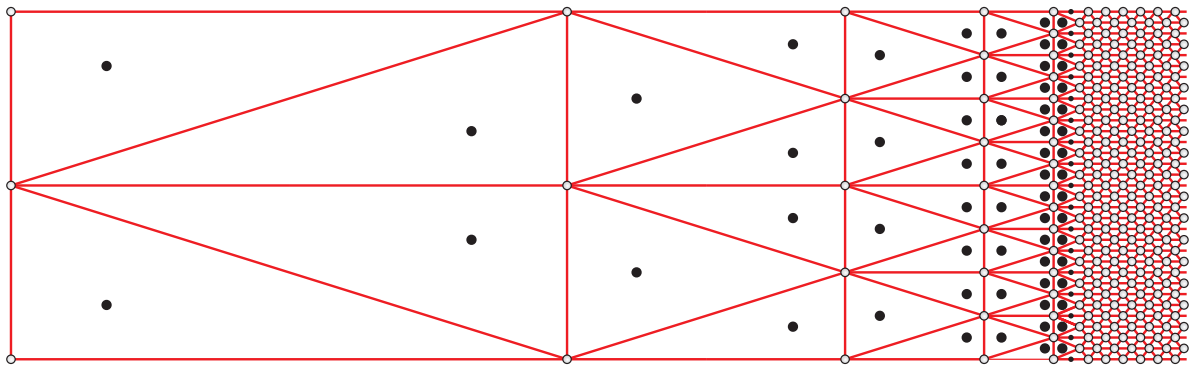


Figure 5.4: Illustration of the proposed central summation rule for a two-dimensional closely packed atomistic lattice including a fully resolved region on the right. The open circles represent repeat atoms as well as discrete sampling atoms, whereas the large dark circles represent central sampling atoms and the small dark circles indicate discrete sampling atoms.

In the central summation rule, the atom closest to the incenter of the triangle (or tetrahedron) is selected as the central sampling atom of each interpolation triangle (i.e. belongs to S). The reason that the incenter of the triangles is used is that it marks the location of the point that is located furthest from each triangle edge (see Fig. 5.5). It therefore marks the location that has the least probability of neighbors in other triangles.

In case a significant number of neighbors of the central atom are present in adjacent triangles, the central atom is the one that has its neighbors most evenly spread over the adjacent triangles. If another atom is used for sampling (in case only one sampling atom is to be selected for computationally efficiency) that is closely located to one adjacent

triangle but further away from the other adjacent triangles, it has a disproportional number of neighbors in the adjacent triangle to which it is closely located, but possibly no or few neighboring atoms in the other adjacent triangles, that are located further away from this atom. For symmetric triangulations this selection ensures a symmetric selection of sampling atoms.

Note that, in some cases, the selection of the central sampling atoms in the proposed summation rule may result in the selection of an atom which has neighbors in adjacent triangles, particularly in small triangles.

In case a triangle or tetrahedron only contains atoms on its corner nodes, edges and faces, and no atoms within the triangle or tetrahedron, all atoms are selected as discrete sampling atoms ($w_i = 1$). This means thus that all central sampling atoms (with $w_i > 1$) exist inside triangles or tetrahedra. This can be seen for the band of triangles in the coarse domain next to the fully resolved domain in Fig. 5.4. Sampling atoms on top of an edge or face may not be selected as a central sampling atom, since this would induce alternating patterns of weight factors for the central sampling atoms that can lead to saddle-point solutions, that are characterized by non-stable equilibria.

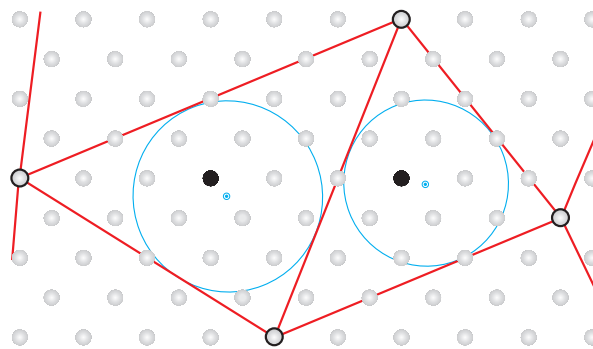


Figure 5.5: Schematic representation of the selection of central sampling atoms (large, dark dots) which are located closest to the incenter (small, blue dots) of two triangles which are marked by the two blue circles in the triangles. Repeatoms (encircled) act as discrete sampling atoms and the remaining atoms (light grey) are accounted for in the weight factors of the corresponding central sampling atoms.

5.5.2 Weight factors

As indicated before, the discrete sampling atoms only represent themselves and therefore have a weight factor $w_i = 1$. The remaining atoms in a particular triangle are summed in the weight factor of the central sampling atom of that triangle, including the central sampling atom itself. Atoms located on a triangle edge are summed half in the weight factor of the central sampling atom of one triangle of the corresponding edge and the other half is summed in the weight factor of the central sampling atom of the other triangle that belongs to that edge.

For three-dimensional atomistic crystals atoms on a tetrahedral face are summed half in the weight factor of the central sampling atom of a tetrahedron which corresponds with that face and the other half is summed in the weight factor of the central sampling atom in the adjacent tetrahedron containing to that face. Atoms located on tetrahedron edges are summed with the different central sampling atoms of tetrahedra that correspond to the particular edge. The fraction attributed to the corresponding weight factors is determined by the angle of the two faces intersecting the edge.

5.5.3 Site-energy computation

The computation of the sampling atoms' site-energies is formulated in an energy setting according to Eq. (5.2), i.e. no force-based formulation is used. All site-energies are furthermore computed nonlocally to ensure that the interatomic bonds which cross triangle edges are correctly incorporated. This means that all neighboring atoms of all (central and discrete) sampling atoms must be addressed to ensure that the site-energies of the sampling atoms are correctly computed. For central sampling atoms in large triangles a nonlocal computation of the site-energy equals the local computation using the Cauchy-Born rule, since all neighbors are located within the same triangle. However, the neighbors of central sampling atoms in small triangles and tetrahedra may be located in other interpolation elements and their nonlocal computation thus results in a dependence on reatoms of several triangles or tetrahedra. Note that this is always the case for discretely sampled atoms, in particular for reatoms.

An efficient and straightforward algorithm of the central summation rule is guaranteed by ensuring that all triangles are treated in the same fashion (see Table 5.1). For this reason the reatoms are also used as discrete sampling atoms in large triangles, although they hardly contribute to the sampled energy of large triangles, since their weight factors ($w_i = 1$) are small compared to the weight factors of the central sampling atoms. It is possible to avoid selecting the reatoms of large triangles and tetrahedra as discrete sampling atoms, but this introduces an extra user-defined parameter in the summation rule. Because the aim here is to obtain a straightforward and unambiguous summation rule, the reatoms of large triangles are used as well as discrete sampling atoms. Furthermore, for small triangles around the fully resolved domains, these discrete sampling atoms are significant and they therefore assure a smooth transition from fully resolved domains to coarse domains.

No spurious surface energies occur at the edges of the model due to the discrete sampling atoms in large triangles, since they hardly contribute because of their small weight factor and because their neighboring atoms outside the model are not taken into account (see ahead to Section 5.7.4). Furthermore, spurious surface energies can be overcome by using correct boundary conditions (e.g. periodic boundary conditions) on all reatoms of the outer triangles of the model (see e.g. the benchmark test in [85] and the numerical example in Section 5.7.2).

The advantage of this summation rule is that, as a result of the nonlocal computation of all site-energies, no internal interface between the interpolated and fully resolved domain exists. A natural and gradual transition is obtained from a near-local QC method in

coarsely discretized regions to a fully nonlocal method in fully resolved regions. No internal interface corrections, for which additional assumptions are often necessary [108], have to be implemented. Although the nonlocal computation of site-energies requires look-up tables (containing sampling atoms and their neighbors) at the expense of book-keeping, the fact that no internal interface corrections have to be updated, guarantees efficient analyses in which fully resolved regions may transform or move significantly.

5.6 Algorithm for the central summation rule

An efficient algorithm for the summation rule is presented in Table 5.1. It is formulated for the more general case of tetrahedra. For triangles it is almost identical, except for a few lines that can be skipped. The algorithm is tetrahedron-based, i.e. it separately selects sampling atoms for every tetrahedron. Only a few checks on sampling atoms of previously considered tetrahedra have to be made to ensure that sampling atoms are not selected twice. The tetrahedron-based algorithm is therefore efficient and straightforward to implement. Parallelization of the presented algorithm is relatively easy, requiring only minor adaptations to further increase the efficiency.

The algorithm is presented in Table 5.1 in such a way that the selection of sampling atoms and computation of corresponding weight factors becomes clear. This part is covered in the second step of the algorithm. Subsequently, the missing neighbors of the sampling atoms are recovered for the nonlocal site-energy computation (third step), the condensation matrix Ψ is assembled (fourth step) and the Newton-Raphson procedure is applied (the fifth step). In the first step, the boundary conditions are incorporated in the columns \mathbf{u}_r and \mathbf{f}_{ext} .

In the second step, every tetrahedron is separately considered to select the appropriate sampling atoms with corresponding weight factors. First, the atoms in and around the considered tetrahedron t are produced. The interpolation function values at the atoms' locations are used to decide which atoms are inside tetrahedron t or on its nodes, edges and faces. It is efficient to use the interpolation function values, because they are also used in the fourth step to assemble the condensation matrix.

The atoms on tetrahedron edges and faces are stored in a provisional list until a central sampling atom is defined in tetrahedron t , because it is a priori unknown if any atoms are present in tetrahedron t . If no central sampling atom can be found in tetrahedron t , this means that either only four atoms are present in the tetrahedron that are all repeatoms (fully resolved region), or tetrahedron t contains atoms that are merely located on nodes, edges and faces. In both cases, all atoms in tetrahedron t are selected as discrete sampling atoms ($w_i = 1$), if they were not selected as such yet. On the other hand, if one or more atoms are located within tetrahedron t , one of them is retrieved as central sampling atom and the provisional list with discrete sampling atoms is discarded after

Table 5.1: Algorithm for the central summation rule for three-dimensional atomistic crystals.

1. Incorporate boundary conditions in \mathbf{u}_r and \mathbf{f}_{ext}

2. Determine sampling atoms per tetrahedron
 - ▷ for every tetrahedron
 - produce atoms in a cube circumscribing tetrahedron t
 - evaluate interpolation functions at the locations of all atoms
 - use interpolation function evaluations to decide which atoms belong to tetrahedron t
 - ▷ for every atom in tetrahedron t
 - ◇ if atom i is a reatom and not present in discrete sampling atoms list
 - add atom i to discrete sampling atoms list
 - ◇ elseif atom i is located on edge or face and not present in discrete sampling atoms list
 - add atom i to provisional discrete sampling atoms list
 - add weight factor of atom i to provisional weight factor of potential adjacent central sampling atom
 - ◇ elseif atom i is located within tetrahedron t
 - ◇ if atom i is closer to incenter of tetrahedron t than previously considered atoms
 - select atom i as central sampling atom
 - add 1 to weight factor of central sampling atom
 - ◇ else
 - add 1 to weight factor of central sampling atom
 - ▷ end
 - ◇ if a central sampling atom in tetrahedron t is selected
 - add provisional weight factor (corresponding with the provisionally modeled sampling atoms) to the weight factor of the central sampling atom of tetrahedron t
 - ◇ else
 - add provisional discrete sampling atoms list to global discrete sampling atoms list
 - ▷ end

3. Recover missing neighbors of all sampling atoms with corresponding evaluated interpolation functions

4. Assemble condensation matrix Ψ with evaluated interpolation functions of sampling atoms and neighbors

5. Use Newton-Raphson procedure
 - ▷ for each increment until residual meets tolerance
 - Produce condensed, summed force column $\mathbf{f}^{r,s}$ and stiffness matrix $\mathbf{K}^{r,s}$ according to Eq. (5.18) & (5.19)
 - Partition $\mathbf{f}^{r,s}$ and $\mathbf{K}^{r,s}$ and update solution according to Eq. (5.14)

they have been accounted for in the weight factor of the central sampling atom. This decision can only be made after all atoms of tetrahedron t have been visited, i.e. at the end of the second step of the algorithm.

5.7 Results

5.7.1 Reference solution of a two-dimensional crystal

As a first numerical example to evaluate the central summation rule, a two-dimensional closely packed atomistic crystal is analyzed with a vacancy in its center. The crystal contains 251 by 285 rows of atoms in horizontal and vertical direction respectively (71,392 atoms). The Lennard-Jones (6-12) potential [70] is used for the interatomic pair potential, E_{ij} in Eq. (5.2). This potential has its minimum at the interatomic lattice spacing r_0 , as depicted in Fig. 5.6. The cut-off radius is set to 2.23 lattice spacings, implying that each atom interacts with 18 neighboring atoms.

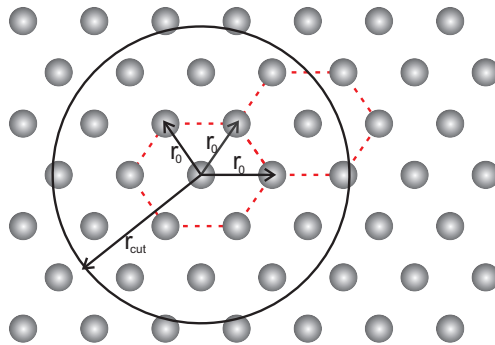


Figure 5.6: Schematic representation of the two-dimensional closely packed atomistic crystal. The atomistic lattice spacing, at which the interatomic Lennard-Jones potential has its minimum, is given by r_0 . The interaction region of a single atom is shown by the circle with cut-off radius r_{cut} . Two unit cells are depicted by the dashed hexagonals.

An example of a triangulation including a fully resolved region around the vacancy is shown in Fig. 5.7. The crystal is loaded to a uniaxial strain of 0.5% in $[10]$ (horizontal) direction. No vertical strain is allowed. Displacement boundary conditions in accordance with this uniaxial strain state are applied to the reatoms of the band of slim triangles that surround the model. This band has a thickness which exceeds twice the cut-off radius to ensure that no edge effects occur (see Fig. 5.7). In all triangulations considered, this band is the same. The size of the fully resolved region around the vacancy is varied using different triangulations. The transition to the coarse domain is made by doubling the triangle size for every extra ring of triangles away from the fully resolved region.

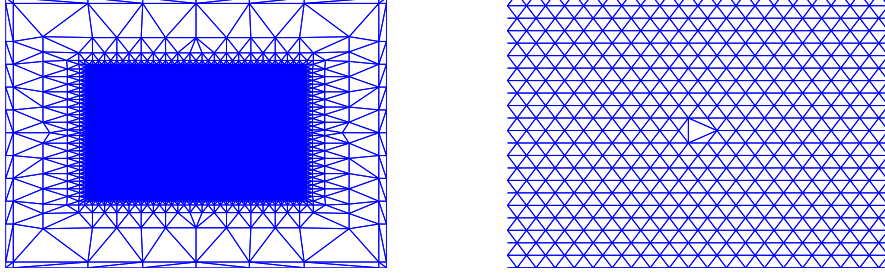


Figure 5.7: The triangulation for the two-dimensional closely packed atomistic crystal with a fully resolved region of 71×70 unit cells around the vacancy that serves as a reference (left). (Right) a zoom around the vacancy. The $[1\ 0]$ direction corresponds to the horizontal direction and the $[0\ 1]$ direction is at an angle of 60° relative to the horizontal direction and -30° relative to the vertical direction.

The semi-QC variant as described in Section 5.5 serves as a reference for assessment of the central summation rule. In this reference model no summation rule is used ($S = N$) and thus no error due to summation occurs. The only remaining error resides in the interpolation, for which a large fully resolved region of 71×70 unit cells in horizontal and vertical direction respectively ensures that this error remains small (see Fig. 5.7). The predicted relative $[1\ 0]$ (horizontal) displacement components u_x^{rel} , which show the influence of the introduced vacancy, are shown as a function of the location of the reatoms in Fig. 5.8. This relative displacement is obtained by subtracting the horizontal displacements of the same model without a vacancy (loaded with the same boundary conditions) from the computed displacements:

$$u_x^{rel}(\vec{X}^i) = u_x(\vec{X}^i) - E_{xx} X_x^i \quad (5.20)$$

where \vec{X}^i is the position vector indicating the original location of atom i , $u_x(\vec{X}^i)$ is the horizontal component of the displacement vector of atom i and E_{xx} is the applied overall strain in $[1\ 0]$ (horizontal) direction. Two distinct peaks, which both have an amplitude of $0.0068r_0$, can be observed at the two reatoms located left and right of the vacancy. In $[1\ 0]$ direction the peaks decay slower than in the vertical direction.

5.7.2 Application of the central summation rule to the two-dimensional atomistic crystal

We illustrate the effect of summation first on a triangulation with a fully resolved region of 3×4 unit cells in horizontal and vertical direction respectively. The sampling atoms selected according to the central summation rule are marked in Fig. 5.9. After the

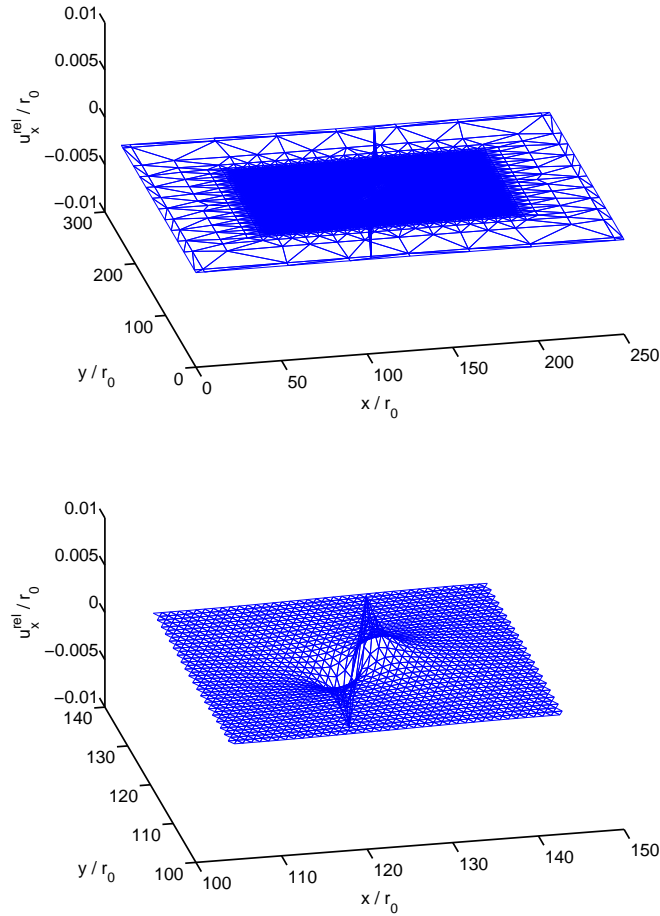


Figure 5.8: The displacement field in $[1\ 0]$ (horizontal) direction of the semi-QC method with a fully resolved region of 71×70 unit cells in horizontal and vertical direction. The predicted relative horizontal displacements are shown, normalized by r_0 , in all reatoms (top) and a zoom around the vacancy (bottom).

identification of the sampling atoms and the recovery of the missing neighbors of the sampling atoms, the atom at the location of the vacancy was removed (see Fig. 5.9, right).

The results computed with the central summation rule for the triangulation of Fig. 5.9 are shown in Fig. 5.10. The peaks on the left and right side of the vacancy are in reasonable agreement with the reference results of Fig. 5.8; their amplitude is $0.0081r_0$. This corresponds with a maximum error of the displacement of these two reatoms of 18.6% for this triangulation. A semi-QC simulation for the triangulation of Fig. 5.9 (not shown here), in which no error due to summation occurs, has indicated that the error due to the interpolation is only 1.0% for this triangulation. It can thus be concluded that the maximum error of 18.6% is mainly caused by the summation. The predicted displacement field however also shows discrepancies with the reference solu-

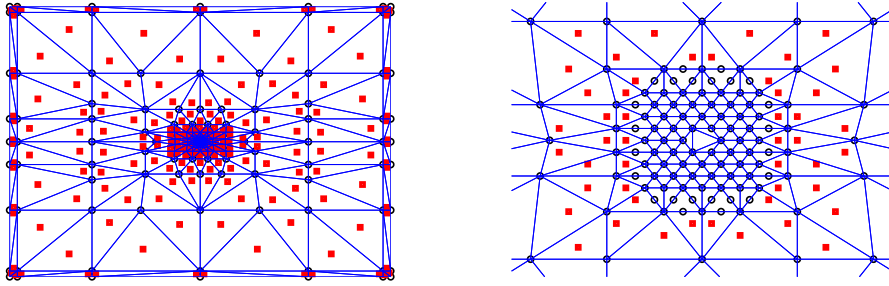


Figure 5.9: A triangulation for the two-dimensional atomistic crystal with a fully resolved region of 3×4 unit cells (left) and a zoom of the fully resolved region that includes the vacancy in the center (right). The discrete sampling atoms (including repatoms; $w_i = 1$) are represented by black circles and the central sampling atoms ($w_i > 1$) by red squares. The remaining neighboring atoms of the sampling atoms are not shown.

tion in Fig. 5.8 in and around the fully resolved region. These discrepancies with a maximum amplitude of $0.0053r_0$ are caused by the error due to summation, since they are not present in the results of the semi-QC variant applied to this triangulation. The fully resolved region of the triangulation shown in Fig. 5.9 is apparently so small that in the first ring of triangles in the coarse domain the site-energies of the atoms within one triangle differ substantially from each other. This use of relatively large triangles in regions where atoms behave differently leads to relatively large summation errors, as could be expected. In the coarse domain however, the summation rule captures the uniaxial strain deformation well, as can be seen on the left in Fig. 5.10.

A straightforward way to improve the predicted displacement field in the region of interest (the region around the vacancy) is to enlarge the fully resolved domain. This ensures that the error due to summation only occurs in regions where the site-energies of the atoms vary little, as assumed in the summation rule. On the left in Fig. 5.11 the maximum errors are presented for triangulations with different sizes of fully resolved regions. The error drops rapidly upon increasing the size of the fully resolved region. If it is sufficiently large, so that the coarse domain, in which the true summation occurs, starts where the site-energies of the atoms are almost identical, the error remains below 5%. This degree of accuracy is reached for fully resolved regions larger than 7×12 unit cells.

The fact that the maximum error does not decrease to zero for increasing fully resolved regions (Fig. 5.11) is caused by the non-zero relative displacements that remain in the coarse domain, just outside the fully resolved region (see Fig. 5.12). The maximum amplitude of these relative displacements for the results shown at the bottom in Fig. 5.12 is $0.0079r_0$. This is close to the obtained value reached at the maximum peak next to the vacancy. The reason for these discrepancies is that a number of neighboring atoms of the central sampling atoms are located in different triangles for these small triangles

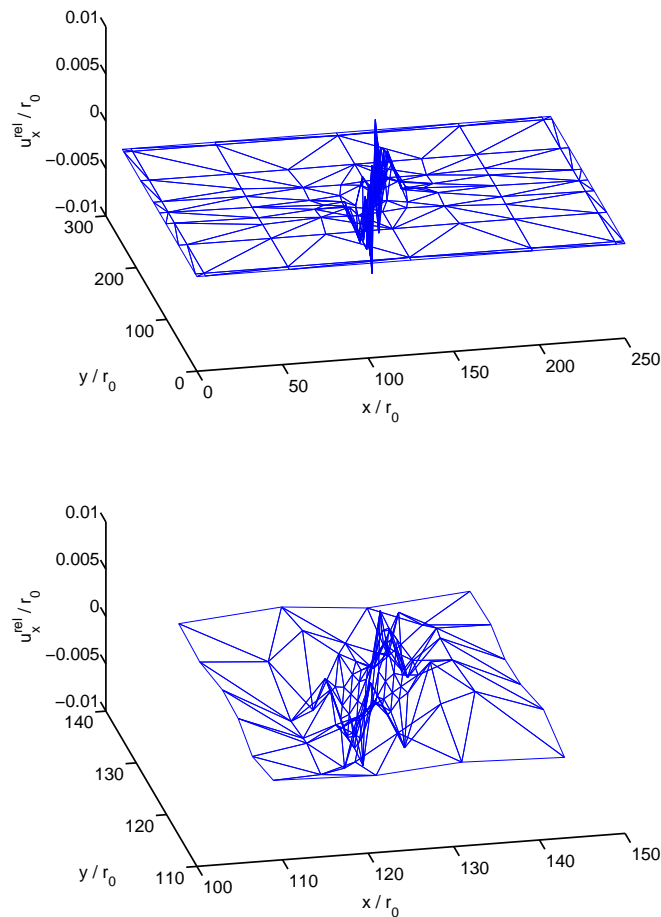


Figure 5.10: The relative displacement field in $[1\ 0]$ (horizontal) direction computed for the triangulation of Fig. 5.9 with a fully resolved region of 3×4 unit cells. The predicted relative horizontal displacements in terms of r_0 are shown as a function of the repeatoms of the entire triangulation (top) and a zoom around the vacancy (bottom).

around the fully resolved region (see Fig. 5.9). If the fully resolved region is not too small, however, this error at the edge of the fully resolved region has little influence on the solution in the central region of interest (in this case the solution around the vacancy).

As can be seen in the diagram on the right in Fig. 5.11, the computational efficiency of the summation rule, expressed in terms of the number of repeatoms and sampling atoms relative to the number of total atoms present in the crystal, is high and remains high for increasing fully resolved regions. The computational efficiency of the summation rule can be further increased if the ratio between the coarse domain (in which many atoms are summed) and the fully resolved domain is increased. This is shown for the summation rule that recovers the exact potential energy for structural lattices with nearest neighbor interactions in [9].

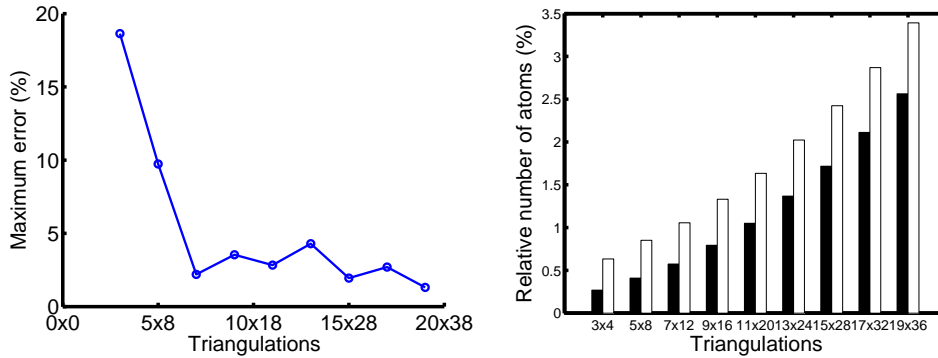


Figure 5.11: (Left) the maximum error at one of the two repeatoms at the peaks of the displacement field in $[1\ 0]$ (horizontal) direction computed using the central summation rule for triangulations with different sizes of fully resolved regions. The maximum error is shown as a function of the sizes of the fully resolved regions. The shapes of the fully resolved regions are kept as square as possible. (Right) the relative number of repeatoms (black) and sampling atoms (white) for the triangulations with different sizes of fully resolved regions.

5.7.3 Comparison with the cluster summation rule for a two-dimensional atomistic crystal

It is interesting to compare the results of the proposed central summation rule to those computed with the cluster summation rule. The cluster summation rule, like the central summation rule proposed here, allows a seamless coupling between coarse domains and fully resolved domains.

The cluster summation rule that is used here is the improved variant as proposed in [36], which is formulated in terms of energy (like the summation rule presented here). No use is made of the hybrid correction strategy proposed in [36]. The cluster summation rule is applied to the triangulation with a fully resolved region of 11 by 20 unit cells. The boundary conditions are identical to those in the previous simulations. The cluster radius is set to 3 atomistic lattice spacings ($3r_0$), which means that a cluster contains 37 sampling atoms, if it is not truncated because of overlap with another cluster. This leads to 6.8% sampling atoms, while the summation rule presented here only needs 1.7% sampling atoms for this triangulation (see right diagram in Fig. 5.11).

The displacement field computed with the cluster summation rule is presented in Fig. 5.13. It corresponds for the greater part with the displacement field obtained by Eidel and Stukowski [36] for the two-dimensional cluster computation without the hybrid correction strategy. The correction strategy involves a computation of the interpolated lattice in which all atoms must be incorporated and thus no summation is used (as in the aforementioned semi-QC method). Since summation rules in the QC method are aimed at avoiding computations in which all atoms are incorporated and since no correction approach is required for the central summation rule, the correction strategy

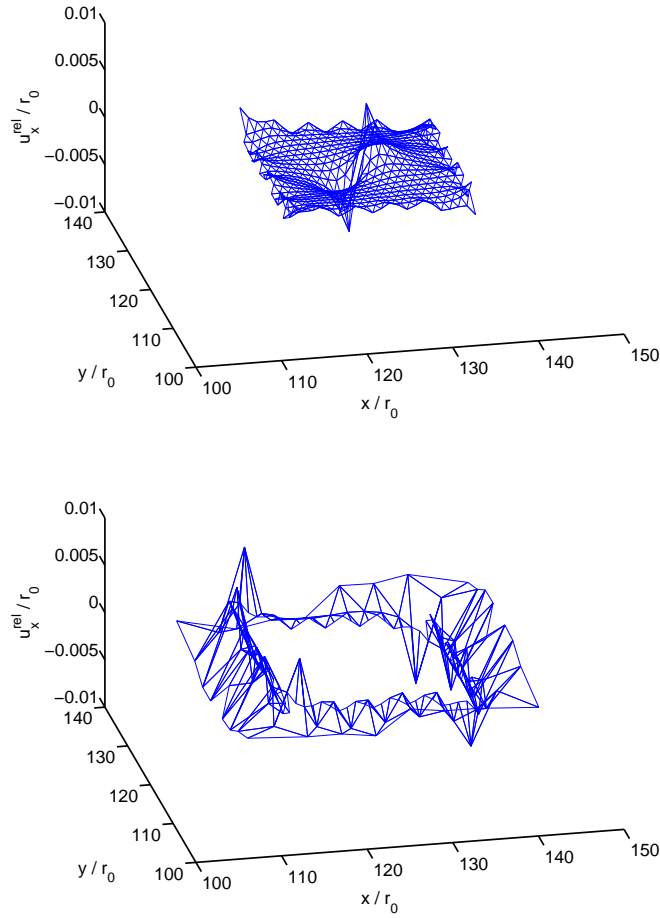


Figure 5.12: The displacement field in $[1\ 0]$ (horizontal) direction of the central summation rule for the triangulation with a fully resolved region of 11 by 20 unit cells, split up into the fully resolved region (top) and the first two rings of triangles in the coarse domain around the fully resolved regions (bottom). The predicted relative horizontal displacements, normalized by r_0 , are shown as a function of the position of the repatoms.

is not used here for the comparison between the cluster summation rule and the central summation rule.

The cluster summation rule without the hybrid correction strategy is clearly not able to accurately capture the uniform strain applied to the crystal. This is not only caused by a poor computation of the weight factors [76], but also by selecting sampling atoms around the repatoms (as mentioned before). This clearly leads to significant discrepancies in large triangles in which many atoms are present that have all their neighbors within the same triangle, while they are sampled by atoms that have many neighbors in other triangles. Although the cluster summation rule computes the sampling atoms' site-energies in the fully resolved region correctly, the error in the coarse domain has such an

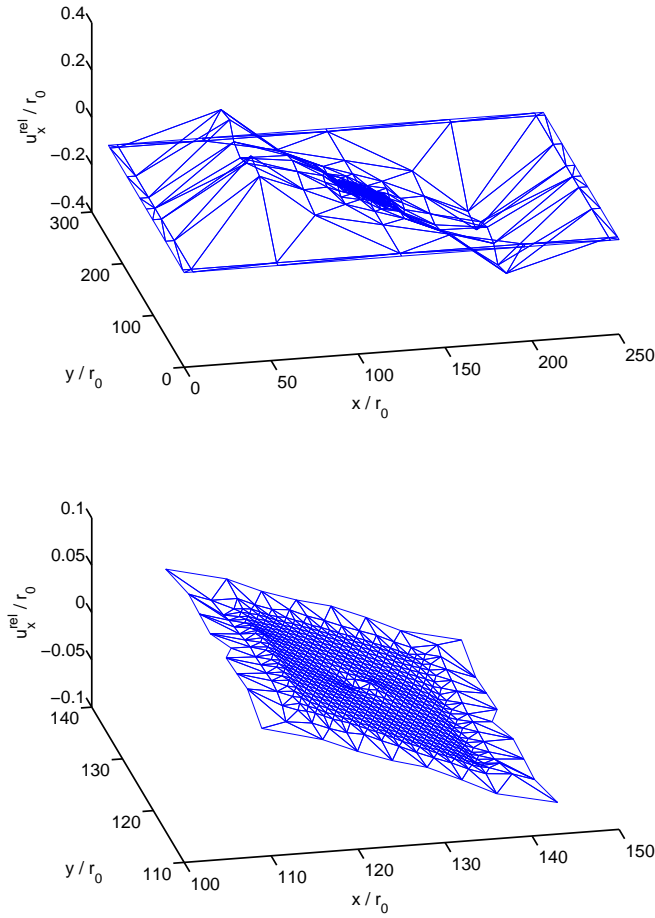


Figure 5.13: The relative displacement field in $[1\ 0]$ (horizontal) direction computed with the cluster summation rule for the triangulation with a fully resolved region of 11 by 20 unit cells. The predicted relative horizontal displacements scaled by r_0 are shown as a function of the reatoms of the entire triangulation (top) and a zoom around the vacancy (bottom). Note the different vertical scales compared to those in Fig. 5.8, 5.10 and 5.12.

influence on the displacements of the entire crystal that the relative $[1\ 0]$ displacements of two peaks in the fully resolved regions equal $-0.0017r_0$ and $0.0007r_0$ which corresponds to a maximum error of 89.7%.

5.7.4 The central summation rule for a three-dimensional atomistic crystal

The use of the central summation rule for three-dimensional atomistic crystals is demonstrated by modelling a vacancy in a three-dimensional cubic FCC crystal. The considered crystal contains 1,074,344 atoms ($64 \times 64 \times 64$ unit cells). Using the triangulation

of Fig. 5.14, results a fully resolved region of $8 \times 8 \times 8$ unit cells, whereby only 8,732 repeatoms and 55,744 sampling atoms need to be used. The computational cost in terms of DOFs (number of repeatoms) and effort to construct the governing equations (sampling atoms) is thus reduced to 0.8% and 5.1% respectively of the full atomistic analysis.

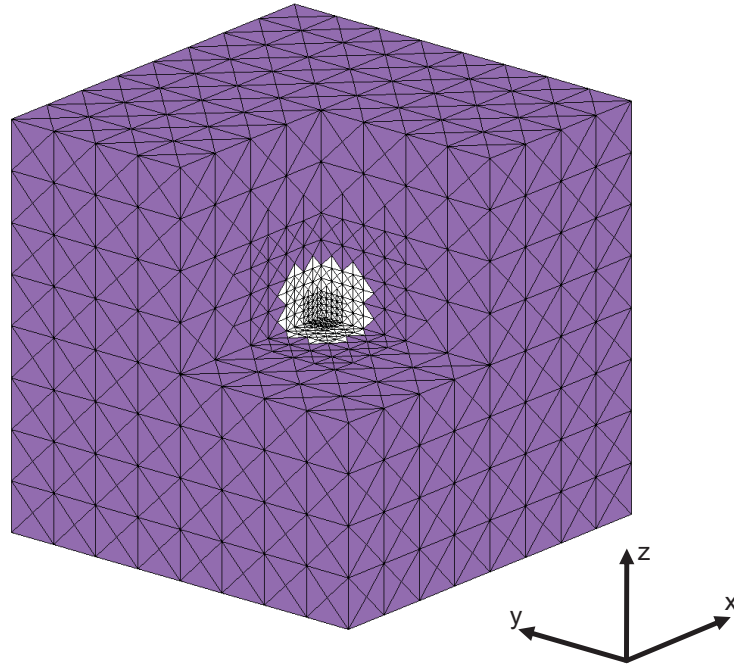


Figure 5.14: Part ($\frac{7}{8}$) of the triangulation for the three-dimensional cubic FCC crystal including a vacancy in the center. The axes correspond to the $\langle 100 \rangle$ orientations of the FCC crystal. The purple tetrahedra contain central sampling atoms. The white tetrahedra contain only discrete sampling atoms because all atoms in these tetrahedra are located on top of the repeatoms (in the fully resolved regions) or on top of tetrahedron nodes, edges and faces (in the coarse domain around the fully resolved region).

The boundary conditions are equivalent with those in the two-dimensional examples. The FCC crystal is uniaxially strained to 0.5% in $[1 0 0]$ direction. Since the outer tetrahedra contain a significant number (approximately 85) of atoms that are sampled by the central sampling atom, the ratio between the number of atoms represented by the central sampling atom and the four discrete sampling atoms (i.e. the repeatoms) in one tetrahedron is large. Therefore, the edge effects are expected to be small and no fully constrained band of tetrahedra is necessary (cf. the slim triangles that surround the two-dimensional models). This saves computational efforts.

To investigate the influence of the vacancy, relative displacements of the repeatoms are computed based on the predicted displacement vectors according to Eq. (5.20). The

relative $[1\ 0\ 0]$ displacement of each repatom $u_{[100]}^{rel}$ is the component of the predicted displacement vector in $[1\ 0\ 0]$ direction relative to the displacement component in $[1\ 0\ 0]$ direction for a FCC crystal without a vacancy subjected to the same uniaxial strain.

The relative $[1\ 0\ 0]$ displacements of the repatoms are presented in Fig. 5.15. A number of observations can be made based on Fig. 5.15 that are distinct from the two-dimensional results, revealing intrinsic differences in three-dimensional crystals.

Eight atoms around the vacancy show distinct relative $[1\ 0\ 0]$ displacements with a magnitude of $0.00149r_0$. This effect decays away from the vacancy over three lattice spacings. The four atoms next to the vacancy in the face given by the $[1\ 0\ 0]$ normal direction show no distinct relative $[1\ 0\ 0]$ displacements. This is caused by the fact that these four neighboring atoms of the vacancy are located in the face given by the normal direction that corresponds to the loading direction.

The most striking difference with the two-dimensional results is that the relative $[1\ 0\ 0]$ displacements of the three-dimensional crystal reveal that the neighboring atoms of the vacancy are moving towards the location of the vacancy whereas the neighboring atoms of the vacancy in the two-dimensional crystal move away from the vacancy. This is caused by the differences in two-dimensional and three-dimensional configurations.

The quality of the summation rule for this three-dimensional example is relatively difficult to evaluate, since the semi-QC model in which $S = N$ is computationally too expensive. However, the accuracy of the relative $[1\ 0\ 0]$ displacements of the repatoms in the fully resolved regions appears to be sufficient, since no significant fluctuations can be observed in the fully resolved domain as in a number of two-dimensional results, e.g. in the bottom image of Fig. 5.12. Apparently, the size of the fully resolved domain ($8 \times 8 \times 8$ unit cells) is sufficiently large to obtain an adequate solution for a vacancy in the considered lattice.

As in the two-dimensional results (see Fig. 5.12), some fluctuations occur in the small tetrahedra around the fully resolved domain (see the left images in Fig. 5.15). However, because for the FCC crystal with the triangulation shown in Fig. 5.14 a relatively large number of small tetrahedra occur that have all their atoms on tetrahedron edges and faces (see the white triangles in Fig. 5.14), a relatively large number of atoms around the fully resolved region are selected as discrete sampling atoms compared to the two-dimensional crystal. For this reason the fluctuations induced in the transition region between the coarse and full resolved domain are smaller compared to the fluctuations in the two-dimensional results.

5.8 Conclusion

The aim of this chapter was to develop an accurate summation rule for the quasicontinuum method [114] that can efficiently deal with atomistic crystals, while avoiding an internal interface. The proposed central summation rule is based on a clear understand-

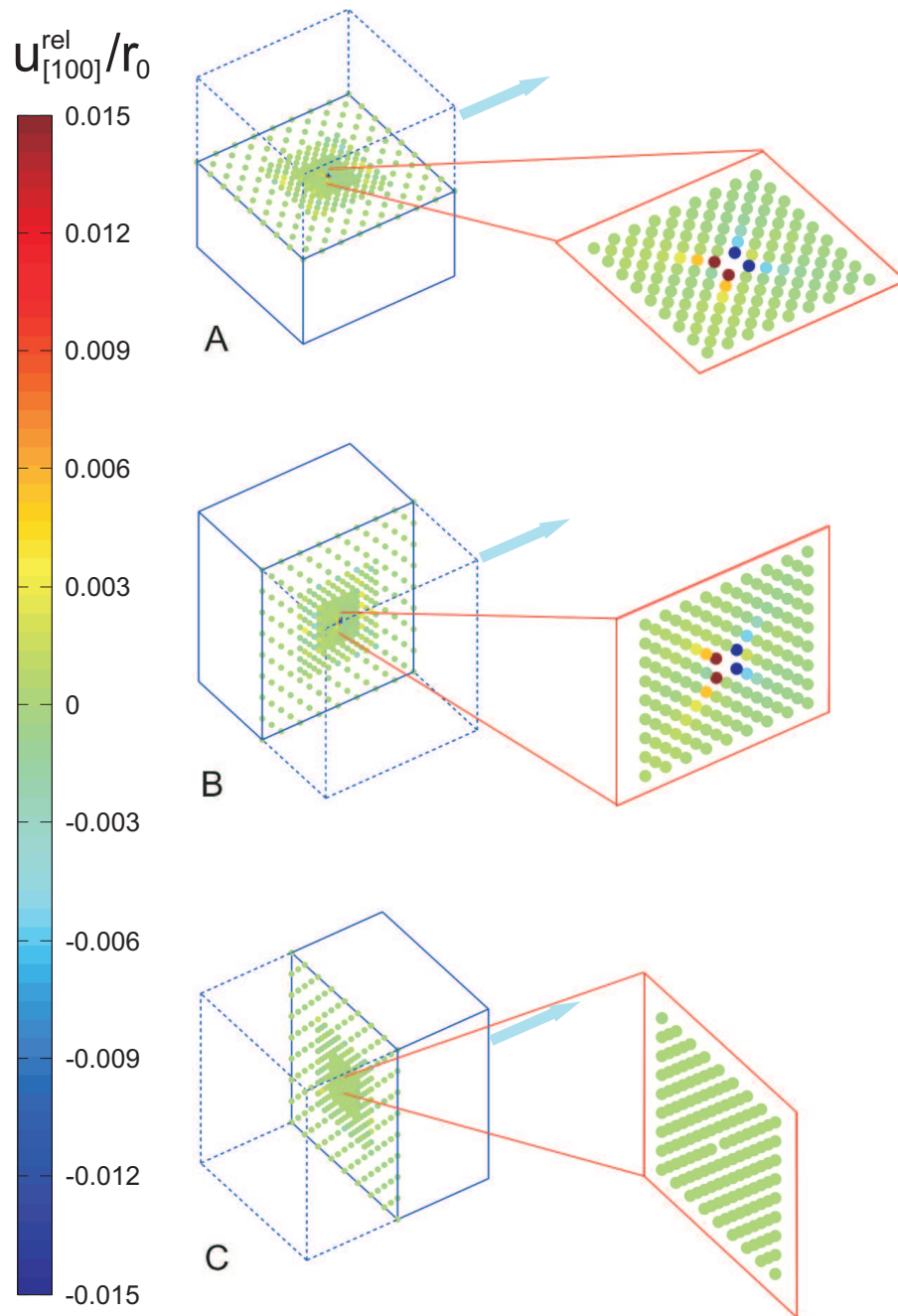


Figure 5.15: The relative displacement components scaled by r_0 in $[1\ 0\ 0]$ direction of the repatoms in three cross-sectional faces with $[0\ 0\ 1]$ normal (image A), $[0\ 1\ 0]$ normal (image B) and $[1\ 0\ 0]$ normal (image C) through the center of the $\langle 100 \rangle$ oriented FCC crystal. Zooms around the vacancy are presented in the right images. The arrows indicate the loading in $[1\ 0\ 0]$ direction.

ing of relation between the potential energy and the interpolation, as the summation rule presented by Beex et al. [9] for structural lattice models. In contrast to the summation rule of Beex et al. [9], which leads to a large number of sampling atoms if applied to atomistic crystals (especially in three dimensions), the number of sampling atoms selected in the central summation rule is small to gain computational efficiency. As a result, the potential energy is estimated instead of determined exactly, but the accuracy nevertheless remains high.

The central summation rule significantly reduces the computational cost of full atomistic computations as a result of the use of the reatoms as sampling atoms, in combination with one extra sampling atom in the center of coarse triangles. The focus of the central summation rule is thus on the center of the triangles and tetrahedra, which is more natural compared to clusters of sampling atoms around the reatoms [36,64]. The algorithm for the summation rule deals with triangles in the coarse domains and fully resolved domains in a unified way and is therefore simple to implement.

The energy-based central summation rule uses a nonlocal site-energy computation in the coarse domain, as well as in the fully resolved domain. Consequently, no internal interface occurs between both domains, similar to the cluster summation rules [36,64]. This ensures that moving and growing/shrinking fully resolved regions can easily be included since no internal interface procedures have to be implemented and updated. Adaptivity can therefore more straightforwardly be implemented in a quasicontinuum framework.

In the presented numerical examples and the comparison with the energy-based cluster summation rule [36], a Lennard-Jones pair potential is used for the interactions between the atoms. In case a larger interaction radius is used, it is expected that the accuracy remains rather similar. The reason is that the contribution of the Lennard-Jones pair potential to a site-energy is rather insignificant, if the distance between the two atoms is large. In case multibody potentials are used, the accuracy is expected to remain similar as well, since the central summation rule is based on energy-minimization instead of force-equilibrium. This ensures that the correct dependance of a sampling atom's site-energy on the displacements of the sampling atoms and the sampling atom's nearest and next-to-nearest neighboring atoms is captured.

The central summation rule has in common with the local-nonlocal summation rule [108, 114] that in the limit of large interpolation triangles and tetrahedra it equals the local summation rule using the Cauchy-Born rule. This is a result of the fact that in large interpolation triangles all neighboring atoms of the central sampling atoms are located in the same interpolation triangles as the central sampling atoms. Furthermore, since the weight factors (w_i) of the central sampling atoms are large in large triangles compared to the weight factors of the discrete sampling atoms ($w_i = 1$), the discrete (corner) sampling atoms' contribution becomes negligible. A natural and smooth transition is thus obtained from a fully nonlocal method in refined regions to an almost local method in coarse regions.

The central summation rule combines most advantageous characteristics of the two main classes of summation rules:

- no internal interface occurs (as in the cluster summation rules),
- it uses almost as few sampling atoms as the local-nonlocal rules,
- it is more accurate than the cluster summation rules.

A disadvantage is that, as in the cluster summation rules, to ensure that no internal interface occurs, the site-energies of all sampling atoms must be computed nonlocally and thus relatively large lookup tables are necessary. However, this seems to be inevitable for summation rules in which internal interfaces are to be eliminated.

A multiscale quasicontinuum method for dissipative lattice models and discrete networks¹

Abstract

Lattice models and discrete networks naturally describe mechanical phenomena at the mesoscale of fibrous materials. A disadvantage of lattice models is their computational cost. The quasicontinuum (QC) method is a suitable multiscale approach that reduces the computational cost of lattice models and allows the incorporation of local lattice defects in large-scale problems. So far, all QC methods are formulated for conservative (mostly atomistic) lattice models. Lattice models of fibrous materials however, often require non-conservative interactions. In this chapter, a QC formulation is derived that is based on the virtual-power formulation of a non-conservative lattice model. By using the virtual-power statement instead of force-equilibrium, errors in the governing equations of the force-based QC formulations are avoided. Nevertheless, the non-conservative interaction forces can still be directly inserted in the virtual-power QC framework. The summation rules for energy-based QC methods can still be used in the proposed framework as shown by two multiscale examples.

¹ Reproduced from: L.A.A. Beex, R.H.J. Peerlings, M.G.D. Geers, A multiscale quasicontinuum method for dissipative lattice models and discrete networks, In preparation.

6.1 Introduction

Structural lattice models and discrete networks that include trusses or beams are frequently used to represent discrete microstructures of fibrous materials [12,20,24,100,110,113,123,130]. Likewise, for investigating the mechanical responses of other materials, e.g. concrete and polymers, lattice models and discrete networks are often applied [28,62,71,92,102,128]. The advantage of discrete models is that they naturally incorporate discrete phenomena occurring in meso- and microstructures of many materials. Individual microscale events such as fiber failure and bond failure, precursors for macroscale failure, can be readily incorporated in lattice models, whereas they are not easily included in continuum models. Even the incorporation of global mechanisms such as large rotations may lead to relatively complex continuum models and finite element implementations [96,117], whereas they are naturally captured by truss networks.

A clear disadvantage of lattice models is the required computational effort for large-scale physically relevant models. This large computational cost essentially results from the construction of the lattice model at the meso- or microscale. Consequently, if lattice models are being used for macroscopic computations, a large number of lattice points is involved. First, this leads to a large number of degrees of freedom (DOFs) making the system of equations computationally expensive to solve. Secondly, the construction of the system of equations is computationally expensive because all lattice points must be visited for this [9].

An approach to reduce the computational cost of lattice models is the quasicontinuum (QC) method. The QC method has been originally developed for the reduction of atomistic lattice models in [114] and has been widely used to investigate phenomena such as intergranular fracture [82] and nanoindentation [64,68,115]. In a previous study [9] the applicability of the QC method has been demonstrated for lattice models of fibrous materials that employ elastic trusses. An overview of several QC frameworks is given in [83].

The benefit of the QC method is its intrinsic multiscale character, allowing the accurate incorporation of local lattice defects in large-scale problems. This is not trivially possible with multiscale methods that are based on computational homogenization [113]. Moreover, the QC method entirely relies on the microstructural lattice topology, unlike approaches such as those in [125] and [38], that need a continuum description in addition to the discrete model. The fact the QC method does not require a continuum description is an advantage, since continuum descriptions for fibrous materials tend to be complex to formulate [96]. Another advantage of the QC method is that a number of QC frameworks [36,9,11,64] do not require a handshaking region or coupling procedure between fully resolved domains (in which the exact lattice model is recovered) and coarse domains (in which an approximation is made). Several other multiscale approaches require such a coupling procedure [38,46,108,125].

The QC method introduces two remedies to reduce the computational cost of lattice models. First, interpolation is applied to the displacements of the lattice points to reduce the number of DOFs and thus reducing the size of the governing set of equations.

In coarse regions, the interpolation triangles are large so that many lattice points are interpolated. In regions of interest, e.g. around lattice defects, the exact lattice model is captured by refining the interpolation such that every lattice point corresponds to a point of the interpolation triangulation (so-called representative point or reppoint).

Secondly, so-called summation rules are used in the QC method to ensure that only a small number of lattice points (so-called sampling points) needs to be visited to construct the governing equations, instead of all lattice points. To obtain an accurate solution, all lattice points in the fully resolved regions are sampling points, while in the coarse regions only a small number of points is used (e.g. [9,11,127]).

Most QC formulations are based on minimizing the total potential energy of the interpolated system [36,82,108,114]. Also the QC formulation in [9], developed for lattice models with elastic interactions only, uses this ansatz. Depending on the application, such an elastic description may be adequate [31,42,48,107,126]. For many applications however, more advanced descriptions of lattice interactions are required that include dissipation in the lattice interactions, e.g. by using plasticity [5,12,20,23,32,34,60,86,110,123] or damage [28]. In these cases, a straightforward minimization of the potential energy can no longer be employed since the dissipation leads to non-conservative interactions. Energy-based QC formulations are thus inadequate for structural lattice models with dissipative interactions.

Existing force-based QC formulations may be appropriate alternatives. The QC formulations that depart from force-equilibrium however [64,68], also appear to be energetically inconsistent for conservative systems. This has for instance been shown in [36] for the widely used cluster QC approach [64].

The aim of this chapter is therefore to develop a thermodynamically consistent QC formulation for non-conservative lattice models. Our point of departure for this is a virtual-power statement in which the non-conservative forces can be directly inserted. As a result, the framework is equivalent to energy minimization for conservative lattices, but its applicability is broader.

Another advantage of using the virtual-power statement is that summation rules proposed in energy-based QC formulations can directly be used in the proposed QC methodology. In this chapter, the summation rule for atomistic lattice models as presented in [11] is used to reduce the computational efforts of the considered lattice model.

The outline of this chapter is as follows. In Section 6.2, the thermodynamics of structural lattice models with dissipative interaction forces are formulated. The lattice model of interest is discussed here as well. In Section 6.3, the virtual-power-based QC formulation is introduced and applied to an elastoplastic lattice model consisting of an equidistant X-braced truss network with elastoplastic interactions. This fairly simple lattice model is chosen in order to show the possibilities of the framework. In Section 6.4, two multiscale numerical examples are simulated to evaluate the accuracy and efficiency of the virtual-power-based QC method and to illustrate some of key features for fibrous materials.

6.2 Structural lattice models with non-conservative interactions

It is useful to formulate structural lattice models, as adopted in the QC method, on a thermodynamic basis. The reason is that most QC methods are based on energy-minimization and that thermodynamical inconsistencies in sampling points are carried over to their corresponding lattice points. These inconsistencies can significantly contribute to the inaccuracy of the QC method [36]. The thermodynamics of dissipative lattice models are therefore first considered. We subsequently particularize the framework to the case of a lattice of elastoplastic trusses and briefly discuss solution methods for it.

The lattice model studied in this chapter is a two-dimensional equidistant X-braced network of elastoplastic trusses (see Fig. 6.1). It can be considered as a discrete representation of the microstructure of a fictitious fibrous material. A unit cell of the truss network contains four truss nodes positioned at the locations where the horizontal, vertical and diagonal trusses meet (see Fig. 6.1). At the center of a unit cell, where the diagonals cross each other, no truss node is present. This means that every truss node in the network is connected to eight other nodes. The considered simple lattice is essentially used to show the possibilities of the virtual-power-based QC method for structural lattice models including dissipative mechanisms.

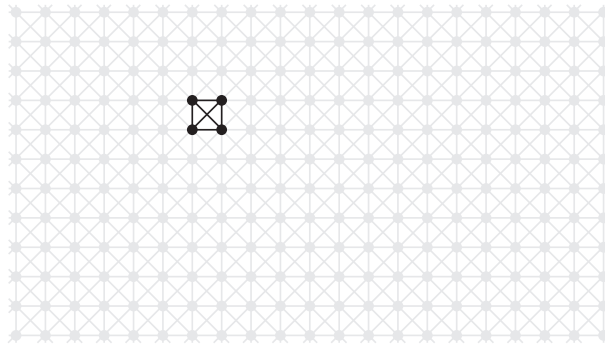


Figure 6.1: The equidistant X-braced lattice model with elastoplastic trusses as considered in this chapter. A unit cell of the truss network is marked in black.

6.2.1 Thermodynamics of non-conservative lattice models

The lattice model considered here merely contains trusses. The DOFs of the system are thus only the displacement components of the lattice nodes. For a solution of the lattice model, the internal power of the lattice equals the external power:

$$\dot{\mathbf{u}}^{Tint} \mathbf{F} = \dot{\mathbf{u}}^{T ext} \mathbf{F} \quad \forall \dot{\mathbf{u}}, \quad (6.1)$$

where \mathbf{u} refers to the column matrix containing the components of the displacement vectors of all n lattice points. The column matrices ${}^{int}\mathbf{F}$ and ${}^{ext}\mathbf{F}$ contain the components of the resulting internal forces and externally applied forces. In Eq. (6.1) $\dot{\mathbf{u}}^T {}^{int}\mathbf{F}$ can be identified as the internal power, ${}^{int}P$, and $\dot{\mathbf{u}}^T {}^{ext}\mathbf{F}$ as the external power, ${}^{ext}P$.

A dissipative lattice model depends not only on a set of the (controllable) kinematic variables, \mathbf{u} , but also on a set of (not directly controllable) internal variables, stored in column matrix \mathbf{z} . The size of this column matrix is $Z \times 1$ and is independent of the number of kinematic variables, $2n$, since it depends on the number of dissipation mechanisms in the lattice. The energy stored in the lattice, E , thus depends on the kinematic and internal variables, i.e. $E = E(\mathbf{u}, \mathbf{z})$. For a lattice model, the total energy stored in the lattice, E , can be written in terms of the stored energy per lattice point i , ${}_iE$, which can be written in terms of the energy stored per interaction (truss) between a lattice point, i , and one of its neighbors, j , ${}_{ij}E$:

$$E(\mathbf{u}, \mathbf{z}) = \sum_{i=1}^n {}_iE(\mathbf{u}, \mathbf{z}) = \sum_{i=1}^n \sum_{j \in {}_iB} \frac{1}{2} {}_{ij}E(\mathbf{u}, \mathbf{z}), \quad (6.2)$$

where ${}_iB$ contains the neighboring points of lattice point i , which is a subset of the index set $N = \{1, \dots, n\}$ containing all n lattice points (${}_iB \subseteq N$). The factor $1/2$ arises because half of the energy ${}_{ij}E$ associated with the interaction between i and j is attributed to node i and the other half to j . Using the chain rule, the rate of the stored energy reads:

$$\dot{E} = \dot{\mathbf{u}}^T \frac{\partial E}{\partial \mathbf{u}} + \dot{\mathbf{z}}^T \frac{\partial E}{\partial \mathbf{z}}. \quad (6.3)$$

Now the internal power and the rate of the stored energy have been defined, the first law of thermodynamics can be used to relate them and determine the dissipation. The first law states that the power performed by a system is the sum of the rate of the stored energy and the rate of dissipation of the system:

$${}^{int}P = \dot{E} + \dot{D}, \quad (6.4)$$

where \dot{D} is the rate of dissipation. Substituting Eq. (6.1) & (6.3) in Eq. (6.4) yields \dot{D} as:

$$\dot{D} = \dot{\mathbf{u}}^T \left({}^{int}\mathbf{F} - \frac{\partial E}{\partial \mathbf{u}} \right) - \dot{\mathbf{z}}^T \frac{\partial E}{\partial \mathbf{z}}. \quad (6.5)$$

Similar to [41], it is now assumed that no dissipation takes place if the internal history variables, \mathbf{z} , which are related to the dissipation mechanisms, remain constant ($\dot{D} = 0$ if $\dot{\mathbf{z}} = \mathbf{0}$). To ensure that this requirement is valid for all (controllable) $\dot{\mathbf{u}}$, the term between brackets in Eq. (6.5) should vanish. The standard expression for the internal forces results:

$${}^{int}\mathbf{F} = \frac{\partial E}{\partial \mathbf{u}}, \quad (6.6)$$

and the rate of dissipation is reduced to:

$$\dot{D} = -\dot{\mathbf{z}}^T \frac{\partial E}{\partial \mathbf{z}}. \quad (6.7)$$

Furthermore, the second law of thermodynamics states that the entropy of a system must remain constant or increase, i.e. $\dot{D} \geq 0$. If we now introduce a column matrix with dissipative forces ${}^z\mathbf{F} = -\frac{\partial E}{\partial \mathbf{z}}$, the following expression is obtained for the dissipation rate:

$$\dot{D} = \dot{\mathbf{z}}^T {}^z\mathbf{F} \geq 0. \quad (6.8)$$

A dissipation potential, Φ , needs to be formulated as functions of the kinematic and internal variables (\mathbf{u} and \mathbf{z} respectively). The dissipation potential can be summed from the dissipation potential of each lattice point, ${}_i\Phi$, (if dissipation takes place in the lattice points) or summed from the dissipation potential of each lattice interaction, ${}_{ij}\Phi$, (if dissipation takes place in the interactions):

$$\Phi(\mathbf{u}, \mathbf{z}) = \sum_{i=1}^n {}_i\Phi(\mathbf{u}, \mathbf{z}) = \sum_{i=1}^n \sum_{j \in {}_iB} \frac{1}{2} {}_{ij}\Phi(\mathbf{u}, \mathbf{z}), \quad (6.9)$$

Note that this expression entails that each interaction is visited twice (one node on each side), as is performed for the stored energy in Eq. (6.2).

At this point, the thermodynamical setting for a dissipative lattice model with trusses is complete, except for the formulation of the stored energy per truss and the formulation of the dissipation potential per point or interaction as functions of the kinematic, \mathbf{u} , and internal variables, \mathbf{z} . Both formulations depend on the specific lattice model of interest. For a lattice with elastoplastic trusses (see Fig. 6.1), the expressions of the energy stored per truss, ${}_{ij}E$ in Eq. (6.2), and the dissipation potential for a truss, ${}_{ij}\Phi$ in Eq. (6.9), (since dissipation takes place in the trusses for a network with elastoplastic trusses) are established below.

6.2.2 Elastoplastic interactions

The formulations of the stored energy per truss and the dissipation potential per truss are derived here for a truss that is connected to lattice point i and neighboring lattice point j . However, the subscripts ij are dropped below for ease of notation.

The elastoplastic trusses in the considered lattice are all of the same material with the same material description. The elastic part of the material description is linear, whereas the hardening behavior is yet to be defined (in the dissipation potential Φ). First the stored energy per truss (${}_{ij}E$ in Eq. (6.2)) is defined in terms of \mathbf{u} and \mathbf{z} .

The total axial strain of one elastoplastic truss, ϵ , is split in an elastic part, ${}^e\epsilon$, and a plastic part, ${}^p\epsilon$, as follows:

$$\epsilon = {}^e\epsilon + {}^p\epsilon. \quad (6.10)$$

The total strain is taken linear in terms of the elongation, λ :

$$\epsilon = \lambda - 1. \quad (6.11)$$

The elongation depends on the kinematic variables, \mathbf{u} , according to:

$$\lambda = \frac{|{}_j\vec{x} + {}_j\vec{u} - {}_i\vec{x} - {}_i\vec{u}|}{|{}_j\vec{x} - {}_i\vec{x}|}, \quad (6.12)$$

where ${}_i\vec{u}$ and ${}_j\vec{u}$ are the displacement vectors of nodes i and j respectively. The original length of the interaction is represented by $|{}_j\vec{x} - {}_i\vec{x}|$ where ${}_i\vec{x}$ is the original position vector of node i . The internal variables, \mathbf{z} , are taken as the plastic strains of all trusses, i.e. ${}^p\epsilon = z$. By inserting ${}^p\epsilon = z$ and Eq. (6.11) & (6.12) in Eq. (6.10), the following expression is obtained for the elastic strain:

$${}^e\epsilon = \frac{|{}_j\vec{x} + {}_j\vec{u} - {}_i\vec{x} - {}_i\vec{u}|}{|{}_j\vec{x} - {}_i\vec{x}|} - 1 - z. \quad (6.13)$$

This relation relates the elastic strain of a truss, ${}^e\epsilon$, to \mathbf{u} and \mathbf{z} .

The elastic part of the material description of all trusses is linear. The stored energy of a truss can then be expressed in terms of ${}^e\epsilon$, according to:

$$E = \frac{1}{2} Y^0 A |_j \vec{x} - {}_i \vec{x}|^e \epsilon^2, \quad (6.14)$$

where Y represents the Young's modulus and 0A the original cross-sectional area. Insertion of Eq. (6.13) in Eq. (6.14) leads to the following expression:

$$E = \frac{1}{2} Y^0 A |_j \vec{x} - {}_i \vec{x}| \left(\frac{|_j \vec{x} + {}_j \vec{u} - {}_i \vec{x} - {}_i \vec{u}|}{|_j \vec{x} - {}_i \vec{x}|} - 1 - z \right)^2. \quad (6.15)$$

Now we can define the expression for the local dissipation potential for each truss (${}_{ij}\Phi$ in Eq. (6.9), although below we drop subscript ij again). The following formulation is regularly used to describe the onset of yielding in a 1D system (the axial direction of a truss):

$$\Phi = |{}^z F| - {}^y F(\xi) \leq 0, \quad (6.16)$$

with

$${}^z F = -\frac{\partial E}{\partial z}, \quad (6.17)$$

where ${}^y F$ is the yield function. This expression entails that no dissipation (plastic deformation) occurs if the force ${}^z F$ remains below the corresponding yield force, ${}^y F$. The full dissipation potential in Eq. (6.9) depends on the column matrix ${}^z \mathbf{F}$, but each local term of the dissipation potential only depends on one component of ${}^z \mathbf{F}$, namely ${}^z F$. Therefore each local term can be locally determined, as commonly done in elastoplastic descriptions. The internal history variable ξ , which for all trusses are stored in column matrix $\boldsymbol{\xi}$, is introduced for one truss by:

$$\dot{z} = \dot{\xi} \frac{\partial \Phi}{\partial {}^z F} = \dot{\xi} \text{sign}({}^z F). \quad (6.18)$$

To ensure a positive or zero rate of dissipation, the following Kuhn-Tucker equations are imposed for each truss:

$$\dot{\xi} \geq 0 \quad \Phi \leq 0 \quad \dot{\xi}\Phi = 0. \quad (6.19)$$

The internal history variable ξ is thereby the effective plastic strain of a truss. Note that since $\text{sign}(z) = \text{sign}({}^zF)$, Eq. (6.8) is satisfied for each individual truss (i.e. each component of $\dot{\mathbf{z}}$ and ${}^z\mathbf{F}$) and thus for the entire lattice.

For the hardening behavior of a truss in the lattice the following formulation is used:

$${}^yF = {}^0A {}^0\sigma |{}_j\vec{x} - {}_i\vec{x}|(1 + H\xi^\alpha), \quad (6.20)$$

where H and α are hardening parameters and ${}^0\sigma$ is the initial yield stress. The same values are used for all trusses.

6.2.3 Solution procedure

The solution of the lattice can be found by solving Eq. (6.1) while taking into account the inequality constraints in Eq. (6.19) for all trusses. This system of equations is non-linear due to the non-linear material description of the trusses (see Eq. (6.20)) and the fact that we allow large rotations (see Eq. (6.15)). A Newton-Raphson procedure can be used to solve Eq. (6.1), for which a first-order Taylor expansion is required:

$$\dot{\mathbf{u}}^T \left({}^{int}\mathbf{F}({}^*\mathbf{u}, {}^*\mathbf{z}) + \mathbf{K}({}^*\mathbf{u}, {}^*\mathbf{z})d\mathbf{u} \right) = \dot{\mathbf{u}}^{T ext}\mathbf{F} \quad \forall \dot{\mathbf{u}}, \quad (6.21)$$

where ${}^*\mathbf{u}$ and ${}^*\mathbf{z}$ are the displacement components and the plastic strains of the previous iteration respectively. The correction to the displacement components computed in the present iteration is represented by $d\mathbf{u}$. The overall stiffness matrix \mathbf{K} is defined here as $\frac{\partial {}^{int}\mathbf{F}}{\partial \mathbf{u}}$ and is thus a second order derivative of the stored energy (since ${}^{int}\mathbf{F}$ is the first order derivative of the stored energy, see Eq. (6.6)). Note that the inequality constraints (see Eq. (6.19) for the constraints acting in each truss) must be met as well, which can be checked locally for each truss of the network.

In the Newton-Raphson scheme, Eq. (6.21) is used to obtain a new estimate of the displacement components, whereas the new plastic strains are determined from these newly obtained displacements by the use of the inequality constraints. The latter are numerically dealt with by a standard return mapping procedure [111,124]. Since each inequality constraint is related to one local dissipation mechanism (in each truss), each inequality constraint is treated individually in the solution procedure.

Although not incorporated in Eq. (6.21), the boundary conditions of the system must be taken into account. Neumann boundary conditions are present in the external force column $^{ext}\mathbf{F}$ and the Dirichlet boundary conditions are incorporated in the displacement column \mathbf{u} . After the system is partitioned in a standard manner, the incremental solution results for the standard Newton-Raphson procedure.

The system of equations is computationally expensive to solve for large-scale lattice models (i.e. n is large). A large number of $2n$ DOFs (displacement components) is involved, making the first expression in Eq. (6.21) computationally expensive to solve. Moreover, all n lattice points need to be visited to construct the system of equations in Eq. (6.21), according to Eq. (6.2), (6.6) & (6.9).

6.3 Virtual-power-based quasicontinuum method

The QC method, developed for (conservative) atomistic lattice models [114], introduces two remedies to improve the efficiency of direct lattice computations. First, interpolation of the displacements of the lattice points ensures that the number of displacement components (DOFs) is reduced. Furthermore, summation is used in the QC method to achieve a more efficient construction of the governing equations. Instead of using all lattice points to construct the governing equations, an estimate of the governing equations is obtained by selecting only a small number of lattice points.

6.3.1 Interpolation

Interpolation is introduced in QC methods by imposing an interpolation triangulation to a lattice model. For the two-dimensional lattice model considered here, an example of a triangulation is shown in Fig. 6.2. Nodes of the triangles are positioned at chosen lattice points and the displacements of the remaining lattice points are interpolated between them. Linear interpolation is generally used as in this chapter, except in [69]. As a result of the interpolation, the displacements of the interpolated lattice points follow directly from the displacements of the lattice points at triangle nodes. The latter are therefore referred to as representative points or reppoints (or repatoms if the method is being used for atomistic lattices). The reppoints, stored in set R , are selected from all lattice points, i.e. $R \subseteq N$.

The use of interpolation of the lattice model ensures that the QC method is a true multi-scale method. Consider for instance Fig. 6.2 in which a number of trusses is significantly stiffer than the regular trusses. In the region surrounding the stiff trusses significant displacement fluctuations are expected. Therefore, a fully resolved interpolation grid is used there to capture these fluctuating displacements, i.e. every lattice point is a reppoint. The exact lattice model is recovered here, while in the remaining regions the lattice model is interpolated and many DOFs are eliminated. As a consequence, the lattice points displace in an affine manner in these coarse domains. Coarse domains (large triangles) are therefore only allowed to be used in regions with smooth displace-

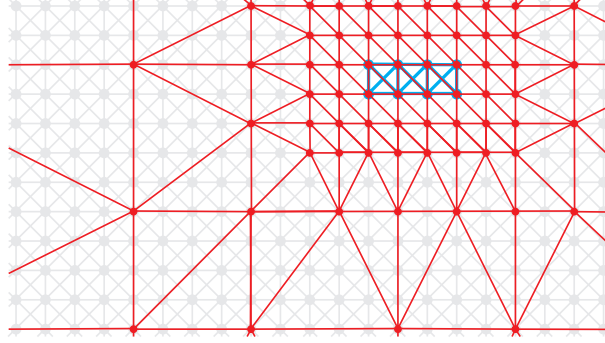


Figure 6.2: The X-braced truss network (grey) with an imposed triangulation (red). The blue bold trusses in the center of the fully resolved region are substantially stiffer than the remaining grey trusses.

ment fluctuations to ensure sufficient accuracy. The fact that in coarse domains the displacements are coarse-grained and in the fully resolved domains the displacements of the individual lattice points are incorporated, gives the QC method its multiscale character.

The displacement components of all lattice points can be expressed as a function of the displacement components of the reppoints by the following expression:

$$\mathbf{u} = \Psi^r \mathbf{u} \quad (6.22)$$

where ${}^r \mathbf{u}$ is the column matrix with the displacement components of the reppoints of size $2r \times 1$ for the two-dimensional truss network of interest. Here, r refers to the number of reppoints. The condensation matrix is denoted by Ψ and its size is $2n \times 2r$. It contains the values of the interpolation functions, evaluated at the positions of all lattice points.

Interpolation directly affects the displacement components, \mathbf{u} , of the lattice according to Eq. (6.22). The interpolated displacements are (C_0 -)continuous as a result of the linear interpolation. According to the inequality constraints in Eq. (6.21), the internal variables follow from the displacements. Consequently, they are only indirectly influenced by the interpolation of \mathbf{u} . The internal variables are (approximately) constant within an interpolation triangle as a consequence of the linear interpolation of the displacements, since they are defined as (plastic) strains, of the order of the gradients of the displacements (kinematic variables).

By substituting Eq. (6.22) in Eq. (6.21) the formulation of the virtual-power statement reads:

$${}^r \dot{\mathbf{u}}^T \left(\Psi^{Tint} \mathbf{F}(\Psi^{*r} \mathbf{u}, {}^* \mathbf{z}) + \Psi^T \mathbf{K}(\Psi^{*r} \mathbf{u}, {}^* \mathbf{z}) \Psi d^r \mathbf{u} \right) = {}^r \dot{\mathbf{u}}^T \Psi^{T ext} \mathbf{F} \quad \forall {}^r \dot{\mathbf{u}}, \quad (6.23)$$

where $\Psi^{Tint}\mathbf{F}$ and $\Psi^T\mathbf{K}\Psi$ can be identified as the condensed internal force column, $^{int,r}\mathbf{F}$ (size $2r \times 1$), and the condensed stiffness matrix, ${}^r\mathbf{K}$ (size $2r \times 2r$), respectively. For the sake of clarity the condensed external force column is not considered in more detail here and below. The condensed counterparts of the internal force column and stiffness matrix are formulated as follows:

$$^{int,r}\mathbf{F} = \Psi^T \sum_{i=1}^n \sum_{j \in_i B} \frac{1}{2} \frac{\partial_{ij} E}{\partial \mathbf{u}}, \quad (6.24)$$

$${}^r\mathbf{K} = \Psi^T \sum_{i=1}^n \sum_{j \in_i B} \frac{1}{2} \frac{\partial^2_{ij} E}{\partial \mathbf{u}^2} \Psi. \quad (6.25)$$

Note that the constraints in all trusses (see Eq. (6.19) for the constraints acting in one truss) must still be satisfied in the condensed system.

To ensure that the condensed governing equations in Eq. (6.23) adequately approach the original governing equations in Eq. (6.21), coarse domains (i.e. large triangles) may only exist in regions with small displacement fluctuations. In these regions, the displacements are linearly interpolated resulting in an equal virtual power of two neighboring lattice points in one triangle (${}^r\dot{\mathbf{u}}^T \Psi^T \frac{\partial_{ij} E}{\partial \mathbf{u}} = {}^r\dot{\mathbf{u}}^T \Psi^T \frac{\partial_{i+1j} E}{\partial \mathbf{u}}$). This is only valid if the virtual powers of these two lattice points in the uncondensed system are practically identically ($\dot{\mathbf{u}}^T \frac{\partial_{ij} E}{\partial \mathbf{u}} \approx \dot{\mathbf{u}}^T \frac{\partial_{i+1j} E}{\partial \mathbf{u}}$).

As a result of Eq. (6.23) and because $r \ll n$, the (condensed) system in Eq. (6.23) is substantially more efficient to solve than the (uncondensed) system in Eq. (6.21). This is in correspondence with other QC methods based on conservative lattices. The inequality constraints for the entire network, which originate from the considered elastoplastic (non-conservative) lattice, remain unaffected by interpolation. Through interpolation, a new estimate of the displacements is computationally more efficiently obtained. Yet, all constraints need to be satisfied individually and still all n lattice points need to be visited for the construction of the governing equations in Eq. (6.23).

6.3.2 Summation

Now the solution space of the system is reduced by means of interpolation, the first cause of the large computational effort has been addressed. However, still all n lattice points must be visited to construct the condensed internal force column, $^{int,r}\mathbf{F}$ and the condensed stiffness matrix, ${}^r\mathbf{K}$.

The remedy adopted in the QC method to avoid accessing all n lattice points is to access only a small number of s lattice points in order to obtain an estimate of the condensed virtual power (i.e. the condensed governing equations). This procedure is

called summation in QC methodologies. The lattice points that are used for this are referred to as sampling points since they sample the virtual power of the lattice points in its vicinity. They are stored in set S and are selected from all lattice points ($S \subseteq N$).

The key principle of summation is that the virtual power of a sampling point i can be used to represent the virtual power of ${}_i w$ lattice points in the vicinity of the sampling point (including sampling point i itself). This entails for the governing equations that:

$${}^r \dot{\mathbf{u}}^T \left({}^{int,rs} \mathbf{F}(\Psi^{*r} \mathbf{u}, * \mathbf{z}) + {}^{rs} \mathbf{K}(\Psi^{*r} \mathbf{u}, * \mathbf{z}) d^r \mathbf{u} \right) = {}^r \dot{\mathbf{u}}^T \Psi^{T ext} \mathbf{F} \quad \forall {}^r \dot{\mathbf{u}} \quad (6.26)$$

with

$${}^{int,rs} \mathbf{F} = \Psi^T \sum_{i \in S} {}_i w \sum_{j \in {}_i B} \frac{1}{2} \frac{\partial {}_{ij} E}{\partial \mathbf{u}}, \quad (6.27)$$

$${}^{rs} \mathbf{K} = \Psi^T \sum_{i \in S} {}_i w \sum_{j \in {}_i B} \frac{1}{2} \frac{\partial^2 {}_{ij} E}{\partial \mathbf{u}^2} \Psi, \quad (6.28)$$

in which ${}^{int,rs} \mathbf{F}$ and ${}^{rs} \mathbf{K}$ are the summed condensed internal force column and summed condensed stiffness matrix respectively.

As a result of the presence of the weight factor, ${}_i w$, the dissipation potential will not show the same elastoplastic behavior for a truss connected to a sampling point. To ensure that the elastoplastic behavior of a truss recovers its response in the direct lattice model (i.e. to ensure equal dissipation), the dissipation potential for the truss between sampling point i and neighbor j in Eq. (6.16), Φ , needs to be modified to (where we use the subscript ij again for clarity):

$${}_{ij}^{rs} \Phi = |{}_{ij}^{z,rs} F| - {}_i w {}^y F({}_{ij} \xi) \leq 0, \quad (6.29)$$

since ${}_{ij}^{z,rs} F = {}_i w \frac{\partial {}_{ij} E}{\partial {}_{ij} z}$, where ${}_{ij} z$ refers to the component of \mathbf{z} that is associated with the truss between points i and j . Eq. (6.29) implies that the yield function ${}^y F$ is to be weighted equally with the same weight factor ${}_i w$.

The advantage of using summation is that only a small number of s sampling points (assuming that $s \ll n$) need to be visited to obtain an approximation of the condensed governing equations, instead of all n lattice points (to determine the condensed governing equations exactly). In this way, the QC method solves the governing equations

more efficiently by interpolation and also gains efficiency to construct them. Since the inequality constraints hold for each truss connected to a sampling point, the inequality constraints apply to all trusses related to sampling points.

An important advantage of the proposed virtual-power-based QC framework is that the internal forces are accurately related to all virtual displacements of influence. This automatically follows from the virtual-power-based framework as was the case for the energy-based QC frameworks [9,36] which did not take dissipation into account. The relation between the virtual displacements and the forces is for instance illustrated by the summed condensed internal force column in Eq. (6.27) in which $\frac{\partial}{\partial \mathbf{u}}$ ensures that stored energy of a truss, represented by ${}_{ij}E$, is related to the virtual displacements of the sampling point itself and also to its neighboring points.

For the summed condensed internal force column in a force-based QC framework [64] however, the following formulation is used:

$${}^{int,rs}\mathbf{F} = \mathbf{\Psi}^T \sum_{i \in S} \left(\left({}_i w \sum_{j \in B} \frac{\partial {}_{ij}E}{\partial {}_i \mathbf{u}} \right)^T {}_i \mathbf{N} \right)^T, \quad (6.30)$$

where for the two-dimensional lattice considered here ${}_i \mathbf{u}$ contains the displacement components of sampling point i (${}_i \mathbf{u} = [u_{2i-1} \quad u_{2i}]^T$) and ${}_i \mathbf{N}$ is of size $2 \times 2n$. The components of ${}_i \mathbf{N}$ are given by:

$${}_i N_{hk} = \begin{cases} 1 & \text{if } (h = 1 \ \& \ k = 2i - 1) \text{ or } (h = 2 \ \& \ k = 2i), \\ 0 & \text{otherwise.} \end{cases} \quad (6.31)$$

Eq. (6.30) illustrates that only the dependence of the stored energy of a truss, ${}_{ij}E$, on the displacement components of the sampling points are considered in the force-based methods (indicated by $\frac{\partial}{\partial {}_i \mathbf{u}}$), but not its dependence on the displacement components of the neighboring points of the sampling points. As a consequence, the accuracy of force-based QC methods is compromised, whereas this is not the case for the proposed virtual-power-based QC method in which the same dependence is recovered as in energy-based QC methodologies. This is explained extensively in [36] for conservative lattice models.

Now the question arises which lattice points are suitable to serve as sampling points. The answer to this question results from the requirement that the virtual power of each sampling point needs to be approximately the same as those of the lattice points represented by each sampling points. Hence, we need to identify lattice points for which ${}^r \dot{\mathbf{u}}^T \mathbf{\Psi}^T \frac{\partial {}_i E}{\partial \mathbf{u}} \approx {}^r \dot{\mathbf{u}}_r^T \mathbf{\Psi}^T \frac{\partial {}_{i+1} E}{\partial \mathbf{u}}$, so that one of them can serve as a sampling point to represent the others. The number of lattice points that each sampling point i represents, the weight factor ${}_i w$, can be determined in different ways and one has to decide if the

virtual power of the sampling points is established in a local or nonlocal fashion. The combination of these three issues (which sampling points to select, how to determine ${}_i w$ and which sampling points are treated locally or nonlocally) is specified in a so-called summation rule of which several have been proposed [9,11,36,64,114,127]. An overview is given in [83].

Although the summation rule presented in [9] has been developed for structural lattice models with only nearest-neighbor interactions (as the truss network considered in this chapter) the modified version of this summation rule [11], the so-called central summation rule, is used here. The reason is that less sampling points are necessary in the central summation rule which leads to an efficient QC method. A disadvantage of the central summation rule compared to the original summation rule [9] is that it only gives an estimate of virtual power. As shown in [11] and below in Section 6.4, the accuracy in the fully resolved regions of interest can be increased by using relatively large fully resolved regions.

In the central summation rule one internal sampling point is selected in the center of each triangle to sample all lattice points in the triangle and on top of the triangle edges (with ${}_i w \geq 1$) while the reppoints of the triangle are selected to only represent themselves (see Fig. 6.3). The reppoints are selected as discrete sampling points (with ${}_i w = 1$) so that in the fully resolved regions the exact lattice model is recovered. In case all lattice points in a triangle are located at triangle edges and triangle nodes, no internal sampling node is selected and all lattice points of the corresponding triangle are selected as discrete sampling nodes to overcome metastable solutions [11]. Furthermore, the virtual powers of all sampling points are computed in a nonlocal fashion so that no internal interface occurs, as for instance in the QC methods presented in [114] and [108] and other multiscale approaches [38,125].

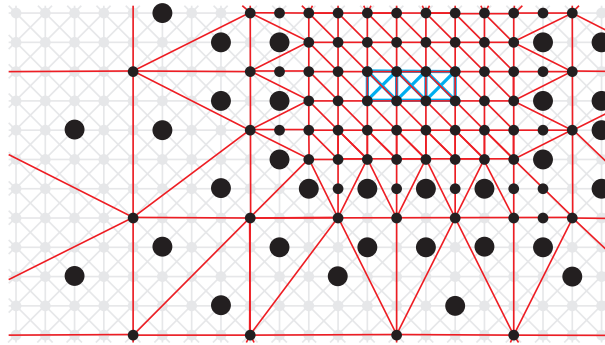


Figure 6.3: Schematic representation of the central summation rule applied to the X-braced truss network. The thick, blue trusses in the fully resolved region are substantially stiffer than the regular trusses. Black dots are discrete sampling points (with ${}_i w = 1$) and large black dots are internal sampling points (with ${}_i w \geq 1$). The neighboring nodes of the sampling nodes that must be taken into account in the nonlocal computation are not highlighted.

6.4 Numerical examples

In this section, the virtual-power-based QC framework including the central summation rule [11] is applied to two numerical examples to illustrate the computational gain and accuracy that can be achieved. The elastoplastic lattice model of Section 6.2 is used in the examples which have a true multiscale character, since large-scale networks with local adaptations are considered. The examples are set up in a dimensionless form.

6.4.1 Problem statement

The lattice spacings in horizontal and vertical direction are set to 1. The length of the diagonal trusses is thus $\sqrt{2}$. The lattice model contains 100×100 unit cells (20,402 DOFs). The parameters of the trusses' material behavior are presented in Table 6.1, corresponding to a purely elastic response up to a strain of 1%. The use of these parameters results in a smooth increase of plastic deformation for strains larger than 1% (see ahead to the left image in Fig. 6.7 for the response of a unit cell).

Table 6.1: Dimensionless material parameters.

Y	1
0A	1
${}^0\sigma$	0.01
H	10
α	0.5

In the numerical examples, a stiff region of 6×6 unit cells is introduced at the center of the lattice by modelling the trusses in this square substantially stiffer than the regular trusses. The Young's modulus of these trusses is therefore increased by a factor of 100 and a large initial yield stress is used so that no plastic deformation occurs in the stiff region. The local stiff region in the lattice model can be regarded as a hard particle or region inside a fibrous material. An example can for instance be the locally thermally bonded material investigated in [53] or an electronic textile with a light-emitting-diode mounted on it [12].

As a result of the local stiff region, large displacement fluctuations are expected near this domain so that a fully resolved region is required in and around it. The displacement fluctuations in the remaining domain are expected to be significantly smaller so that coarse triangles can be used. This results in a true multiscale example that forms a representative test case for the virtual-power-based QC method.

The local influence of this stiff region on the lattice is investigated for uniform loading using periodic boundary conditions [66]. It can thus be considered as a representative

volume element in a periodic structure. To this end, the cross-sectional area of the trusses of which both lattice points are located on the model edges is only half of the area of the other trusses. Uniform deformation is applied in horizontal direction up to a strain of 10%. The maximum strain is reached in 100 increments in the QC simulations as well as in the direct lattice computations. Note that in the direct lattice computation, used to evaluate the QC framework, the boundary conditions are directly applied to the lattice points (truss nodes), whereas they are applied to the reppoints only in the QC model.

6.4.2 Computational efficiency

Four different triangulations are used to investigate the smallest possible size of the fully resolved region that still gives sufficiently accurate results (see Fig. 6.4). The fully resolved region is centered around the central stiff region since this is the region of interest where significantly fluctuating displacements occur. The coarse domain is kept similar (i.e. a similar coarseness) in the four triangulations so that only the influence of the size of the fully resolved region is investigated. Another reason to keep the coarse domain as coarse as possible is that the refinement of the coarse domain leads to a relatively large extra number of reppoints and sampling points for only a limited increase of the accuracy [9].

The diagram in Fig. 6.4 shows that the number of reppoints and sampling points of the four triangulations is only 5-20% of the number of points used in direct lattice computations. This significant reduction of the direct lattice computation indicates that the reduction strategy proposed in the QC method is efficient for lattice models. Especially considering that in this case study the coarse domain (in which the reduction takes place) is relatively small compared to the fully resolved domain. Cases in which significantly larger coarse domains are present, are widely existing. An example may be if local failure occurs in large-scale models, as in [46].

6.4.3 Accuracy

Results of the direct lattice computation and QC simulation for the triangulation with a fully resolved region of 14×14 unit cells are presented in Fig. 6.5. The results of the trusses that are not shown in the top-right image of Fig. 6.5 belong to the summed lattice points. This means that they are represented by the internal sampling points.

The results predicted by the virtual-power-based QC method adequately correspond to those of the direct lattice computation for uniform deformation. The horizontal trusses on the left and right of the stiff region experience large plastic strains in tension, while the vertical trusses above and below the stiff region are plastically more compressed than the other vertical trusses. The trusses with the maximum plastic strains are located at the four corners of the stiff region.

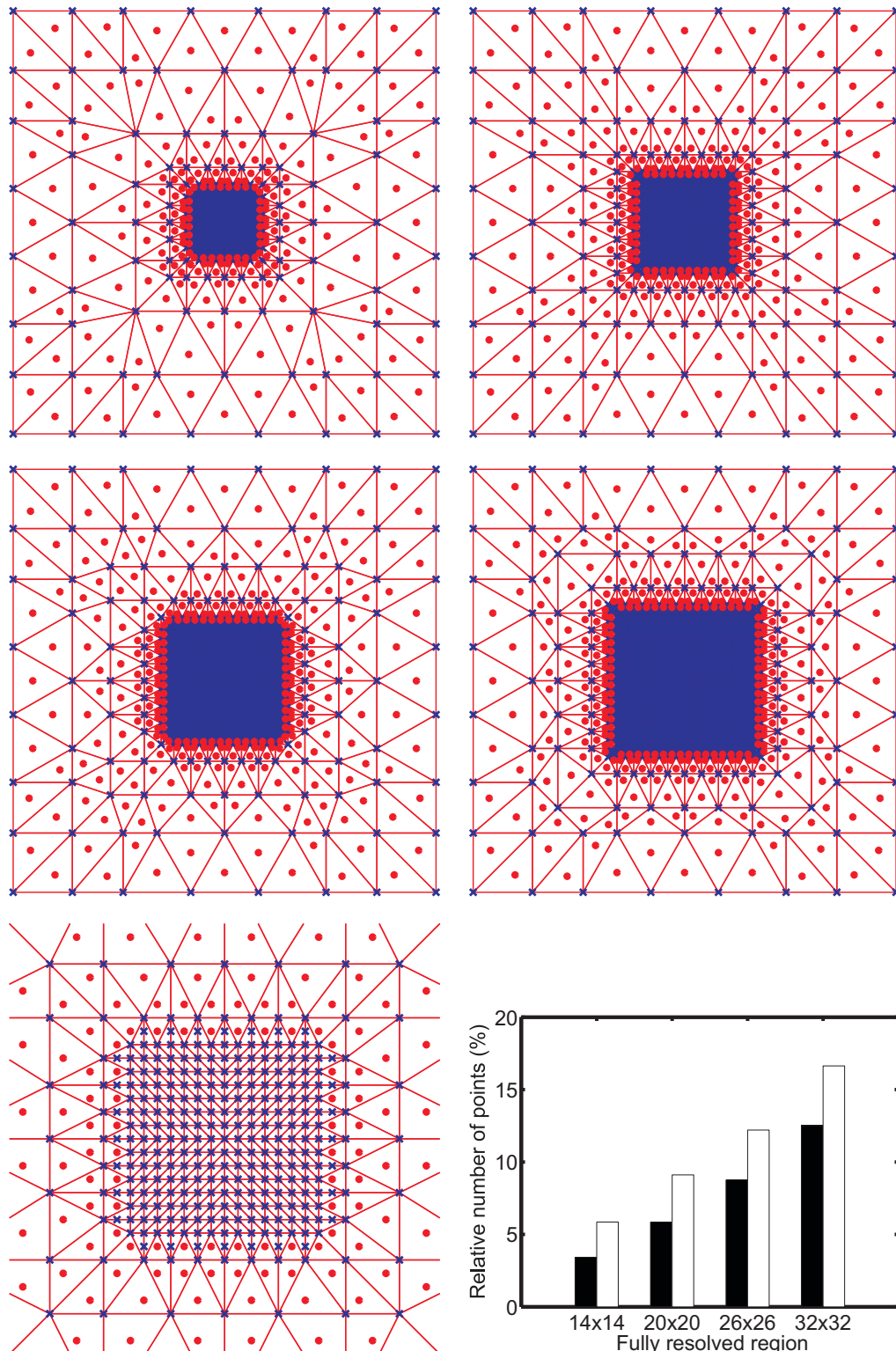


Figure 6.4: The four triangulations used to investigate the influence of a stiff region in the lattice. For clarity, trusses are not shown. Red circles represent internal sampling points ($iw \geq 1$) and blue crosses represent discrete sampling points ($iw = 1$). The triangulations have fully resolved regions of 14×14 (top-left), 20×20 (top-right), 26×26 (middle-left) and 32×32 unit cells (middle-right). A zoom of the fully resolved region with 14×14 unit cells can be seen in the bottom-left image. The diagram on the bottom-right shows the number of reppoints (black bars) and sampling points (white bars) relative to the total number of points for the four triangulations.

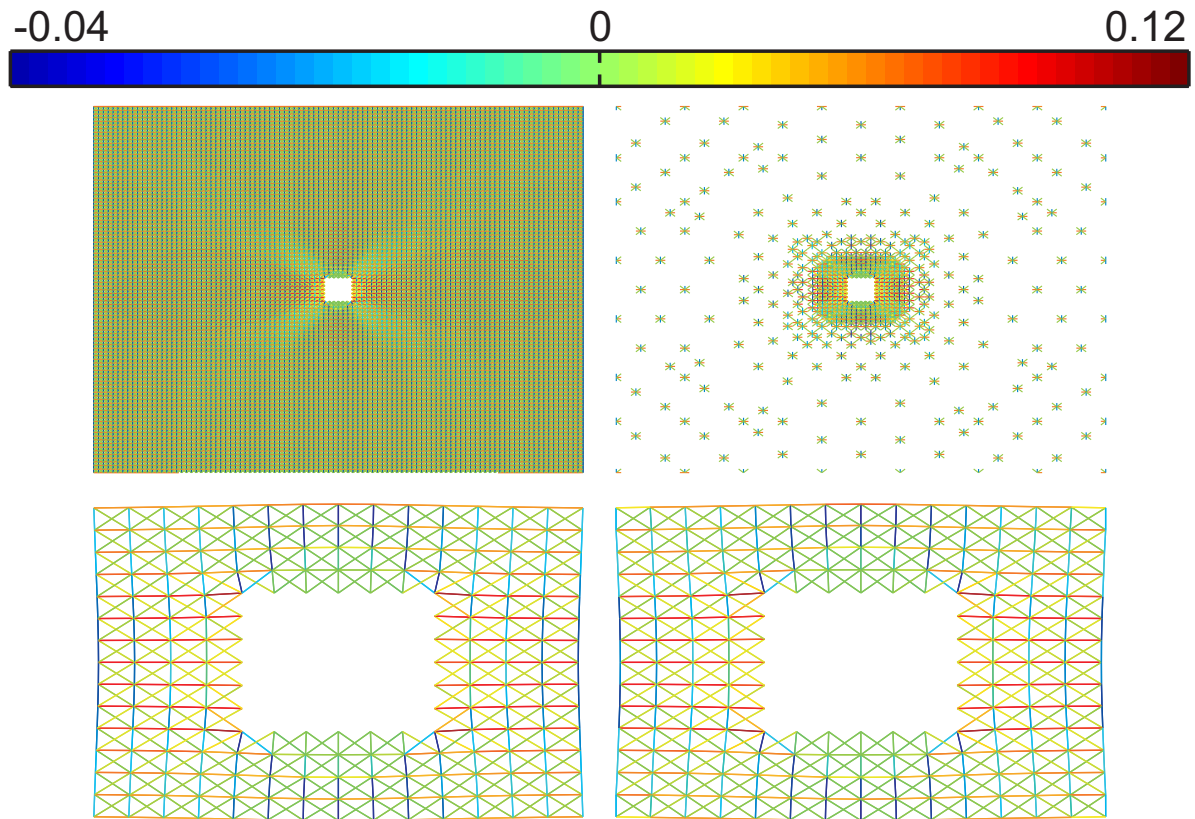


Figure 6.5: The plastic strains in the trusses at the maximum uniform deformation computed by the direct lattice computation (left) and the virtual-power-based QC computation (right) for the triangulation with a fully resolved region of 14×14 unit cells (see Fig. 6.4). The triangulation is not shown. The top images show the entire models and the bottom images show zooms of the fully resolved region around the stiff region (white).

To evaluate the accuracy of the QC results in a quantitative manner, the plastic strains at maximum deformation of twelve trusses are considered in more detail. The twelve interactions of interest are shown on the left in Fig. 6.6. The local average relative error, $rel\bar{\epsilon}$, for a given triangulation is based on the following expression:

$$rel\bar{\epsilon} = \frac{1}{12} \sum_{i=1}^{12} \left| \frac{qc_i v - dlc_i v}{dlc_i v} \right| \cdot 100\% \quad (6.32)$$

where $_i v$ represents the variable of interest (the axial plastic strain) of truss i . The superscript qc refers to the solution of the virtual-power-based QC model for a particular triangulation and superscript dlc refers to the solution of the direct lattice computation. The local average relative errors of the plastic strains for the four triangulations shown

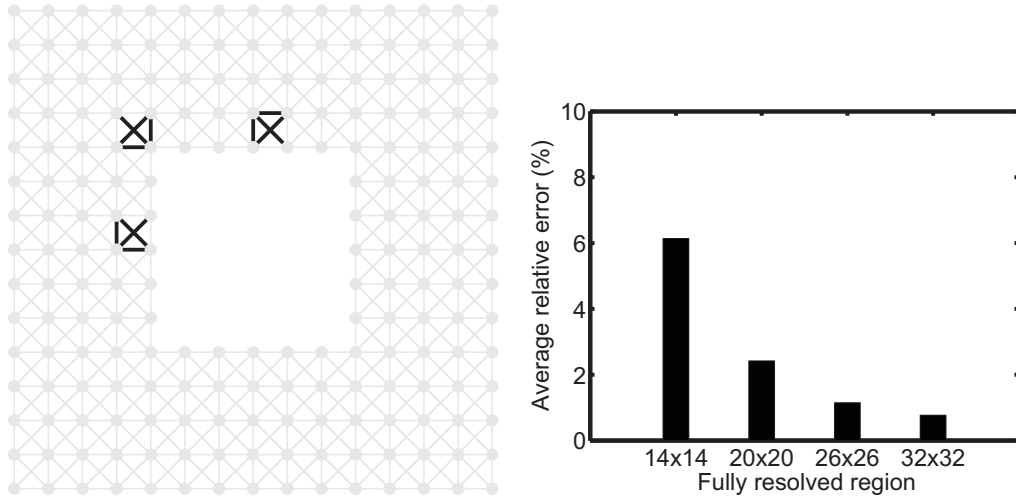


Figure 6.6: The twelve interactions selected around the stiff region (left) and (right) the local average relative errors of the plastic strains of the twelve interactions shown in the left image for the four triangulations shown in Fig. 6.4.

in Fig. 6.4 are shown on the right in Fig. 6.6. The trend of the local average relative errors is decreasing for an increasing size of the fully resolved domain. A pronounced decrease is noticed between the error of the triangulation with a fully resolved domain of 14×14 unit cells and the error of the triangulation with a fully resolved domain of 20×20 unit cells. For triangulations with fully resolved regions larger than 20×20 unit cells, a relatively small decrease can be observed. This is in agreement with the results in [11] in which the central summation rule is used for atomistic lattice models. In the results in [11], the error also decreases significantly if the size of the fully resolved domain is enlarged so that all local displacement fluctuations occur inside the fully resolved domain. For a further increase of the size of the fully resolved domain, only a minor decrease of the error was observed. In [11], it has been shown that if an error in the fluctuations field remains at the border of the fully resolved domain, the error remains non-zero. This is in agreement with the local average relative errors in Fig. 6.6.

The most important observation based on Fig. 6.6 is that for the triangulation with a fully resolved region of 20×20 unit cells, the local average relative error is below 5%. This indicates that this triangulation gives results that may often be considered to be accurate enough, while the computational cost is low (see Fig. 6.4). A triangulation with a larger fully resolved region can be used if a larger accuracy is required, but this is at the expense of the computational efficiency.

6.4.4 Textile-like lattice model

To illustrate that the virtual-power-based QC framework picks up trends if the lattice model is changed, the Young's modulus of the diagonal trusses is next decreased by a factor of 10. In this way the mechanical response of the lattice more or less corresponds

to a general response of lattice models for woven fabrics [12,107]. In such lattice models, the relatively stiff horizontal and vertical interactions represent two families of yarns and the compliant diagonal trusses represent the rotational stiffness between the two families of yarns. Except for the stiffness of the diagonal trusses, all other model parameters and boundary conditions are the same as before. The stiff region in this case may represent a light-emitting-diode placed on a patch of electronic textile [12].

The homogenized stress-strain responses of a unit cell of the textile-like lattice model is compared to the response of the original lattice on the left in Fig. 6.7. The initial stiffness (during macroscopic uniform deformation) reduces to approximately 80% of the original stiffness. The initial stiffness during macroscopic shear deformation however decreases to approximately 10% of the original stiffness (not shown here). This is caused by the fact that during macroscopic shear deformation mainly the diagonal trusses are loaded, whereas during macroscopic uniform deformation the diagonal and vertical trusses are also loaded through the horizontal trusses.

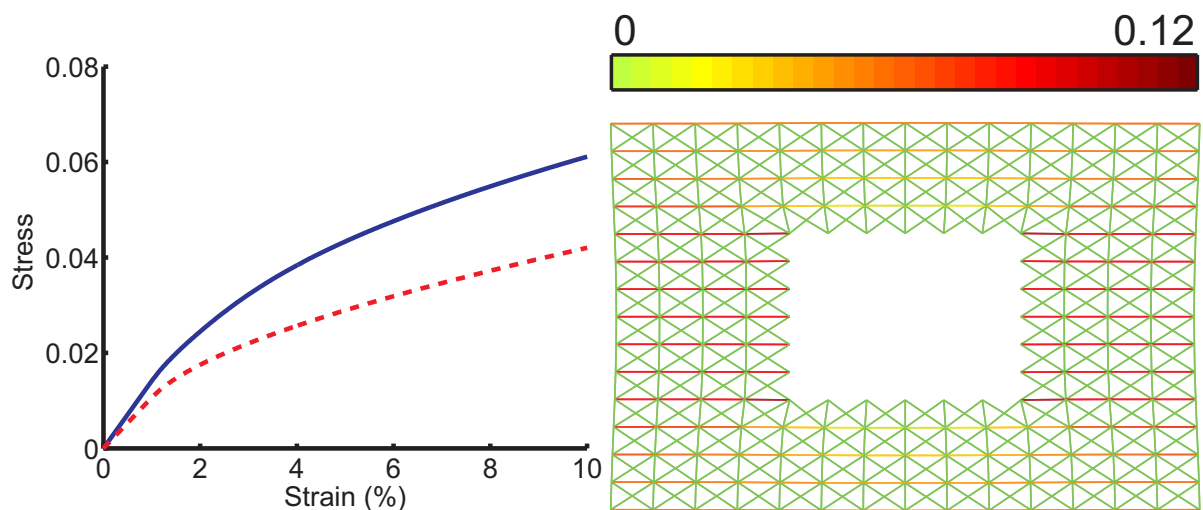


Figure 6.7: Left: the homogenized engineering stress-strain responses of an original unit cell (solid line) and of a unit cell with compliant diagonal interactions (dashed line) for uniform loading. Right: the plastic strains in the fully resolved region computed by the virtual-power-based QC model for the triangulation with a fully resolved region of 20×20 unit cells (at maximum applied uniform deformation).

The plastic strains predicted with the virtual-work-based QC framework for the lattice with compliant diagonal trusses are presented on the right in Fig. 6.7. They show a clear difference with the previous results. In this case only the horizontal interactions are plastically elongated. Because the diagonal interactions only yield at an axial strain of 10% (due to their small Young's modulus), no yield of the diagonal interactions can be observed at maximum uniform loading. Because the diagonal trusses only transfer small loads, the vertical trusses are also not plastically deformed. The virtual-power-based QC framework is thus well applicable a wide range of dissipative lattice models.

6.5 Conclusion

Lattice models and discrete networks are appropriate to describe the mechanical behavior of fibrous and heterogeneous materials, since they automatically incorporate mesoscale phenomena that dominate the material response of these materials. Large-scale computations of lattice models and discrete networks that are necessary for physically relevant simulations, involve substantial computational efforts since a large number of lattice points is required. The quasicontinuum (QC) method is a suitable multiscale approach to reduce the computational efforts of lattice models and discrete networks because it

- allows the accurate incorporation of the mesoscopic lattice model in regions of interest,
- completely relies on the lattice model and not on accompanying continuum descriptions that can be complex to construct for fibrous materials and
- does not require a coupling or handshaking procedure (in the proposed framework).

Several QC methods presented so far, are based on energy-minimization and can thus only deal with conservative lattice models. Many lattice models for fibrous materials however, are non-conservative. In this chapter, a virtual-power-based QC formulation is presented that can deal with non-conservative lattice models. Since it is based on the virtual-power statement, the construction of the governing equations is accurate in contrast to force-based QC methods which relate the internal forces incompletely to the virtual displacements of the lattice points. This is caused by the fact that in the virtual-power-based QC formulation the virtual power is sampled (summed), instead of the forces. The dissipation involved in non-conservative lattice models is naturally incorporated by the constraints that follow from the virtual-power statement.

In the numerical examples, two straightforward lattice models with elastoplastic trusses are used to show the possibilities of the method. The examples are truly multiscale in nature. Since no continuum descriptions are necessary and no internal interfaces occur, the QC counterparts of the direct lattice models are surprisingly easy to implement. The two elastoplastic lattice models show different results that are adequately captured the virtual-power-based QC framework. Comparisons with the results of direct lattice computations indicate that the local average relative error in the results of the virtual-power-based QC method are below 5% for a specific triangulation. Compared to the direct lattice simulations, the computational efficiency of the QC computation for this triangulation is 6% in terms of degrees of freedom and 9% in terms of effort to construct the governing equations (i.e. the number of sampling points). Since the considered problems are representative studies only, the computational gain is expected to be even larger for large-scale models in which a higher grade of scale separation is present. This makes the virtual-power-based QC framework a powerful method to reduce the computational cost of dissipative lattice models while ensuring a high accuracy in regions of interest.

A multiscale quasicontinuum framework for lattice models with bond failure and fiber sliding¹

Abstract

Structural lattice models incorporating trusses and beams are frequently used to mechanically model fibrous materials, because they accurately capture (local) mesoscale phenomena. Physically relevant lattice computations are however computationally expensive. A suitable multiscale approach to reduce the computational cost of large-scale lattice computations is the quasicontinuum (QC) method. This method resolves local mesoscale phenomena in regions of interest and coarse grains elsewhere, using only the lattice model. In the previous chapter, a virtual-power-based QC framework is proposed for lattice models that include local dissipative mechanisms. In this chapter, the virtual-power-based QC method is adopted for lattice models in which bond failure and subsequent fiber frictional sliding are incorporated - which are of significant importance for fibrous materials. Bond failure and fiber sliding are nonlocal dissipative mechanisms and to deal with this nonlocality, the virtual-power-based QC method is equipped with a mixed formulation in which the kinematic variables, as well as the internal history variables are interpolated. Previously defined summation rules can still be used to sample the governing equations in this QC framework. Illustrative examples are presented.

¹ Reproduced from: L.A.A. Beex, R.H.J. Peerlings, M.G.D. Geers, A multiscale quasicontinuum framework for lattice models with bond failure and fiber sliding, In preparation.

7.1 Introduction

Structural lattice models and discrete networks using trusses and beams are often used for the mechanical modelling of fibrous materials with discrete fibers and yarns at the mesoscale and microscale [25,48,53,87,103,100,110,126]. They are typically used to model biological materials [5,4,22,54,113], paper networks [7,20,67,73,112] and textiles [12,15,16,60,107,130]. The discrete elements in lattice models naturally represent the discrete fibers and yarns of these materials. Therefore, lattice models intrinsically capture discrete mechanical phenomena that occur at the mesoscale or microscale, such as fiber fracture, failure of interfiber bonds and fiber sliding. Even global phenomena such as large rotations of yarns are naturally incorporated in lattice models, whereas these are complex to include in continuum descriptions of fibrous materials [96,117].

Also the mechanical microscale behavior of other materials, for which a discrete representation seems not directly relevant, are nowadays often modeled with lattice models and discrete networks. Reasons are the simplicity and intrinsic discreteness of lattice models and the ability to capture highly anisotropic behavior. Failure of concrete is for instance regularly modeled using lattice models [23,72], whereas they are also used to investigate polymer behavior [59,92,102,128] and delamination of thin films [121].

A disadvantage is the computational cost for physically relevant macroscale lattice computations [72], since lattice models are constructed at the level of the mesoscale or microscale. Consequently, macroscale lattice computations have a large number of degrees of freedom (DOFs) which makes their governing equations inefficient to solve. Also the computational effort to construct the large number of governing equations is significant.

Multiscale techniques can be adopted to increase the efficiency of large-scale structural lattice computations. In [113], a classical homogenization scheme is used for a lattice model of a collagen network. Classical homogenization schemes are able to capture macroscale properties such as the effective stiffness, but they are unable to capture local discrete events such as the fracture of a single fiber. Individual failure events are important to include because they are often the precursor of macroscale failure of fibrous materials. In another multiscale approach, continuum descriptions in coarse domains are coupled to lattice models in regions of interest. This is for instance used in [46] to model ballistic impact of a woven textile. Failure of discrete fibers and bonds can be modeled by such a multiscale scheme in regions where the lattice model is used. Disadvantages are that the required continuum models for fibrous materials are not trivial to formulate (as mentioned before) and the non-trivial procedure to couple continuum regions to discretely resolved lattice regions.

Other multiscale approaches that are promising for structural lattice models (using trusses and beams) are frameworks that increase the efficiency of atomistic lattice computations. Like structural lattice models, atomistic lattice models include discrete interactions. Several of these [27,38,125] also combine continuum descriptions with lattice models, also involving a considerable complexity. The quasicontinuum (QC) method [114] however, only relies on the lattice model and is successfully used for atomistic lattice computations [68,69,82,83,115]. Conveniently, a continuum description is thus

not required. Several QC methods still require a coupling procedure for the internal interface between coarse domains and fully resolved domains of interest [108,109,114,115], but some avoid this internal interface [11,13,36,43,64]. A number of QC methodologies are therefore potentially convenient for structural lattice models and discrete networks. In [9], the QC method has first been adopted to deal with (conservative) structural lattice models.

In the previous chapter, a QC framework has been proposed that is based on the virtual-power statement of non-conservative lattice models since many structural lattice models include dissipation. This is in contrast to other QC methods [9,11,36] developed for conservative atomistic lattice models that are based on energy minimization and cannot deal with dissipative lattice models. Using a virtual-power approach, non-conservative lattice forces can be directly inserted in the QC framework proposed in the previous chapter. This has been shown for a structural lattice model with elastoplastic trusses.

The aim of this chapter is to include interfiber bond failure and subsequent frictional fiber sliding in the previously proposed virtual-power-based QC framework. The failure of interfiber bonds (and subsequent fiber sliding) is an important cause of failure of fibrous materials. Different studies have been carried out to investigate bond failure in paper networks [45,52,56,67,73,123]. Bond failure for a nonwoven glass structure is modeled in [100] and fiber sliding (i.e. slippage) in textiles is investigated in [129].

In this chapter, the lattice model for bond failure and subsequent fiber sliding of Chapter 3 is used. Since the model proposed in Chapter 3 only allows small sliding displacements, the expression for the energy stored in the lattice is reformulated to allow large sliding displacements. Furthermore, a viscous dissipation potential is used, leading to a continuous dissipation potential, in contrast to the discontinuous dissipation potential of proposed in Chapter 3.

In the previous virtual-power-based QC methodology, local dissipative mechanisms have been considered (by using elastoplastic trusses). Bond failure and fiber sliding are however nonlocal, since they depend on the bond failure and fiber sliding in neighboring lattice points. To address this nonlocal interaction, not only the displacements are interpolated - as is normally done in QC methods -, but also the sliding displacements. The resulting QC framework thereby entails a mixed formulation.

The same type of linear interpolation is used for the sliding displacements (internal history variables) as for the regular displacements (kinematic variables). Consequently, the summation rule of Chapter 5, in which only one internal sampling point in each interpolation triangle is selected, can be used. The extension of the virtual-power-based QC framework is validated by comparing the results of multiscale QC examples, in which bond failure and subsequent fiber sliding occur, to the results of direct lattice computations.

The outline of the chapter is as follows. First, the lattice model of Chapter 3 is reformulated, including a viscous dissipation and an extension that allows for large sliding displacements. In the subsequent section, the main principles of the virtual-power-based QC method are considered, as well as the incorporation of the lattice model for bond

failure and fiber sliding. In Section 7.4, multiscale examples are shown and their results are compared to those of the direct lattice computations. Finally, conclusions and recommendations are presented in Section 7.5.

7.2 Lattice thermodynamics for bond failure and fiber sliding

QC frameworks increase the efficiency of lattice computations by means of interpolation of the displacements and summation rules to approximate the governing equations instead of resolving them exactly - this is discussed in more detail in the next section. Using summation rules, the potential energy (in this framework the virtual-power) of only a small number of lattice points (so-called sampling points) is determined, instead of determining the potential energy (or virtual-power) of all lattice points. Structural lattice models must be thermodynamically consistent so that no errors occur in the potential energy (or virtual-power) of these sampling points. The reason is that the error in a sampling point is also present in the lattice points that are represented by the sampling point. This can result in a poor accuracy. The formulation of a thermodynamically consistent structural lattice model including bond failure and fiber sliding is therefore first considered along the lines of [41], as well as a possible solution strategy.

The lattice model considered in this chapter is an equidistant X-braced network with linear elastic trusses, see Fig. 7.1. It can be observed that in general every lattice point (truss node) is connected to eight neighboring points. Lattice points are only present at crossings of horizontal, vertical and diagonal trusses and not at the locations where only diagonal trusses cross each other. The trusses that are located on the same line can be regarded as fibers or yarns of a fictitious fibrous material. An individual fiber or yarn is thus modeled by a chain of trusses. As a result, fibers are oriented in four directions in the considered lattice. Some of the fibers in the lattice are of a finite length, which can be observed in Fig. 7.1 by the disconnected curves. A missing truss can be interpreted as the end or start of a fiber, or as an initially broken fiber.

In each lattice point four fibers are connected to each other. A lattice point can therefore be regarded as the collection of four interfiber bonds. Each of these bonds are modeled such that they can fail, leading to frictional sliding of the fibers (trusses) through the nodes (see Fig. 7.2). A certain sliding force has to be achieved to accommodate fiber sliding after bond failure has taken place. After the deformation is removed, the sliding displacements through the nodes remain present. Consequently, the energy associated with bond failure and frictional sliding, is lost. This entails that bond failure and sliding are dissipative mechanisms.

7.2.1 A thermodynamical formulation for non-conservative truss networks

The two-dimensional lattice model in Fig. 7.1 only contains trusses. The kinematic variables are the displacement components of the lattice points. These are stored in

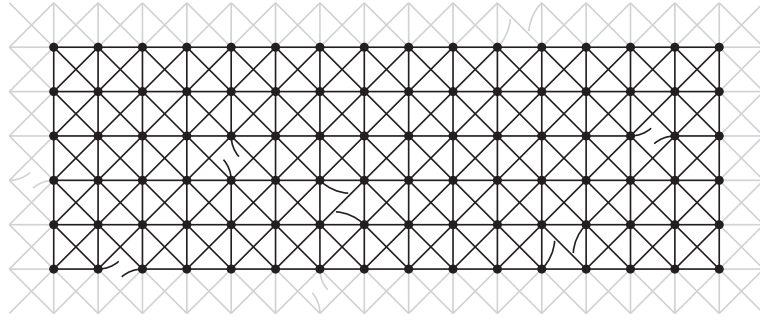


Figure 7.1: Part of an equidistant X-braced lattice model with linear elastic trusses that can slide through nodes if bonds fail. A number of truss interactions are initially not present. At these locations, half of a truss remains connected to each node. This is indicated by the disconnected curves.

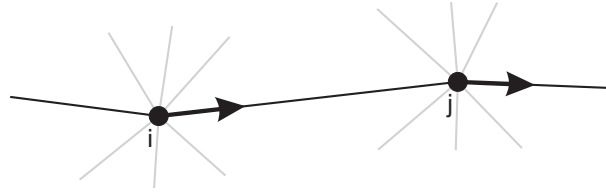


Figure 7.2: A part of a fiber (or yarn) shown in black is modeled by a chain of trusses of which only the truss between nodes i and j is completely shown. The other trusses connected to the nodes are shown in grey. The different sliding displacements of the black fiber through nodes i and j are indicated by arrows.

column matrix \mathbf{u} of size $2n \times 1$. Here, n refers to the number of lattice points of the entire lattice, which are stored in index set $N = \{1, \dots, n\}$.

For a thermodynamically consistent lattice model, the internal power equals the external power for an arbitrary variation of the kinematic variables, which is expressed as follows:

$$\dot{\mathbf{u}}^{Tint} \mathbf{F} = \dot{\mathbf{u}}^{Text} \mathbf{F} \quad \forall \dot{\mathbf{u}}, \quad (7.1)$$

where $\dot{\mathbf{u}}^{Tint} \mathbf{F}$ is the internal power, ${}^{int}P$, and $\dot{\mathbf{u}}^{Text} \mathbf{F}$ the externally applied power. The column matrices containing the decomposed internal forces and external forces are represented by ${}^{int} \mathbf{F}$ and ${}^{ext} \mathbf{F}$ respectively. They are both of size $2n \times 1$. The internal power is the rate of energy stored in the lattice, \dot{E} , and the rate of energy dissipated by the lattice, \dot{D} , according to the first law of thermodynamics:

$${}^{int}P = \dot{E} + \dot{D}. \quad (7.2)$$

For a dissipative lattice model the stored energy is a function of the kinematical variables, \mathbf{u} , and a set of internal history variables, \mathbf{z} , i.e. $E = E(\mathbf{u}, \mathbf{z})$. These internal variables are associated with z dissipation mechanisms in the lattice that are stored in index set $Z = \{1, \dots, z\}$. Consequently, \mathbf{z} is of size $z \times 1$. The rate of the stored energy can be formulated using the chain rule according to:

$$\dot{E} = \dot{\mathbf{u}}^T \frac{\partial E}{\partial \mathbf{u}} + \dot{\mathbf{z}}^T \frac{\partial E}{\partial \mathbf{z}}. \quad (7.3)$$

Substitution of Eq. (7.3) in Eq. (7.2) leads to the following expression for the rate of dissipation:

$$\dot{D} = \dot{\mathbf{u}}^T \left({}^{int}\mathbf{F} - \frac{\partial E}{\partial \mathbf{u}} \right) - \dot{\mathbf{z}}^T \frac{\partial E}{\partial \mathbf{z}}. \quad (7.4)$$

Since the second law of thermodynamics requires the dissipation to be constant or increase, the rate of dissipation can only be zero or positive, i.e. $\dot{D} \geq 0$. It is assumed that only a change of the internal history variables leads to a change of dissipation, i.e. $\dot{D} = 0$ if $\dot{\mathbf{z}} = \mathbf{0}$. To ensure that this is the case for any rate of the kinematic variables, the following relation is formulated for the internal forces:

$${}^{int}\mathbf{F} = \frac{\partial E}{\partial \mathbf{u}}. \quad (7.5)$$

The term between brackets in Eq. (7.4) vanishes and the formulation of the rate of dissipation in Eq. (7.4) reduces to:

$$\dot{D} = \dot{\mathbf{z}}^T {}^z\mathbf{F} \geq 0, \quad (7.6)$$

with

$${}^z\mathbf{F} = -\frac{\partial E}{\partial \mathbf{z}}. \quad (7.7)$$

Now any dissipation potential Φ is allowed as long as $\dot{D} \geq 0$. The formulation of the dissipation potential is, together with the formulation of the energy stored in the lattice,

E , the only ingredient yet to determine. They both depend on the mechanical behavior to describe and are formulated below for the lattice model including bond failure and subsequent frictional fiber sliding. These two formulations differ from those proposed in Chapter 3, where only small sliding displacements are allowed. Moreover, a continuous dissipation potential will be considered here.

7.2.2 Incorporation of bond failure and subsequent sliding

First, the stored energy, E , is expressed as a function of \mathbf{u} and \mathbf{z} for the case including bond failure and fiber sliding. If half of the energies stored in each truss are projected on node i , its nodal energy, ${}_iE$, can be expressed as:

$${}_iE = \sum_{j \in {}_iB} \frac{1}{2} {}_{ij}E, \quad (7.8)$$

where ${}_{ij}E$ represents the energy stored in the truss connecting lattice point i and j . The subset ${}_iB$ (${}_iB \subseteq N$) contains the neighboring points of point i and can thus contain a maximum of eight nodes for the presented lattice model. By considering all n points of the lattice, the energy stored in the entire lattice, E , can be established according to:

$$E = \sum_{i=1}^n {}_iE = \sum_{i=1}^n \sum_{j \in {}_iB} \frac{1}{2} {}_{ij}E. \quad (7.9)$$

The mechanical behavior of each truss in the lattice is linear elastic. The Young's modulus Y and the cross-sectional area of each truss A are independent of the deformation, i.e. they remain constant. The same Young's modulus and area are used for all trusses. Consequently, the energy stored in a linear elastic truss between points i and j , ${}_{ij}E$, can be expressed as follows:

$${}_{ij}E = \frac{1}{2} Y A {}_{ij}^{rel} L {}_{ij} \epsilon^2 = \frac{1}{2} Y A {}_{ij}^{rel} L \left(\frac{{}_{ij}^{def} L}{{}_{ij}^{rel} L} - 1 \right)^2, \quad (7.10)$$

where ${}_{ij}^{rel} L$ is the relaxed length of the truss between nodes i and j , i.e. the length of the interaction between points i and j that remains after the deformation is removed. The axial elastic strain acting on the relaxed length of the truss is represented by ${}_{ij} \epsilon$, which is expressed in terms of ${}_{ij}^{rel} L$ and ${}_{ij}^{def} L$, where ${}_{ij}^{def} L$ is the deformed length of the truss between nodes i and j .

Expressions for the relaxed length, ${}_{ij}^{rel}L$, and the deformed length, ${}_{ij}^{def}L$, are trivially extracted from the geometry, see Fig. 7.3. The internal history variables, \mathbf{z} , are defined as the sliding displacements that remain after the deformation has been removed (see Fig. 7.3). Consequently, $z = 4n$. Based on Fig. 7.3, the length of the interaction between nodes i and j that remains after deformation is removed, ${}_{ij}^{rel}L$, can be formulated according to:

$${}_{ij}^{rel}L = \|{}_j\vec{x} - {}_i\vec{x}\| + z_p - z_q, \quad (7.11)$$

where ${}_i\vec{x}$ is the original location vector of lattice point i and z_p and z_q are the p th and q th component of \mathbf{z} respectively. They correspond to the sliding displacements - after deformation is removed - of the truss (between nodes i and j), through nodes i and j respectively. Each sliding displacement is a scalar ($z_p \in \mathbb{R} \quad \forall p \in Z$), since sliding always takes place in the axial direction of the trusses in the lattice model (see Fig. 7.3). The length of the interaction between nodes i and j during deformation, ${}_{ij}^{def}L$, trivially reads:

$${}_{ij}^{def}L = \|{}_j\vec{x} + {}_j\vec{u} - {}_i\vec{x} - {}_i\vec{u}\|, \quad (7.12)$$

where ${}_i\vec{u}$ refers to the displacement vector of lattice point i (see Fig. 7.3).

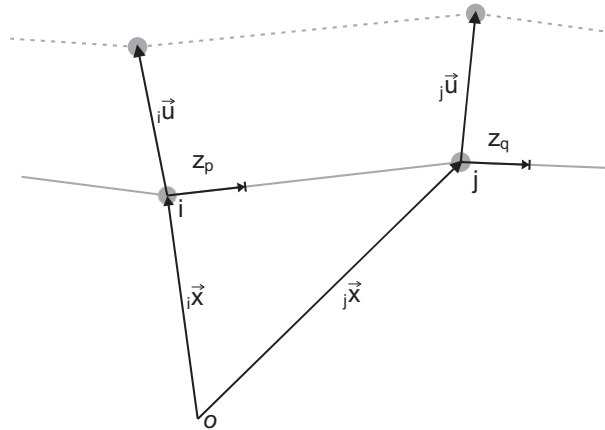


Figure 7.3: A truss between nodes i and j in the deformed configuration (dashed, grey) and in the relaxed configuration after sliding has occurred through both nodes (solid, grey).

By substitution of Eq. (7.11) & (7.12) in Eq. (7.10), the following expression is obtained that relates ${}_{ij}E$ - and also E via Eq. (7.9) - to \mathbf{u} and \mathbf{z} :

$${}_{ij}E = \frac{1}{2}YA(\|{}_j\vec{x} - {}_i\vec{x}\| + z_p - z_q) \left(\frac{\|{}_j\vec{x} + {}_j\vec{u} - {}_i\vec{x} - {}_i\vec{u}\|}{\|{}_j\vec{x} - {}_i\vec{x}\| + z_p - z_q} - 1 \right)^2. \quad (7.13)$$

At this point, the only missing ingredient of the thermodynamical formulation of the lattice model is the dissipation potential, Φ . In principal, the same dissipation potential of Chapter 3 is used, which is a straightforward Coulomb friction law. The disadvantage of this is the need of an active set strategy that determines which bonds fail, which depends on user-dependent implementation choices. In this chapter, a viscous friction law is therefore used. The following dissipation potential is proposed:

$$\Phi = \sum_{p=1}^z {}_p\Phi = \sum_{i=1}^n \sum_{p \in {}_iC} {}_p\Phi \quad (7.14)$$

with

$${}_p\Phi = {}^zF_p - {}^cF_p \frac{2}{\pi} \tanh(\kappa z_p) = 0, \quad (7.15)$$

where subset ${}_iC$ contains the bonds in lattice point i (${}_iC \subseteq Z$). Furthermore, cF_p is the p th component of ${}^c\mathbf{F}$, which is the column matrix of size $z \times 1$ containing the critical force values at which bond failure occurs as well as subsequent sliding. Parameter κ is a measure for the slope of the arc tangent function that approaches the Coulomb friction law. The value of $2/\pi$ normalizes the arc tangent. The viscous formulation in Eq. (7.15) implicitly assumes that all bonds are always active and the solution algorithm is free of user choices. Note furthermore that since $\text{sign}(z_p) = \text{sign}({}^cF_p \frac{2}{\pi} \tanh(\kappa z_p))$, the condition for the dissipation in Eq. (7.6) is met for each bond and thus also for the sum of all bonds.

The nonlocality of the presented dissipation formulation can be recognized in the term zF_p in Eq. (7.15) for bond p . This term (equal to $-\partial E/\partial z_p$) depends not only on the sliding displacement of this bond, z_p , but also on the sliding displacements of two bonds adjacent to bond p which are connected to the same fiber.

7.2.3 Solution procedure

The system of equations resulting from the thermodynamical formulation that need to be solved are the virtual-power statement in Eq. (7.1) and the dissipation constraints (see Eq. (7.15)). The governing equations can be expressed according to:

$$\dot{\mathbf{u}}^T \mathbf{F}(\mathbf{u}, \mathbf{z}) = \dot{\mathbf{u}}^T \mathbf{F} \quad \forall \dot{\mathbf{u}} \quad (7.16)$$

$${}^z \mathbf{F}(\mathbf{u}, \mathbf{z}) - \mathbf{M}(\mathbf{z}) {}^c \mathbf{F} = \mathbf{0}, \quad (7.17)$$

where \mathbf{M} is a diagonal matrix of size $z \times z$ ($4n \times 4n$) that contains the dissipation equation of each bond on one of its diagonal entries (see also Eq. (7.20) & (7.23) further on).

Eq. (7.16) & (7.17) can be solved simultaneously using a Newton-Raphson procedure, requiring a consistent linearization. This results in the following expressions:

$$\dot{\mathbf{u}}^T \left({}^{int} \mathbf{F}(*\mathbf{u}, *\mathbf{z}) + {}^{int} \mathbf{K}(*\mathbf{u}, *\mathbf{z}) d\mathbf{u} \right) = \dot{\mathbf{u}}^T \mathbf{F} \quad \forall \dot{\mathbf{u}} \quad (7.18)$$

$${}^z \mathbf{F}(*\mathbf{u}, *\mathbf{z}) - \mathbf{M}(*\mathbf{z}) {}^c \mathbf{F} + \left({}^z \mathbf{K}(*\mathbf{u}, *\mathbf{z}) - \frac{\partial \mathbf{M}(*\mathbf{z}) {}^c \mathbf{F}}{\partial \mathbf{z}} \right) d\mathbf{z} = \mathbf{0}, \quad (7.19)$$

where $*\mathbf{u}$ and $*\mathbf{z}$ are the displacement components and sliding displacements of the previous iteration respectively. The corrections on the displacement components and sliding displacements are represented by $d\mathbf{u}$ and $d\mathbf{z}$ respectively. The matrices ${}^{int} \mathbf{F}$, ${}^{int} \mathbf{K}$, ${}^z \mathbf{F}$, ${}^z \mathbf{K}$, \mathbf{M} and $\frac{\partial \mathbf{M} {}^c \mathbf{F}}{\partial \mathbf{z}}$ are assembled from the contributions of each node:

$$\begin{aligned} {}^{int} \mathbf{F} &= \sum_{i=1}^n {}^{int} \mathbf{F}_i & {}^{int} \mathbf{K} &= \sum_{i=1}^n {}^{int} \mathbf{K}_i \\ {}^z \mathbf{F} &= \sum_{i=1}^n {}^z \mathbf{F}_i & {}^z \mathbf{K} &= \sum_{i=1}^n {}^z \mathbf{K}_i \\ \mathbf{M} {}^c \mathbf{F} &= \sum_{i=1}^n \sum_{p \in {}_i C} p \mathbf{M} {}^c \mathbf{F} & \frac{\partial \mathbf{M} {}^c \mathbf{F}}{\partial \mathbf{z}} &= \sum_{i=1}^n \sum_{p \in {}_i C} \frac{\partial_p \mathbf{M} {}^c \mathbf{F}}{\partial \mathbf{z}}, \end{aligned} \quad (7.20)$$

with

$${}^i_{int}F_h = \frac{\partial {}^iE}{\partial u_h} \quad {}^i_{int}K_{hk} = \frac{\partial^2 {}^iE}{\partial u_h \partial u_k}, \quad (7.21)$$

where h and k run over all $2n$ components of \mathbf{u} and with

$${}^zF_p = \frac{-\partial {}^iE}{\partial z_p} \quad {}^zK_{pq} = \frac{-\partial^2 {}^iE}{\partial z_p \partial z_q}, \quad (7.22)$$

where p and q run over all $4n$ components of \mathbf{z} and with

$${}_pM_{pp} = \frac{2}{\pi} \tanh(\kappa z_p) \quad \left(\frac{\partial {}_p\mathbf{M}^c\mathbf{F}}{\partial \mathbf{z}} \right)_{pp} = \frac{\partial ({}_p\mathbf{M}^c\mathbf{F})_p}{\partial z_p}. \quad (7.23)$$

For clarity the external forces are left out of consideration.

Dirichlet boundary conditions are used for \mathbf{u} and \mathbf{z} (required for the nonlocal plastic formulation). Neumann boundary conditions are incorporated in ${}^{ext}\mathbf{F}$. Even though possible, no Neumann boundary conditions are adopted for the nonlocal plastic formulation. To resolve the viscous terms in \mathbf{M} and $\partial \mathbf{M}^c\mathbf{F} / \partial \mathbf{z}$ in Eq. (7.19), a backward Euler scheme is used, since implicit schemes are more stable than explicit schemes.

The procedure to simultaneously solve the governing equations in Eq. (7.18) & (7.19) is computationally inefficient for lattice models with a large number of n lattice nodes. The reason for this is twofold. First, the total system contains $6n$ DOFs, of which $2n$ DOFs are associated with the displacement components and $4n$ DOFs with the sliding displacements. This is a substantial number since n is significant for large-scale lattice computations. Large systems are inefficient to solve, even if Cholesky decomposition or an iterative solver is used. Moreover, the effort associated with the construction of the governing equations in Eq. (7.18) & (7.19) is significant, since all n lattice points have to be visited according to the formulations in Eq. (7.20).

7.3 Virtual-power-based QC method with a mixed formulation

The QC method is originally developed for large-scale atomistic lattice computations [114], aiming to remedy the two aforementioned causes of high computational cost. The QC method uses two reduction steps for this (see Fig. 7.4). First, the number of displacements is reduced by means of interpolation (see the center image in Fig. 7.4). Second, the potential energy, or here the virtual-power, (i.e. the governing equations) is approximated by sampling the potential energy, or the virtual-power, of a small number of sampling points, instead of determining it exactly by visiting all lattice points (see the second step in Fig. 7.4). In both reduction steps an error may be introduced that influences the potential energy, or virtual-power, and thus the obtained solution. If both steps are performed adequately however, these errors are negligibly small.

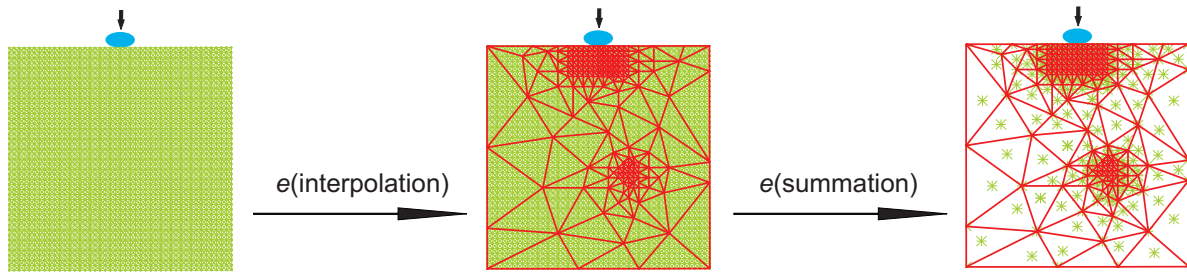


Figure 7.4: Schematic representation of the two reduction steps in the QC method. In the left image, the full lattice model is shown. In the center image, a triangulation is superimposed to the lattice model and in the right image a small number of lattice points is depicted, which are used to sample the potential energy, or virtual-power (i.e. the governing equations). During both reduction steps an error, e , may be introduced.

7.3.1 Interpolation

Interpolation in QC methodologies applies to lattice models by the use of interpolation triangles (see the center image in Fig. 7.4). The interpolation triangles are spanned by the same interpolation functions as used in finite element (FE) methods. Consequently, well established techniques developed for FE methods, e.g. adaptive meshing, can be used in QC methodologies. In general, linear interpolation triangles are used in QC frameworks. The triangle nodes of the interpolation triangles coincide with a limited number of lattice points. These lattice points represent the displacement of the entire lattice and are often referred to as reppoints or reppnodes (or repatoms if used for atomistic lattice models). The remaining lattice points are interpolated between the reppoints. Consequently, their displacements entirely depend on the displacements of the reppoints.

The advantage of using interpolation triangles is that in regions in which small displacement fluctuations are expected, the reppoints can be chosen far away from each other. This results in relatively large triangles in which a large number of lattice nodes are constrained and a large reduction of displacements takes place. In regions in which large displacement fluctuations are expected, all the lattice points are selected as reppoints (triangle nodes), i.e. the exact lattice model is captured in these regions. In Fig. 7.4, two fully resolved regions are present. One is located in the region where an indenter makes contact with the lattice and the other is located near a lattice defect (e.g. a failed truss).

The r reppoints, stored in index set R , are selected from set N containing all n lattice points, i.e. $R \subseteq N$. To achieve a substantial computational gain, the number of reppoints must be significantly smaller than the total number of lattice points ($r \ll n$). The displacements of all lattice points, \mathbf{u} , can be expressed as a function of the displacements of the reppoints, ${}^r\mathbf{u}$, as follows:

$$\mathbf{u} = {}^u\Psi {}^r\mathbf{u}, \quad (7.24)$$

where ${}^u\Psi$ is the displacement condensation matrix with size $2n \times 2r$ for two-dimensional lattices. It contains the interpolation functions evaluated at the locations of all lattice points.

So far, most QC frameworks are used for (conservative) atomistic lattice models [11,36,64,82,114] including only kinematic variables (\mathbf{u}). Here, non-conservative lattice models are considered that include internal history variables (\mathbf{z}) associated with dissipation. In case the dissipation mechanisms are local, it suffices to use internal history variables that are constant in (the internal parts of) each interpolation triangle. Consequently, they are not (C_0 -)continuous across interpolation triangles, whereas this is the case for the condensed displacements. This is shown in previous work on the virtual-power-based QC method [13] for elastoplastic trusses.

In case of a lattice model with bond failure and subsequent frictional sliding, the dissipation mechanisms are nonlocal, because the sliding displacements directly depend on each other. This can be observed in Eq. (7.17). Since nonlocal dissipation mechanisms exist here, the internal history variables depend on each other and are not constant within an interpolation triangle. To allow the internal history variables (\mathbf{z}) to vary within an interpolation triangle, they are interpolated as well. The condensed sliding displacement can be expressed in terms of the sliding displacements of the reppoints according to:

$$\mathbf{z} = {}^z\Psi {}^r\mathbf{z}, \quad (7.25)$$

where ${}^z\Psi$ is the sliding displacement condensation matrix with size $z \times 4r$ ($4n \times 4r$) and ${}^r\mathbf{z}$ is the column matrix of size $4r \times 1$ containing the sliding displacements of the reppoints. The same interpolation functions evaluated at the locations of all lattice points are present in ${}^z\Psi$. As a result, the interpolated internal history variables are also (C_0 -)continuous of the interpolation triangles. Although the size of ${}^z\Psi$ differs from the size of ${}^u\Psi$, they both contain the same interpolation function evaluations. Consequently, almost no additional effort is involved in the construction of both ${}^z\Psi$ and ${}^u\Psi$, compared to the construction of ${}^u\Psi$ only.

An important advantage of using the same interpolation for the internal history variables is the fact that no complex interplay between two types of interpolations occurs. Such an interplay may have a substantial influence on the summation rules. Because the same interpolation is used, previously proposed summation rules can still be used, as explained below.

If Eq. (7.24) & (7.25) are inserted in Eq. (7.18) & (7.19), the following formulations for the condensed governing equations are obtained:

$${}^r \dot{\mathbf{u}}^T \left({}^u \Psi^T \mathbf{int} \mathbf{F} + {}^u \Psi^T \mathbf{int} \mathbf{K} {}^u \Psi d^r \mathbf{u} \right) = {}^r \dot{\mathbf{u}}^T {}^u \Psi^T \mathbf{ext} \mathbf{F} \quad \forall {}^r \dot{\mathbf{u}} \quad (7.26)$$

$${}^z \Psi^T {}^z \mathbf{F} - {}^z \Psi^T \mathbf{M}^c \mathbf{F} + \left({}^z \Psi^T {}^z \mathbf{K} {}^z \Psi - {}^z \Psi^T \frac{\partial \mathbf{M}^c \mathbf{F}}{\partial \mathbf{z}} {}^z \Psi \right) d^r \mathbf{z} = \mathbf{0}. \quad (7.27)$$

Note that the term ${}^z \Psi^T$ in the terms ${}^z \Psi^T {}^z \mathbf{F}$ and ${}^z \Psi^T {}^z \mathbf{K} {}^z \Psi$ in Eq. (7.27) originates from substitution of Eq. (7.25) in Eq. (7.6). Furthermore, to ensure that the equality constraints in the direct lattice model are similar to those for the condensed lattice model, ${}^z \Psi^T$ is introduced in Eq. (7.27) in the terms ${}^z \Psi^T \mathbf{M}^c \mathbf{F}$ and ${}^z \Psi^T \frac{\partial \mathbf{M}^c \mathbf{F}}{\partial \mathbf{z}} {}^z \Psi$.

The terms ${}^u \Psi^T \mathbf{int} \mathbf{F}$, ${}^u \Psi^T \mathbf{int} \mathbf{K} {}^u \Psi$, ${}^z \Psi^T {}^z \mathbf{F}$, ${}^z \Psi^T {}^z \mathbf{K} {}^z \Psi$, ${}^z \Psi^T \mathbf{M}^c \mathbf{F}$ and ${}^z \Psi^T \frac{\partial \mathbf{M}^c \mathbf{F}}{\partial \mathbf{z}} {}^z \Psi$ represent the condensed counterparts of the corresponding expressions in Eq. (7.20). Like their uncondensed counterparts, they can be assembled by contributions of each node:

$$\begin{aligned} {}^{int,r} \mathbf{F} &= \sum_{i=1}^n {}^u \Psi_i^T \mathbf{int} \mathbf{F} & {}^{int,r} \mathbf{K} &= \sum_{i=1}^n {}^u \Psi_i^T \mathbf{int} \mathbf{K} {}^u \Psi \\ {}^{z,r} \mathbf{F} &= \sum_{i=1}^n {}^z \Psi_i^T {}^z \mathbf{F} & {}^{z,r} \mathbf{K} &= \sum_{i=1}^n {}^z \Psi_i^T {}^z \mathbf{K} {}^z \Psi \\ {}^r \mathbf{M}^c \mathbf{F} &= \sum_{i=1}^n {}^z \Psi_i^T \sum_{p \in {}_i C} {}^p \mathbf{M}^c \mathbf{F} \\ \frac{\partial {}^r \mathbf{M}^c \mathbf{F}}{\partial {}^r \mathbf{z}} &= \sum_{i=1}^n {}^z \Psi_i^T \sum_{p \in {}_i C} \frac{\partial {}^p \mathbf{M}^c \mathbf{F}}{\partial \mathbf{z}} {}^z \Psi, \end{aligned} \quad (7.28)$$

where the superscript r refers to the condensed counterparts of the force columns and stiffness matrices in Eq. (7.20).

To ensure that the virtual-power of the condensed system adequately approximates that of the original system, only little difference in the virtual-power of the lattice points may exist. This entails that large interpolation triangles (i.e. coarse domains) can only be used in regions with small displacement fluctuations and (in contrast to

regular QC methodologies) with small sliding displacement fluctuations. Indeed, linear interpolation enforces that the virtual-power of a lattice point in a large triangle is identical to the value in its neighboring point (i.e. ${}^r \dot{\mathbf{u}}^T u \Psi^T \frac{\partial_i E}{\partial \mathbf{u}} = {}^r \dot{\mathbf{u}}^T u \Psi^T \frac{\partial_{i+1} E}{\partial \mathbf{u}}$). This is only allowed if the virtual-power of these lattice points is nearly equal in the direct lattice model (i.e. $\dot{\mathbf{u}}^T \frac{\partial_i E}{\partial \mathbf{u}} \approx \dot{\mathbf{u}}^T \frac{\partial_{i+1} E}{\partial \mathbf{u}}$).

By means of interpolation the number of governing equations is reduced from $6n$ to $6r$. This makes the condensed system significantly more efficient to solve (assuming that $r \ll n$). However, still all n lattice points need to be visited to construct the condensed governing equations in Eq. (7.26) & (7.27) compromising the computational cost.

7.3.2 Summation

The second step proposed in the QC method aims to reduce of the computational effort to construct the governing equations. Rather than visiting all n lattice points to construct the governing equations according to Eq. (7.28), only a small number of s sampling points are selected to sample the virtual-power and thus the the governing equations (see the right step in Fig. 7.4). This is called summation in QC terminology. The sampling points, stored in subset S , are selected from all lattice points (ie. $S \subseteq N$).

As a result of summation, the expressions for the virtual-power and equality constraints remain the same as in Eq. (7.26) & (7.27). The construction of the force columns and stiffness matrices changes however. They are now expressed according to:

$$\begin{aligned}
 {}^{int,rs} \mathbf{F} &= \sum_{i \in S} {}_i w^u \Psi^T {}_i^{int} \mathbf{F} & {}^{int,rs} \mathbf{K} &= \sum_{i \in S} {}_i w^u \Psi^T {}_i^{int} \mathbf{K} {}_i^u \Psi \\
 {}^{z,rs} \mathbf{F} &= \sum_{i \in S} {}_i w^z \Psi^T {}_i^z \mathbf{F} & {}^{z,rs} \mathbf{K} &= \sum_{i \in S} {}_i w^z \Psi^T {}_i^z \mathbf{K} {}_i^z \Psi \\
 {}^{rs} \mathbf{M}^c \mathbf{F} &= \sum_{i \in S} {}_i w^z \Psi^T \sum_{p \in {}_i C} {}_p \mathbf{M}^c \mathbf{F} \\
 \frac{\partial {}^{rs} \mathbf{M}^c \mathbf{F}}{\partial {}^r \mathbf{z}} &= \sum_{i \in S} {}_i w^z \Psi^T \sum_{p \in {}_i C} \frac{\partial {}_p \mathbf{M}^c \mathbf{F}}{\partial \mathbf{z}} {}_i^z \Psi,
 \end{aligned} \tag{7.29}$$

where ${}_i w$ is the weight factor of sampling point i , which equals the number of lattice points that are represented by sampling point i (including sampling point i itself). The superscript rs refers to the summed, condensed counterparts of the force columns and stiffness matrices. Furthermore, the weight factor ${}_i w$ is introduced in the formulations of

${}^{rs}\mathbf{M}^c\mathbf{F}$ and $\frac{\partial {}^{rs}\mathbf{M}^c\mathbf{F}}{\partial r\mathbf{z}}$ to ensure that in the summed, condensed system the same amount of dissipation occurs as in the condensed system (see Eq. (7.26) & (7.27)).

Summation in the QC method is only computationally beneficial if the number of sampling points is substantially smaller than the number of lattice points in the full lattice model ($s \ll n$). Furthermore, to ensure a sufficient accuracy of the QC method (i.e. to ensure that the summed, condensed governing equations are a good representation of the condensed governing equations), sampling points must be selected such that the virtual-power of the sampling points approximates that of the lattice points they represent. This entails that if for two neighboring lattice points in a large triangle $r\dot{\mathbf{u}}^T u \Psi^T \frac{\partial {}_i E_i}{\partial \mathbf{u}} \approx r\dot{\mathbf{u}}^T u \Psi^T \frac{\partial {}_{i+1} E}{\partial \mathbf{u}}$, then one of them can be used to sample the virtual-power of the other lattice point.

The way in which the sampling points are selected, the computation of their weight factors and the manner in which their potential energy, or here virtual-power, are determined (locally or nonlocally) are established in so-called summation rules. Two general classes of summation rules can be distinguished. Local-nonlocal summation rules [82,108,109,114,115] compute the potential energy (here virtual-power) of sampling points in coarse domains in a local fashion. In the fully resolved region the sampling points are treated in a nonlocal fashion, so that the exact lattice model is captured in these regions. Local-nonlocal summation rules come with internal interfaces between coarse and fully resolved domains. Corrective procedures have been formulated for the interfaces [108,109], involving additional assumptions.

Nonlocal summation rules treat all sampling points in a nonlocal fashion [9,11,36,43,64]. As a consequence, no internal interface occurs between coarse domains and fully resolved domains. Therefore, no interface corrections are required. The relatively large lookup tables that are involved can be considered as a disadvantage, but the fact that no corrective procedures are required (and updated during remeshing) is a computational advantage. More information on summation rules can be found for instance in [36,83] and [11].

The summation rule employed in this chapter is the central summation rule [11], because it uses a small number of sampling points ($s \ll n$) resulting in a high efficiency. Furthermore, since all sampling points are treated in a nonlocal fashion, no internal interface occurs. In the central summation rule, only one lattice point near the incenter of each triangle is selected as an internal sampling point representing all lattice points inside the triangle and half of those on triangle edges (this number determines its corresponding weight factor, ${}_i w \geq 1$), see Fig. 7.5. The reppoints are selected as discrete sampling points, i.e. they only sample themselves (${}_i w = 1$). As a result, the exact lattice model is recovered in the fully resolved regions as desired. Lattice points in triangles in which no internal lattice points occurs, i.e. all lattice points of a triangle are located on triangle edges, are selected as discrete sampling points as well (see Fig. 7.5). Hence, for the central summation rule, it holds that $R \subseteq S \subseteq N$.

The central summation rule is appropriate to sample the virtual-power in the QC framework presented here, because its fundamental principle also holds for the mixed formulation proposed here. The ansatz of the central summation rule is that, except near

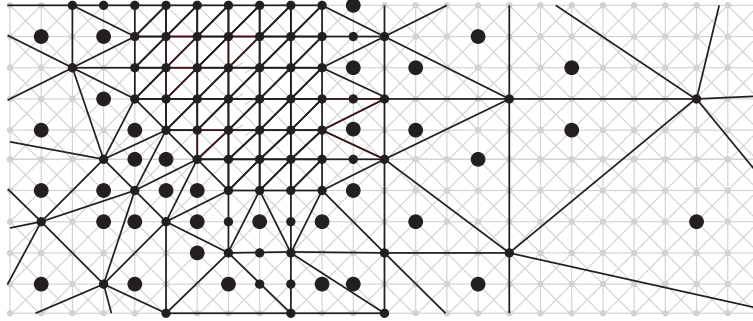


Figure 7.5: The central summation rule applied to the lattice model (grey) with a triangulation (black) that includes a fully resolved region around three missing horizontal interactions. The discrete sampling points (with $iw = 1$) are shown as black dots and internal sampling points (with $iw \geq 1$) as large black dots.

triangle edges [9,11], the potential energies of all lattice points within an interpolation triangle are equal, because each type of interaction (e.g. the horizontal interactions) deforms the same inside a triangle due to the linear interpolation used. Since in the method proposed here, the same linear interpolation is used for the displacements as well as the sliding displacements, each type of interaction fully inside a triangle deforms in the same way, which is the main principle of the central summation rule.

7.4 Performance of the QC framework

Two numerical test cases are considered to illustrate the computational gain and accuracy that can be achieved with the proposed QC framework for bond failure and frictional fiber sliding. Both numerical cases have a true multiscale character since local mesoscale lattice defects (a small number of initially missing trusses) are present in an otherwise perfectly regular large-scale network. The numerical examples are formulated in a dimensionless setting.

7.4.1 Problem description

In both numerical examples the proposed QC method is used for a lattice model containing 99×99 unit cells (see Fig. 7.6). The considered lattice model is based on the equidistant X-braced lattice model with linear elastic trusses as formulated in Section 7.2, whereby only horizontal trusses (fibers) can slide through lattice points. The horizontal and vertical lengths of a unit cell are set to 1 (lattice spacing). Diagonal trusses are thus of length $\sqrt{2}$. In the lower center of the model, 25 horizontal trusses are missing, starting from the bottom of the model (see Fig. 7.6). These 25 horizontal fibers can thus be regarded as initially broken. The fiber (truss) overlengths at these points are so large that no pull-out occurs in the computations.

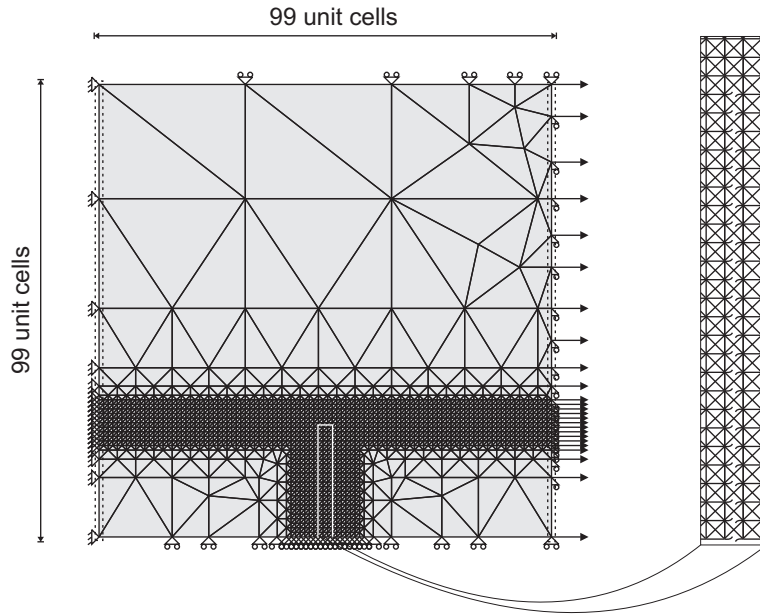


Figure 7.6: Schematic representation of the numerical examples including the adopted triangulation. The boundary conditions on the sliding displacements are shown by dashed rectangles at the left and right edges. The zoom on the right shows the central vertical row with missing trusses without interpolation triangles. Diagonal fiber segments (trusses) are still present.

All bond strengths (and thus also all critical friction forces) are set to 1. This means that all components of ${}^c\mathbf{F}$ in Eq. (7.15) & (7.19) equal 1. Furthermore, the parameter defining the arc tangent function in Eq. (7.15), κ , is set to 100. The stiffness per unit of length of all trusses (YA in Eq. (7.13)) is set to 10^6 in the first example and to 10^3 in the second example. In this way, sliding displacements in a large number of points are expected in the first example and only a few points are expected to slide in the second example.

The boundary conditions applied to the model are shown in Fig. 7.6 as well. In the QC computations the boundary conditions are applied to reppoints and in the direct lattice computations they are applied to lattice points. It may be clear that the points on the left edge are fixed in horizontal (x-)direction and vertical (y-)direction (see Fig. 7.6). The points on the top, bottom and right edge are fixed in y-direction. The points on the right edge are displaced in horizontal direction. Furthermore, the sliding displacements of the points on the left and right edges of the model are constrained.

7.4.2 Computational efficiency

The computational efficiency of a QC framework directly depends on the triangulation used. A fully resolved region is used in the domain in which sliding displacement fluctuations are expected. This is the case close to the removed trusses, where large

sliding displacement fluctuations are triggered, since the stiffness of the trusses is large compared to the bond strength. Furthermore, it is expected that negligible sliding displacements occur in the region above the centrally removed trusses. Therefore, a discrete step in the sliding displacements (large sliding displacement fluctuations) is expected over the entire width of the model at a height of 24 lattice spacings. Since this cannot be accurately resolved by large interpolation triangles, this region is also fully resolved.

In the direct lattice computation 10,000 lattice points are involved, resulting in 30,000 DOFs, of which 20,000 DOFs for the displacement components and 10,000 for the horizontal sliding displacements. In the triangulation in Fig. 7.6, a relatively large number of reppoints is present because of the relatively large fully resolved domain. Accordingly, also a large number of sampling points is involved, since every reppoint is a discrete sampling point as well ($i_w = 1$). In total 1,655 reppoints are present in the triangulation of Fig. 7.6 and 2,140 sampling points (see also ahead to the right image in Fig. 7.7). Hence, the computational gain obtained by the QC framework is a factor of 6 in terms of DOFs (associated with the effort to solve the governing equations) and a factor of 5 in terms of sampling points (related to the computational cost to construct the governing equations). The expected computational gain is clearly significant, even though a large part of the model is fully resolved.

7.4.3 Accuracy

The sliding displacements predicted by the direct lattice computation and QC computation are presented in Fig. 7.7 for an applied macroscopic horizontal strain of 1.5% (corresponding to an applied horizontal displacement of 1.485 in terms of lattice spacings). The stiffness per unit of length of each truss equals 10^6 . Significant sliding displacements occur in the domains next to the vertical row of missing trusses. No sliding displacements are present above this domain.

Fig. 7.7 reveals that the sliding displacements predicted by the QC computation with the triangulation shown in Fig. 7.6 are similar to those predicted by the direct lattice computation. This includes the sliding near the missing trusses and the discrete jump across a horizontal line above them. The accurate solution essentially results from the use of a fully resolved region where needed.

The sliding displacements predicted by the QC computation in the coarse domain on the left and right of the vertical row with missing trusses are adequately captured (see Fig. 7.7). Note that if the sliding displacements would not be interpolated and kept constant in each triangle (as done for the dissipation variables by [13]), the sliding displacement field would not be captured accurately. The fact that the sliding displacements are accurately resolved in the coarse domain, is emphasized by the left diagram in Fig. 7.8, in which the sliding displacements computed by the direct lattice computation and QC computation are shown along a horizontal line at a height of 13 lattice spacings.

In the right plot of Fig. 7.8 the sliding displacements are shown to be uniform for both

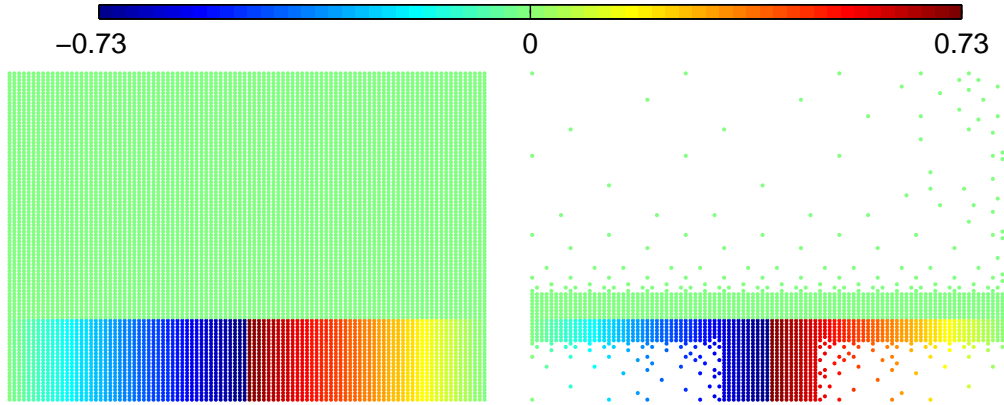


Figure 7.7: Horizontal sliding displacements in the lattice - stiffness per unit of length of each truss is 10^6 . Left: direct lattice computation, right: QC computation.

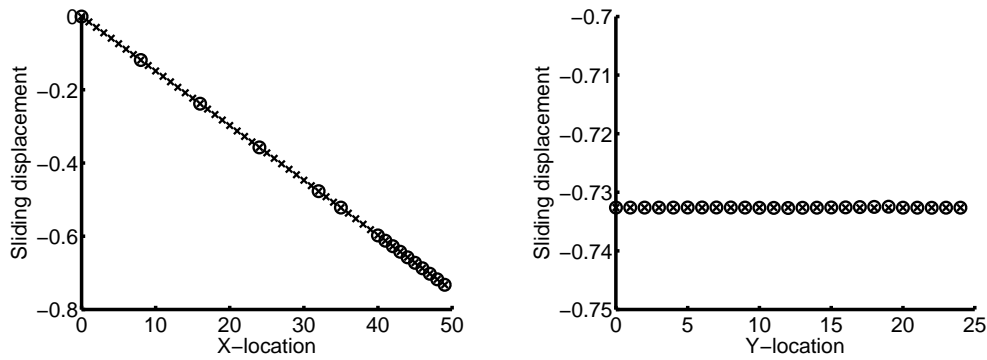


Figure 7.8: Sliding displacements in the lattice (stiffness per unit of length of each truss 10^6) computed by the direct lattice computation (x) and the QC computation (o) along a horizontal line (left) at a height of 13 lattice spacings, starting from the left edge (at $x = 0$) and ending at the vertical row with missing trusses (at $x = 49$) and (right) along a vertical line at a distance of 49 lattice spacings from the left edge of the model, just to the left of the missing trusses (starting at $y = 0$ and ending at $y = 24$).

computations along a vertical line at a distance of 49 lattice spacings from the left edge of the model. This vertical line is thus (almost) in the center of the fully resolved domain. These are the relevant sliding displacements, because the fully resolved domains are typically the domains of interest in QC frameworks. Indeed, local mesoscale phenomena are typically to be enclosed in fully resolved domains in a QC methodology.

The accuracy of the sliding displacements computed by the QC computation over this vertical line is investigated in more detail. An average local relative error, $^{rel}\bar{\epsilon}$, is introduced according to:

$${}^{rel}\bar{\epsilon} = \frac{1}{|D|} \sum_{i \in D} \left| \frac{{}_i^{qc}v - {}_i^{dlc}v}{{}_i^{dlc}v} \right| \cdot 100\% \quad (7.30)$$

where ${}_i v$ represents the variable of interest (i.e. the sliding displacement) in point i and D is the subset that contains the considered lattice points ($D \subseteq R \subseteq S \subseteq N$). The superscript qc refers to the solution of the QC framework and the superscript dlc refers to the solution of the direct lattice computation. The resulting average local relative error is only 0.004% for the sliding displacements along the considered vertical line. The accuracy of the mixed formulation framework is excellent for these sliding displacements with the adopted model parameters.

In Fig. 7.9 the relative horizontal displacements of the lattice points are presented (in terms of lattice spacings). The horizontal displacements relative to the defect free configuration, ${}^{rel,x}u$, are determined according to:

$${}^{rel,x}u({}_i\vec{x}) = {}^x u({}_i\vec{x}) - {}^{xx}E {}_i x, \quad (7.31)$$

where ${}^{xx}E$ is the applied overall strain in x-direction and ${}_i x$ is the horizontal component of the position vector of point i .

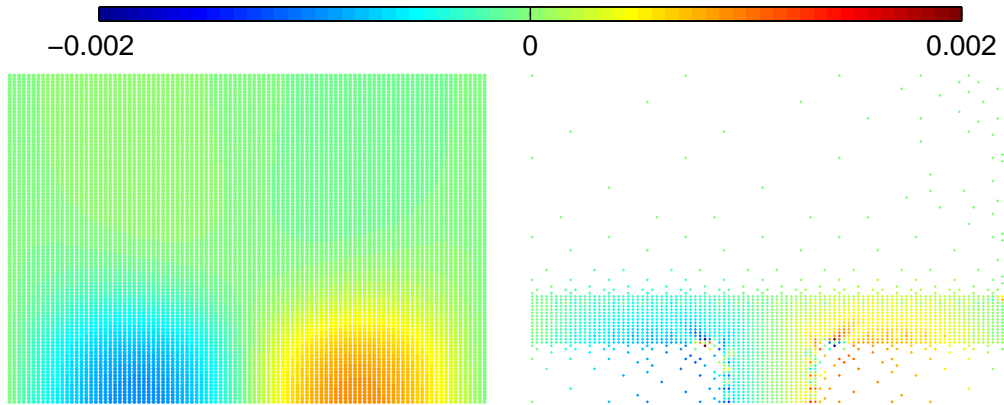


Figure 7.9: The relative horizontal displacements in the lattice (stiffness per unit of length of each truss 10^6) predicted by the direct lattice computation (left) and the QC computation (right).

Fig. 7.9 reveals that the minimum and maximum relative horizontal displacements are located between the center and the edges of the model and not in the center as one might expect. This results from the fact that sliding occurs in all lattice points associated

with the first 25 horizontal fibers, starting from the bottom of the model. The QC computation is able to capture this relative displacement field relatively well, but not exactly, as can be seen on the right in Fig. 7.9. These displacements are resolved in relatively large triangles and they do not vary exactly linearly within these triangles. The accuracy of the displacements is thus not as good as that of the sliding displacements with this triangulation. Adaptivity - i.e. remeshing of these domains - can be used to improve the accuracy of the relative displacement field, if these local fluctuations are to be resolved more accurately.

The predicted sliding displacements for the second case, in which the stiffness per unit of length is 10^3 , are shown in Fig. 7.10 for the same applied macroscopic horizontal strain of 1.5%. Sliding displacements occur only in the lattice points in and near the vertical row of missing trusses due to the substantially smaller stiffness of the trusses. With a stiffness that is 1000 times smaller than in the first example, significantly larger truss deformations - requiring substantially larger macroscopic horizontal strains - are required to obtain substantial sliding in a significant amount of lattice points.

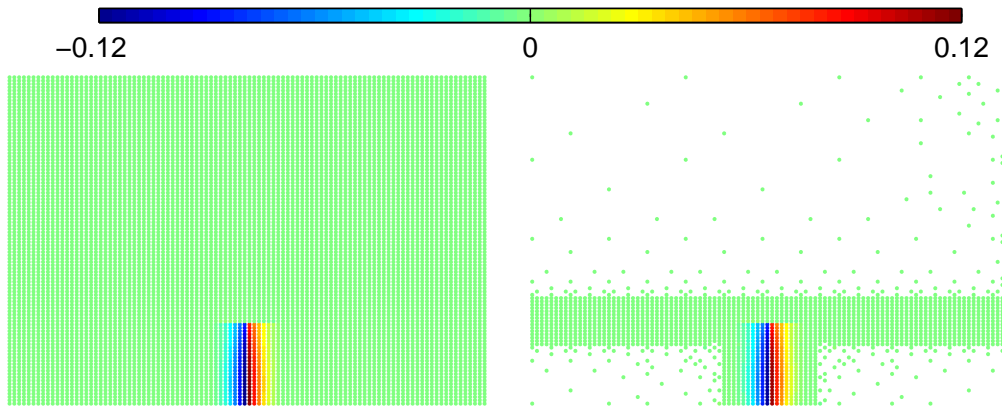


Figure 7.10: Horizontal sliding displacements in the lattice (stiffness per unit of length of each truss 10^3) predicted by the direct lattice computation (left) and the QC computation (right).

The localization of sliding displacements is emphasized in Fig. 7.11, in which the sliding displacements are shown along the horizontal line at a height of 13 lattice spacings and along the vertical line at a distance of 49 lattice spacings from the left edge. In the right plot of Fig. 7.11, it can be noticed that the sliding displacements are non-uniform over the height. This is caused by the smaller stiffness of the trusses that results in less uniform deformation.

If the sliding displacements along the vertical line predicted by both computations are compared, some small discrepancies persist (see Fig. 7.11). The average local relative error of the sliding displacements along this vertical line, computed by Eq. (7.30), is larger than in the first example; namely 2.3% with a maximum local relative error of

5.6% occurring in the lattice point at $y = 0$. This is however still quite satisfactory in terms of accuracy.

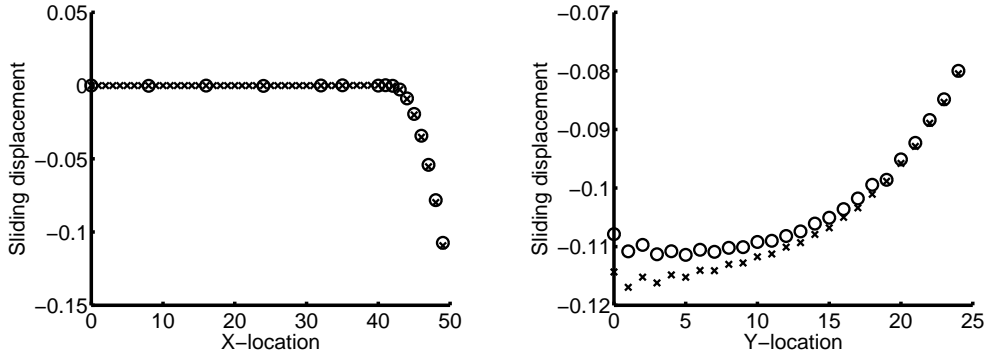


Figure 7.11: The sliding displacements in the lattice (stiffness per unit of length of each truss 10^3) computed by the direct lattice computation (x) and the QC computation (o) along a horizontal line (left) at a height of 13 lattice spacings, starting from the left edge (at $x = 0$) and ending at the initially missing trusses (at $x = 49$), and (right) along a vertical line at a distance of 49 lattice spacings from the left edge of the model, i.e. to the left of the missing trusses (starting at $y = 0$ and ending at $y = 24$).

It is remarkable that the error in the sliding displacements is larger for the second example, in which non-zero sliding displacements only seem to be present in the fully resolved domain, whereas in the first example, non-zero sliding displacements are clearly present in the fully resolved region and coarse domain. This is due to the small sliding displacements that are present in coarse domains in the second example. The left diagram in Fig. 7.11 reveals no sliding displacements in the solution of the direct lattice computation. However, because the dry friction is modeled continuously in this framework, small sliding displacements are also present here, influencing those in the fully resolved domain. Separate computations (not shown here) indicate that these sliding displacements are not linearly distributed in space. Consequently, the mixed formulation framework in which the sliding displacements are linearly interpolated is not able to fully capture these non-linear small sliding displacements. This explains why the accuracy in the fully resolved region in the second example is less good compared to the first example, even though sliding displacements are only noticeable in the fully resolved domain in the second example.

The relative horizontal displacements, computed using Eq. (7.30), for the second example at an applied macroscopic horizontal strain of 1.5% are shown in Fig. 7.12. In contrast to the first example, they clearly show their minimum and maximum values close the vertical row with missing trusses. This is caused by the fact that (significant) sliding is only present in this domain. Since the most pronounced relative horizontal displacements are present in the fully resolved domain they are generally better cap-

tured by the QC model than in the first example. However, non-zero relative horizontal displacements also occur in coarse domains, which are not that accurately captured. Here as well, adaptive remeshing can be used if such local details are of interest.

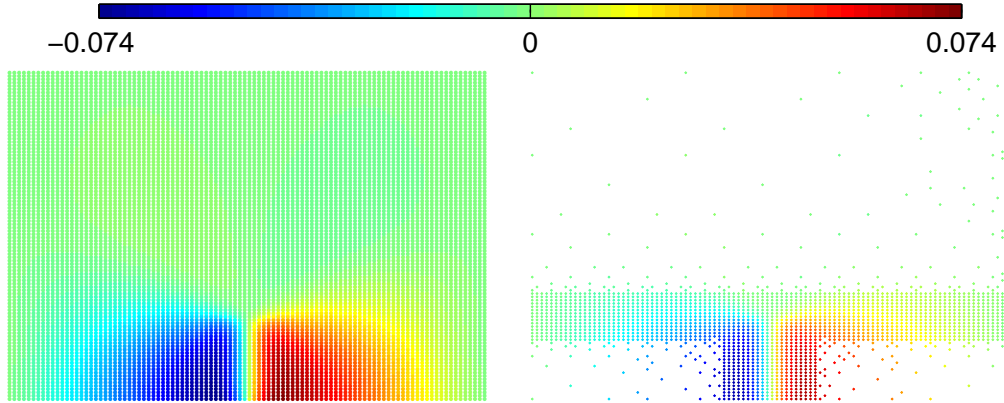


Figure 7.12: The relative horizontal displacements in the lattice (stiffness per unit of length of each truss 10^3) predicted by the direct lattice computation (left) and the QC computation (right).

7.5 Conclusion

Lattice models employing trusses and beams can straightforwardly and accurately describe mechanical mesoscale phenomena of fibrous materials. Bond failure, including subsequent frictional fiber sliding, is one of these mesoscale phenomena that are important for the (macroscale) failure behavior of several fibrous materials. The disadvantage of lattice models is the computational cost for macroscale (the engineering scale) computations, because of their solution and construction at the mesoscale. Different multiscale techniques can be used to decrease the computational effort of lattice models but they all have their specific scope. In this chapter, the quasicontinuum (QC) method is adopted for lattice models with bond failure and subsequent fiber sliding. The QC method

- allows the accurate incorporation of the mesoscopic lattice model in regions of interest,
- completely relies on the underlying discrete lattice model and not on a homogenized continuum description that is difficult to obtain for dissipative fibrous materials
- does not require a coupling or handshaking procedure (in the proposed framework).

QC methods are based on (i) interpolation of the lattice displacements to decrease the number of degrees of freedom and (ii) summation rules in which a small number of lattice points is sampled to approximate the governing equations. Most QC methods are based on energy minimization and cannot deal with dissipative mechanisms, which are intrinsic to lattice models with bond failure and fiber sliding. To this end, the virtual-power-based QC method proposed in the previous chapter is exploited that can deal with dissipative (non-conservative) lattice models. In this chapter, the virtual-power-based QC framework is equipped with a mixed formulation, because bond failure and fiber sliding are intrinsically nonlocal dissipative mechanisms and the previously introduced virtual-power-based QC framework can only deal with local dissipative mechanisms.

The internal dissipation variables (the sliding displacements) are interpolated in the proposed methodology, next to the kinematic variables (the regular displacements), ensuring their direct mutual coupling. The same interpolation triangles are used for this, which has the advantage that previously proposed summation rules remain applicable. Consequently, the new QC framework with the mixed formulation has a similar efficiency and accuracy as previously defined QC methodologies. This is shown for the predicted sliding displacements in two multiscale test cases in which local mesoscale defects are included in an otherwise perfectly regular large-scale lattice.

Chapter eight

Conclusions and outlook

The aim of this thesis was to develop a computational multiscale tool that can predict the mechanical behavior of fibrous materials. Discrete network models, in particular those with a periodic structure (i.e. lattice models), have been used in this thesis, because they are able to capture mechanical mesoscale phenomena of fibrous materials as a result of their discrete mesostructure. The discrete elements of mesoscale network models, such as trusses or beams, represent fiber and yarn segments, whereas the nodes represent interfiber bonds. The proposed computational tool had to be multiscale, since discrete network models are constructed at the mesoscale, making macroscale, physically relevant computations expensive. The quasicontinuum (QC) method, originally proposed for discrete atomistic computations [114], is adopted to reduce the computational cost of discrete models of fibrous materials in macroscale computations.

The QC method, in contrast to other multiscale approaches, such as computational homogenization schemes and approaches in which discrete models are coupled to continuum descriptions, combines the following advantages:

- the mesoscopic discrete model can be used in regions of interest,
- it only requires the discrete model and no accompanying continuum description and
- coarse domains can be connected to fully resolved domains, in which the mesoscopic discrete model is used, without a coupling or handshaking procedure.

8.1 Summary of the results

In the first two chapters of this thesis, two lattice models of fibrous materials are formulated. The first is constructed for woven fabrics, such as electronic textile. Its formulation guarantees a separate experimental identification of the three families of discrete

elements by three tensile tests. The predicted mechanical responses are not only significantly more accurate than those predicted with the use of continuum descriptions, but the physical meaning of the material parameters is clearer and large rotations are naturally incorporated in the lattice model [37,39,96,117,118]. The second lattice model describes bond failure and subsequent fiber sliding in fibrous materials. It is formulated in a thermodynamical setting, that allows the methodical investigation of the influence of mesoscale parameters, such as the fiber length and the bond strength. The investigation of such mesoscale parameters is not trivially performed with continuum models. The resulting lattice model is a discrete non-local elastoplastic description.

The computational cost of lattice computations is reduced by the QC method in this thesis. This method uses interpolation to reduce the number of degrees of freedom (DOFs) and a small selection of lattice points to estimate the governing equations, instead of determining them exactly by regarding all lattice points. Different selection procedures of sampling points (i.e. summation rules) have been proposed in literature [36,43,64,83,108,109,114], but in this thesis two new rules are formulated that are based on a clear comprehension of the relation between the interpolated lattice and the governing equations. This comprehension leads to a first summation rule in which the sampled governing equations are exact. Because a relatively large number of sampling points is regarded in this rule, a second, 'central' summation rule is proposed that uses significantly less sampling points. As in the well-known cluster summation rules [36,64], no interface procedures need to be employed, while it is computationally more efficient and more accurate than the cluster rules [36,64]. Results in this thesis indicate that the computational gain achieved by the central summation rule is a factor of 5-20 in terms of sampling points (effort to construct the governing equations), whereas errors of only 0-5% are observed.

Previously proposed QC methodologies [36,43,64,83,108,109,114] can only deal with conservative lattice models, because they are only used for (conservative) atomistic lattice computations. They are based on the minimization of the potential energy or on force equilibrium, that results from energy minimization. Discrete models of fibrous materials however, often involve dissipation and are thus non-conservative. In this thesis, a QC framework is proposed that is based on the virtual-power statement of non-conservative lattice models, so that dissipation can accurately be accounted for. Consequently, discrepancies in the governing equations of force-based QC frameworks, that at first sight seem to be suitable for non-conservative lattice models, are avoided. Because lattice models may include not only local, but also non-local dissipative mechanisms, as that for bond failure and subsequent fiber sliding proposed in Chapter 3, the virtual-power-based QC methodology is also equipped with a mixed formulation. In the mixed formulation, the kinematic variables are interpolated, as well as the internal variables related to dissipation. Although it is not necessary to use the same interpolation for both sets of variables, the advantage of using the same interpolation is that previously defined summation rules can directly be used. It must be noted that this also depends on the formulation of the stored energy. A complex interplay between both interpolations may occur, if they are different from each other, which ultimately may lead to the necessity to define new summation rules. This will also influence the computational gain and accuracy observed in this thesis.

8.2 Application of the virtual-power-based QC method

The virtual-power-based QC frameworks proposed in this thesis can directly be applied to a number of fibrous materials. A requirement however is that the fibrous materials can be represented by regular truss networks with local and/or nonlocal dissipative mechanisms. One example is the electronic textile considered in Chapter 2, that can be represented by a network of nonlinear elastoplastic trusses. The influence of a stiff electronic component on the compliant electronic textile is investigated in Chapter 6 using the virtual-power-based QC method, substantially reducing the computational effort.

The second and last example mentioned here, because it incorporates several mesoscale mechanisms that also occur in lattice models of other fibrous materials, is paper and paper materials, such as paperboard and corrugated cardboard. The mechanical behavior of paper is generally considered to result from three mesoscale phenomena: (i) the mechanical response of the individual fiber is elastoplastic [93], (ii) a significant number of interfiber bonds break [44,52,55,56,67,73], followed by frictional fiber sliding [52,67] and (iii) a small number of fibers break [73]. Here, the dependence on strain rate, temperature and moisture are neglected, although they can be incorporated in lattice models and therefore, most likely also in QC methods. These three mesoscale phenomena can be captured in the virtual-power-based QC frameworks. Elastoplastic behavior of fibers and bond failure and subsequent fiber sliding are yet incorporated in the virtual-power-based QC method. Only fiber failure is not incorporated in the proposed QC frameworks, but this can possibly straightforwardly be included, since this has been studied elaborately [26,72,73]. Furthermore, the proposed use of virtual-power in QC methodologies guarantees a correct incorporation of already proposed fiber failure models and the dissipation involved.

8.3 Future developments

A topic of great interest is the initiation and growth of local mesoscale phenomena in fibrous materials, such as consecutive bond failures and fiber failures. If local discrete events occur in coarse domains in QC methodologies, they cannot properly be described. Hence, local events are only allowed to take place in fully resolved regions. Because it is not always known a priori where they take place, an adaptive interpolation and summation should be used. This is not considered in this thesis, although the summation rules in Chapter 4 and 5 are proposed such that no internal interface corrections are present and they therefore also need not be updated during remeshing. Adaptivity has been studied extensively for the finite element method [58,80,81,90], as well as for QC methodologies [64,69,83,94,108] and therefore, several starting points can be found to include this in the virtual-power-based QC frameworks.

The QC methodologies in this thesis only treat regular (periodic) discrete models, although numerous irregular fibrous materials exist [4,20,24]. Regular discrete models

can to some extent still be used to describe fibrous materials consisting of irregular mesoscale fiber networks [73], since they at least incorporate the intrinsic discreteness of fibrous materials. However, irregular discrete models are clearly more suitable for these materials and cannot be incorporated in the proposed QC frameworks, because the interpolation enforces an affine deformation to them and the summation rules employ periodicity.

A future development that will increase the applicability of QC frameworks for fibrous materials, is thus to establish a QC methodology that can deal with irregular discrete models. It is questionable if the displacements of all lattice points can be interpolated for these irregular models, as this might lead to a too stiff response. Possibly, the displacements of only a small number of lattice points need to be strictly interpolated, while internal displacements are incorporated for the remaining lattice points that are consequently interpolated in a 'loose' sense. Internal displacements have been used for QC modelling of carbon nanotubes, although to a limited extent, since only one internal displacement needs to be incorporated for this [94,95]. Another route that may lead to QC frameworks that can deal with irregular networks, might be to define representative volume elements to which periodic boundary conditions are applied [4,113]. However, separation of scales must be valid for this, which is not the case in the transition region from coarse domains to fully resolved domains in QC triangulations. Hence, this is not trivially incorporated.

Only trusses are incorporated in the QC frameworks proposed here. A significant development that can help to increase the QC method's applicability is to define QC variants in which networks of beams can be used. The bending stiffness of individual fibers may be relevant for several fibrous materials, such as paper [20]. This depends on the ratio of the length of the fiber segments in between two consecutive bonds and the cross-sectional area of the fibers. In case the length of the fiber segments is small compared to their cross-sectional area, the fiber segments need to be modeled as beams.

One possible way to incorporate beams is to interpolate the rotations of the lattice points, besides the displacements. This will lead to a variant that is akin to Cosserat theory in continuum mechanics [21]. It is clear that the incorporation of beams (with rotations) in QC methods that only interpolate displacements is not evident.

Hence, future steps to make the QC method even more compatible with discrete network models of fibrous materials, are not trivial. However, difficulties in continuum models of fibrous materials are avoided, as well as the unnatural step to describe a discrete fiber network with a continuum, that is subsequently discretized with finite elements. More importantly, the demonstrated advantage of a discrete basis will remain.

Appendix A

Partitioning of the linearized system

The linearized system in Eq. (3.17) can be reformulated as:

$$\begin{pmatrix} \delta \mathbf{F}_u \\ \delta \mathbf{F}_s \end{pmatrix} = \begin{pmatrix} \mathbf{K}_{uu} & \mathbf{K}_{us} \\ \mathbf{K}_{su} & \mathbf{K}_{ss} \end{pmatrix} \begin{pmatrix} \delta \mathbf{u} \\ \delta \mathbf{s} \end{pmatrix}. \quad (\text{A.1})$$

Partitioning of this system of equations on the basis of the free-constrained and active-passive distinctions, as explained in Section 3.3.2, results in:

$$\begin{pmatrix} \delta \mathbf{F}_{u,f} \\ \delta \mathbf{F}_{u,c} \\ \delta \mathbf{F}_{s,a} \\ \delta \mathbf{F}_{s,p} \end{pmatrix} = \begin{pmatrix} \mathbf{K}_{uu,ff} & \mathbf{K}_{uu,fc} & \mathbf{K}_{us,fa} & \mathbf{K}_{us,fp} \\ \mathbf{K}_{uu,cf} & \mathbf{K}_{uu,cc} & \mathbf{K}_{us,ca} & \mathbf{K}_{us,cp} \\ \mathbf{K}_{su,af} & \mathbf{K}_{su,ac} & \mathbf{K}_{ss,aa} & \mathbf{K}_{ss,ap} \\ \mathbf{K}_{su,pf} & \mathbf{K}_{su,pc} & \mathbf{K}_{ss,pa} & \mathbf{K}_{ss,pp} \end{pmatrix} \begin{pmatrix} \delta \mathbf{u}_f \\ \delta \mathbf{u}_c \\ \delta \mathbf{s}_a \\ \delta \mathbf{s}_p \end{pmatrix}. \quad (\text{A.2})$$

By using $\delta \mathbf{u}_c = \mathbf{0}$ and $\delta \mathbf{s}_p = \mathbf{0}$, this system can be simplified to:

$$\begin{pmatrix} \delta \mathbf{F}_{u,f} \\ \delta \mathbf{F}_{u,c} \\ \delta \mathbf{F}_{s,a} \\ \delta \mathbf{F}_{s,p} \end{pmatrix} = \begin{pmatrix} \mathbf{K}_{uu,ff} & \mathbf{K}_{us,fa} \\ \mathbf{K}_{uu,cf} & \mathbf{K}_{us,ca} \\ \mathbf{K}_{su,af} & \mathbf{K}_{ss,aa} \\ \mathbf{K}_{su,pf} & \mathbf{K}_{ss,pa} \end{pmatrix} \begin{pmatrix} \delta \mathbf{u}_f \\ \delta \mathbf{s}_a \end{pmatrix}. \quad (\text{A.3})$$

The equations in this system that correspond to $\delta \mathbf{u}_c$ and $\delta \mathbf{s}_p$ (the second and fourth equations) are left out of consideration. This can be done since the solution $\delta \mathbf{u}_f$ and $\delta \mathbf{s}_a$ is found by specifying the terms $\delta \mathbf{F}_{u,f}$ and $\delta \mathbf{F}_{s,a}$ and solving the first and third equations of this system. These equations can be reformulated as:

$$\begin{aligned} \delta \mathbf{F}_{u,f} &= \mathbf{K}_{uu,ff} \delta \mathbf{u}_f + \mathbf{K}_{us,fa} \delta \mathbf{s}_a \\ \delta \mathbf{F}_{s,a} &= \mathbf{K}_{su,af} \delta \mathbf{u}_f + \mathbf{K}_{ss,aa} \delta \mathbf{s}_a. \end{aligned} \quad (\text{A.4})$$

Bibliography

- [1] Abadie, J., Carpentier, J., 1969, Generalization of the Wolfe reduced gradient method to the case of nonlinear constraints, Optimization, Academic Press, New York, United States, 37-49.
- [2] Allaoui, S., Aboura, Z., Benzeggagh, M.L., 2009, Phenomena governing uni-axial tensile behaviour of paperboard and corrugated cardboard, Composite Structures, Vol. 87, 80-92.
- [3] Apedo, K.L., Ronel, S., Jacquelin, E., Bennani, A., Massenzio, M., 2010, Non-linear finite element analysis of inflatable beams made from orthotropic woven fabric, International Journal of Solids and Structures, Vol. 47, 2017-2033.
- [4] Argento, G., Simonet, M., Oomens, C.W.J., Baaijens, F.P.T., Multi-scale mechanical characterization of scaffolds for heart valve tissue engineering, Submitted.
- [5] Arnoux, P.J. , Bonnoit, J., Chabrand, P., Jean, M., Pithioux, M., 2002, Numerical damage models using a structural approach: application in bones and ligaments, The European Physical Journal of Applied Physics, Vol. 17, 65-73.
- [6] Badel, B., Vidal-Sallé, E., Boisse, P., 2007, Computational determination of in-plane shear mechanical behaviour of textile composite reinforcements, Computational Materials Science, Vol. 40, 439-448.
- [7] Batchelor, W., 2008, An analytical solution for the load distribution along a fibre in a nonwoven network, Mechanics of Materials, Vol. 40, 975-981.
- [8] Beex, L.A.A., Peerlings, R.H.J., 2009, An experimental and computational study of laminated paperboard creasing and folding, International Journal of Solids and Structures, Vol. 46, 4192-4207.
- [9] Beex, L.A.A., Peerlings, R.H.J., Geers, M.G.D., 2011, A quasicontinuum methodology for multiscale analyses of discrete microstructures, International Journal for Numerical Methods in Engineering, Vol. 87, 701-718.

-
- [10] Beex, L.A.A., Peerlings, R.H.J., 2012, On the influence of delamination on laminated paperboard creasing and folding, *Philosophical Transactions of the Royal Society A*, Vol. 370, 1912-1924.
- [11] Beex, L.A.A., Peerlings, R.H.J., Geers, M.G.D., Central summation in the quasicontinuum method, Submitted to the *Journal of the Mechanics and Physics of Solids*.
- [12] Beex, L.A.A., Verberne, C.W., Peerlings, R.H.J., 2012, Experimental identification of a lattice model for woven fabrics: application to electronic textile, Submitted to *Composites Part A*.
- [13] Beex, L.A.A., Peerlings, R.H.J., Geers, M.G.D., 2012, A multiscale quasicontinuum method for dissipative lattice models and discrete networks, In preparation.
- [14] Ben Boubaker, B., Haussy, B., Ganghoffer, J.F., 2007, Discrete models of woven structures. Macroscopic approach, *Composites: Part B*, Vol. 38, 498-505.
- [15] Ben Boubaker, B., Haussy, B., Ganghoffer, J.F., 2007, Discrete woven structure model: yarn-on-yarn friction, *C.R. Mecanique*, Vol. 335, 150-158.
- [16] Ben Boubaker, B., Haussy, B., Ganghoffer, J.F., 2007, Considerations of the yarn-yarn interactions in meso/macro discrete model of fabric Part II: Woven fabric under uniaxial and biaxial extension, *Mechanics Research Communications*, Vol. 34, 371-378.
- [17] Boisse, P., Gasser, A., Hivet, G., 2001, Analyses of fabric tensile behaviour: determination of the biaxial tension-strain surfaces and their use in forming simulations, *Composites: Part A*, Vol. 32, 1395-1414.
- [18] Boisse, P., Zouari, B., Daniel, J.L., 2006, Importance of in-plane shear rigidity in finite element analyses of woven fabric composite preforming, *Composites: Part A*, Vol. 37, 2201-2212.
- [19] Bolander, J.E., Sukumar, N., 2005, Irregular lattice model for quasistatic crack propagation, *Physical Review B*, Vol. 71, 094106.
- [20] Bronkhorst, C.A., 2003, Modelling paper as a two-dimensional elastic-plastic stochastic network, *International Journal of Solids and Structures*, Vol. 40, 5441-5454.
- [21] Casolo, S., 2006, Macroscopic modelling of structured materials: relationship between orthotropic Cosserat continuum and rigid elements, *International Journal of Solids and Structures*, Vol. 43, 475-496.
- [22] Chandran, P.L., Barocas, V.H., 2007, Affine versus non-affine fibril kinematics in collagen networks: theoretical studies of network behavior, *Journal of Biomechanical Engineering*, Vol. 128, 259-270.

-
- [23] Chen, G., Baker, G., 2003, Influence of bond slip on crack spacing in numerical modeling of reinforced concrete, *Journal of Structural Engineering*, Vol. 129, 1514-1521.
- [24] Clyne, T.W., Markaki, A.E., Tan, J.C., 2005, Mechanical and magnetic properties of metal fibre networks, with and without a polymeric matrix, *Composites Science and Technology*, Vol. 65, 2492-2499.
- [25] Cui, X., Zhang, Y., Zhao, H., Lu, T.J., Fang, D., 2011, Stress concentration in two-dimensional lattices with imperfections, *Acta Mechanica*, Vol. 216, 105-122.
- [26] Curtin, W.A., Scher, H., 1990, Brittle fracture in disordered materials: A spring network model, *Journal of Materials Research*, Vol. 5, 3535-3553.
- [27] Curtin, W.A., Miller, R.E., 2003, Atomistics/continuum coupling in computational materials science, *Modelling and Simulation in Materials Science and Engineering*, Vol. 11, 33-68.
- [28] Cusatis, G., Bažant, Z.P., Cedolin, L.C., 2003, Confinement-shear lattice model for concrete damage in tension and compression: 1. Theory, *Journal of Engineering Mechanics*, Vol. 129, 1439-1448.
- [29] Dalton, A.B., Colins, S., Muñoz, E., Razal, J.M., Von Howard, E., Ferraris, J.P., Coleman, J.N., Kim, B.G., Baughman, R.H., 2003, Super-tough carbon-nanotube fibres, *Nature*, Vol. 423, 703.
- [30] Delaplace, A., Pijaudier-Cabot, G., Roux, S., 1996, Progressive damage in discrete models and consequences on continuum modelling, *Journal of the Mechanics and Physics of Solids*, Vol. 44, 99-136.
- [31] Delincé, M., Delannay, F., 2004, Elastic anisotropy of a transversely isotropic random network of interconnected fibres: non-triangulated network model, *Acta Materialia*, Vol. 52, 1013-1022.
- [32] Desphande, V.S., Fleck, N.A., Ashby, M.F., 2001, Effective properties of the octet-truss lattice material, *Journal of the Mechanics and Physics of Solids*, Vol. 49, 1747-1769.
- [33] Dobson, M., Elliott, R.S., Luskin, M., Tadmor, E.B., 2007, A multilattice quasi-continuum for phase transformation materials: cascading cauchy-born kinematics, *Journal of Computer-Aided Materials Design*, Vol. 14, 219-237.
- [34] Doyoyo, M., Hu, J.W., 2006, Plastic failure analysis of an auxetic foam or inverted strut lattice under longitudinal and shear loads, *Journal of the Mechanics and Physics of Solids*, Vol. 54, 1479-1492.
- [35] Edmison, J., Jones, M., Nakad, Z., Martin, T., 2002, Using piezoelectric materials for wearable electronic textiles, *Proceedings of the 6th International Symposium on Wearable Computers*, 41-48.

-
- [36] Eidel, B., Stukowski, A., 2009, A variational form of the quasicontinuum method based on energy sampling in clusters, *Journal of the Mechanics and Physics of Solids*, Vol. 57, 87-108.
- [37] Feron, M.J.M., 2008, *Mechanics of electronic textiles*, Master's thesis (MT 08.21). Eindhoven University of Technology, Eindhoven, The Netherlands.
- [38] Fish, J., Nugggehally, M.A., Shephard, M.S., Picu, C.R., Badia, S., Parks, M.L., Gunzburger, M., 2007, Concurrent AtC coupling based on a blend of the continuum stress and the atomistic force, *Computer Methods in Applied Mechanics and Engineering*, Vol. 196, 4548-4560.
- [39] Fonteyn, M.T.J., 2010, *Modelling of electronic textiles*, Master's thesis (MT 10.07). Eindhoven University of Technology, Eindhoven, The Netherlands.
- [40] Gavini, V., Bhattacharya, K., Ortiz, M., 2007, Quasicontinuum orbital-free density functional theory: a route to multi-million atom non-periodic DFT calculation, *Journal of the Mechanics and Physics of Solids*, Vol. 55, 697-718.
- [41] Germain, P., 1973, The method of virtual power in continuum mechanics Part 2: microstructure, *SIAM Journal on Applied Mathematics*, Vol. 25, 556-575.
- [42] Gonella, S., Ruzzene, M., 2008, Homogenization of vibrating periodic lattice structures, *Applied Mathematical Modelling*, Vol. 32, 459-482.
- [43] Gunzburger, M., Zhang, Y., 2010, A quadrature-rule type approximation to the quasi-continuum method, *Multiscale Modeling and Simulation*, Vol. 8, 571-590.
- [44] Häggglund, R., Isaksson, P., 2008, On the coupling between macroscopic material degradation and interfiber bond fracture in an idealized fiber network, *International Journal of Solids and Structures*, Vol. 45, 868-878.
- [45] Hamila, N., Boisse, P., 2008, Simulations of textile composite reinforcement draping using a new semi-discrete three node finite element, *Composites: Part B*, Vol. 39, 999-1010.
- [46] Ha-Minh, C., Kanit, T., Boussu, F., Imad, A., 2011, Numerical multi-scale modeling for textile woven fabric against ballistic impact, *Computational Materials Science*, Vol. 50, 2172-2184.
- [47] Han, D., Tsai, S.W., 2011, Interlocked composite grids design and manufacturing, *Journal of Composite Materials*, Vol. 37, 287-316.
- [48] Hatami-Marbini, H., Picu, R.C., 2009, An eigenstrain formulation for the prediction of elastic moduli of defective fiber networks, *European Journal of Mechanics A/Solids*, Vol. 38, 305-316.
- [49] Hayes, R.L., Fago, M., Ortiz, M., Carter, E.A., 2005, Density-functional-theory-based local quasicontinuum method: prediction of dislocation nucleation, *Physical Review B*, Vol. 90, 100102.

-
- [50] Heegaard, J.H., Curnier, A., 1993, An augmented Lagrangian method for discrete large-slip contact problems, *International Journal for Numerical Methods in Engineering*, Vol. 36, 569-593.
- [51] Herrmann, H.J., Roux, S., 1990, *Statistical models for the fracture of disordered media*, North Holland, Amsterdam, The Netherlands.
- [52] Heyden, S., *Network modelling for the evaluation of mechanical properties of cellulose fibre fluff*. Lund University, Lund, Sweden, 2000.
- [53] Hou, X., Acar, M., Silberschmidt, V.V., 2009, 2D finite element analysis of thermally bonded non-woven materials: continuous and discontinuous models, *Computational Materials Science*, Vol. 46, 700-707.
- [54] Intrigila, B., Melatti, I., Tofani, A., Macchiarelli, G., 2007, Computational models of myocardial endomysial collagen arrangement, *Computer Methods and Programs in Biomedicine*, Vol. 86, 232-244.
- [55] Isaksson, P., Gradin, P.A., Kulachenko, A., 2006, The onset and progression of damage in isotropic paper sheets, *International Journal of Solids and Structures*, Vol. 43, 713-726.
- [56] Isaksson, P., Hägglund, R., 2007, Evolution of bond fractures in a randomly distributed fiber network, *International Journal of Solids and Structures*, Vol. 44, 6135-6147.
- [57] Iyer, M., Gavini, V., 2011, A field theoretical approach to the quasi-continuum method, *Journal of the Mechanics and Physics of Solids*, Vol. 59, 1506-1535.
- [58] Javani, H.R., Peerlings, R.H.J., Geers, M.G.D., 2010, A remeshing strategy for three dimensional elasto-plasticity coupled with damage applicable to forming processes, *International Journal of Material Forming*, Vol. 3, 915-918.
- [59] Jin, Y.J., Wang, T.J., 2009, Three-dimensional numerical modeling of the damage mechanism of amorphous polymer network, *Computational Materials Science*, Vol. 46, 632-638.
- [60] Kato, S., Minami, H., Yoshino, T., Namita, T., 1997, Analysis of membrane structures based on fabric lattice model considering viscous characteristics, *Proceedings of the IASS international symposium on shell & spatial structures*, Singapore.
- [61] Kawabata, S., Niwa, M., Kawai, H., 1973, The finite-deformation theory of plain-weave fabrics. Part II: the uniaxial-deformation theory, *Journal of the Textile Institute*, Vol 64, 47-61.
- [62] Kim, H., Buttlar, W.G., 2009, Discrete fracture modeling of asphalt concrete, *International Journal of Solids and Structures*, Vol. 46, 2593-2604.

- [63] King, M.J., Jearanaisilawong, P., Socrate, S., 2005, A continuum constitutive model for the mechanical behavior of woven fabrics, *International Journal of Solids and Structures*, Vol. 42, 3867-3896.
- [64] Knap, J., Ortiz, M., 2001, An analysis of the quasicontinuum method, *Journal of the Mechanics and Physics of Solids*, Vol. 49, 1899-1923.
- [65] Knap, J., Ortiz, M., 2003, Effect of indenter radius size on Au(001) nanoindentation, *Physical Review Letters*, Vol. 90, 226102.
- [66] Kouznetsova, V., Brekelmans, W.A.M., Baayens, F.P.T., 2001, An approach to micro-macro modeling of heterogeneous materials, *Computational Mechanics*, Vol. 27, 37-48.
- [67] Kulachenko, A., Uesaka, T., 2012, Direct simulation of fiber network deformation and failure, *Mechanics of Materials*, Vol. 51, 1-14.
- [68] Kulkarni, Y., Knap, J., Ortiz, M., 2008, A variational approach to coarse graining of equilibrium and non-equilibrium atomistic description at finite temperature, *Journal of the Mechanics and Physics of Solids*, Vol. 56, 1417-1449.
- [69] Kwon, S., Lee, Y., Park, J.Y., Sohn, D., Lim, J.H., Im, S., 2009, An efficient three-dimensional adaptive quasicontinuum method using variable-node elements, *Journal of Computational Physics*, Vol. 228, 4789-4810.
- [70] Lennard-Jones, J.E., 1937, The equation of state of gases and critical phenomena, *Physica IV*, Vol. 10, 941-956.
- [71] Lilliu, G., Van Mier, J.G.M., 2003, 3D lattice type fracture model for concrete, *Engineering Fracture Mechanics*, Vol. 70, 927-941.
- [72] Lilliu, G., Van Mier, J.G.M., 2006, On the relative use of micro-mechanical lattice analysis of 3-phase particle composites, *Engineering Fracture Mechanics*, Vol. 74, 1174-1189.
- [73] Liu, J.X., Chen, Z.T., Li, K.C., 2010, A 2D lattice model for simulating the failure of paper, *Theoretical and Applied Fracture Mechanics*, Vol. 54, 1-10.
- [74] Lomov, S.V., Verpoest, I., 2006, Model of shear of woven fabrics and parametric description of shear resistance of glass woven reinforcements, *Composites Science and Technology*, Vol. 66, 919-933.
- [75] Lomov, S.V., Ivanov, D.S., Verpoest, S., Zako, M., Kurashiki, T., Nakai, H., Hirose, S., 2007, Meso-FE modelling of textile composites: Road map, data flow and algorithms, *Composite Science and Technology*, Vol. 67, 1870-1891.
- [76] Luskin, M., Ortner, C., 2008, An analysis of node-based cluster summation rules in the quasicontinuum method, *SIAM Journal on Numerical Analysis*, Vol. 47, 3070-3086.

- [77] Marian, J., Knap, J., Campbell, G.H., 2008, A quasicontinuum study of nanovoid collapse under uniaxial loading in Ta, *Acta Materiala*, Vol. 56, 2389-2399.
- [78] Marian, J., Venturini, G., Hansen, B.L., Knap, J., Ortiz, M., Campbell, G.H., 2010, Finite-temperature extensions of the quasicontinuum method using Langevin dynamics: entropy losses and analysis of errors, *Modelling and Simulations in Material Science and Engineering*, Vol. 18, 015003.
- [79] Marlescu, D., Marlescu, R., Zamora, N.H., Stanley-Marbell, P., Khosla, P.K., Park, S., Jayaraman, S., Jung, S., Lauterbach, C., Weber, W., Kirstein, T., Cottet, D., Grzyb, J., Tröster, G., Jones, M., Martin, T., Nakad, Z., 2003, Electronic textiles: a platform for pervasive computing, *Proceedings of the IEEE*, Vol. 91, 1995-2018.
- [80] Materna, D., Barthold, F.J., 2009, Goal-oriented r-adaptivity based on variational arguments in the physical and material spaces, *Computer Methods in Applied Mechanics and Engineering*, Vol. 198, 3335-3351.
- [81] Mediavilla, J., Peerlings, R.H.J., Geers, M.G.D., 2006, A robust and consistent remeshing-transfer operator for ductile fracture simulations, *Computer and Structures*, Vol. 84, 604-623.
- [82] Miller, R., Ortiz, M., Phillips, R., Shenoy, V., Tadmor, E.B., 1998, Quasicontinuum models of fracture and plasticity, *Engineering Fracture Mechanics*, Vol. 61, 427-444.
- [83] Miller, R.E., Tadmor, E.B., 2002, The quasicontinuum method: overview, applications and current directions, *Journal of Computer-Aided Materials Design*, Vol. 9, 203-239.
- [84] Miller, R.E., Rodney, D., 2008, On the nonlocal nature of dislocation nucleation during nanoindentation, *Journal of the Mechanics and Physics of Solids*, Vol. 56, 1203-1223.
- [85] Miller, R.E., Tadmor, E.B., 2009, A unified framework and performance benchmark of fourteen multiscale atomistic/continuum coupling methods, *Modelling and Simulation in Materials Science and Engineering*, Vol. 17, 053001.
- [86] Mohr, D., 2005, Mechanism-based multi-surface plasticity model for ideal truss lattice materials, *International Journal of Solids and Structures*, Vol. 42, 3235-3260.
- [87] Ngan, A.H.W., 2009, Canonical ensemble for static elastic structures with random microstructures, *Journal of the Mechanics and Physics of Solids*, Vol. 57, 803-811.
- [88] Nilakantan, G., Keefe, M., Bogetti, T.A., Adkinson, R., Gillespie, J.W.Jr., 2010, On the finite element analysis of woven fabric impact using multiscale modeling techniques, *International Journal of Solids and Structures*, Vol. 47, 2300-2315.

-
- [89] Niskanen, K., 1998, Paper physics, Fapet Oy, Helsinki, Finland.
- [90] Oden, J.T., Prudhomme, S., 2001, Goal-oriented error estimation and adaptivity for the finite element method, *Computers and Mathematics with Applications*, Vol. 41, 735-756.
- [91] Ostoja-Starzewski, M., 2002, Lattice models in micromechanics, *Applied Mechanics Reviews*, Vol. 55, 35-60.
- [92] Ostoja-Starzewski, M., Wang, G., 2006, Particle modeling of random crack patterns in epoxy plates, *Probabilistic Engineering Mechanics*, Vol. 21, 267-275.
- [93] Page, D.H., El-Hosseiny, F., 1983, The mechanical properties of single wood pulp fibres. Part VI. Fibril angle and the shape of the stress-strain curve, *Journal of Pulp and Paper Science*, Vol. 9, 99-100.
- [94] Park, J.Y., Im, S., 2008, Adaptive nonlocal quasicontinuum for deformations of curved crystalline structures, *Physical Review B*, Vol. 77, 184109.
- [95] Park, J.Y., Park, C.H., Park, J.S., Kong, K., Chang, H., Im, S., 2010, Multi-scale computation for carbon nanotubes based on a hybrid QC/QM (quantum mechanical and quasicontinuum) approach, *Journal of the Mechanics and Physics of Solids*, Vol. 77, 184109.
- [96] Peng, X.Q., Cao, J., 2005, A continuum mechanics-based non-orthogonal constitutive model for woven composite fabrics, *Composites Part A*, Vol. 36, 859-874.
- [97] Picu, R.C., 2000, Atomistic-continuum simulation of nano-indentation in molybdenum, *Journal of Computed-Aided Materials Design*, Vol. 7, 77-87.
- [98] Potluri, P., Manan, A., 2007, Mechanics of non-orthogonally interlaced textile composites, *Composites: Part A*, Vol. 38, 1216-1226.
- [99] Potluri, P., Sagar, T.V., 2008, Compaction modelling of textile preforms for composite structures, *Composite Structures*, Vol. 86, 177-185.
- [100] Ridruejo, A., González, C., Llorca, J.L., 2010, Damage micromechanisms and notch sensitivity of glass-fiber non-woven felts: An experimental and numerical study, *Journal of the Mechanics and Physics of Solids*, Vol. 58, 1628-1645.
- [101] Ridruejo, A., González, C., Llorca, J.L., 2011, Micromechanisms of deformation and fracture of polypropylene nonwoven fabrics, *International Journal of Solids and Structures*, Vol. 48, 153-162.
- [102] Rinaldi, A., Krajcinovic, D., Peralta, P., Lai, Y.C., 2008, Lattice models of polycrystalline microstructures: a quantitative approach, *Mechanics of Materials*, Vol. 40, 17-36.

-
- [103] Ryvkin, M., Slepyan, L., 2010, Crack in a 2D beam lattice: analytical solution for two bending modes, *Journal of the Mechanics and Physics of Solids*, Vol. 58, 902-917.
- [104] Schlangen, E., Van Mier, J.G.M., 1992, Experimental and numerical analysis of micromechanisms of fracture of cement-based composites, *Cement Concrete Composites*, Vol. 14, 105-118.
- [105] Schwint, O.A., Labraga, M., Cervino, C.O., Haffar, M., Sequeiros, P.H., Aldana Marcos, H.J., 2004, A modification of the staining technique of reticular fibres for image analysis of the cardiac collagen network, *Cardiovascular Pathology*, Vol. 13, 213-220.
- [106] Sharma, S.B., Sutcliffe, M.P.F., Chang, S.H., 2003, Characterization of material properties for draping of dry woven composite material, *Composites: Part A*, Vol. 34, 1167-1175.
- [107] Sharma, S.B., Sutcliffe, M.P.F., 2004, A simplified finite element model for draping of woven material, *Composites: Part A*, Vol. 35, 637-643.
- [108] Shenoy, V.B., Miller, R., Tadmor, E.B., Rodney, D., Phillips, R., Ortiz, M., 1999, An adaptive finite element approach to atomistic scale mechanics-the quasicontinuum method, *Journal of the Mechanics and Physics of Solids*, Vol. 47, 611-642.
- [109] Shimokawa, T., Mortensen, J.J., Schiøtz, J., Jacobsen, K.W., 2004, Matching conditions in the quasicontinuum method: Removal of the error introduced at the interface between the coarse-grained and fully atomistic region, *Physical Review B*, Vol. 69, 214104.
- [110] Silberstein, M.N., Pai, C.L., Rutledge, G.C., Boyce, M.C., 2012, Elastic-plastic behavior of non-woven fibrous mats, *Journal of the Mechanics and Physics of Solids*, Vol. 60, 295-318.
- [111] Simo, J.C., Taylor, R.L., 1986, A return mapping algorithm for plane stress elastoplasticity, *International Journal for Numerical Methods in Engineering*, Vol. 22, 649-670.
- [112] Strömbro, J., Gudmundson, P., 2008, An anisotropic fibre-network model for mechano-sorptive creep in paper, *International Journal of Solids and Structures*, Vol. 45, 5765-5787.
- [113] Stylianopoulos, T., Barocas, V.H., 2007, Volume-averaging theory for the study of the mechanics of collagen networks, *Computer Methods in Applied Mechanics and Engineering*, Vol. 196, 2981-2990.
- [114] Tadmor, E.B., Phillips, R., Ortiz, M., 1996, Mixed atomistics and continuum models of deformation in solids, *Langmuir*, Vol. 12, 4529-4534.

-
- [115] Tadmor, E.B., Ortiz, M., Phillips, R., 1996, Quasicontinuum analysis of defects in solids, *Philosophical Magazine A*, Vol. 73, 1529-1563.
- [116] Tadmor, E.B., Miller, R., Phillips, R., Ortiz, M., 1999, Nanoindentation and incipient plasticity, *Journal of Materials Research*, Vol. 14, 2233-2250.
- [117] Ten Thije, R.H.W., Akkerman, R., Huétink, J., 2007, Large deformation simulation of anisotropic material using an updated Lagrangian finite element method, *Computer Methods in Applied Mechanics and Engineering*, Vol. 196, 3141-3150.
- [118] Ten Thije, R.H.W., Akkerman, R., 2008, Solutions to intra-ply shear locking in finite element analyses of fibre reinforced materials, *Composites: Part A*, Vol. 39, 1167-1176.
- [119] Thakkar, B.K., Gooren, L.G.J., Peerlings, R.H.J., Geers, M.G.D., 2009, Experimental and numerical investigation of creasing in corrugated paperboard, *Philosophical Magazine*, Vol. 88, 3299-3310.
- [120] Tserper, K.I., Labeas, G.N., 2009, Progressive fracture analysis of planar lattices and shape-morphing Kagome-structure, *Theoretical and Applied Fracture Mechanics*, Vol. 51, 41-47.
- [121] Vellinga, W.P., Van den Bosch, M., Geers, M.G.D., 2008, Interaction between cracking, delamination and buckling in brittle elastic thin films, *International Journal of Fracture*, Vol. 154, 195-209.
- [122] Verberne, C.W., 2011, A structural lattice model for electronic textile, Master's thesis (MT 11.19). Eindhoven University of Technology, Eindhoven, The Netherlands.
- [123] Wilbrink, D.V., Beex, L.A.A., Peerlings, R.H.J., 2012, A discrete network model for bond failure and frictional sliding in fibrous materials, Submitted to the *International Journal of Solids and Structures*.
- [124] Wilkins, M.L, 1963, Calculation of elastic-plastic flow, In: Balder, B. et al. (Eds.), *Methods of Computational Physics 3*, Academic Press, New York, 1964.
- [125] Xiao, B.K., Belytschko, T., 2004, A bridging domain method for coupling continua with molecular dynamics, *Computer Methods in Applied Mechanics and Engineering*, Vol. 193, 1645-1669.
- [126] Zeman, J., Peerlings, R.H.J., Geers, M.G.D., 2011, Non-local energetics of random heterogeneous lattices, *Journal of the Mechanics and Physics of Solids*, Vol. 59, 1214-1230.
- [127] Zhang, Y., Gunzburger, M., 2010, Quadrature-rule type approximations to the quasicontinuum method for long-range interatomic interactions, *Computer Methods in Applied Mechanics and Engineering*, Vol. 199, 648-659.

-
- [128] Zhao, X.H., 2012, A theory for large deformation and damage of interpenetrating polymer networks, *Journal of the Mechanics and Physics of Solids*, Vol. 60, 319-332.
- [129] Zhu, B., Yu, T.X., Tao, X.M., 2007, Large deformation and slippage mechanism of plain woven composite in bias extension, *Composites: Part A*, Vol. 38, 1821-1828.
- [130] Zohdi, T.I., Powell, D., 2006, Multiscale construction and large-scale simulation of structural fabric undergoing ballistic impact, *Computer Methods in Applied Mechanics and Engineering*, Vol. 195, 94-109.
- [131] Zohdi, T.I., 2007, A computational framework of network modeling of fibrous biological tissue deformation and rupture, *Computer Methods in Applied Mechanics and Engineering*, Vol. 196, 2972-2980.

Samenvatting

Structurele roostermodellen en discrete netwerkmodellen bestaande uit staven of balken worden met regelmaat gebruikt om de mechanica van vezelmaterialen te beschrijven. De discrete elementen representeren individuele vezels en draden op de mesoschaal op een natuurlijke manier. Als gevolg daarvan kunnen relevante mesoscopische fenomenen, zoals de breuk van individuele vezels en bindingen, resulterend in totale, macroscopische breuk, adequaat in rekening worden gebracht. Zelfs macroscopische fenomenen, zoals grote rotaties van draden en de resulterende evoluerende anisotropie, worden automatisch gegenereerd in roostermodellen, terwijl ze apart verdisconteerd moeten worden in continue modellen van vezelmaterialen.

Een ander voordeel van roostermodellen is, dat ze op relatief simpele wijze kunnen worden aangepast, opdat elke familie van discrete elementen de mechanische respons in een karakteristieke richting van een vezelmateriaal beschrijft. Dit zorgt voor een duidelijke, experimentele identificatie van de parameters van de elementen. In dit proefschrift is een dergelijke methode ontwikkeld voor een roostermodel van elektronisch textiel. Een roostermodel voor het falen van bindingen tussen draden en het eropvolgende glijden van draden is ook geformuleerd. De thermodynamische basis van dit roostermodel staat ervoor in dat het op een consistente manier gebruikt kan worden om de effecten van mesoscopische parameters, zoals de bindingssterkte en vezellengte, op de macroscopische respons te onderzoeken.

Roosterberekeningen op fysisch relevante, grote schaal zijn rekenkundig duur, omdat roostermodellen zijn geconstrueerd op de mesoschaal. Hierdoor, vereisen berekeningen op grote schaal een grote hoeveelheid vrijheidsgraden en uitgebreide inspanningen om de systeemvergelijkingen op te stellen. Principes van de quasicontinue (QC-)methode worden aangewend in dit proefschrift om de rekentijd van roosterberekeningen op grote schaal te verminderen. De QC-methode staat de directe en precieze beschrijving toe van lokale mesoscopische fenomenen in interessante gebieden (regions of interest), terwijl elders aanzienlijke besparingen worden gerealiseerd. Een ander voordeel is dat de QC-methode geheel uitgaat van het roostermodel en geen formulering van een equivalent continu model vereist.

De QC-methode gebruikt interpolatie om het aantal vrijheidsgraden te beperken en sommatieregels om de rekentijd die noodzakelijk is voor het opstellen van de systeemverge-

lijkingen te verminderen. Grote interpolatiedriehoeken worden gebruikt in gebieden met kleine verplaatsingsfluctuaties. In volledig beschreven gebieden zijn de afmetingen van de interpolatiedriehoeken dusdanig klein dat het exacte roostermodel wordt gerepresenteerd. Sommatieregels worden gebruikt om de bijdrages van alle knooppunten aan de systeemvergelijkingen te benaderen, waarbij gebruik wordt gemaakt van een klein aantal knooppunten. In dit proefschrift wordt een sommatieregel voorgesteld die de systeemvergelijkingen exact bepaalt, hoewel een grote vermindering van het aantal relevante knooppunten wordt bereikt. Deze sommatieregel is efficiënt voor structurele roostermodellen met uitsluitend interacties tussen directe burens, maar hij is inefficiënt voor atomaire roosterberekeningen die interacties over langere afstanden bevatten. Daarom wordt nog een tweede, 'centrale' sommatieregel voorgesteld, waarin beduidend minder knooppunten worden gebruikt om de numerieke efficiëntie te vergroten, dit ten koste van de kwaliteit van de benadering.

De QC-methode is oorspronkelijk voorgesteld voor (conservatieve) atomaire roostermodellen en is gebaseerd op energiminimalisatie. Roostermodellen voor vezelmaterialen daarentegen, zijn vaak niet-conservatief en dus kunnen QC-methodes die gebaseerd zijn op energiminimalisatie niet simpelweg aangewend worden. Voorbeelden hiervan zijn het roostermodel voorgesteld voor geweven stoffen en het roostermodel dat het falen van bindingen tussen draden en het eropvolgende glijden van draden beschrijft. Daarom wordt een algemener QC-raamwerk voorgesteld dat is gebaseerd op de virtueelvermogensbalans van een niet-conservatief roostermodel. Als gevolg hiervan, kunnen dissipatieve mechanismes worden opgenomen in het QC-raamwerk, terwijl dezelfde sommatieregels volstaan. De geldigheid van het raamwerk wordt aangetoond voor een roostermodel met elastoplastische staven. De QC-methode die gebaseerd is op virtueelvermogen is ook gebruikt voor het roostermodel dat het falen van bindingen tussen draden en het eropvolgende glijden van draden beschrijft, dat gepresenteerd is in dit proefschrift. In tegenstelling tot elastoplastische interacties die intrinsiek lokaal zijn, brengt het falen van bindingen tussen draden en het daaropvolgende glijden van draden niet lokaal dissipatieve mechanismes mee. Daarom is de QC-methode die gebaseerd is op virtueelvermogen ook uitgerust met een gemengde formulering waarin niet alleen de verplaatsingen worden geïnterpoleerd, maar ook de interne variabelen die verbonden zijn met dissipatie.

Acknowledgements

It may be clear that this thesis would have looked different if I would not have had the help and support of a number of people.

Als eerste ben ik mijn promotor, prof. Marc Geers, dankbaar voor zijn supervisie in de afgelopen jaren bij de vele technische details, het overzicht over de mechanica wereld dat hij met mij heeft gedeeld en de vrijheid die hij mij heeft gegeven. Het was grappig om te zien hoe hij regelmatig tussen mij en mijn copromotor Ron Peerlings in kwam te staan om ons gedrieën tot een gezamenlijke beslissing te laten komen. Dit kwam er in de praktijk op neer dat ik Ron meestal gelijk gaf, omdat hij het ook had. Het blijft was ik en ben ik nog steeds met zijn vertrouwen gedurende de tijd dat ik het persoonlijk moeilijk had. Ik ben ervan overtuigd dat hij het beste voor mij heeft gedaan in deze situatie: mij de tijd geven om te herstellen. Ik hoop dat het hem goed gaat en ik hem snel mag weerzien.

Veel dank ben ik verschuldigd aan mijn copromotor, Ron Peerlings. Het is evident dat hij op de universiteit de persoon is waar ik de meeste onderzoeksvaardigheden van geleerd heb tijdens mijn afstuderen en promoveren. Niet alleen vanuit vakinhoudelijk oogpunt ben ik hem dankbaar, maar ook vanuit collegiaal oogpunt: het boterde goed tussen ons. Na tweeduizend emails en 199 sneertjes ligt er een proefschrift waar hij hopelijk ook trots op is, aangezien hij er veel tijd en moeite in heeft gestoken. Ik ben er zeker van dat we elkaar in de toekomst weer zullen ontmoeten, zeker als ik in de academische wereld werkzaam blijf. Dan zal het moment daar zijn dat ik niet alleen gelijk heb, maar het ook krijg.

Twee andere mensen die ik wil bedanken zijn David Wilbrink en Cyriel Verberne, omdat zij medeverantwoordelijk zijn voor het tweede en derde hoofdstuk van dit proefschrift. Het was voor mij leuk om met hen samen te werken en voor ons allen prettig dat we het met papers konden afronden. Veel plezier in de toekomst!

I would also like to thank the committee members prof. William Curtin, prof. Stefan Diebels, prof. Stefan Luding, Steven Luitjens and prof. Mark Peletier for their constructive comments on my thesis and for traveling to Eindhoven. Furthermore, I would like to thank prof. Anton van Steenhoven for chairing the defense.

De industriële partners wil ik bedanken voor hun interesse in mijn werk. Mijn hulde gaat

uit naar Steven Luitjens en Koen van Os, namens Koninklijke Philips Electronics N.V., voor de begeleiding van Cyriel en de zorg voor de aansluiting van Cyriels werk bij het mijne. Aangezien Louis Saes namens Océ-Nederland B.V. aanvankelijk niet betrokken was bij mijn project, wil ik zeker zijn oprechte interesse in ons model en zijn scherpte tijdens menig bijeenkomst roemen.

Alice, Leo, Marc en Rachel ben ik erkentelijk voor een verscheidenheid aan zaken en de sfeer die daarom heen hing; Alice en Rachel voor alle administratieve zaken en voor het luisteren naar een enkele klacht die mij van het hart moest; Marc tevens voor het luisteren - al hebben mijn oren het nog drukker gehad - en niet te vergeten voor de hulp in het lab met mijn studenten; Leo voor zijn hulp op computergebied en de gezellige rookpauzes.

I express my sincere gratitude to all other MoM-members, in particular those with whom I had intense contact: Juan-Carlos for all the BBQs and for letting me be the unofficial godfather of Juan Carlos III; Kim for being my and Elitsa's adoption son; Leong Hien for letting JC bbq for us; Erica for serving as a UN soldier separating me and JC; Emanuela and Benoit. I also thank my roommates that made the walls of WH 4.13 vanish; Bart voor de format longs van deze wereld; Gwen voor haar (relatief) goedkope appartement; Rene; Rudy; Peter; Hamid; Murthy; Roy; Giulia; Agnese; Roman and Cem. Ik dank tevens David, Lieke en Willemijn van het Hora Est bestuur voor een gezellig jaar.

Lest best wil ik mijn ouders en Elitsa bedanken voor hun onvoorwaardelijke steun en liefde. Ik ben er zeker van dat ik mijn promotie niet zonder jullie steun had kunnen afronden. Zeker toen ik door een zwarte periode ging, was jullie liefde datgene wat me staande hield. Ondanks dat Elitsa en ik waarschijnlijk naar het buitenland gaan, zal ik de steun van mijn ouders nodig hebben en zeker ook voelen, al zal de communicatie wat meer via de telefoonlijn verlopen. Voor nu bedank ik jullie drie voor alles wat jullie voor mij gedaan hebben de afgelopen vier jaar!

Lars

Eindhoven, Juli 2012.

Curriculum Vitae

- 4.1.1984 Born in Tilburg, The Netherlands.
- 1996–2002 Sint Oelbertgymnasium (cum laude), Oosterhout, The Netherlands.
- 2002–2005 BSc (cum laude), Mechanical Engineering, Eindhoven University of Technology, Eindhoven, The Netherlands.
- 2005–2008 MSc (cum laude), Mechanics of Materials, Mechanical Engineering, Eindhoven University of Technology, Eindhoven, The Netherlands.
Research topic: ‘An experimental and computational study of laminated paperboard creasing and folding’, under the supervision of prof.dr.ir. M.G.D. Geers and dr.ir. R.H.J. Peerlings.
- 2008–2012 PhD, Mechanics of Materials, Mechanical Engineering, Eindhoven University of Technology, Eindhoven, The Netherlands.
Research topic: ‘Multiscale quasicontinuum modelling of fibrous materials’, under the supervision of prof.dr.ir. M.G.D. Geers and dr.ir. R.H.J. Peerlings.